

Lifshitz transition in some recently discovered iron based superconductors

By

Abyay Ghosh

PHYS03201504005

Raja Ramanna Centre for Advanced Technology, Indore

A thesis submitted to the

Board of Studies in Physical Sciences

In partial fulfilment of requirements

For the Degree of

DOCTOR OF PHILOSOPHY

of

HOMI BHABHA NATIONAL INSTITUTE

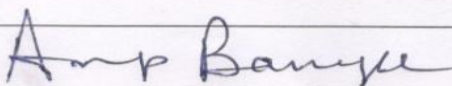
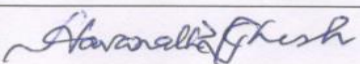
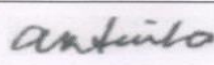
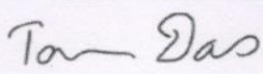
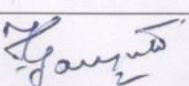
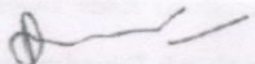
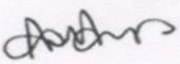
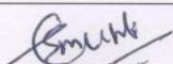


June, 2021

Homi Bhabha National Institute¹

Recommendations of the Viva Voce Committee

As members of the Viva Voce Committee, we certify that we have read the dissertation prepared by Abyay Ghosh entitled "Lifshitz transition in some recently discovered iron based superconductors" and recommend that it may be accepted as fulfilling the thesis requirement for the award of Degree of Doctor of Philosophy.

Chairman – Dr. Arup Banerjee,		15/06/2021
Guide / Convener – Dr. Haranath Ghosh		15/06/2021
Co-guide - Dr. Anil Kumar Sinha,		15/06/2021
Examiner - Dr. Tanmoy Das		15/06/2021
Member 1- Dr. Tapas Ganguli		15/06/2021
Member 2- Dr. A. K. Karnal		15/06/2021
Member 3 – Dr. Ashok Arya		15/06/2021
Member 3- Dr. S. M. Gupta		15/06/2021

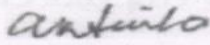
Final approval and acceptance of this thesis is contingent upon the candidate's submission of the final copies of the thesis to HBNI.

¹ This page is to be included only for final submission after successful completion of viva voce.

We hereby certify that we have read this thesis prepared under our direction and recommend that it may be accepted as fulfilling the thesis requirement.

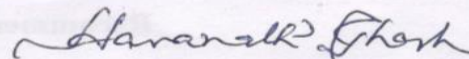
Date: 15/06/2021

Place: RRCAT



Signature

Co-guide (if any)



Signature

Guide

STATEMENT BY AUTHOR

This dissertation has been submitted in partial fulfilment of requirements for an advanced degree at Homi Bhabha National Institute (HBNI) and is deposited in the Library to be made available to borrowers under rules of the HBNI.

Brief quotations from this dissertation are allowable without special permission, provided that accurate acknowledgement of source is made. Requests for permission for extended quotation from or reproduction of this manuscript in whole or in part may be granted by the Competent Authority of HBNI when in his or her judgement the proposed use of the material is in the interests of scholarship. In all other instances, however, permission must be obtained from the author.



Abyay Ghosh

DECLARATION

I, hereby declare that the investigation presented in the thesis has been carried out by me.
The work is original and has not been submitted earlier as a whole or in part for a degree
/ diploma at this or any other Institution / University.



Abyay Ghosh

List of publications arising from the thesis

Journal:

1. Abyay Ghosh, S. Sen and Haranath Ghosh, "1144 Fe based superconductors: natural example of orbital selective self-doping and pressure induced Lifshitz transition", Computational Materials Science **186**, 109991 (2021).
2. W. Hong, L. Song, B. Liu, Z. Li, Z. Zeng, Y. Li, D. Wu, Q. Sui, T. Xie, S. Danilkin, Haranath Ghosh, Abyay Ghosh, J. Hu, L. Zhao, X. Zhou, X. Qiu, Shiliang Li, H. Luo, "Neutron spin resonance in a quasi-two-dimensional iron-based superconductor", Physical Review Letters **125**, 117002 (2020).
3. Abyay Ghosh, Soumyadeep Ghosh and Haranath Ghosh, "Electron correlation induced orbital selective Lifshitz transition in new hybrid 12442 iron based superconductors" Computational Materials Science **183**, 109802 (2020).
4. Abyay Ghosh, Haranath Ghosh, S. Sen, "Lifshitz transition in new doped 112 superconductors", Intermetallics **107**, 126–136 (2019).
5. T. Xie, D. Gong, Haranath Ghosh, Abyay Ghosh, M. Soda, T. Masuda, S. Itoh, F. Bourdarot, L.-P. Regnault, S. Danilkin, S. Li, H. Luo, "Neutron Spin Resonance in the 112-Type Iron-Based Superconductor", Physical Review Letters **120**, 137001 (2018).
6. Abyay Ghosh and Haranath Ghosh, "Orbital selective bandwidth renormalization, Lif-

shitz transition in Rare Earth doped 112 iron based superconductors", Computational Materials Science **160**, 62–71 (2019).

7. Abyay Ghosh and Haranath Ghosh, "Possible enhancement of superconductivity by Sb doping in rare earth doped 112 compounds: an ab-initio study" International Journal of Environmental Analytical Chemistry, 1-12 (2019).

Communicated:

1. Abyay Ghosh, Soumyadeep Ghosh and Haranath Ghosh, "Nematicity and crystal field splitting in newly discovered hybrid 12442 iron based superconductors", manuscript communicated (2021).

Conference:

1. Abyay Ghosh and Haranath Ghosh, "Density Functional Theory based first principles electronic structure study on 112 Fe based superconductors: Fermiology and Lifshitz transition", AIP Conference Proceedings **2005**, 050004 (2018).

Other Publications (not included in the thesis):

1. H. Ghosh, S. Sen, Abyay Ghosh, "Electronic origin of structural transition in 122 Fe based superconductors", Journal of Physics and Chemistry of Solids **102**, 157–167 (2017).

2. H. Ghosh, S. Ghosh, Abyay Ghosh, "Doping site identification in 112 iron pnictides through first principles core electron spectroscopic study", Journal of Synchrotron Radiation **26**, 4 (2019).

3. R. Pervin, Abyay Ghosh, H. Ghosh, P. M. Shirage, "Study of Transport Properties in Se Deficit and Fe Intercalated NbSe₂ Single Crystals: Experiment and Theory", Journal of Materials Science **55**, 250-262 (2020).

Abyay Ghosh

Dedicated

to

My Family

ACKNOWLEDGEMENTS

First of all, I want to express my sincere gratitude to my thesis supervisor Dr. Haranath Ghosh for his motivation, encouragement, continuous support and guidance during my Ph.D years. His constructive criticism, valuable suggestions, critical reading and deep involvement in all my scientific works have enriched me both scientifically as well as a person. I would like to acknowledge HBNI and RRCAT for the financial support during my Ph.D. I would like to thank Dr. H. Luo for experimental collaborations with us. I want to thank Dr. A. Banerjee, chairman of the doctoral committee and Head, HRDS for his valuable suggestions, comments. I am also extremely grateful to other members of my Ph.D doctoral committee - Dr. T. Ganguli, Dr. A. Arya, Dr. S. M. Gupta, Dr. A. K. Karnal for monitoring the progress of my research work over these years. I would like to thank Mr. P. Thander and the scientific computing group, Computer Centre, RRCAT for providing computational facility. I am also thankful to all the members of SUS and HRDS for providing enjoyable and stimulating working atmosphere. My special thanks are also to my seniors Smritida, Tufanda, Gangada, Arijitda, Debada; my juniors Soumyadeep, Joydip, Jayanta, Nitish for their help and company during this period. I would also like to acknowledge Smritida, Soumyadeep, Amit for fruitful scientific discussions and collaborations. It is my pleasure to thank all my friends, specially Sahadeb, Azam, Sabyasachi, Kiran, Arka for their help, positive support and fruitful advices at several stages of my PhD days. Finally, I would like to convey my deepest regards to my parents, my brother Bikram, my wife Mousumi and all the members of Ghosh-family for their never-ending love, affection and support to me in all situations.

Contents

List of Figures	xviii
------------------------	--------------

List of Tables	xxix
-----------------------	-------------

1 Introduction	2
1.1 High temperature superconductivity	2
1.2 Iron based superconductors	4
1.2.1 1111 family	4
1.2.2 122 family	5
1.2.3 111 family	6
1.2.4 11 family	6
1.3 Some recently discovered Fe based superconductors	7
1.3.1 112 compounds	7
1.3.2 1144 compounds	9
1.3.3 12442 compounds	12
1.4 Lifshitz transition and Superconductivity in iron based superconductors .	13

2	Theory and Computational methods	18
2.1	Lifshitz Transition (LT)	18
2.1.1	Lifshitz transition in weakly interacting electron gas	19
2.2	Density Functional Theory(DFT):	26
2.2.1	DFT for practical electronic structure calculations:	35
2.2.2	Virtual Crystal Approximation (VCA):	43
2.2.3	DFT+U method:	44
3	Electronic structure, Lifshitz transition and its possible impact on superconductivity in 112 compounds	47
3.1	Theory and Computational Method	48
3.2	Electronic structure of doped 112 materials	50
3.2.1	La doping at Ca site	50
3.2.2	Ni, Co and Mn doping at Fe site	56
3.3	Discussions and Conclusions	69
4	Effect of rare earth (<i>f</i>-atom) doping on 112 materials; orbital selectivity, bandwidth renormalization and Lifshitz transition	70
4.1	Theory and Computational Method	71
4.2	Relative stability of rare earth doped 112 materials and Formation enthalpy	72
4.3	Electronic structure of rare earth doped 112 materials	73
4.3.1	Ce doping at Ca site	73
4.3.2	Pr doping at Ca site	77

4.3.3	Nd doping at Ca site	78
4.3.4	Sm doping at Ca site	80
4.3.5	Gd doping at Ca site	82
4.4	Bandwidth renormalization and orbital selectivity	87
4.5	Conclusions	95
5	Doping As site sensitivity in 112 compounds	98
5.1	Theory and Computational Method	99
5.2	Sb doping at As site - chain vs layer	100
5.3	Electronic structure of the Sb doped 112 compounds	105
5.4	Effect of RE/Sb doping on Fe partial DOS	111
5.5	Effect of only RE or RE/Sb doping on As partial DOS	112
5.6	Discussions and Conclusions	115
6	Chemical pressure induced orbital selective Lifshitz transition in hybrid 1144 compounds	116
6.1	Theory and Computational Method	117
6.2	Electronic structure of 1144 materials	118
6.2.1	CaAFe ₄ As ₄ (A = K, Rb, Cs)	119
6.2.2	SrAFe ₄ As ₄ (A = K, Rb, Cs)	127
6.2.3	EuAFe ₄ As ₄ (A = K, Rb, Cs)	133
6.3	Chemical pressure induced Orbital selective Lifshitz transition	142

6.4	Effect of electron correlation and spin orbit coupling on the electronic structure	145
6.5	Orbital Selective Bandwidth renormalization	150
6.6	Conclusions	154
7	Correlation induced Lifshitz transition and nematicity in 12442 compounds	156
7.1	Theory and Computational Method	157
7.2	Electronic structure of 12442 compounds	158
7.3	Effect of electron correlation and Spin Orbit Coupling (SOC) on the electronic structure of 12442 compounds	170
7.4	Wannier fitted band structure of 12442 compounds	178
7.5	Orbital Anisotropy	180
7.6	Intrinsic band splitting	185
7.7	Crystal field splitting	190
7.8	Conclusions	192
8	Summary and Conclusions	196
	Bibliography	203

List of Figures

1.1	Timeline of superconductors showing yearwise evolution of superconducting transition temperature in different materials.	3
1.2	Different families of Fe based superconductors.	4
1.3	Recently discovered families of Fe based superconductors.	7
2.1	Example of the Lifshitz transition with the change of the Fermi surface topology (disruption of the "neck" of a Fermi surface).	19
2.2	Example of the topological transition with the change of the Fermi surface topology (disruption of the "neck" of a Fermi surface).	22
2.3	Schematic diagram of Kohn Sham approach	35
3.1	[137] Calculated Fermi surfaces of $\text{Ca}_{1-x}\text{La}_x\text{FeAs}_2$ system within VCA method. Doping levels (x) of La are (a) $x = 0.10$, (b) $x = 0.15$, (c) $x = 0.20$, (d) $x = 0.25$, and (e) $x = 0.30$ respectively. We have shown three different views of FSs in the same row for a particular value of doping. In middle and last column, FSs in 45° clockwise rotated BZ are shown. Upper view of the FSs is presented in the middle column.	51

3.2	[137] Calculated band structures of $\text{Ca}_{1-x}\text{La}_x\text{FeAs}_2$ system within VCA method around high symmetry points. Doping levels are (a) $x = 0.10$, (b) $x = 0.15$, (c) $x = 0.20$, (d) $x = 0.25$, and (e) $x = 0.30$. The corresponding bands around Γ point for various doping values along with orbital natures are shown in (f), (g), (h), (i), (j). Fermi level is denoted by horizontal red line at zero energy.	52
3.3	[137] Calculated orbital projected band structures of undoped CaFeAs_2 around high symmetry points. The weight of the different Fe 3d and As 4p orbitals for different bands is shown with varying sizes of the circles and colours - (a) d_{yz} , (b) d_{xz} , (c) $d_{x^2-y^2}$, (d) d_{xy} , (e) d_{z^2} , and (f) $4p_z$. Sizes of the circles correspond to the degree of relative contributions. Fermi level is denoted by horizontal dotted green line at zero energy.	54
3.4	[137] Fermi surfaces of $\text{Ca}_{0.82}\text{La}_{0.18}\text{Fe}_{1-y}\text{Ni}_y\text{As}_2$ for doping levels (a) $y = 0.005$, (b) $y = 0.010$, (c) $y = 0.015$, and (d) $y = 0.020$. We have shown three different views of FSs in the same row for a particular value of doping. In middle and last column, FSs in 45° clockwise rotated BZ are shown. Upper view of the FSs is presented in the middle column.	57
3.5	[137] Band structures of $\text{Ca}_{0.82}\text{La}_{0.18}\text{Fe}_{1-y}\text{Ni}_y\text{As}_2$ for doping levels (a) $y = 0.005$, (b) $y = 0.010$, (c) $y = 0.015$, and (d) $y = 0.020$. The corresponding bands around Γ point with the respective dopings along with orbital nature is shown in (e), (f), (g), (h). Fermi level is denoted by horizontal red line at zero energy.	58

- 3.6 [137] Calculated Fermi surfaces of $\text{Ca}_{1-x}\text{La}_x\text{Fe}_{1-y}\text{Co}_y\text{As}_2$ system within VCA method. We have shown three different views of FSs in the same row for same doping . Doping levels are (a) $x = 0.10, y = 0.03$; (b) $x = 0.10, y = 0.05$; (c) $x = 0.10, y = 0.10$; and (d) $x = 0.10, y = 0.20$. We have shown three different views of FSs in the same row for a particular value of doping. In middle and last column, FSs in 45° clockwise rotated BZ are shown. Upper view of the FSs is presented in the middle column. 62
- 3.7 [137] Band structures of $\text{Ca}_{1-x}\text{La}_x\text{Fe}_{1-y}\text{Co}_y\text{As}_2$ for doping levels (a) $x = 0.10, y = 0.03$; (b) $x = 0.10, y = 0.05$; (c) $x = 0.10, y = 0.10$; and (d) $x = 0.10, y = 0.20$. The corresponding bands around Γ point with the respective dopings along with orbital nature is shown in (e), (f), (g), (h). Fermi level is denoted by horizontal red line at zero energy. 63
- 3.8 [137] Calculated Fermi surfaces of $\text{Ca}_{1-x}\text{La}_x\text{Fe}_{1-y}\text{Mn}_y\text{As}_2$ system within VCA method. We have shown three different views of FSs in the same row for same doping . Doping levels are (a) $x = 0.10, y = 0.03$; (b) $x = 0.10, y = 0.05$; (c) $x = 0.10, y = 0.10$; and (d) $x = 0.10, y = 0.20$. We have shown three different views of FSs in the same row for a particular value of doping. In middle and last column, FSs in 45° clockwise rotated BZ are shown. Upper view of the FSs is presented in the middle column. . 64
- 3.9 [137] Band structures of $\text{Ca}_{1-x}\text{La}_x\text{Fe}_{1-y}\text{Mn}_y\text{As}_2$ for doping levels (a) $x = 0.10, y = 0.03$; (b) $x = 0.10, y = 0.05$; (c) $x = 0.10, y = 0.10$; and (d) $x = 0.10, y = 0.20$. Fermi level is denoted by horizontal red line at zero energy. 65
- 3.10 Phase diagram of 112 compounds with (a)[31] La-doping, (b)[40] Ni doping with La co-doping (c) doping normalized to Lifshitz transition. 65

3.11	[137] (a) Total DOS of La doped ($x = 0.125$) 112, (b) total DOS of Co doped at Fe site 112 with doping level $x = 0.125$, $y = 0.125$; (c) total DOS of Mn doped at Fe site 112 with doping level $x = 0.125$, $y = 0.125$; (d) spin dependent partial DOS of Co in Co doped 112 with doping level $x = 0.125$, $y = 0.125$; (e) spin dependent partial DOS of Mn in Mn doped 112 with doping level $x = 0.125$, $y = 0.125$; and (f) difference in up and down spin density of states of Co and Mn in Co and Mn doped 112 respectively.	66
4.1	[138] Calculated Fermi surfaces (FSs) and band structures (BNSs) of $\text{Ca}_{1-x}\text{Ce}_x\text{FeAs}_2$ system within VCA method. We have shown the FS and BNS with same doping in the same row. Doping levels (x) of Ce are (a) $x = 0.01$, (b) $x = 0.03$, (c) $x = 0.05$, (d) $x = 0.10$ and (e) $x = 0.15$ respectively and (f), (g), (h), (i), (j) show BNSs with respective doping. . .	75
4.2	[138] Calculated orbital projected band structures of undoped CaFeAs_2 around the high symmetry points. The weight of the different Fe 3d and As 4p orbitals for different bands is shown with varying size of the circles and colours. Sizes of the circles correspond to degree of relative contribution. Fermi level is denoted by horizontal green line at zero energy. . .	76
4.3	[138] Calculated Fermi surfaces (FSs) and band structures (BNSs) of $\text{Ca}_{1-x}\text{Pr}_x\text{FeAs}_2$ system within VCA method. We have shown the FS and BNS with same doping in the same row. Doping levels (x) of Pr are (a) $x = 0.01$, (b) $x = 0.03$, (c) $x = 0.05$, (d) $x = 0.10$ respectively and (e), (f), (g), (h) show BNSs with respective doping.	79

4.4	[138] Calculated Fermi surfaces (FSs) and band structures (BNSs) of $\text{Ca}_{1-x}\text{Nd}_x\text{FeAs}_2$ system within VCA method. We have shown the FS and BNS with same doping in the same row. Doping levels (x) of Nd are (a) $x = 0.01$, (b) $x = 0.03$, (c) $x = 0.05$, (d) $x = 0.10$ respectively and (e), (f), (g), (h) show BNSs with respective doping.	81
4.5	[138] Calculated Fermi surfaces (FSs) and band structures (BNSs) of $\text{Ca}_{1-x}\text{Sm}_x\text{FeAs}_2$ system within VCA method. We have shown the FS and BNS with same doping in the same row. Doping levels (x) of Sm are (a) $x = 0.01$, (b) $x = 0.03$, (c) $x = 0.05$, (d) $x = 0.10$ respectively and (e), (f), (g), (h) show BNSs with respective doping.	83
4.6	[138] Calculated Fermi surfaces (FSs) and band structures (BNSs) of $\text{Ca}_{1-x}\text{Gd}_x\text{FeAs}_2$ system within VCA method. We have shown the FS and BNS with same doping in the same row. Doping levels (x) of Gd are (a) $x = 0.01$, (b) $x = 0.03$, (c) $x = 0.05$, (d) $x = 0.10$ respectively and (e), (f), (g), (h) show BNSs with respective doping.	85
4.7	[138] (a) Variation of calculated bandwidth of d_{xy} band with doping for different rare earth elements, (b) variation of calculated bandwidth of (d_{yz}, d_{xz}) band with doping for different rare earth elements, and (c) variation of band renormalization ratio with doping for different rare earth elements. The shaded region in (c) is the region of onset of Lifshitz transition. The slope of R vs doping in (c) changes sign whenever there is onset of electronic topological transition.	92
5.1	[137] Fermi surfaces of $\text{Ca}_{1-x}\text{La}_x\text{Fe}(\text{As}_{1-y}\text{Sb}_y)_2$ for Sb doping at As chain: (a) for $x = 0.15$, $y = 0.10$; (b) for $x = 0.20$, $y = 0.1$; and (c) for $x = 0.20$, $y = 0.15$. Two different views of FSs have been shown in the same row at a particular doping.	101

5.2	[137] Fermi surfaces of $\text{Ca}_{1-x}\text{La}_x\text{Fe}(\text{As}_{1-y}\text{Sb}_y)_2$ for Sb doping at FeAs layer: (a) $x = 0.15$ (b) $x = 0.20$; (c) $x = 0.15$, $y = 0.10$; and (d) for $x = 0.20$, $y = 0.10$	102
5.3	[137] Partial density of states of As for (a) undoped (without Sb doping) and Sb doping at two different sites (As -chain and FeAs layer), (b) Sb doping at As chain, and (c) Sb doping at FeAs layer of $\text{Ca}_{1-x}\text{La}_x\text{Fe}(\text{As}_{1-y}\text{Sb}_y)_2$. Fermi level is denoted by vertical black line at zero energy.	103
5.4	[139] Electronic structure of $\text{Ca}_{0.82}\text{La}_{0.18}\text{Fe}_{0.96}\text{Ni}_{0.04}\text{As}_2$; (a) band structure, (b) orbital projected band, (c) 2D Fermi surface, (d) 3D Fermi surface.	104
5.5	[140] Band structure of undoped CaFeAs_2 . The orbital weight of different bands is shown with circles of varying radius and designating a particular colour to a particular orbital (Fe-3d, As-4p).	105
5.6	[140] Calculated (a) BNSs, (b) DOS, and (c) FSs of $\text{CaFe}(\text{As}_{0.95}\text{Sb}_{0.05})_2$ system within VCA method. In (c) two different view of the same FSs is presented.	106
5.7	[140] Calculated BNSs of $\text{Ca}_{0.90}\text{R}_{0.10}\text{Fe}(\text{As}_{0.95}\text{Sb}_{0.05})_2$ system within VCA method for rare earth = (a) Pr, (b) Nd, (c) Sm.	107
5.8	[140] Calculated FSs of $\text{Ca}_{0.90}\text{R}_{0.10}\text{Fe}(\text{As}_{0.95}\text{Sb}_{0.05})_2$ system for RE = (a) Pr, (b) Nd, (c) Sm. We have shown two different views of FS with same doping in a particular row.	109
5.9	[140] Partial density of states of Fe with different RE/Sb doping at As chain. The magnified partial DOS of Fe at a smaller energy window is shown in the inset.	111

5.10	[140] Partial DOS of As in rare earth doped CaFeAs_2 . The magnified partial DOS of As at a smaller energy window is shown in the inset. . . .	112
5.11	[140] Partial DOS of As in rare earth and Sb co-doped CaFeAs_2 . The magnified partial DOS of As at a smaller energy window is shown in the inset.	113
6.1	[141] Crystal structure of 1144 iron based superconducting materials. . .	118
6.2	[141] Calculated orbital projected band structures of (a) $\text{CaKFe}_4\text{As}_4$, (b) $\text{CaRbFe}_4\text{As}_4$, and (c) $\text{CaCsFe}_4\text{As}_4$ around high symmetry points. The weight of the different Fe 3d and As 4p orbitals for different bands is shown with varying sizes of the circles and colours. Sizes of the circles correspond to degree of relative contributions. Fermi level is denoted by the horizontal green line at the zero energy.	120
6.3	[141] Calculated orbital projected Fermi surfaces (FSs) on different Fe-3d and As- p_z orbitals for (A) $\text{CaKFe}_4\text{As}_4$, (B) $\text{CaRbFe}_4\text{As}_4$, and (C) $\text{CaCsFe}_4\text{As}_4$. The FSs are derived from (a) $d_{x^2-y^2}$, (b) d_{xy} , (c) d_{xz} , (d) d_{yz} , (e) d_{z^2} and (e) $4p_z$ orbitals. The colour scheme denotes increased contributions from different orbitals as we move from blue to red.	122
6.4	[141] Partial density of states of different Fe-3d and As-4p orbital derived states for (a) $\text{CaKFe}_4\text{As}_4$, (b) $\text{CaRbFe}_4\text{As}_4$, and (c) $\text{CaCsFe}_4\text{As}_4$. The Fermi level is denoted by the dotted blue vertical line at zero energy. . . .	125
6.5	[141] Calculated orbital projected band structures of (a) $\text{SrKFe}_4\text{As}_4$, (b) $\text{SrRbFe}_4\text{As}_4$, and (c) $\text{SrCsFe}_4\text{As}_4$ around high symmetry points. The weight of the different Fe 3d and As 4p orbitals for different bands is shown with varying size of the circles and colours. Sizes of the circles correspond to degree of relative contribution. Fermi level is denoted by horizontal green line at zero energy.	128

6.6	[141] Calculated projected Fermi surfaces (FSs) on different Fe-3d and As- p_z orbitals for (A) SrKFe ₄ As ₄ , (B) SrRbFe ₄ As ₄ , and (C) SrCsFe ₄ As ₄ . The FSs are derived from (a) $d_{x^2-y^2}$, (b) d_{xy} , (c) d_{xz} , (d) d_{yz} , (e) d_{z^2} , and (e) $4p_z$ orbitals. The colour scheme denotes increased contribution from different orbitals as we move from blue to red.	129
6.7	[141] Partial density of states of different Fe-3d and As-4p orbital derived states for (a) SrKFe ₄ As ₄ , (b) SrRbFe ₄ As ₄ , and (c) SrCsFe ₄ As ₄ . The Fermi level is denoted by dotted blue vertical line at zero energy.	131
6.8	[141] Calculated orbital projected band structures of (a) EuKFe ₄ As ₄ , (b) EuRbFe ₄ As ₄ , and (c) EuCsFe ₄ As ₄ around high symmetry points. The weight of the different Fe 3d and As 4p orbitals for different bands is shown with varying size of the circles and colours. Sizes of the circles correspond to degree of relative contribution. Fermi level is denoted by horizontal green line at zero energy.	134
6.9	[141] Calculated projected Fermi surfaces (FSs) on different Fe-3d and As- p_z orbitals for (A) EuKFe ₄ As ₄ , (B) EuRbFe ₄ As ₄ , and (C) EuCsFe ₄ As ₄ . The FSs are derived from (a) $d_{x^2-y^2}$, (b) d_{xy} , (c) d_{xz} , (d) d_{yz} , (e) d_{z^2} , and (e) $4p_z$ orbitals. The colour scheme denotes increased contribution from different orbitals as we move from blue to red.	135
6.10	[141] Partial density of states of different Fe-3d and As-4p orbital derived states for (a) EuKFe ₄ As ₄ , (b) EuRbFe ₄ As ₄ , and (c) EuCsFe ₄ As ₄ . The Fermi level is denoted by dotted blue vertical line at zero energy.	136
6.11	[141] Partial density of states of different Eu-5d orbital derived states for (a) EuKFe ₄ As ₄ , (b) EuRbFe ₄ As ₄ , and (c) EuCsFe ₄ As ₄ . The Fermi level is denoted by dotted blue vertical line at zero energy.	137

6.12	[141] The evolution of inner most hole-like Fermi surface and electron-like Fermi surfaces for different 1144 compounds - A: (a) $\text{CaKFe}_4\text{As}_4$, (b) $\text{CaRbFe}_4\text{As}_4$, (c) $\text{CaCsFe}_4\text{As}_4$, B: (a) $\text{SrKFe}_4\text{As}_4$, (b) $\text{SrRbFe}_4\text{As}_4$, (c) $\text{SrCsFe}_4\text{As}_4$, C: (a) $\text{EuKFe}_4\text{As}_4$, (b) $\text{EuRbFe}_4\text{As}_4$, and (c) $\text{EuCsFe}_4\text{As}_4$. .	141
6.13	[141] The evolution of (A) hole-like bands around Γ -point and (B) electron-like bands around M-point for different 1144 compounds - (a) $\text{CaKFe}_4\text{As}_4$, (b) $\text{CaRbFe}_4\text{As}_4$, (c) $\text{CaCsFe}_4\text{As}_4$, (d) $\text{SrKFe}_4\text{As}_4$, (e) $\text{SrRbFe}_4\text{As}_4$, (f) $\text{SrCsFe}_4\text{As}_4$, (g) $\text{EuKFe}_4\text{As}_4$, (g) $\text{EuRbFe}_4\text{As}_4$, and (i) $\text{EuCsFe}_4\text{As}_4$	142
6.14	[141] Comparison of electronic band structure of EuA44 compounds for various A within GGA and GGA+U methods. Indicated values of U are in eV.	146
6.15	[141] Electronic structure within GGA+U method for – (a) EuCs44 with Fe U=3.0, Eu U=6.0 without spin orbit coupling (SOC), and (b) EuK44 with Fe U=3.0, Eu U=6.0, (c) EuRb44 with Fe U=3.0, Eu U=6.0, (d) EuCs44 with Fe U=3.0, Eu U=6.0 in presence of SOC. Indicated values of U are in eV.	148
7.1	[142] Crystal structure of 12442 family of iron based superconductors. . .	159
7.2	[142] Calculated orbital projected band structures (BNSs) on different Fe-3d orbitals for (A) $\text{KCa}_2\text{Fe}_4\text{As}_4\text{F}_2$, (B) $\text{RbCa}_2\text{Fe}_4\text{As}_4\text{F}_2$, and (C) $\text{CsCa}_2\text{Fe}_4\text{As}_4\text{F}_2$ around high symmetry points. Individual orbital contribution is shown with individual colours and the size of the circles are proportional to orbital weight. The Fermi level is denoted by dashed red horizontal line at zero energy.	161
7.3	[142] Partial density of states of different Fe-3d and As-4p orbital derived states for (A) $\text{KCa}_2\text{Fe}_4\text{As}_4\text{F}_2$, (B) $\text{RbCa}_2\text{Fe}_4\text{As}_4\text{F}_2$, and (C) $\text{CsCa}_2\text{Fe}_4\text{As}_4\text{F}_2$. The Fermi level is denoted by dotted blue vertical line at zero energy. . .	163

7.4	[142] Calculated orbital projected Fermi surfaces (FSs) of (A) $\text{KCa}_2\text{Fe}_4\text{As}_4\text{F}_2$, (B) $\text{RbCa}_2\text{Fe}_4\text{As}_4\text{F}_2$, and (C) $\text{CsCa}_2\text{Fe}_4\text{As}_4\text{F}_2$. Weights of the different Fe 3d orbitals for different FSs are shown using varying colours. The "red" colour denotes 'maximum' contribution while "blue" denotes 'minimum' contribution.	165
7.5	[142] Upper view of the Fermi surfaces. Each hole and electron pocket is designated with different names – $\alpha, \beta, \gamma, \delta$ and $\theta, \epsilon, \zeta, \eta$ respectively. . .	167
7.6	[142] Comparison of calculated band structures using GGA and GGA+U methods respectively for (A) $\text{KCa}_2\text{Fe}_4\text{As}_4\text{F}_2$, (B) $\text{RbCa}_2\text{Fe}_4\text{As}_4\text{F}_2$, and (C) $\text{CsCa}_2\text{Fe}_4\text{As}_4\text{F}_2$	170
7.7	[142] Comparison of calculated Fermi surfaces using GGA and GGA+U methods respectively for (A) $\text{KCa}_2\text{Fe}_4\text{As}_4\text{F}_2$, (B) $\text{RbCa}_2\text{Fe}_4\text{As}_4\text{F}_2$, and (C) $\text{CsCa}_2\text{Fe}_4\text{As}_4\text{F}_2$ for different U (in eV).	171
7.8	[142] Change in total density of states of (a) $\text{KCa}_2\text{Fe}_4\text{As}_4\text{F}_2$, (b) $\text{RbCa}_2\text{Fe}_4\text{As}_4\text{F}_2$, and (c) $\text{CsCa}_2\text{Fe}_4\text{As}_4\text{F}_2$ with different U values in eV.	173
7.9	[142] Band structure along Γ -X direction used to measure bandwidth. Hole like bands with different orbital characters around Γ -point are marked as α, β, γ , and δ	176
7.10	[142] Comparison of calculated band structures within GGA and GGA + Spin Orbit Coupling (SOC) for (a) $\text{KCa}_2\text{Fe}_4\text{As}_4\text{F}_2$, (b) $\text{RbCa}_2\text{Fe}_4\text{As}_4\text{F}_2$, and (c) $\text{CsCa}_2\text{Fe}_4\text{As}_4\text{F}_2$ respectively.	177
7.11	[142] Tight binding fitted band structures of (A) $\text{KCa}_2\text{Fe}_4\text{As}_4\text{F}_2$, (B) $\text{RbCa}_2\text{Fe}_4\text{As}_4\text{F}_2$, and (C) $\text{CsCa}_2\text{Fe}_4\text{As}_4\text{F}_2$	178
7.12	(Colour online) Parital density of states of different Fe-3d orbitals for (a) $\text{KCa}_2\text{Fe}_4\text{As}_4\text{F}_2$, (b) $\text{RbCa}_2\text{Fe}_4\text{As}_4\text{F}_2$, and (c) $\text{CsCa}_2\text{Fe}_4\text{As}_4\text{F}_2$	182

7.13 (Colour online) Orbital character of different bands for (a) $\text{KCa}_2\text{Fe}_4\text{As}_4\text{F}_2$, (b) $\text{RbCa}_2\text{Fe}_4\text{As}_4\text{F}_2$, and (c) $\text{CsCa}_2\text{Fe}_4\text{As}_4\text{F}_2$. The contribution from each orbital is shown with individual colour and orbital weight are proportional to size of the circles.	183
7.14 (Colour online) Calculated orbital character of the Fermi surfaces for (A) $\text{KCa}_2\text{Fe}_4\text{As}_4\text{F}_2$, (B) $\text{RbCa}_2\text{Fe}_4\text{As}_4\text{F}_2$, and (C) $\text{CsCa}_2\text{Fe}_4\text{As}_4\text{F}_2$. The or- bital nature d_{xy} , d_{yz} and d_{xz} are shown in column (a), (b) and (c) respec- tively. The relative contribution of the different Fe 3d orbitals for different FSs are shown using varying colours. The "red" colour denotes ‘maxi- mum’ contribution while "blue" colour denotes ‘minimum’ contribution. .	184
7.15 (Colour online) Orbital character of different bands for (a) $\text{KCa}_2\text{Fe}_4\text{As}_4\text{F}_2$, (b) $\text{RbCa}_2\text{Fe}_4\text{As}_4\text{F}_2$, and (c) $\text{CsCa}_2\text{Fe}_4\text{As}_4\text{F}_2$. The contribution from each orbital is shown with individual colour and orbital weight are proportional to size of the circles.	186
7.16 (Colour online) Splitting of bands around Brillouin zone corner for (a) $\text{KCa}_2\text{Fe}_4\text{As}_4\text{F}_2$, (b) $\text{RbCa}_2\text{Fe}_4\text{As}_4\text{F}_2$, and (c) $\text{CsCa}_2\text{Fe}_4\text{As}_4\text{F}_2$ calculated with GGA.	188
7.17 (Colour online) Splitting of bands around brillouin zone corner for (a) $\text{KCa}_2\text{Fe}_4\text{As}_4\text{F}_2$, (b) $\text{RbCa}_2\text{Fe}_4\text{As}_4\text{F}_2$, and (c) $\text{CsCa}_2\text{Fe}_4\text{As}_4\text{F}_2$ calculated with GGA + spin orbit coupling (SOC).	189
7.18 Tight binding fitted band structure of (a) $\text{KCa}_2\text{Fe}_4\text{As}_4\text{F}_2$, (b) $\text{RbCa}_2\text{Fe}_4\text{As}_4\text{F}_2$, and (c) $\text{CsCa}_2\text{Fe}_4\text{As}_4\text{F}_2$	190
7.19 Calculated crystal field splitting of Fe-3d orbitals in the tight binding parametrization for (a) $\text{KCa}_2\text{Fe}_4\text{As}_4$, (b) $\text{RbCa}_2\text{Fe}_4\text{As}_4$, (c) $\text{CsCa}_2\text{Fe}_4\text{As}_4$.	191

List of Tables

1.1	Highest T_c and Lifshitz transition	15
3.1	Magnetic Moment (in μB)	68
4.1	Formation energy of $\text{Ca}_{0.875}\text{RE}_{0.125}\text{FeAs}_2$	73
4.2	Doping dependent bandwidth of $\text{Ca}_{1-x}\text{RE}_x\text{FeAs}_2$	87
4.3	Variation of c-axis and FeAs layer to As-chain distance of $\text{Ca}_{1-x}\text{RE}_x\text{FeAs}_2$	90
5.1	Variation of c-axis and FeAs layer to As-chain distance with different doping	104
5.2	Lattice parameters of the undoped and different doped 112 compounds . .	106
5.3	Variation of FeAs layer to As-chain distance, Z_{As} , and $\angle As - Fe - As$ with different doping	114
6.1	Atomic radius of different substituted elements	143
6.2	Highest T_c and Lifshitz transition	144
6.3	Bandwidth of different 1144 IBSCs	151

7.1	Comparison of theoretically calculated structural parameters with that of experimental results ([55])	158
7.2	Pocket size of electron and hole like FSs	168
7.3	Bandwidth of different 12442 IBSCs	174
7.4	Nearest neighbor (NN) hoppings t_{ij} (in eV) from maximally projected Wannier function calculation	179
7.5	Band splitting (BS) of d_{xz} & d_{yz}	188

Chapter 8

Summary and Conclusions

The thesis deals with detailed electronic structure studies of several recently discovered families of Fe based superconductors like i) $\text{Ca}_{1-x}\text{R}_x\text{Fe}_{1-y}\text{T}_y(\text{As}_{1-z}\text{Sb}_z)_2$ [112-family] (R = Rare Earth metals: La, Ce, Pr, Nd, Sm, Gd; T = Transition Metals: Co, Ni, Mn), ii) $\text{AeAFe}_4\text{As}_4$ [1144-family] (Ae = Alkaline or rare earth metal: Ca, Sr or Eu; A = Alkali metals: K, Rb, Cs), iii) $\text{ACa}_2\text{Fe}_4\text{As}_4\text{F}_2$ [12442-family] (A = K, Rb, Cs). Several important aspects of these large number of iron based compounds are addressed with regard to their evolution of electronic structure with doping, chemical pressure, electron correlation and spin orbit coupling. Many important new results are emerged from our discussions in the previous chapters of the thesis.

A detailed electronic structure investigations on $\text{Ca}_{1-x}\text{La}_x\text{FeAs}_2$ [La-112] compound presented in Chapter-3 correlates the evolution of electronic structure with the phase diagram of this compound. In the theoretically computed electronic structures of 112 compounds, there exists three hole like bands and two electron like bands crossing the Fermi level (E_F). The orbital resolved electronic structure reveals that the two upper lying hole like bands have dominantly d_{xy} and $d_{xz/yz}$ character respectively, whereas the lower lying hole like band above the E_F possess dominant As-4 p_z character. The hole like bands around the Fermi level starts shifting below it with gradually increasing La doping. At about

15% doping, the hole like band having $4p_z$ character just touches the E_F leading to a band singularity at this doping where the highest T_c is observed experimentally. If we increase the doping further, the $4p_z$ band shifts below the E_F causing segregation of the inner most Fermi surface (FS). This kind of electronic topological modifications are known as Lifshitz transition (LT) which is found/predicted to have a great impact on physical properties of different compounds. In iron based superconductors the highest superconducting transition temperature is found in close proximity to LT. When La doping is increased upto 25%, all the three hole like bands are drifted below the E_F leading to full disappearance of hole FSs around the Γ -point. At this particular doping where Lifshitz transition occurs, superconductivity is completely suppressed. Our study on La doped 112 with Ni, Co co-doping at Fe site also disclose same kind of correlation among superconductivity, band singularity and Lifshitz transition. Therefore, interrelationship between superconductivity and Lifshitz like topological transition in this compound is established by comparing the experimental phase diagram with electronic structure. Our *ab initio* spin polarised electronic structure calculations with striped antiferromagnetic state as magnetic ground state show significant reduction in local Fe magnetic moment due to Co doping with small Co local moment. Therefore, Co doping favours superconductivity by reducing Fe magnetic moment. On the other hand, the presence of large Fe as well as Mn magnetic moment in Mn doped 112 compounds explains fatality of Mn doping regarding superconductivity.

Chapter-4 is attributed to the discussion on evolution of electronic structure of different rare earth doped 112 compounds. The superconducting transition temperature in 112 compounds with rare earth doping $\text{Ca}_{1-x}\text{R}_x\text{FeAs}_2$ ($\text{R} = \text{Ce, Pr, Nd, Sm, Gd}$) (R-112), is observed to gradually decrease as one moves from the left (La) to right (Gd) of the lanthanides series. Inspired by the success of electronic structure calculations on La-112 compounds, we extended our investigations on the electronic structure of each R-112 compounds with varying rare earth doping. A common characteristic in the electronic structure of all the RE doped 112 compounds is a gradual disappearance of the hole like Fermi surfaces near Γ -point with increased doping leading to Lifshitz transition. A sys-

tematic trend of Lifshitz transition at lower doping as we gradually move from left to right of the lanthanide series may explain the relative occurrence of lower T_c at a particular doping in R-112 compounds consisting rare earth ions with higher atomic number. A delicate inter connection between the bandwidth renormalization and Lifshitz transition is established where “orbital selectivity” is in built. These suggests that “orbital selectivity” would also play a decisive role in the superconductivity of the RE doped 112 materials. To demonstrate the connection between bandwidth renormalization and Lifshitz transition and their implications on superconductivity of these compounds we have calculated the bandwidth of the hole like bands derived from d_{xy} , $d_{xz/yz}$ and $4p_z$ orbitals. Rare earth doping does not affect all the bands equally. The renormalization ratio (RR) defined as the ratio of bandwidth of d_{xy} band to the bandwidth of $d_{xz/yz}$ band shed light on the orbital selectivity of the bands. The variation of RR with different rare earth doping is very much similar to the variation of bandwidth of d_{xy} . The RR vs doping plot shows that the onset of the Lifshitz transition corresponds to the change in sign of the slope of RR vs doping plot. This indicates to the fact that there is a connection between orbital selectivity and Lifshitz transition. The RE doping at the Ca site renormalizes the bandwidth of the Fe-3d derived hole like bands around Γ -point in such a way that it in turn influences the topological changes in FSs leading to orbital selective Lifshitz transition.

The effect of Sb doping at As site is the main topic of discussion of Chapter-5. It is very interesting that the 112 compounds posses As atoms at two different crystallographic positions – i) at FeAs-layer with valency -3 and ii) at As-chain in between the FeAs-layers with valency -1. The As-chain in between the FeAs-layers is conducting. As the electronic structure investigations on La-112 compounds reveal a significant contribution of As- $4p_z$ orbitals to the hole like bands around the E_F as well as to the density of states (DOS), the effect of Sb doping at both the As sites is worth investigating. The modifications in FSs of the La-112 with Sb co-doping are found to be significantly different for Sb doping at the As site of As-chain and FeAs-layer. The hole like FSs around Γ -point and electron like FS around X-point diminish due to Sb doping at As-chain. These mod-

ifications are quite different for Sb doping at FeAs-layer. In the later case, both the hole and the electron like FSs surge in size and become more 2D like. From the diminishing electron pockets around X-point due to Sb doping at As-chain it may be concluded that the nesting exists only between the 3D hole like pockets around the Γ/Z -point and the 2D electron like pockets around M-point. This observation is confirmed by neutron spin resonance experiments where only a 2D spin resonance around $Q = (1,0)$ corresponding to the wave vector Q from Γ/Z to M is found. These experimental observations supported by theoretical results lead to the denouement that the $s\pm$ pairing may only happens around the 3D hole pockets around the Γ/Z -point and the 2D electron like pockets around M-point. Experiments also show Sb doping at As-site to be very much impactful to the enhancement of superconductivity. Sb doping at both the As-sites increases the partial DOS of As at the E_F . Increment in DOS is larger in case of As-chain site doping. The enhanced superconductivity due to Sb doping at As-site can be attributed to the increase in partial DOS of As at the E_F . Similar kind of evolution of the electronic structure due to Sb doping is found in 112 compounds with other rare earth elements like Pr, Nd, Sm, Gd doping. Our electronic structure results also predict possible preference of Sm doping over other rare earth elements (like Pr, Nd, Sm) as far as the enhancement of superconductivity via Sb doping at As-chain is concerned.

The electronic structure of nine different hybrid 1144 compounds which are concoction of two different 122 compounds, is discussed in Chapter-6. The 1144 compounds ($AeAFe_4As_4$) have alternate Ae and A atoms in between the FeAs-layers. Due to varying atomic radii of Ae and A, there exists a natural internal chemical pressure on the FeAs-layers. Our study reveals its multi-orbital derived multi-band nature of electronic structure where the orbital contributions are mainly from Fe-3d orbitals, but finite contribution also from As-4 p_z . This leads to multi Fermi sheets (usually six hole like and four electron like), orbital characters of which changes from one family member to another orbital selectively. Due to natural chemical pressure an orbital selective evolution of electronic structure is observed. There is hole doping to the $d_{x^2-y^2}$ derived hole like

bands and electron doping to the d_{z^2} , $4p_z$ derived bands. Different chemical potential of different orbital derived electron/hole bands *i.e.*, self doping causes the bands with d_{z^2} , $4p_z$ character to shift below the Fermi level, leading to orbital selective chemical pressure induced topological Lifshitz transition. This natural chemical pressure induced orbital selective Lifshitz transition of hole bands is a unique characteristic of 1144 compounds. The robustness of these modifications in the electronic structure is further confirmed by DFT+U simulation together with spin-orbit interaction calculations. Moderate electron correlation as well as spin orbit coupling do not act as impediment to Lifshitz transition. This orbital selective Lifshitz transition may limit the highest possible superconducting transition temperature in 1144 compounds. The orbital resolved FSs confirm existence of strong intra orbital inter band nesting between the electron and hole FSs which hints towards s^\pm type pair mechanism of superconductivity. Our study with bandwidth of different orbital derived bands reveals orbital selective bandwidth renormalization in these compounds.

Chapter-7 presents detailed discussions of hybrid 12442 iron based superconductors which are synthesized by the mixture of compounds from two different family of IBSCs – 1111 and 122 with lattice mismatch tuning. Mixed multi orbital character of the electronic structure is revealed by our *ab initio* electronic structure calculations. In contrast to the hybrid 1144 compounds, negligible contributions from As- $4p_z$ orbital is revealed in 12442 compounds. These compounds are also example of self-doped systems due to existence of natural chemical pressure. Due to the presence of atoms with gradually increasing atomic radii, chemical pressure is exerted on the FeAs-layers. This chemical pressure influences electronic structure orbital selectively. As K is replaced by Rb or Cs, the peak of Fe d_{xy} partial DOS shifts towards E_F indicating electron doping, whereas the d_{yz} partial DOS peak displaces away itself from the E_F towards higher energy indicating hole doping. The orbital resolved Fermi surfaces reveal very weak intra orbital inter band nesting between the inner most hole like and the outer most electron like FSs which is also observed in experiments. Contrary to most of the Fe based superconductors very poor nesting be-

tween the electron and hole like FSs exists leading to an incommensurate neutron spin resonance mode. In all the three 12442 compounds two nearly degenerate electron like bands with $d_{xz/yz}$ nature show band singularity and are in close proximity with Lifshitz transition. Even a small electron correlation (U) of 1 eV to the Fe 3d orbitals pushes the two nearly degenerate electron bands above the E_F leading to correlation induced Lifshitz transition. The electron correlation also affects the electronic structure orbital selectively. The bandwidth of the hole like bands having orbital nature other than d_{xz} are increased due to increased onsite electron correlation, whereas it is decreased in case of bands with dominant d_{xz} character. Therefore, orbital selective bandwidth renormalization is very much apparent in these compounds. The Wannier fitted tight binding band structures reveal some unique character of the nearest neighbour hopping in these compounds. Unlike other iron based compounds, the intra-orbital hopping in d_{z^2} is larger than the intra-orbital hopping in $d_{x^2-y^2}$. Orbital selective decrease in the intra-orbital hopping of d_{xy} and d_{yz} due to change in chemical pressure induced by substitution of alkali atoms Rb or Cs is disclosed in these compounds. Due to C_{2v} symmetry of Fe atoms, degeneracy of the $d_{xz/yz}$ orbitals are lifted in tetragonal phase of these compounds. The detailed electronic structure investigations reveal orbital anisotropy and band reconstruction leading to nematic like splitting of electron bands having $d_{xz/yz}$ character around Brillouin zone corner. Although this kind of splitting generally features close to tetragonal to orthorhombic structural transition in 122 and 1111 compounds, its appearance in the tetragonal phase in 12442 compounds (even in absence of any structural transition) is a remarkable feature. Our crystal field splitting calculations with maximally localized Wannier functions further confirms the degeneracy lifting of $d_{xz/yz}$ orbitals.

Therefore, Lifshitz transition is established to be a common feature of the electronic structure of all the discussed Fe based superconductors. The correlation between superconductivity and Lifshitz transition in these newly discovered compounds set up a firm ground on the role of Lifshitz transition on superconductivity of iron based superconductors which was already predicted in most of the previously discovered compounds. The inter connec-

tion among orbital selectivity, bandwidth renormalization and Lifshitz transition in iron based superconductors is also entrenched for all the studied compounds.

SUMMARY

This thesis deals with the detailed study of electronic structure of several recently discovered Fe based superconductors like i) $\text{Ca}_{1-x}\text{R}_x\text{Fe}_{1-y}\text{T}_y(\text{As}_{1-z}\text{Sb}_z)_2$ [112-family] (R = Rare Earth metals: La, Ce, Pr, Nd, Sm, Gd; T = Transition Metals: Co, Ni, Mn), ii) $\text{AeAFe}_4\text{As}_4$ [1144-family] (Ae = Alkaline or rare earth metal: Ca, Sr or Eu; A = Alkali metals: K, Rb, Cs), iii) $\text{ACa}_2\text{Fe}_4\text{As}_4\text{F}_2$ [12442-family] (A = K, Rb, Cs) with Density Functional Theory (DFT) based first principles calculations.

A) A unique inter connection between superconducting phase diagram and electronic structure of 112 compounds is revealed for rare earth doping at Ca site and Co, Ni, Mn doping at Fe site. Superconducting transition temperature (T_C) is found to be directly connected with band edge van Hove singularity and Lifshitz transition.

B) The evolution of electronic structure of 112 compounds with rare earth doping is disclosed to be orbital selective in which bandwidth renormalization of d_{xy} is much more in comparison to $d_{xz/yz}$ orbital.

C) Increased As/Sb partial density of states at the Fermi level due to Sb doping at As chain site hints towards increased T_C due to Sb doping. A possible preference of Sm doping over other rare earth doping is predicted in case of enhanced superconductivity due to Sb doping. The diminishing Fermi surface (FS) around X-point due to Sb doping at As-chain signals towards the fact that nesting between electron FS around the M-point and hole FS around the Γ point is responsible for superconductivity. This theoretical fact is verified with Neutron Spin Resonance (NSR) experiment where only one 2D spin resonance mode

is found.

D) Lifshitz transition driven by chemical pressure induced orbital selective self-doping – hole doping to $d_{x^2-y^2}$ derived bands and electron doping to $d_{z^2}/4p_z$ derived bands is revealed for hybrid 1144 Fe based superconductors through our electronic structure calculations. Superconducting transition temperature in all the compounds of this family is found to be limited by Lifshitz transition.

E) Band edge van Hove singularity near Fermi level of the two nearly degenerate bands having $d_{xz/yz}$ nature and correlation induced orbital selective Lifshitz transition is the main feature of electronic structure of all 12442 compounds. Orbital anisotropy in electronic structure and nematic like band splitting induced by degeneracy lifting of d_{xz} and d_{yz} due to reduced Fe site symmetry is revealed in 12442 compounds. This degeneracy lifting is also reflected in the calculated crystal field splitting of Fe-3d orbitals.

Chapter 1

Introduction

1.1 High temperature superconductivity

The discovery of superconductivity in mercury at liquid He temperature in 1911 was a landmark event in the field of condensed matter Physics. It made the impossible possible: the dc resistivity vanished at finite temperature. This event led to very dedicated research in this direction and many compounds were discovered in subsequent years. Also the mechanism of superconductivity was understood by means of electron-phonon interaction leading effective attraction between two electrons (Cooper pair) by Bardeen-Cooper-Schrieffer (BCS) and coherent motion of these Cooper pairs lead to zero resistivity at finite temperature. But it was the work of Bednorz and Müller in 1986 where they discovered superconductivity in non-stoichiometric cuprate lanthanum barium copper oxide with a superconducting transition temperature (T_c) above 30K, that brought about a surge in the research of high temperature superconductivity. It also challenged the conventional mechanism of Cooper pairing. In next ten years thousands of papers on cuprate superconductors were published and it was possible to raise the T_c upto liquid nitrogen as well as liquid carbon tetrafluoride (CF_4). Subsequent theoretical works hinted towards the importance of electron correlation and electronic structure on superconductivity. In the year

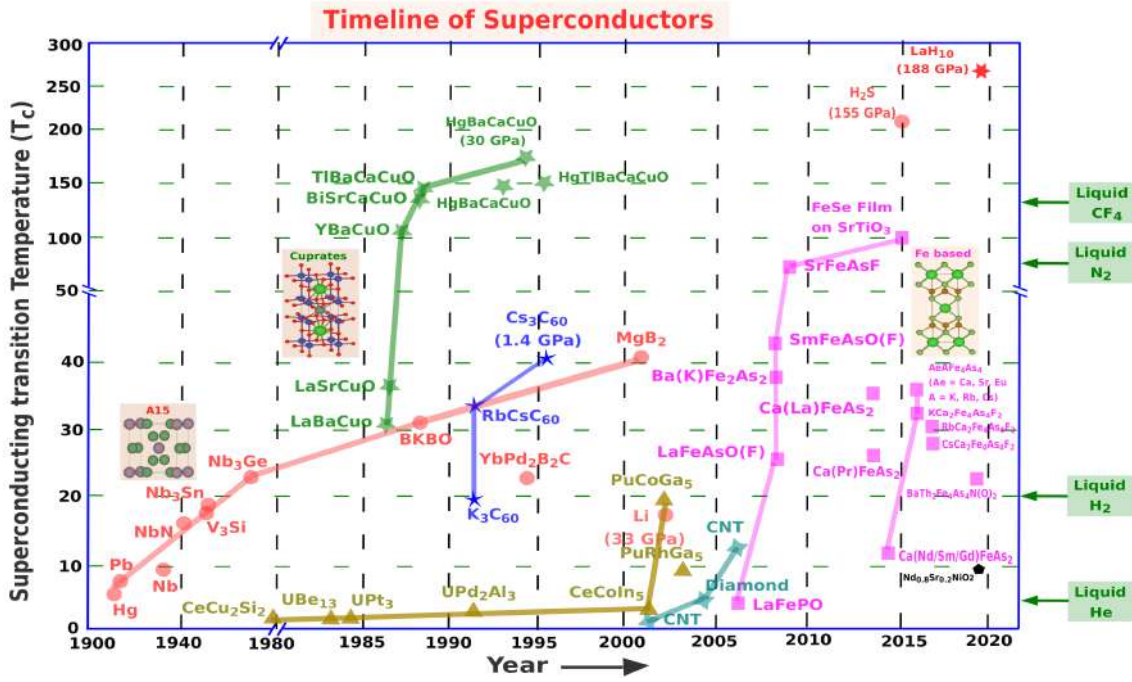


Figure 1.1: Timeline of superconductors showing yearwise evolution of superconducting transition temperature in different materials.

2008, physicists were in another juncture of the history when Y. Kamihara, H. Hosono and co-workers reported high temperature superconductivity in iron pnictide LaFeAsO(F) [1]. At that time, it was a very significant incident to get a superconducting compound which comprises an element like Fe having large spin magnetic moment. Following years saw a surge in the research of iron based superconductors and the copper age of superconductivity was replaced with iron age. Many iron based superconductors have been discovered till today with T_c as high as liquid N₂ temperature range with another advantage over cuprates *i.e.*, its very high critical current density. From theoretical point of view it was even more important because it revealed superconductivity and magnetism are intimately connected with each other rather than being independent. The modern methods of electronic structure investigations also disclosed an inter relationship between electronic structure and superconductivity.

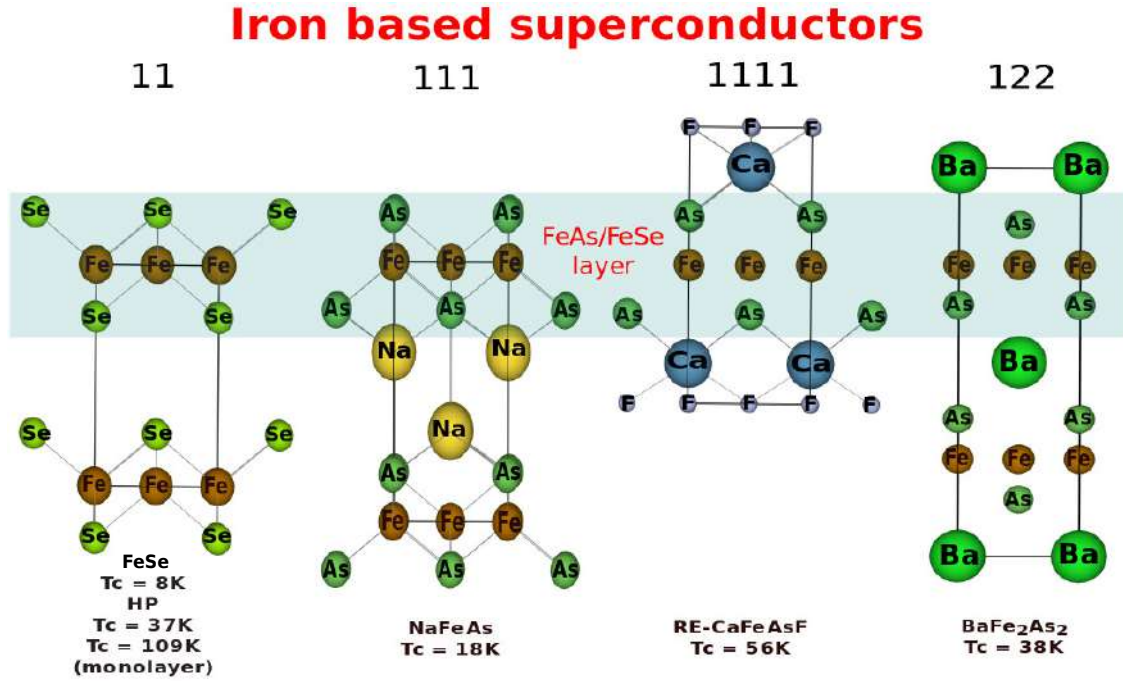


Figure 1.2: Different families of Fe based superconductors.

1.2 Iron based superconductors

In the subsequent years after the discovery of superconductivity in LaFeAsO(F), several families like $REFeAsO(F)$ (RE =rare earth elements) [1111-family] [2, 3, 4], $AEFe_2As_2$ (AE =alkaline earth metals)[122-family] [5, 6], FeSe [11-family] [7], $AEFeAs$ [111-family] [8, 9, 10] were tracked down. One very common feature in the structure of all iron based superconductors (IBSC) is the presence of FeAs-layer which is visible from Fig.1.3. Now we will discuss about different families of IBSC.

1.2.1 1111 family

This family includes compounds like LaFePO and $REFeAsO(F)$.

Structural aspect:

Negatively charged FeP or FeAs-layer with Fe atoms in square planer lattice and positively charged REO-layers are present in all the 1111 compounds. Undoped LaFeAsO undergoes structural transition from tetragonal ($P4/nmm$) to monoclinic ($P112/n$) phase

at about temperature 155K [11].

Magnetism & Superconductivity:

LaFePO is nonmagnetic and superconducting with transition temperature (T_c) 4K without any doping. On the other hand, superconductors like REFeAsO are antiferromagnetic in undoped compounds. Superconductivity can only be introduced in these compounds by suppressing magnetism with electron or hole doping. For example, the measured T_c value of different 1111 compounds are – 26K LaFeAsO_{0.89}F_{0.11}, 41 K in CeFeAsO_{0.84}F_{0.16}, 52 K in PrFeAsO_{0.89}F_{0.11}, 55 K in SmFeAsO_{0.9}F_{0.1} [11, 12, 13, 14].

1.2.2 122 family

Compounds like AEF₂As₂ where AE = Ba, Ca, Sr or Eu are members of 122 family. There exist over 450 distinct 122 compounds [15]. All of them are not Fe based superconductors though.

Structural aspect:

Unlike 1111 family, the spacer blocking layer in between FeAs-layers consist of alkaline earth metals like Ba or Eu in 122 family. At room temperature, 122 compounds crystallize in tetragonal structure (I4/mmm) and undergoes a structural transition to orthorhombic phase (Fmmm) at lower temperature. For example, BaFe₂As₂ goes through this kind of transition at about temperature 140K [16].

Magnetism & Superconductivity:

A systematic doping at all the sites in BaFe₂As₂ like the alkali metal K at Ba site, transition metal Co, Ni at Fe site, or Sb, P at As site almost universally suppresses the non-superconducting antiferromagnetic state of parent compound to a superconducting nonmagnetic phase. This kind of transition from antiferromagnetic to the superconducting state can also be induced by applying external hydrostatic pressure. The measured T_c in 122 compounds are – 38 K in Ba_{0.6}K_{0.4}Fe₂As₂, 32 K in Sr_{0.6}K_{0.4}Fe₂As₂, 26 K in Sr_{0.6}Na_{0.4}Fe₂As₂, and 21 K in Ca_{0.6}Na_{0.4}Fe₂As₂ [17, 18, 19].

1.2.3 111 family

Compounds like LiFeAs, NaFeAs belongs to 111 family.

Structural aspect:

These compounds resemble the CeFeSi tetragonal structure (P4/nmm) with each alkaline earth element of the 122 compounds substituted by two alkali elements. NaFeAs shows structural transition from tetragonal to orthorhombic phase at 53K [20].

Magnetism & Superconductivity:

NaFeAs shows a magnetic transition from paramagnetic to spin density wave (SDW) at temperature 40K, whereas the suppression of SDW and emergence of superconductivity occurs at 23K. Transition metal doping like Co, Ni at Fe site can further enhance superconductivity in these compounds. Measured T_c in 111 family materials include 18 K in Li_xFeAs , 9 K in Na_xFeAs [21, 22].

1.2.4 11 family

This family includes iron chalcogenides like FeSe, $\text{FeTe}_{1-x}\text{Se}_x$, $\text{FeTe}_{1-x}\text{S}_x$.

Structural aspect:

11 compounds have simplest structure in comparison to other IBSC, iron chalcogenide layers are simply stacked together. Structural transition is observed in superconducting $\text{Fe}_{1.01}\text{Se}$ at 90 K from tetragonal to an orthorhombic phase [23]. But its nonsuperconducting variant $\text{Fe}_{1.03}\text{Se}$ doesn't show any structural transition.

Magnetism & Superconductivity:

In 11 compounds no magnetic ordering is observed. The superconducting transition temperature is 8K of FeSe at ambient pressure and 36.7 K in FeSe under pressure of 8.9 GPa, and 14 K in $\text{FeTe}_{0.5}\text{Se}_{0.5}$, 2 K in $\text{Fe}_{1.13}\text{Te}_{0.85}\text{S}_{0.1}$, and 10 K in $\text{FeTe}_{0.8}\text{S}_{0.2}$ [24, 25, 26].

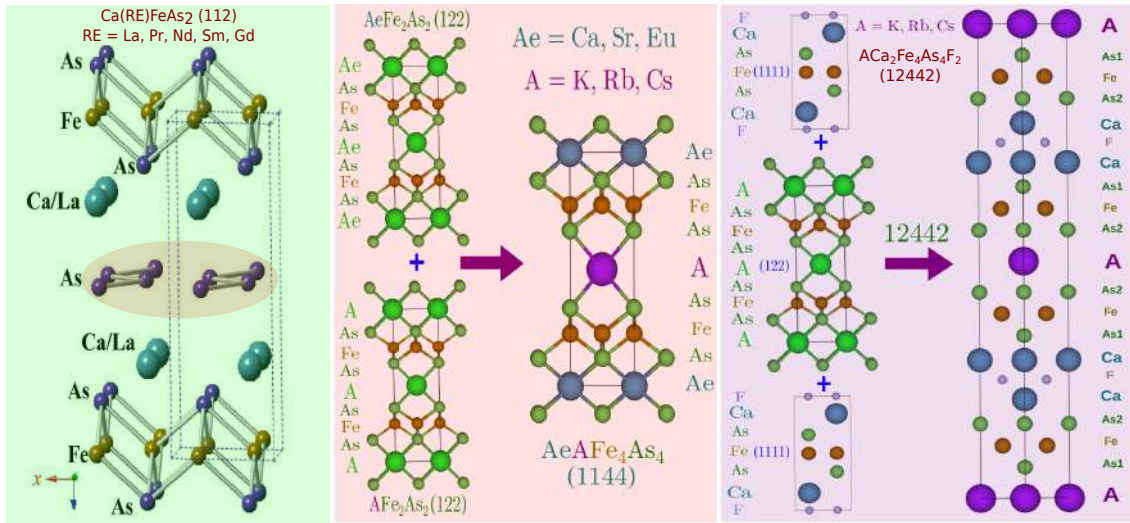


Figure 1.3: Recently discovered families of Fe based superconductors.

1.3 Some recently discovered Fe based superconductors

In recent years some new iron based superconductors have been discovered which are quite different from the previously discussed compounds in many aspects like – they do not show many exotic phases like magnetism through spin density wave (SDW), or structural transitions.

1.3.1 112 compounds

The recently discovered 112-family (that has chemical formula $\text{Ca}_{1-x}\text{RE}_x\text{FeAs}_2$) is quite different from other iron pnictide families in various aspects.

Structural aspect:

These compounds crystallize in less symmetric monoclinic structure P2_1 [27, 28] (for La, Ce, Nd, Sm, Eu, Gd-112) or $\text{P2}_1/\text{m}$ [29] (for Pr-112) whereas other iron pnictide families have usually tetragonal or orthorhombic structure. The 112 compounds also have layered structure with alternate stacking of FeAs planes. But the blocking layers are composed of Ca(RE) spacer atoms and specially, the As_2 zigzag chains which are absent in all other classes of Fe-based superconductors (Fig.1.3). For iron based superconductors other than

112 the spacer layer is insulating and acts as charge reservoir whereas the CaAs layer is metallic and couple strongly with the FeAs layers in case of 112 IBSCs [30].

Magnetism & Superconductivity:

The latest available phase diagram of 112 iron pnictides with La doping at Ca site shows doping enhanced antiferromagnetism [31] with superconductivity which is quite different from other families where superconductivity emerges only after suppressing antiferromagnetism by doping [32]. Established phase diagram of 112 compound with rare earth doping other than La is not still available. The 112 compound with La doping level $x = 0.27$ at Ca site which is non superconducting, has monoclinic to triclinic phase transition at temperature 58 K [33]. But the superconducting phase doesn't show any structural transition.

The parent compound CaFeAs_2 is unstable. It can only be stabilized by doping rare earth atoms (like La, Ce, Pr, Nd, Sm, Eu, Gd) [28, 34]. The highest critical temperature (T_c) for the La-doped 112 superconductor is achieved at La-doping level $\sim x = 0.16$ with critical temperature 35 K. The critical temperature decreases with increasing La concentration further and superconductivity is eventually destroyed if La concentration is greater than 0.25 [35]. For other RE doped 112 compounds the transition temperatures are 24K, 11.9K, 11.6K, 9.3K and 12.6K for Pr, Nd, Sm, Eu and Gd respectively [29, 28]. There is no understanding developed so far as to why T_c gradually reduces as the nature of doping changes. There is a general trend of decreasing critical temperature with decreasing radius of the lanthanide. This is in contradiction to already known behaviour of T_c (that rises with decreasing lattice constant) with RE in 1111 compounds [36] where T_c is believed to be related with Pn(Ch)-Fe-Pn(Ch) angle (α) corresponding to a regular tetrahedron and pnictogen (chalcogen) height (h_{Pn}). Whether such factors (α or h_{Pn}) are important in determining superconductivity in RE doped 112 compounds, is still not clear [35]. In another class of Fe based materials like CaFeAsH , CaFeAsF which are non-

superconducting in ambient conditions but produces strong superconductivity ($T_c = 47$ K) when La is doped at Ca site. Thus electronic structure of IBSC with RE-doping is extremely important and is the subject matter of the present thesis. Our doping dependent theoretical study of electronic structure shed light on these aspects.

Highest critical temperature upto 47K was achieved so far in 112 family for Sb doping at As-site with doping level 0.10 in $x=0.12$ La-doped compound [37, 38]. Such studies on the effect of Sb doping on critical temperature of RE doped 112 other than La is not known so far. Experimentally, the effect of Co and Mn doping at Fe site in rare-earth (La, Ce, Pr, Nd, Sm, Eu, Gd) doped CaFeAs_2 compound was studied [34, 39]. The enhancement of superconducting transition temperature was realized in Co-doping at the Fe site whereas superconductivity was suppressed by Mn-doping [34]. Superconductivity was also induced in the Ce doped compound with transition metal codoping at Fe [39]. The phase diagram of CaFeAs_2 with Ni doping at Fe site for a particular La doping at Ca site has been studied experimentally [40].

1.3.2 1144 compounds

More recently, a new family of IBSCs $\text{CaAFe}_4\text{As}_4$ ($A = \text{K, Rb, Cs}$), $\text{SrAFe}_4\text{As}_4$ ($A = \text{Rb, Cs}$) [41] and $\text{EuAFe}_4\text{As}_4$ ($A = \text{Rb, Cs}$) [42] [1144] was discovered which gained a significant attention among the scientific community due to its interesting properties.

Structural aspect:

This 1144 family are the sandwich of two different kinds of 122 compounds where alkaline earth element and alkali element occupy different atomic positions in its crystal structure (Fig.1.3). There is alternate alkali metal (K, Rb, Cs) and alkaline earth metal (Ca, Sr) or Eu spacer layer in between the FeAs-layers. Unlike the 122 compounds which crystallize in body-centered tetragonal structure with space group $I4/mmm$, 1144 compounds crystallize in primitive tetragonal structure having space group $P4/mmm$ [41]. There are two inequivalent atomic sites for As-atoms in FeAs-layer.

Magnetism & Superconductivity:

The $\text{AeAFe}_4\text{As}_4$ (=AeA44) iron pnictides show quite similar superconducting transition temperatures 33.1K, 35K, 31.6K, 35.1K, 36.8K, 36K, 35K for CaK44, CaRb44, CaCs44, SrRb44, SrCs44, EuRb44, EuCs44 compounds respectively. Recent experimental studies also revealed difference in vortex dynamics indicating distinct origins of vortex pinning in 122 and 1144 superconductors [43]. The iron based superconductors in general show diverse types of magnetic orders. Magnetic order in iron based superconductors can be described by the spatial variation of Fe magnetic moments at position \mathbf{R} ,

$$\mathbf{m}(\mathbf{R}) = \mathbf{M}_1 \cos(\mathbf{Q}_1 \cdot \mathbf{R}) + \mathbf{M}_2 \cos(\mathbf{Q}_2 \cdot \mathbf{R}) \quad (1)$$

, where $\mathbf{Q}_1 = (\pi, 0)$ and $\mathbf{Q}_2 = (0, \pi)$ are symmetry equivalent propagation vectors related to antiferromagnetism. The magnetic order parameters \mathbf{M}_1 and \mathbf{M}_2 defines three types of magnetic orders in Fe based compounds. In case of orthorhombic striped spin density wave (SSDW) order only one $\mathbf{M}_i \neq \mathbf{0}$. A spin charge density wave (SCDW) corresponds to the superposition of two contributions with $\mathbf{M}_1 = \pm \mathbf{M}_2 \neq \mathbf{0}$ ($\mathbf{M}_1 \parallel \mathbf{M}_2$). The tetragonal spin vortex crystal (SVC) order corresponds to $|\mathbf{M}_1| = |\mathbf{M}_2|$ with noncollinear vectors $|\mathbf{M}_1| \perp |\mathbf{M}_2|$, both in the Fe-plane. Although SSDW type magnetic order is observed in a majority of the IBSCs, some hole doped 122 compounds show a transition from SSDW to SCDW magnetic states [44, 45]. The magnetic ground state of 1144 compounds is also very interesting in this regard. Although the parent compounds $\text{AeAFe}_4\text{As}_4$ (Ae=Ca, Sr) do not show any magnetic order [46], Hedgehog SVC type magnetic state was observed to be stabilized in hole compensated (Ni or Co doping at Fe site) 1144 compounds [47, 48]. Thus, all the three types of magnetic order *i.e.*, SSDW, SCDW and SVC are possible for IBSCs. The SVC magnetic phase is stabilized by the reduced symmetry of the $\text{AeAFe}_4\text{As}_4$ crystal. The existence of large configuration space for magnetic fluctuations is believed to promote high temperature superconductivity [48]. In 122 compounds

a collapsed tetragonal (cT) phase transition is observed due to variation of chemical or mechanical pressure leading to a modification of the whole structure and suppression of superconductivity [49]. Unlike 122 family, 1144 family show half cT (hcT) transition with external pressure and the transition is layer selective. The first collapsed tetragonal transition is observed at an external pressure 4GPa where the transition is induced due to As-As p_z bonding across Ca layer with suppression of superconductivity. The second cT transition appeared at the pressure of 12GPa across the K-layer [50]. This hcT phase transition can be predicted by DFT based *ab-initio* calculations only by invoking the Hedgehog type long range spin order which is not found experimentally in the superconducting states of the undoped 1144 superconductors [50]. This magnetic order has only been realized experimentally in hole compensated CaK44 superconductors. Recently, layer selective two consecutive hcT transitions at different pressures were predicted in all the 1144 compounds [51]. On the other hand, The EuA44 (A=Rb, Cs) superconductors got much attention due to its peculiar magnetic properties in the superconducting phase [52]. Experimentally it was found that EuRbFe₄As₄ shows superconductivity with transition temperature (T_c) 36.5K and Eu spin ferromagnetism with Curie temperature (T_{Curie}) 15K [53]. Thus, EuRb44 is a ferromagnetic superconductor (FMSC). In EuCs44 compound ferromagnetic superconductivity was observed with $T_c=35.2\text{K}$ and $T_{\text{Curie}}=15.5\text{K}$ [54]. Experimental phase diagram with respect to Ni doping at Fe site of EuRb44 reveals that from FMSC EuRb44 gradually transform into superconducting ferromagnet (SCFM) with $T_c=11.2\text{K}$ and $T_{\text{Curie}}=15.1\text{K}$ at around 7% Ni doping. The superconductivity is completely suppressed when Ni doping is greater than 8% due to compensation of self hole doping with the addition of extra itinerant electrons of Ni. The hole depletion also seems to recover the SDW order at Ni doping greater than 5%. This might improve our understanding about the interplay between superconductivity and magnetism. Therefore, the overall dynamics of magnetism of 1144 compounds seems very different compared to that in other iron based superconductors; most of the undoped compounds other than EuA44 do not show any long range magnetic order. Also in EuA44 compounds no magnetic

order of Fe is observed. Furthermore, irrespective of the underlying magnetic structure or structural details superconducting transition temperature is nearly uniform in all the 1144 family members suggesting magnetic structure may not influence superconductivity in these compounds.

1.3.3 12442 compounds

More recently, a copious amount of IBSCs were discovered from concoction of two different families of iron based compounds – 1111 and 122 with lattice mismatch tuning.

Structural aspect:

The $\text{KCa}_2\text{Fe}_4\text{As}_4\text{F}_2$ compound is the inter-growth of CaFeAsF and KFe_2As_2 [55]. Soon after the discovery of $\text{KCa}_2\text{Fe}_4\text{As}_4\text{F}_2$, two more 12442 iron based fluoride superconductors were synthesized – $\text{RbCa}_2\text{Fe}_4\text{As}_4\text{F}_2$, $\text{CsCa}_2\text{Fe}_4\text{As}_4\text{F}_2$ which are hybrid mixtures of CaFeAsF with RbFe_2As_2 and CaFeAsF with CsFe_2As_2 respectively [56]. The crystal structure of 12442 fluorides consist of Fe_2As_2 double layers with alkali metal ($A = \text{K}, \text{Rb}, \text{Cs}$) atoms sandwiched and separated by Ca_2F_2 layers (Fig.1.3). This resembles the CuO_2 double planes in high T_c cuprate superconductors. All the 12442 iron based compounds crystallize in body centered tetragonal structure with space group $I4/mmm$ [55, 56] in contrast to 1144 compounds which crystallize in primitive tetragonal structure with space group $P4/mmm$. As atoms occupy two inequivalent crystallographic sites in the FeAs -layer very similar to that in 1144 compounds. Thus, it is a legitimate issue to verify whether As atoms play a significant contribution to the electronic structure in these compounds like that in 1144 compounds or not.

Magnetism & Superconductivity:

The superconducting transition temperature in $\text{KCa}_2\text{Fe}_4\text{As}_4\text{F}_2$, $\text{RbCa}_2\text{Fe}_4\text{As}_4\text{F}_2$ and $\text{CsCa}_2\text{Fe}_4\text{As}_4\text{F}_2$ was observed to be 33K, 30.5K, 28.2K respectively. The exotic phases like spin density wave (SDW) [57, 58], nematicity [59, 60], tetragonal to orthorhombic structural

transition [61] etc. are absent in both the hybrid family compounds, 1144 and 12442 although they are derived from 122 compounds that exhibit these various exotic phases. To explore the nature of superconducting gap in these compounds μ SR experiments were performed which revealed multi-gap nodal superconductivity with (s + d)-wave nature in both $\text{KCa}_2\text{Fe}_4\text{As}_4\text{F}_2$ and $\text{CsCa}_2\text{Fe}_4\text{As}_4\text{F}_2$ compounds [62, 63]. This is in sharp contrast to the other hybrid 1144 compounds where multi-gap nodeless superconductivity with s^\pm symmetry just like that observed in 112 compounds was found from neutron spin resonance measurements [64, 65]. However, the gap probed by heat transport measurements in $\text{CsCa}_2\text{Fe}_4\text{As}_4\text{F}_2$ showed multiple nodeless superconducting gaps which are quite similar to that in $\text{CaKFe}_4\text{As}_4$ [66]. The 12442 compounds are self hole doped compounds with 0.25 holes/ Fe^{2+} and superconductivity is believed to be induced due to this self hole doping in these compounds. Electron doping with Co at Fe site was proved to be fatal to superconductivity as far as $\text{KCa}_2\text{Fe}_4\text{As}_4\text{F}_2$ compound is concerned [67]. It also did not induce any structural transition or spin density wave (SDW) like order in this compound which is in contrast to the most of the iron based superconductors. Theoretical studies on $\text{KCa}_2\text{Fe}_4\text{As}_4\text{F}_2$ indicates striped antiferromagnetic state as the magnetic ground state [68] which is very different from Hedge-hodge spin vortex state in 1144 compounds [69]. Muon spin resonance measurements also reveal some magnetic phase below 10K but it does not compete with superconductivity [62, 63]. Thus the evolution of electronic structure in non magnetic phase might reveal sufficiently correct information about superconductivity in these compounds.

1.4 Lifshitz transition and Superconductivity in iron based superconductors

Lifshitz transition is an electronic topological transition at absolute zero temperature at which Fermi surface topology of metals change abruptly. In this kind of transition there is

not any spontaneous symmetry breaking. Lifshitz transition is observed in different condensed matter systems like $\text{Bi}_2\text{Sr}_2\text{CaCu}_2\text{O}_{8+\delta}$ cuprate superconductor [70], 3D Dirac Semi metal Na_3Bi [71], bilayer graphene [72], quantum hall liquids [73] *etc.* Iron-based superconductors (FeSCs) are multiple-band superconductors. Although typically Fe based superconductors have multiple hole as well as electron like Fermi surfaces, however there are a number of materials in which the hole Fermi surface is probably missing. For example, $\text{Ba}_{1-x}\text{K}_x\text{Fe}_2\text{As}_2$ near $x \sim 0.8$ [74], $\text{LiFe}_{1-x}\text{Co}_x\text{As}$ for $x \leq 0.1$ [75], FeSe single layer grown on SrTiO_3 (FeSe/STO) substrate, [76], K-doped FeSe thin films [77, 78], the intercalated compound (LiFe)OHFeSe [79] *etc.* Because of multi band nature of electronic structure close to the Fermi Level, it is possible to drift (top or bottom of) any one or a number bands upward or downward depending on which high symmetry points in momentum space it crosses the Fermi Level through various perturbations caused by doping [80], pressure [81] or even magnetic field [82] *etc.* causing Lifshitz transitions. Most of the Fe-based superconductors in which the hole FS is missing (or not detectable by ARPES) have quite high T_c *e.g.*, the record high T_c 100 K in FeSe/STO [76]. This is probably due to consequence of Lifshitz transition [83]. As a result, Fe-based superconductors have become proto-type systems where Lifshitz transition and its probable heed to superconductivity may be studied [84]. Superconductivity in (LiFe)OHFeSe exists beyond 50% electron doping [85, 86], in a rigid band description this should result in a complete wipe out of the hole Fermi surface. Due to absence of good single crystal this is not yet confirmed experimentally however it is proved in case of $\text{K}_y\text{Fe}_{2-x}\text{As}_2$ [13], $\text{K}_y\text{Fe}_{2-x}\text{Se}_2$ [87] and FeSe/STO [76, 78, 88] as mentioned above. We systematically show through out this thesis that the electronic structure modifications in whether doped 112 or undoped 1144/ 12442 are very similar to the above scenario where a fine tuning of the edges of several bands, pushed across the Fermi level with doping, chemical pressure or electron correlation leading to Lifshitz transition where high T_c are found separately experimentally.

Detailed studies on the electronic structure of a large number of Fe based superconduct-

Table 1.1: Highest T_c and Lifshitz transition

IBSC	T_{cmax} in K	Doping(x) at T_{cmax}	LT at doping(x)
$Ba_{1-x}K_xFe_2As_2$	~ 38	~ 0.50	~ 0.50 [89, 90]
$Ba_{1-x}Na_xFe_2As_2$	~ 34	~ 0.50	~ 0.50 [89, 91]
$BaFe_{2-x}Co_xAs_2$	~ 26	~ 0.10	~ 0.10 [89, 92]
$BaFe_2(As_{1-x}P_x)_2$	~ 27	~ 0.35	~ 0.37 [89, 93]
$Ca_{1-x}La_xFe_2As_2$	~ 35	~ 0.16	~ 0.15 [94, 95]
$Ca_{0.82}La_{0.18}Fe_{1-x}Ni_xAs_2$	~ 35	~ 0.005	~ 0.005 [94, 96]

tors have given a clear indication of interconnection between the highest T_c and Lifshitz like topological transitions at an optimal doping [97, 98]. Highest superconducting transition temperature is observed to be in close proximity of Van Hove singularities (VHS) at the Fermi level where the edges *i.e.*, top or bottom of certain bands are in the vicinity of Lifshitz transition (LT). The electronic structure of Fe based materials are of multi orbital nature having contributions mostly from d_{xy} , d_{xz} , d_{yz} . But the bands with d_{xz}/d_{yz} character have the largest superconducting gaps [99, 100, 101], making them the most important as far as superconductivity is concerned. These kinds of empirical correlation between LT- T_c is observed in most of the Fe based compounds like optimally hole doped $Ba_{1-x}K_xFe_2As_2$ [102], $Ba_{1-x}Na_xFe_2As_2$ [103], $Ca_{1-x}Na_xFe_2As_2$ [104] *etc.* as well as optimally electron doped $Ba(Fe_{1-x}Co_x)_2As_2$ [105]. The same trend holds for $LiFeAs$ [106], $NaFeAs$ [107] and $A_xFe_{2-y}Se_2$ (K, Rb, Cs) [108]. Furthermore, it has also been observed that transition temperature also increases with the increasing number of band edge VHS on the verge of LT. For example, the 1038 family compound $(CaFeAs)_{10}Pt_{3.58}As_8$ which have three band edges VHS at E_F , has a T_c of 35K. This is greater than that of $(CaFe_{0.95}Pt_{0.05}As)_{10}Pt_3As_8$ having only one band edge VHS at E_F [109]. The same argument goes for $SmFe_{0.92}Co_{0.08}AsO$ [110] and $NdFeAsO_{0.6}F_{0.4}$ [111], where two to three bands are found to be on the verge of LT. In Table. 1.1, we have presented experimental T_c , doping percentage at which the highest T_c is observed and the doping at which theoretical calculations show LT. It is very much evident that there exist a close proximity between theoretically predicted LT and the highest transition temperature at a particular doping. The LT has very important impacts on the electronic properties like heat capacity,

magnetic susceptibility, thermo electric power *etc.* which has been discussed [112, 113] in a great detail and is beyond the scope of this thesis. One point worth mentioning is that LT causes giant anomaly in kinetic characteristics of metals like thermoelectric power and the growth of thermoelectric power is correlated to the changes in T_c .

Although the study of Fermi surface topology and Lifshitz transition is widely accepted to understand the phenomenon of superconductivity in iron based superconductors, the study of bandwidth of different orbital derived band can also enhance our understanding to superconductivity in these compounds [114]. Recently thorough experiments on (low temperature) electronic structure of various Fe-based superconductors are performed based on ARPES and DFT studies. From phosphides to arsenides to chalcogenides bandwidths decrease orbital selectively. In the same sequence band renormalization increases also to specific electronic bands with selective orbital weight *e.g.*, bands with d_{xy} orbital character only. An orbital selective strong renormalization of d_{xy} bands leading to orbital selective Mott phase, is observed in some of the iron chalcogenides. In fact, it is shown that the orbital selectivity is at the heart of all the realized phases namely the magnetic spin density wave (SDW) state, the orbital order, nematic order and superconductivity too. On the other hand, band width reduction (or renormalization) in general is usually visualized as manifestation of overall electron correlation. For example, a systematic angle-resolved photoemission spectroscopy study of the electronic structure of $\text{Rb}_{0.8}\text{Fe}_2(\text{Se}_{1-z}\text{S}_z)_2$ ($z = 0, 0.5, 1$) reveals that superconductivity is continuously suppressed into a metallic phase [115]. In this superconducting to non-superconducting transition little change in Fermi surface topology is observed, but a reduction in overall bandwidth is significant. This leads to the conclusion that the study of bandwidth which is one of the manifestations of electron correlation might be an important tuning parameter for superconductivity. It is also found that moderate electron correlation is favourable to high T_c in iron chalcogenides. The low temperature electronic structure study on iron chalcogenides $\text{FeTe}_{0.56}\text{Se}_{0.44}$, monolayer FeSe grown on SrTiO_3 and $\text{K}_{0.76}\text{Fe}_{1.72}\text{Se}_2$ by M. Yi *et al.*, reveals the fact that there exist a universal strong orbital dependent correlation

effect in iron chalcogenides [116]. Although role of Fermi surface topology, Lifshitz transition and the ensuing orbital selective bandwidth renormalization for the occurrence of superconductivity is well accepted in literature, RE doping induced electronic band renormalization and its effect on FS topology of 112, 1144, 12442 superconductors is not available yet. From above discussion there is a clear demarkation between the two classes of Fe-based superconductors (pnictides and chalcogenide) exist as far as evidence of electron correlation through band renormalization is concerned. Fe-pnictides show very weak renormalization as compared to the Fe-chalcogenides. Therefore such studies, both experimental as well as theoretical for all these compounds are very much desirable.

It is very much conspicuous from the above discussion that it is worth investigating the details of electronic structure of the newly discovered three iron based superconducting families – 112, 1144 & 12442; and possibility of LT in them. Detailed theoretical investigations on these compounds reveal many important conclusions which will be discussed in the following chapters.

Chapter 2

Theory and Computational methods

2.1 Lifshitz Transition (LT)

Lifshitz transition is related to the electron transition at $T = 0$ in metals at which topology of the Fermi surface changes abruptly leading to gradual reduction (or vanishing) of some Fermi surfaces (FS) at a particular point of the Brillouin zone or emergence of new FSs at another point. It can be induced in a metal by isotropic compression, uniaxial deformation, a gradual change of composition or even magnetic field. LT occurs in close proximity to van Hove singularities (VHS) at the Fermi level (E_F) where the edges *i.e.*, top or bottom of certain bands crosses the E_F . It has been noticed both theoretically as well as experimentally that the LT like topological transitions have great impact on the electronic properties like heat capacity, magnetic susceptibility, thermo electric power and superconductivity. In the Fig.2.1 we have shown the evolution of 3D FSs in LT. LT can be demonstrated with –

$$\epsilon(p) = \frac{p_x^2 + p_y^2 - p_z^2}{2m} \pm \mu \quad (1)$$

where μ is the chemical potential of the system. The system has parametric dependence on μ . It can be manipulated with external pressure, chemical doping *etc.* Now if we look

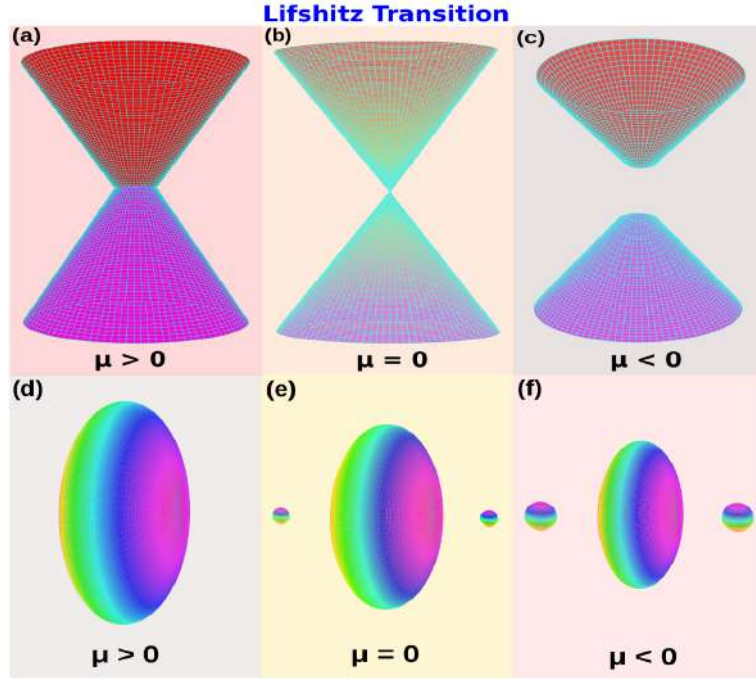


Figure 2.1: Example of the Lifshitz transition with the change of the Fermi surface topology (disruption of the "neck" of a Fermi surface).

into the FSs in Fig.2.1, we have the following observations –

- i. The complete FS at $\mu > 0$ (Fig.2.1(a)) forms a 'neck' when $\mu = 0$ (Fig.2.1(b)) and is at the verge of Lifshitz like topological transition.
- ii. At $\mu < 0$ (Fig.2.1(c)), the neck is disrupted and the FS gets separated leading to LT.
- iii. There might also be creation (or destruction) of new (or old) FSs during LT. Fig.2.1(d), (e), (f) show gradual appearance of new FSs at the cost of old one in the process of variation of chemical potential μ .

2.1.1 Lifshitz transition in weakly interacting electron gas

Let us consider a weakly bound electronic system so that their interaction with the crystal may be considered as a perturbation. Free electron wave function in case of one dimensional chain of atoms can be written as $\psi(x) = \frac{1}{\sqrt{L}} e^{\frac{ipx}{\hbar}}$, where L is length of the chain. Energy of electrons is $\epsilon(p) = \frac{p^2}{2m}$. Let us consider periodic potential in the lattice to be

$U(x) = \sum_n U_n e^{\frac{2\pi i n x}{a}}$, where $\frac{2\pi n}{a}$ is period of the reciprocal lattice. The matrix elements of $U(x)$ considering free electron wavefunction may be written as –

$$U(p, p') = \frac{1}{L} \int U(x) e^{\frac{-i(p-p')x}{\hbar}} dx \quad (2)$$

Condition for the matrix elements $U(p, p')$ to be non-zero is

$$p - p' = \frac{2\pi n \hbar}{a}$$

It is also clear that $U(p, p') = U_n$. First order correction to the energy $\epsilon^{(0)}(p)$ is $\epsilon^{(1)}(p) = U(p, p') = U_0$, which is a constant. This can shift only the origin of energy scale. So, we consider the second-order correction term

$$\epsilon^{(2)}(p) = \sum_{n \neq 0} \frac{|U_n|^2}{\epsilon^{(0)}(p) - \epsilon^{(0)}(p - \frac{2\pi n \hbar}{a})} \quad (3)$$

In case of a simple weakly interacting periodic system, if we consider only the two possible states which have energy splitting at the Brillouin zone (BZ) boundary, the energy dispersion is –

$$\epsilon = \frac{\epsilon_1 + \epsilon_2}{2} \pm \sqrt{\frac{(\epsilon_1 - \epsilon_2)^2}{4} + |U_n|^2} \quad (4)$$

where, ϵ_1 & ϵ_2 are energies of the two states at the first BZ boundary and U_n is the periodic potential of the crystal. Any electron moving in the lattice is characterised by its crystal momentum $\mathbf{p}' \rightarrow \mathbf{p} - \hbar \mathbf{K}$. So, every energy eigenvalue at any point of the reciprocal space can be represented by its value inside the first BZ (reduced zone). In three dimension as the potential is periodic, we can represent it as $U(\mathbf{r}) = \sum_{\mathbf{K}} U_{\mathbf{K}} e^{i\mathbf{K} \cdot \mathbf{r}}$, where \mathbf{K} is lattice translation vector in reciprocal lattice space. At the BZ boundary,

$$\epsilon^{(0)}(\mathbf{p}) = \epsilon^{(0)}(\mathbf{p} - \hbar \mathbf{K}) \quad (5)$$

$$\Rightarrow \frac{\hbar^2 p^2}{2m} = \frac{\hbar^2 (\mathbf{p} - \hbar \mathbf{K})^2}{2m}$$

$$\Rightarrow \frac{\hbar^2 K^2}{2m} = \frac{\hbar \mathbf{p} \cdot \mathbf{K}}{m}$$

$$\Rightarrow \mathbf{p} \cdot \hat{\mathbf{K}} = \frac{\hbar K}{2}$$

$$\Rightarrow p \cos \theta = \frac{\hbar K}{2} \quad (6)$$

The above equation represents a plane in momentum space which is perpendicular to \mathbf{K} and intersects it at a distance $\frac{\hbar \mathbf{K}}{2}$ from the origin. Just like in 1D case, there will be energy jump in the plane. If \mathbf{K} is the smallest period in the corresponding direction, the plane represent BZ boundary. If we consider only the first BZ *i.e.*, smallest period in \mathbf{K} , the 1D dispersion can be applicable to 3D also [117]. Therefore, we can write –

$$\epsilon(\mathbf{p}) = \frac{1}{2} [\epsilon^{(0)}(\mathbf{p}) + \epsilon^{(0)}(\mathbf{p} - \hbar \mathbf{K})] \pm \left[\frac{1}{4} (\epsilon^{(0)}(\mathbf{p}) - \epsilon^{(0)}(\mathbf{p} - \hbar \mathbf{K}))^2 + |U_K|^2 \right]^{1/2} \quad (7)$$

Now choosing p_z along $\hbar \mathbf{K}$, introducing a new variable $p_{z1} = p_z - \frac{\hbar K}{2}$ and substituting $\epsilon^{(0)} = \frac{p^2}{2m}$, we get the energy dispersion of a weakly interacting electron gas –

$$\epsilon^{(0)}(p) = \frac{p_{\perp}^2 + p_{z1}^2 + (\hbar \mathbf{K}/2)^2}{2m} \pm \left[\left(\frac{p_{z1} \hbar K}{2m} \right)^2 + |U_K|^2 \right]^{1/2} \quad (8)$$

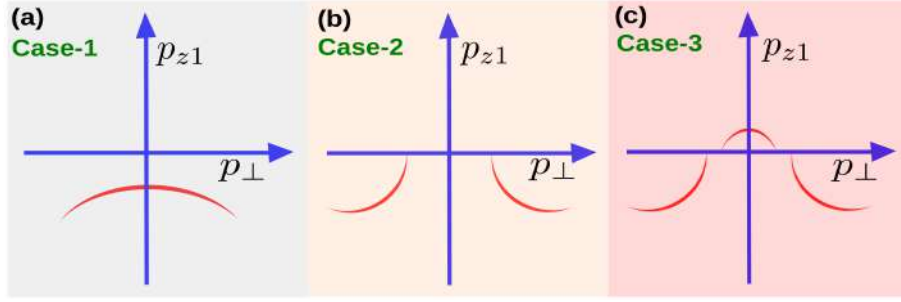


Figure 2.2: Example of the topological transition with the change of the Fermi surface topology (disruption of the "neck" of a Fermi surface).

If $p_{z1} = 0$, $p_z = \frac{\hbar K}{2} \Rightarrow p_{z1} = 0$ plane represents boundary of the Brillouin zone. At BZ boundary, $p_{z1} = 0$ & $p_{\perp} = 0$

$$\Rightarrow \epsilon(0) = \frac{(\hbar K/2)^2}{2m} \pm |U_K| \quad (9)$$

These are energy eigen values at which the surface $\epsilon(p) = \text{constant}$, passes through the point $p_{z1} = p_{\perp} = 0$.

Case-1:

If, $\epsilon < \frac{(\hbar K/2)^2}{2m} - |U_K|$

the surface $\epsilon(p) = \text{const.}$ does not intersect boundary. Therefore, the constant energy plane looks like Fig. 2.2(a). The 3D visualization would just look like Fig. 2.1(c) where the FS segregates into two parts due to LT.

Case-2:

If, $\frac{(\hbar K/2)^2}{2m} - |U_K| < \epsilon < \frac{(\hbar K/2)^2}{2m} + |U_K|$

the surface $\epsilon(p) = \text{const.}$ intersects the boundary at some points and the constant energy plane near $p_{z1} = 0$ looks like Fig. 2.2(b). This would correspond to the 3D Fig. 2.1(a).

Case-3:

If, $\epsilon > \frac{(\hbar K/2)^2}{2m} + |U_K|$

the surface $\epsilon(p) = \text{const.}$ intersects the boundary at several points and some new constant energy planes near $p_{z1} = 0$ appears (Fig. 2.2(c)).

The weak coupling theory provides a good description of the qualitative behaviour of energy dispersion in the vicinity of Brillouin zone boundary. We have shown how external conditions like isotropic compression, hydrostatic pressure, uniaxial deformation, or gradual change of composition can entail modification on the topology of Fermi surface by means of tuning chemical potential of the system in Fig. 2.1. Now we will find the singularity in total energy while changing shape of the FS from 2.2(a) to 2.2(b). The number of states corresponding to the interior of the FS is given by,

$$n(\mu) = \frac{2}{(2\pi\hbar)^3} \int 2\pi p_{\perp} dp_{\perp} dp_{z1} = \frac{1}{4\pi^2\hbar^3} \int dp_{\perp}^2 dp_{z1} \quad (10)$$

Integral over p_{z1} is taken

- i. for Fig. 2.2(a), finite value (lower limit) $p_{z1}^0 \rightarrow P$ (some upper limit),
- ii. for Fig. 2.2(b), $0 \rightarrow P$. From energy dispersion of weakly interacting system we get

$$2m\mu = p_{\perp}^2 + p_{z1}^2 + (\hbar\mathbf{K}/2)^2 \pm \left[(p_{z1}\hbar K)^2 + 4m^2|U_K|^2 \right]^{1/2} \quad (11)$$

The value of p_{z1}^0 is determined by the above equation by putting $p_{\perp}^2 = 0$. We are interested in small values of p_{z1} ($\rightarrow 0$) and $\Delta\mu = \mu - \mu_c$, where

$$\mu_c = \left(\frac{\hbar K}{2m} \right)^2 - |U_K|$$

where μ_c is the value of μ at which there is tangency. Now, we know

$$\begin{aligned} p_{\perp}^2 &= 2m\mu - p_{z1}^2 - (\hbar\mathbf{K}/2)^2 + \left[(p_{z1}\hbar K)^2 + 4m^2|U_K|^2 \right]^{1/2} \\ &= 2m\mu - p_{z1}^2 - (\hbar\mathbf{K}/2)^2 + 2m|U_K| \left[1 + \frac{(p_{z1}\hbar K)^2}{4m^2|U_K|^2} \right]^{1/2} \\ &\simeq 2m\mu - p_{z1}^2 - (\hbar\mathbf{K}/2)^2 + 2m|U_K| \left[1 + \frac{1}{2} \frac{(p_{z1}\hbar K)^2}{4m^2|U_K|^2} \right] \end{aligned} \quad (12)$$

$$\begin{aligned}
&= 2m\mu - p_{z1}^2 - (\hbar\mathbf{K}/2)^2 + 2m|U_K| + \frac{(p_{z1}\hbar K)^2}{4m|U_K|} \\
&= 2m\left[\mu - \frac{(\hbar\mathbf{K}/2)^2}{2m} + |U_K|\right] - p_{z1}^2 + \frac{(p_{z1}\hbar K)^2}{4m|U_K|} \\
&= 2m\left[\mu - \mu_c\right] - p_{z1}^2 + \frac{(p_{z1}\hbar K)^2}{4m|U_K|} \\
&= 2m\Delta\mu + \frac{(1/2)(p_{z1}\hbar K)^2 - 2m|U_K|p_{z1}^2}{2m|U_K|} \\
&= 2m\Delta\mu + \frac{p_{z1}^2\left[(1/2)(\hbar K)^2 - 2m|U_K|\right]}{2m|U_K|} \tag{13}
\end{aligned}$$

If we set $p_{\perp} = 0$, we get

$$\begin{aligned}
2m\Delta\mu &= \frac{p_{z1}^{(0)2}\left[2m|U_K| - (1/2)(\hbar K)^2\right]}{2m|U_K|} \\
p_{z1}^{(0)2} &= \frac{(2m)^2\Delta\mu|U_K|}{\left[2m|U_K| - (1/2)(\hbar K)^2\right]} \\
\Rightarrow p_{z1}^{(0)} &= 2m(\Delta\mu)^{1/2}|U_K|^{1/2}\left[2m|U_K| - (1/2)(\hbar K)^2\right]^{-1/2} \tag{14}
\end{aligned}$$

The number of states corresponding to the interior of the FS is given by

$$n(\mu) = \frac{1}{4\pi^2\hbar^3} \int dp_{\perp}^2 dp_{z1} \tag{15}$$

The main part of the above equation correspond to large p_{z1} . But here we are interested in the singular part which depend on $\Delta\mu$; it is determined by the value of the integral at lower limit. Thus we have $\Delta\mu < 0$ and the conditional upper limit to be $P = \frac{\hbar}{a}$. Therefore,

$$n(\mu) = \frac{1}{4\pi^2\hbar^3} \int_{p_{z1}^{(0)}}^P \left(2m\Delta\mu + \frac{p_{z1}^2\left[(1/2)(\hbar K)^2 - 2m|U_K|\right]}{2m|U_K|}\right) dp_{z1} \tag{16}$$

$$\Rightarrow n(\mu) = \frac{1}{4\pi^2\hbar^3} \left[2m\Delta\mu(P - p_{z1}^{(0)}) + \frac{(P^3 - p_{z1}^{(0)3})}{3} \frac{[(1/2)(\hbar K)^2 - 2m|U_K|]}{2m|U_K|} \right] \quad (17)$$

$$\Rightarrow n(\mu) = n_{reg} - \frac{1}{4\pi^2\hbar^3} \left[2m\Delta\mu p_{z1}^{(0)} + \frac{p_{z1}^{(0)3}}{3} \frac{[(1/2)(\hbar K)^2 - 2m|U_K|]}{2m|U_K|} \right] \quad (18)$$

Putting the value of $p_{z1}^{(0)}$ in the above equation we get

$$n(\mu) = n_{reg} + \frac{1}{6\pi^2\hbar^3} (2m)^2 |U_K|^{1/2} \left[(\hbar K)^2 / 2 - 2m|U_K| \right]^{-1/2} |\Delta\mu|^{3/2} \quad (19)$$

When $\Delta\mu > 0$, only n_{reg} part of n_μ exist. An increment in the total energy is given by $-\int^\mu n(\mu_1) d\mu_1$. Therefore, the singular part exists at $\mu < \mu_c$ and is proportional to $|\mu - \mu_c|^{5/2}$ on one side of the transition point.

$$n(\mu) \propto |\Delta\mu|^{3/2}$$

$$\Rightarrow n(\mu) \propto |\mu - \mu_c|^{3/2} \quad (20)$$

Now an increment in energy

$$\Delta E = - \int^\mu n(\mu_1) d\mu_1$$

$$\Delta E = -K |\mu - \mu_c|^{5/2} \quad (21)$$

i. At $\mu > \mu_c$, $\Delta E < 0$

ii. At $\mu < \mu_c$, $\Delta E > 0$

Therefore, there is a discontinuity in derivative of energy at $\mu = \mu_c$. If we choose the variable external factor to be isotropic compression (pressure p), in this case $|p - p_c| \propto |\mu - \mu_c|$. Thus the singular part of the total energy change is proportional to $|p - p_c|^{5/2}$ at one side of the transition point. This resembles to the case of second order phase transition. Therefore, Lifshitz transition can be considered to be second-and-half (2.5) order transition.

The fundamental difference between Lifshitz transition (LT) and second-order phase transition is that the later is associated with spontaneous symmetry breaking and occurs along entire (T,p) curve of the phase diagram, but LT occurs at T=0 and there is no symmetry breaking associated with it. Although LT occurs at absolute zero temperature, in real metals the $\left(\frac{T}{\mu}\right)$ ratio is quite small and practically there remains a marked trace from the singularity of the Lifshitz transition. There is another kind of Lifshitz transition that occurs in 2D materials like bilayer graphene and can be described by 2D Hamiltonian

$$H = \tau_1(p_x^2 - p_y^2 + vp_x) + \tau_2(2p_xp_y - vp_y) \quad (22)$$

where τ 's are Pauli matrices in the Bogoliubov-Nambu particle-hole space. At Lifshitz like topological transitions, the parameter $v = 0$ and there exist point node with multiple topological charge in the spectrum. For a detailed discussion on this kind of Lifshitz transition in 2D systems and its comparison with cases in 3D, interested readers may look into [118].

2.2 Density Functional Theory(DFT):

There exist two approaches to solve the many body electronic Schrödinger equation –

- i. wavefunction based approaches (*e.g.*, Hartree-Fock, configuration interaction *etc.*)
- ii. density based approach (*e.g.*, DFT). But the many body wave function involves 3N coordinates. Thus it is quite tedious to work with the wavefunction. So it is quite advantageous to work with density ($n(\mathbf{r})$) which depends on just one variable. This is quite reasonable because knowing the wavefunction implies we also know the density:

$$n(\mathbf{r}) = N \int \cdots \int |\Psi(\mathbf{r}, \dots, \mathbf{r}_N)|^2 d\mathbf{r}_2 \dots d\mathbf{r}_N \quad (23)$$

and number of electrons

$$\int n(\mathbf{r})d\mathbf{r} = N \quad (24)$$

Energy in terms of Density

Our goal in density functional theory is to eliminate the wavefunction by writing all terms making up the total ground state energy of the electronic system in terms of density. This is because we would then like to minimize the electronic energy with respect to the density to obtain the ground state energy and the corresponding electronic density. The electronic many body Hamiltonian is given by (in atomic unit)

$$H = - \sum_{i=1}^N \frac{\nabla_{\mathbf{r}_i}^2}{2} + \sum_{i=1}^N \sum_{J=1}^{N_n} \frac{-Z_J}{|\mathbf{r}_i - \mathbf{R}_J|} + \sum_{i=1}^N \sum_{j>i}^N \frac{1}{|\mathbf{r}_i - \mathbf{r}_j|} \quad (25)$$

Suppose now that we have somehow managed to solve the many-body Schrödinger equation and have obtained the wavefunction. The expectation value of the nuclei-electron interaction term is given by

$$\begin{aligned} & \langle \Psi(\mathbf{r}_1, \dots, \mathbf{r}_n) | V_{ne} | \Psi(\mathbf{r}_1, \dots, \mathbf{r}_n) \rangle \\ &= - \sum_{i=1}^N \sum_{J=1}^{N_n} \int \Psi^*(\mathbf{r}_1, \dots, \mathbf{r}_n) \frac{Z_J}{|\mathbf{r}_i - \mathbf{R}_J|} \Psi(\mathbf{r}_1, \dots, \mathbf{r}_n) d\mathbf{r}_1 \dots d\mathbf{r}_N \end{aligned} \quad (26)$$

Since the term does not contain any derivatives, we may collect the wavefunction and its conjugate under a common norm square

$$\langle \Psi(\mathbf{r}_1, \dots, \mathbf{r}_n) | V_{ne} | \Psi(\mathbf{r}_1, \dots, \mathbf{r}_n) \rangle = - \sum_{i=1}^N \sum_{J=1}^{N_n} \int \frac{Z_J}{|\mathbf{r}_i - \mathbf{R}_J|} |\Psi(\mathbf{r}_1, \dots, \mathbf{r}_n)|^2 d\mathbf{r}_1 \dots d\mathbf{r}_N \quad (27)$$

Next, we proceed in a way that is much similar to the one we followed in the calculation

of the density. Let's expand the sum over the electronic index i

$$\begin{aligned} \langle \Psi(\mathbf{r}_1, \dots, \mathbf{r}_N) | V_{ne} | \Psi(\mathbf{r}_1, \dots, \mathbf{r}_N) \rangle = & - \sum_{J=1}^{N_n} \left[\int \frac{Z_J}{|\mathbf{r}_1 - \mathbf{R}_J|} |\Psi(\mathbf{r}_1, \dots, \mathbf{r}_N)|^2 d\mathbf{r}_1 \dots d\mathbf{r}_N \right. \\ & \left. + \int \frac{Z_J}{|\mathbf{r}_2 - \mathbf{R}_J|} |\Psi(\mathbf{r}_1, \dots, \mathbf{r}_N)|^2 d\mathbf{r}_1 \dots d\mathbf{r}_N + \dots \right] \end{aligned} \quad (28)$$

For each of the N_e terms in the sum we separate the integral over the variable in the Coulombic terms from the others and using the definition of density we get

$$E_{ne} = -\frac{1}{N_e} \sum_{J=1}^{N_n} \left[\int \frac{Z_J}{|\mathbf{r}_1 - \mathbf{R}_J|} n(\mathbf{r}_1) d\mathbf{r}_1 + \int \frac{Z_J}{|\mathbf{r}_2 - \mathbf{R}_J|} n(\mathbf{r}_2) d\mathbf{r}_2 + \dots \right] \quad (29)$$

Since for each term an integral over the argument of the density is taken, we may replace these variables by a dummy variable, then all the terms become equal and since there are N_e of them the electron-nucleus interaction energy may be written takes the compact form

$$E_{ne} = - \sum_{J=1}^{N_n} \int \frac{Z_J}{|\mathbf{r} - \mathbf{R}_J|} n(\mathbf{r}) d\mathbf{r} = \int n(\mathbf{r}) V_{ne}(\mathbf{r}) d\mathbf{r} \quad (30)$$

The electron-electron interaction term cannot be written in terms of the single-particle density, instead only in terms of the two-particle density given by

$$E_{ee} = \frac{1}{2} \iint d\mathbf{r} d\mathbf{r}' \frac{n^{(2)}(\mathbf{r}, \mathbf{r}')}{|\mathbf{r} - \mathbf{r}'|} \quad (31)$$

where $n^{(2)}$ may be interpreted as the probability that an electron exists at point \mathbf{r} given that a second electron exists at point \mathbf{r}' . However, the method that we are about to describe does not allow for the existence of such a two-particle density but instead only the one-particle density. So, we are forced to make an approximation- if the two electrons were completely uncorrelated then the two-particle density would just be the product of one-particle densities. Here, we write $n^{(2)}$ in terms of this product plus a correction.

$$n^{(2)}(\mathbf{r}, \mathbf{r}') = n(\mathbf{r})n(\mathbf{r}') + \Delta n^{(2)}(\mathbf{r}, \mathbf{r}') \quad (32)$$

The electron-electron energy may then be written as,

$$E_{ee} = \frac{1}{2} \iint d\mathbf{r} d\mathbf{r}' \frac{n(\mathbf{r})n(\mathbf{r}')}{|\mathbf{r} - \mathbf{r}'|} + \Delta E_{ee} \quad (33)$$

where the second term obviously comes from the correction.

Since the kinetic energy operator contains a derivative term, there is no way we can write it in terms of the density. It is impossible to collect the wavefunction and its conjugate as a single norm square. In order to tackle the kinetic energy, we assume that the density can be written as the sum norm squares of a collection of single-particle orbitals

$$n(\mathbf{r}) = \sum_n^{N_e} |\phi_n(\mathbf{r})|^2$$

These orbitals are called Kohn-Sham orbitals and they are initially completely unspecified. The above form cannot really be considered an approximation. It simply says that instead of the full many-particle system we consider an auxiliary system of single-particle orbitals that have the same ground state density as the real system. Writing the density as in the above equation, suggests that we write the kinetic energy as the sum of the kinetic energies of the Kohn-Sham orbitals. Once again then we express the kinetic energy as the single-particle kinetic energy plus a correction.

$$T = -\frac{1}{2} \sum_n^{N_e} \int d\mathbf{r} \phi_n^*(\mathbf{r}) \nabla^2 \phi_n(\mathbf{r}) d\mathbf{r} + \Delta T \quad (34)$$

Finally putting together everything, the total ground state energy may be written as

$$\begin{aligned} E = & -\frac{1}{2} \sum_n^{N_e} \int d\mathbf{r} \phi_n^*(\mathbf{r}) \nabla^2 \phi_n(\mathbf{r}) d\mathbf{r} + \int n(\mathbf{r}) V_{ne}(\mathbf{r}) d\mathbf{r} \\ & + \frac{1}{2} \iint d\mathbf{r} d\mathbf{r}' \frac{n(\mathbf{r})n(\mathbf{r}')}{|\mathbf{r} - \mathbf{r}'|} + \Delta E_{ee} + \Delta T \end{aligned} \quad (35)$$

The kinetic energy as written cannot be differentiated directly with respect to $n(\mathbf{r})$. But it can be minimized with respect to the orbitals which is equivalent to minimizing with

respect to $n(\mathbf{r})$. Now the only thing that remains to be done is to write the last two (correction) terms in terms of the density as well. The sum of the correction terms is called exchange-correlation energy.

$$E_{xc} = \Delta E_{ee} + \Delta T \quad (36)$$

The origin of this term is the difference between a system of N interacting and non interacting particles. More specifically, the origin of exchange energy is the Pauli repulsion, omitted in the Hartree term and correlation energy is the repulsion between electrons. Several well-developed approximations to this sum exists but here we shall only consider the local approximation given by [119]

$$E_{xc} = \int d\mathbf{r} n(\mathbf{r}) \epsilon_{xc}(n) \quad (37)$$

where $\epsilon_{xc}(n)$ is a simple function of n . Thus, within this approximation, the total energy may be written as,

$$\begin{aligned} E = & -\frac{1}{2} \sum_n^{N_e} \int d\mathbf{r} \phi_n^*(\mathbf{r}) \nabla^2 \phi_n(\mathbf{r}) d\mathbf{r} + \int n(\mathbf{r}) V_{ne}(\mathbf{r}) d\mathbf{r} \\ & + \frac{1}{2} \iint d\mathbf{r} d\mathbf{r}' \frac{n(\mathbf{r})n(\mathbf{r}')}{|\mathbf{r} - \mathbf{r}'|} + \int d\mathbf{r} n(\mathbf{r}) \epsilon_{xc}(n) \end{aligned} \quad (38)$$

Thus we can see that the energy expression can be fully written in terms of density.

The Thomas-Fermi Model

The first attempt to use the electron density rather than the wave function for obtaining information about atomic and molecular systems was taken by Thomas and Fermi in 1927. At the centre of this approach taken by Thomas and Fermi is a quantum statistical model of electrons which, in its original formulation, takes into account only the kinetic energy while treating the nuclear-electron and electron-electron contributions in a completely classical way. In their model Thomas and Fermi arrived at the following, very simple

expression for the kinetic energy based on the uniform electron gas of constant density.

$$T_{TF}[n(\mathbf{r})] = \frac{3}{10}(3\pi^2)^{\frac{2}{3}} \int n^{\frac{2}{3}}(\mathbf{r})d\mathbf{r} \quad (39)$$

If this is combined with the nuclear-electron attractive potential and the electron-electron repulsive potential we have the famous Thomas-Fermi expression for the energy of an atom,

$$E_{TF}[n(\mathbf{r})] = \frac{3}{10}(3\pi^2)^{\frac{2}{3}} \int n^{\frac{2}{3}}(\mathbf{r})d\mathbf{r} - Z \int \frac{n(\mathbf{r})}{r}d\mathbf{r} + \frac{1}{2} \iint \frac{n(\mathbf{r}_1)n(\mathbf{r}_2)}{r_{12}}d\mathbf{r}_1d\mathbf{r}_2 \quad (40)$$

The above equation is a prescription for how to map a density $n(\mathbf{r})$ onto an energy E without any required additional information. So we have a functional expressing the energy in terms of the density. To this end, the Thomas-Fermi model employs the variational principle. It is assumed that the ground state of the system is connected to the electron density for which the energy can be minimized under the constraint of $\int n(\mathbf{r}_1)d\mathbf{r}_1 = N$.

The Hohenberg-Kohn Theorem

DFT is made possible by two very simple theorems given by Hohenberg and Kohn in 1964 [120].

Theorem I

For any system of interacting particles in an external potential $V_{ext}(\mathbf{r})$, the density is uniquely determined. In other words, the external potential is a unique functional of density.

Proof

Let us assume that there exist two potential – $V_{ext}^{(1)}(\mathbf{r})$ and $V_{ext}^{(2)}(\mathbf{r})$ differing by more than a constant and giving rise to the same ground state density, $n(\mathbf{r})$. Obviously, $V_{ext}^{(1)}(\mathbf{r})$ and $V_{ext}^{(2)}(\mathbf{r})$ belong to distinct Hamiltonians $H_{ext}^{(1)}(\mathbf{r})$ and $H_{ext}^{(2)}(\mathbf{r})$, which give rise to distinct wavefunctions $\Psi_{ext}^{(1)}(\mathbf{r})$ and $\Psi_{ext}^{(2)}(\mathbf{r})$. According to the variational principle, no wavefunc-

tion can give an energy less than the energy of $\Psi_{ext}^{(1)}(\mathbf{r})$ for $H_{ext}^{(1)}(\mathbf{r})$. So,

$$E^{(1)} = \langle \Psi^{(1)} | H^{(1)} | \Psi^{(1)} \rangle < \langle \Psi^{(2)} | H^{(2)} | \Psi^{(2)} \rangle \quad (41)$$

Here we have assumed that the ground state is not degenerate. As we have identical ground state densities for two Hamiltonians, we can rewrite the expectation value in equation(1) as

$$\langle \Psi^{(2)} | H^{(1)} | \Psi^{(2)} \rangle = \langle \Psi^{(2)} | H^{(2)} | \Psi^{(2)} \rangle + \int d\mathbf{r} [V_{ext}^{(1)}(\mathbf{r}) - V_{ext}^{(2)}(\mathbf{r})] n_0(\mathbf{r}) \quad (42)$$

Exchanging the levels in equation(2)

$$\langle \Psi^{(1)} | H^{(2)} | \Psi^{(1)} \rangle = \langle \Psi^{(1)} | H^{(1)} | \Psi^{(1)} \rangle + \int d\mathbf{r} [V_{ext}^{(2)}(\mathbf{r}) - V_{ext}^{(1)}(\mathbf{r})] n_0(\mathbf{r}) \quad (43)$$

Adding equation (2) and (3), we obtain

$$E^{(1)} + E^{(2)} < E^{(2)} + E^{(1)} \quad (44)$$

which is clearly a contradiction. Thus, the theorem has been proved.

Theorem II

A universal functional for energy $E[n]$ can be defined in terms of the density. The exact ground state is the global minimum value of this functional.

Proof

Since the external potential is uniquely determined by the density and since the potential in turn uniquely determines the ground state wavefunction, all other observables such as kinetic energy are uniquely determined. Then one may write the energy as a functional of

density.

$$E[n] = T[n] + E_{int}[n] + \int V_{ext}(\mathbf{r})n(\mathbf{r})d\mathbf{r} + E_{II} = F[n] + \int V_{ext}(\mathbf{r})n(\mathbf{r})d\mathbf{r} + E_{II} \quad (45)$$

where $F[n]$ is a universal functional because the treatment of the kinetic and internal potential energies are same for all systems.

In the ground state the energy is defined by the unique ground state density, $n^{(1)}(\mathbf{r})$,

$$E^{(1)} = E[n^{(1)}] = \langle \Psi^{(1)} | H^{(1)} | \Psi^{(1)} \rangle$$

By variational principle, a different density, $n^{(2)}(\mathbf{r})$ will necessarily give a higher energy

$$E^{(1)} = E[n^{(1)}] = \langle \Psi^{(1)} | H^{(1)} | \Psi^{(1)} \rangle < \langle \Psi^{(2)} | H^{(1)} | \Psi^{(2)} \rangle = E^{(2)} \quad (46)$$

Thus minimizing the total energy of the system written as a functional of $n(\mathbf{r})$, w.r.t $n(\mathbf{r})$, one finds the total energy of the ground state. The correct density that minimizes the energy is then the ground state density.

The Kohn-Sham Equations

Let us assume that we have an auxiliary system of non-interacting electrons that has the same ground state density as the real interacting system. This is known as Kohn-Sham approach [121]. The auxiliary system is another manifestation of mean field. The non-interacting electrons move in an effective potential $V = V_{aux}(\mathbf{x}) = V_{eff}(\mathbf{x})$. V_{eff} does not have to be a physically meaningful potential, nor the total wave function have to be physical. The main advantage of the auxiliary system is that we know how to deal with it. The full many body Hamiltonian becomes a sum of single particle ones. From Hartree

Fock (HF) we know -

$$h_{aux}(\mathbf{x}_i)\varphi_i(\mathbf{x}_i) = \epsilon_i\varphi_i(\mathbf{x}_i) \quad (47)$$

Therefore the many body wave function is a single Slater determinant, but it will be different from the HF solution, the orbital $\varphi_i(\mathbf{x}_i)$ are different. In terms of density and the orbitals we can write the Coulomb energy

$$E_H[n] = \frac{1}{2} \iint \frac{n(\mathbf{r})n(\mathbf{r}')}{|\mathbf{r} - \mathbf{r}'|} d\mathbf{r}d\mathbf{r}' \quad (48)$$

and the kinetic energy

$$T_s[n] = -\frac{1}{2} \sum_{i=1}^n \int \langle \varphi_i | \nabla^2 | \varphi_i \rangle d\sigma \quad (49)$$

Therefore,

$$E_{aux}[n] = T_s[n] + \int V_{eff}(\mathbf{r})n(\mathbf{r}')d\mathbf{r} + E_H + E_{xc} \quad (50)$$

E_{xc} is the only term that contains interactions beyond Hartree and is called “exchange correlation”. Now we can write the Lagrangian with constraints

$$\mathcal{L}[n] = E_{aux}[n] - \sum_{i=1}^n \sum_{j=1}^n \lambda_{ij} \left[\int \varphi_i^*(\mathbf{x})\varphi_j(\mathbf{x})d\mathbf{x} - \delta_{ij} \right] \quad (51)$$

Now minimizing w.r.t φ_i^* we get,

$$\sum_{j=1}^n \lambda_{ij}\varphi_j = \frac{\delta T_s}{\delta \varphi_i^*} + \left[\frac{\delta E_{aux}}{\delta n} + \frac{\delta E_H}{\delta n} + \frac{\delta E_{xc}}{\delta n} \right] \frac{\delta n}{\delta \varphi_i^*} \quad (52)$$

$$\sum_{j=1}^n \lambda_{ij}\varphi_j = -\frac{1}{2}\nabla^2\varphi_i(\mathbf{x}) + [V_{aux} + V_H + V_{xc}]\varphi_i(\mathbf{x}) \quad (53)$$

Simplifying we get,

$$\left[-\frac{1}{2}\nabla^2\varphi + V_{eff} \right] \varphi_i(\mathbf{r}) = \lambda_i\varphi_i(\mathbf{r}) \quad (54)$$

, Where

$$V_{eff} = V_{aux} + V_H + V_{xc}$$

The above equation is a system of equations, which when solved simultaneously represent the many particle systems in terms of single particle orbitals. Each of these equations resembles to

$$[\hat{T} + V_{eff}] \phi_i(\mathbf{r}) = \epsilon_i \phi_i(\mathbf{r}) \quad (55)$$

. V_{eff} is the exact effective potential under the influence of which the electrons move. The full complexity of the real system and all many body interactions have been wrapped into

$$V_{xc} = \frac{\delta E_{xc}}{\delta n}.$$

2.2.1 DFT for practical electronic structure calculations:

The schematic of Kohn-Sham approach is shown in Fig. 2.2.1.

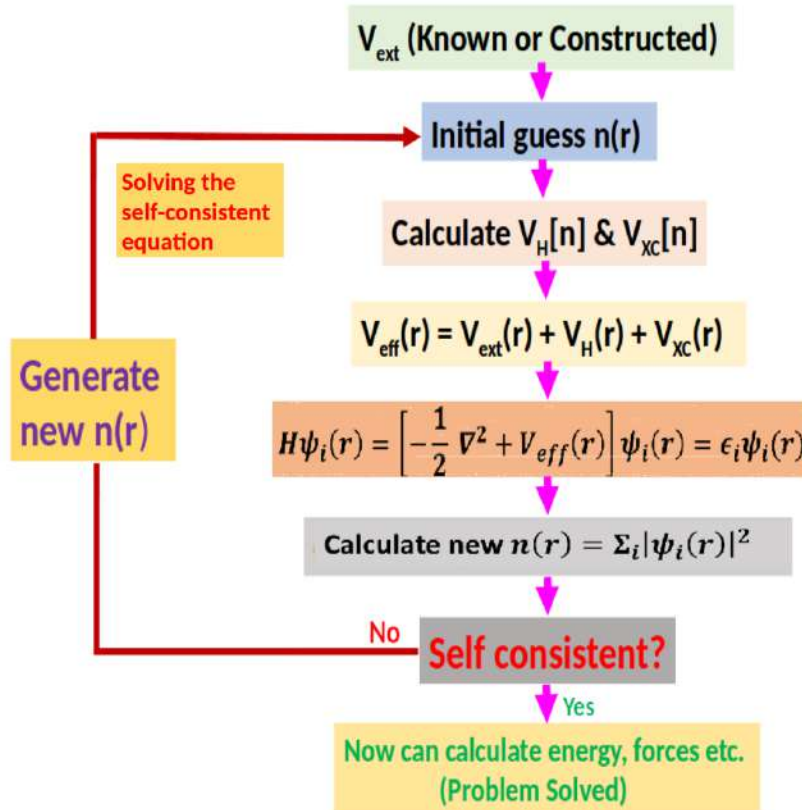


Figure 2.3: Schematic diagram of Kohn Sham approach

Due to functional dependence on density, Kohn-Sham (KS) equations form a set of non-linear coupled equations. The standard procedure to solve KS equation is to iterate until the self consistency is achieved. Next we discuss the primary steps followed in a practical DFT based calculation.

Step-1:

In general some initial model density ($n_0(\mathbf{r})$) has to be supplied for starting the iteration process. In principle, any positive function which is normalized to total number of electrons works. But it is always advantageous to use a smart guess for $n_0(\mathbf{r})$ as it can speed up the convergence to a great extent. For molecular or solid state systems the sum of atomic densities may be used to construct $n_0(\mathbf{r})$ –

$$n_0(\mathbf{r}) = \sum_{\alpha} n_{\alpha}(\mathbf{r} - \mathbf{R}_{\alpha}) \quad (56)$$

where \mathbf{R}_{α} is the position of the nucleus α & n_{α} is the atomic density of the nucleus α . For an atom the convenient choice of $n_0(\mathbf{r})$ is Thomas-Fermi density.

Step-2:

It involves with the evaluation of KS potential (V_{eff}) with density.

$$V_{eff} = V_{ext} + V_H + V_{xc} \quad (57)$$

i. The first term V_{ext} is typically sum of nuclear potentials centred at atomic positions –

$$V_{ext}(\mathbf{r}) = \sum_{\alpha} V_{\alpha}(\mathbf{r} - \mathbf{R}_{\alpha}) \quad (58)$$

In some cases, $V_{\alpha}(\mathbf{r}) = \frac{Z_{\alpha}}{r}$, (where Z_{α} is nuclear charge) is the simple Coulomb attraction between the bare nucleus and electrons. In other cases $V_{\alpha}(\mathbf{r})$ is chosen to be constructed with pseudopotentials. The electronic structure calculations presented in this thesis are

based on the plane wave pseudopotential method. Here we will discuss about pseudopotentials very briefly.

Pseudopotential:

Considering full nuclear potential for solving KS equation sometimes becomes computationally very much demanding. To a good approximation it may be considered that the core electrons do not take part in chemical bonding and the valence electrons only take part actively in the bonding. Therefore, the potential due to nucleus and core electrons may be replaced with some fictitious potential (pseudopotential). In pseudopotential method the singularity of potential near the nucleus is removed by considering smooth potential under the condition that after a certain radius the potential is same as in real case. Here we discuss briefly the steps of generation of atomic pseudopotentials.

First an electronic reference state is chosen and an all electron calculation is performed. From this calculation we obtain the following quantities:

$\hat{V}_{AE} \Rightarrow$ all electron potential, $E_{tot}^{AE} \Rightarrow$ total all electron energy, $\phi_{nl}^{AE} \Rightarrow$ all electron wavefunctions, $\epsilon_{nl}^{AE} \Rightarrow$ eigenvalues corresponding to wavefunctions. Now, pseudopotential (\hat{V}_{PS}) and pseudo wavefunctions (ϕ_{nl}^{PS}) are chosen to satisfy –

$$(\hat{T} + \hat{V}_H[\rho] + \hat{V}_{xc}[\rho] + \hat{V}_{PS})|\phi_{nl}^{PS}\rangle = \epsilon_{nl}^{AE}|\phi_{nl}^{PS}\rangle \quad (59)$$

where, $\hat{T} \Rightarrow$ single particle kinetic energy operator, $\hat{V}_H[\rho] \Rightarrow$ self consistent Hartree operator, $\hat{V}_{xc}[\rho] \Rightarrow$ exchange correlation energy operators. Total electron density $\rho(\mathbf{r}) = \sum_{nl} f_{nl} |\phi_{nl}^{PS}(\mathbf{r})|^2$. The conditions for pseudopotential construction are:

a) $\hat{V}_{PS}(\mathbf{r}) = \hat{V}_{AE}(\mathbf{r})$ for $\mathbf{r} \geq \mathbf{r}_c$

b) $\phi_{nl}^{PS}(\mathbf{r}) = \phi_{nl}^{AE}(\mathbf{r})$ for $\mathbf{r} \geq \mathbf{r}_c$, where r_c is the core radius. \hat{V}_{PS} can be expressed as the sum of a local potential which is diagonal in real space basis and l -dependent correction terms: $\hat{V}_{PS} = \hat{V}^{loc} + \sum_l \Delta \hat{V}^l$. For a fully separable non local pseudopotential $\Delta \hat{V}_l$ is formed according to –

$$\Delta \hat{V}_l^{NL} = \frac{\Delta \hat{V}_l^{SL} |\phi_{nl}^{PS}\rangle \langle \phi_{nl}^{PS}| \Delta \hat{V}_l^{SL}}{\langle \phi_{nl}^{PS} | \Delta \hat{V}_l^{SL} | \phi_{nl}^{PS} \rangle} \quad (60)$$

where $\Delta\hat{V}_l^{SL}$ is short ranged correction term to local potential. As we are interested in plane wave basis for solid state calculations, we need to compute $V(q, q')$, where q, q' are reciprocal lattice vectors. So,

$$\hat{V}^{loc} = \sum_{\mathbf{q}} \sum_{\mathbf{q}'} |\mathbf{q}'\rangle V^{loc}(|\mathbf{q} - \mathbf{q}'|) \langle \mathbf{q}| \quad (61)$$

The non local correction term can be expressed as –

$$\Delta\hat{V}_l^{NL} = \sum_{\mathbf{q}} \sum_{\mathbf{q}'} \frac{|\mathbf{q}'\rangle \langle \mathbf{q}'| \Delta\hat{V}_l^{SL} |\phi_{nl}^{PS}\rangle \langle \phi_{nl}^{PS}| \Delta\hat{V}_l^{SL} |\mathbf{q}\rangle \langle \mathbf{q}|}{\langle \phi_{nl}^{PS}| \Delta\hat{V}_l^{SL} |\phi_{nl}^{PS}\rangle} \quad (62)$$

Local Fourier space matrix elements are given by $\langle \mathbf{q}' | \hat{V}^{loc} | \mathbf{q}' \rangle$, and non local Fourier space matrix elements are $\langle \mathbf{q}' | \hat{V}_l^{SL} | \mathbf{q}' \rangle$.

ii. The second term in the KS potential is the Hartree potential:

$$V_H(\mathbf{r}) = \int d\mathbf{r}' \frac{n(\mathbf{r}')}{|\mathbf{r} - \mathbf{r}'|} \quad (63)$$

This term can be evaluated either by direct integration while solving atomic KS equation, or solving equivalent Poisson's differential equation: $\nabla^2 V_H(\mathbf{r}) = -4\pi n(\mathbf{r})$.

iii. The third term in KS potential is V_{xc} , exchange correlation potential. We will discuss about this term and its evaluation in some detail.

We know that

$$E_{HK}[n] = T[n] + V^{ee}[n] + \int V_{ext}(\mathbf{r})n(\mathbf{r})d\mathbf{r} \quad (64)$$

and

$$E_{KS}[n] = T_s[n] + \int V_{ext}(\mathbf{r})n(\mathbf{r})d\mathbf{r} + E_H[n] + E_{xc}[n] \quad (65)$$

From the above equations the exchange correlation energy functional is

$$E_{xc}[n] = T[n] - T_s[n] + V^{ee}[n] - E_H[n] \quad (66)$$

The first term is the difference between the kinetic energy of the interacting and non-interacting electrons, and the second term is the difference between the full electron-electron interaction energy and the classic Coulomb energy.

The Local Density Approximation (LDA)

Here we will introduce the model system on which virtually all approximate exchange-correlation functionals are based. For inhomogeneous systems with a slowly varying density, the system locally looks like it has a constant density. Therefore the external potential will also be constant and the system is similar to the homogeneous electron gas. Now we will construct a local approximation to exchange correlation [119]

$$E_{xc}[n] = \int n(\mathbf{r}) \epsilon_{xc}(n(\mathbf{r})) d\mathbf{r} \quad (67)$$

where $\epsilon_{xc}(n(\mathbf{r}))$ denotes the energy density (*i.e.*, energy per electron) at point \mathbf{r} in space, that depends only on the density at this point. Now

$$\begin{aligned} \epsilon_{xc}(n(\mathbf{r})) &= \frac{3k_F}{4\pi} \\ k_F &= [3\pi^2 n(\mathbf{r})]^{1/3} \\ \epsilon_{xc}(n(\mathbf{r})) &= \frac{3}{4} \left[\frac{3}{\pi} n(\mathbf{r}) \right]^{1/3} \\ \Rightarrow E_{xc}[n] &= \int n(\mathbf{r}) \epsilon_{xc}(n(\mathbf{r})) d\mathbf{r} \\ &= \frac{3}{4} \left(\frac{3}{\pi} \right)^{1/3} \int n(\mathbf{r})^{4/3} d\mathbf{r} \end{aligned} \quad (2.1)$$

In the above expression we need to know the density at any given point in space and the

exchange energy is then simply the integral over the density to the power 4/3. The exchange contribution to V_{xc} can be calculated straight forwardly as the functional derivative :

$$V_x(\mathbf{r}) = \frac{\delta E_x[n]}{\delta n(\mathbf{r})} = \epsilon_{xc}(n(\mathbf{r})) + n(\mathbf{r}) \frac{\delta \epsilon_x(n(\mathbf{r}))}{\delta n(\mathbf{r})}$$

$$\Rightarrow V_x(\mathbf{r}) = \left(\frac{3}{\pi}\right)^{\frac{1}{3}} n^{\frac{1}{3}}(\mathbf{r})$$

The above expression is the final and very simple expression for the exchange contribution to the exchange-correlation potential in the local density approximation.

The local density approximation can also be extended to the spin polarized case [122]:

$$E_{xc}^{LSDA}[n^\uparrow, n^\downarrow] = \int n(\mathbf{r}) \epsilon_{xc}(n^\uparrow(\mathbf{r}), n^\downarrow(\mathbf{r})) d\mathbf{r} \quad (68)$$

If we write in terms of spin polarization $\eta(\mathbf{r}) = \frac{n^\uparrow(\mathbf{r}) - n^\downarrow(\mathbf{r})}{n(\mathbf{r})}$ we get

$$E_{xc}^{LSDA}[n, \eta] = \int n(\mathbf{r}) \epsilon_{xc}(n(\mathbf{r}), \eta(\mathbf{r})) d\mathbf{r} \quad (69)$$

The local density approximation is by construction exact or at least very accurate for the homogeneous electron gas and thus is expected to perform well for systems with slowly varying density *e.g.*, simple metals. However, LDA has problems with self-interaction and systems with rapidly varying densities *e.g.*, atoms and is therefore not suited for thermochemistry.

Generalized Gradient Approximations (GGA)

LDA is based on the assumption of a homogeneous density. But for real systems the density is not homogeneous. To approach more realistic situation, the logical first step

was the suggestion of using not only the information about the density $n(\mathbf{r})$, at a particular point \mathbf{r} , but to supplement the density with information about the gradient of the charge density, $\nabla n(\mathbf{r})$ in order to account for the non-homogeneity of the true electron density. The exchange correlation energy functional in GGA is given by [123, 124],

$$E_{xc}^{GGA}[n^\uparrow, n^\downarrow] = \int n(\mathbf{r}) \epsilon_{xc}(n^\uparrow(\mathbf{r}), n^\downarrow(\mathbf{r}), |\nabla n^\uparrow(\mathbf{r})|, |\nabla n^\downarrow(\mathbf{r})|) d\mathbf{r} \quad (70)$$

Instead of using the gradient directly, it makes sense with a scaled gradient:

$$S(\mathbf{r}) = \frac{|\nabla n(\mathbf{r})|}{2k_F(\mathbf{r})n(\mathbf{r})} \quad (71)$$

which measures the gradient on the scale of the density itself. A major advantage of this rescaling is that the gradient remains well-behaved even close to the nucleus. One famous GGA exchange correlation functional is Perdew–Burke–Ernzerhof (PBE) functional which is very frequently used in electronic structure calculations of metals. The PBE exchange correlation functional is given by [125],

$$E_{xc}^{GGA}[\hat{n}_\uparrow - \hat{n}_\downarrow] = \int d^3r n \epsilon_x^{unif}(n) F_{xc}(r_s, \xi, s) \quad (72)$$

where F_{xc} is known as enhancement factor. In the PBE functional, $n = n_\uparrow + n_\downarrow = \frac{3}{4\pi r_s^3}$, r_s is the Seitz radius, $\epsilon_x^{unif}(n) = -\frac{3e^2 k_F}{4\pi}$, $s = \frac{|\Delta n|}{2k_F n}$, and relative spin polarization $\xi = \frac{n_\uparrow - n_\downarrow}{n}$. We have used this PBE functional in most of our calculations.

Step-3:

As we already have KS potential, now we can solve the KS equation. We want to obtain the p^{th} lowest eigenstates of the KS Hamiltonian. KS equation can be reduced to 1D differential equation in case of atoms. In this case an efficient integration method is employed. But in case of solids or other complex systems basis sets, plane-waves or real space methods are used. In these cases the KS Hamiltonian matrix has to be diagonalized.

But this method is computationally very costly. Therefore, iterative methods are chosen for which it is never necessary to write the full Hamiltonian; the knowledge of how KS Hamiltonian is applied to a test wavefunction, is sufficient. In case of calculations with solids, the general choice of basis set is plane waves due to validity of Bloch's theorem. Although handling a large number of plane waves is computationally costly, the number can be reduced significantly by finding plane wave cut off energy and choosing proper pseudopotential.

Step-4:

In case of self consistent calculations, it is necessary to set convergence criterion. We get electronic density as KS equation is solved. The convergence criterion is set on the basis of difference of total energies or densities for i^{th} and $(i - 1)^{th}$ iteration and the cycle is stopped when either $|E^{(i)} - E^{(i-1)}| < \eta_E$ or $\int d^3r |n^{(i)} - n^{(i-1)}| < \eta_n$, where η_E & η_n are energy and density tolerance respectively.

Step-5:

If the convergence criterion is not satisfied, the self consistency cycle is restarted with a new density. It may be the out put density of the previous cycle. But most of the time this leads to instabilities. This condition is avoided by mixing densities from previous iteration. So, new density $n^{(i+1)} = \beta n' + (1 - \beta)n^{(i)}$, where β is the mixing parameter.

Step-6:

At the end of the calculation we get total energy. From this energy we can obtain equilibrium geometry, phonon dispersion, ionization potential *etc.*

2.2.2 Virtual Crystal Approximation (VCA):

In order to study the effect of impurity on the electronic properties of a system theoretically, Virtual Crystal Approximation (VCA) is used [126]. VCA has been proved to be very efficient for simulating disordered systems within primitive unit cell. In VCA method, same atomic coordinates are used for the atom in the compound and the impurity introduced. The actual atoms are replaced with fictitious virtual atoms consisting a mixed character of the pure atom & impurity and having same periodicity in the crystal. In VCA method, weighted real space averaging of pseudopotentials is executed in order to create pseudopotential of the fictitious atom. The created pseudopotential for the mixed atom can be represented by –

$$V_{ext}(\mathbf{r}, \mathbf{r}') = \sum_I \sum_{\alpha} \omega_{\alpha}^I V_{PS}^{\alpha}(\mathbf{r} - \mathbf{R}_{I\alpha}, \mathbf{r}' - \mathbf{R}_{I\alpha}) \quad (73)$$

where I is the site index, α atomic index, ω is weight of the atom in compound. Let us consider a virtual atom construction for two atoms A & B . The virtual atom is $A_{\alpha}B_{\beta}$ where $\alpha + \beta = 1$. If the atomic pseudopotential for A & B be \hat{V}_{PS}^A & \hat{V}_{PS}^B respectively, the potentials are then averaged according to $\hat{V}_{PS}^{VC2} = \alpha \hat{V}_{PS}^A + \beta \hat{V}_{PS}^B$. But this construction do not guarantee accurate representation of the electronic properties of a true hybrid atom because it doesn't consider the energy restriction. Therefore, to improve electronic behavior of virtual atom an average eigenvalue constraint is introduced. The average eigenvalue, $\epsilon_{nl}^{avg} = \alpha \epsilon_{nl}^A + \beta \epsilon_{nl}^B$, where ϵ_{nl}^A & ϵ_{nl}^B are all electron eigenvalue of nl^{th} state of atom A & B respectively. A virtual potential is constructed which guarantees that $\epsilon_{nl}^{VC3} = \epsilon_{nl}^{avg}$.

The electronic structure included in the thesis are mostly calculated using ultrasoft pseudopotential. These pseudopotentials are prone to produce ghost states within VCA framework. To check the validity of VCA *w.r.t* ghost states one should always examine the value of the derivative of total energy *w.r.t* E_{cut} , during finite basis set correction. The derivative should be of the same order as that of the derivatives of the end member of the structures.

Validity of VCA is checked for each of our calculations.

2.2.3 DFT+U method:

We have used DFT+U method to investigate the effect of electron correlation on the electronic structure of Fe based superconductors. The concept of DFT+U calculations primarily originated from Hubbard model for treating strongly correlated systems [127]. To capture the characteristic of electrons having strong localization Hubbard model is used. The Hubbard Hamiltonian,

$$H_{Hub} = t \sum_{\langle i,j,\sigma \rangle} (c_{i,\sigma}^\dagger c_{j,\sigma} + h.c.) + U \sum_i n_{i\uparrow} n_{i\downarrow} \quad (74)$$

where t represents the hopping strength, c_i^\dagger and c_j are the creation and annihilation operators at the respective sites, U is Hubbard correlation strength, n is the number operator. When electrons are strongly localized, their motion is described by "hopping" process from one atomic site to its neighbouring sites. t is proportional to the bandwidth of the valence electronic states and represents single particle term of the total energy. U represent the strength of the onsite Coulomb repulsion and is only accounted for electrons on the same site. DFT+U approach is one of the simplest corrective approaches that were formulated to improve the accuracy of the DFT functionals in describing ground state of the correlated systems having localized d or f orbitals. In LDA+U approach a local correction to LDA is introduced based on a mean-field (HF) treatment of the Hubbard model. The total energy of a system within LDA+U can be written as –

$$E_{LDA+U}[\rho(r)] = E_{LDA}[\rho(r)] + E_{Hub}[n_{mm'}^{I\sigma}] - E_{dc}[n_{I\sigma}] \quad (75)$$

where $n_{I\sigma}$ is the local density matrix, E_{Hub} contain the electron-electron interaction as modeled in Hubbard Hamiltonian, double counting term E_{dc} removes the part that is already included in the LDA total energy (E_{LDA}). The LDA+U approach can remark-

ably improve the treatment of strongly correlated systems with respect to LDA without introducing much computational effort, and has therefore become very popular in first-principles modeling of d - and f -electron systems.

Chapter 3

Electronic structure, Lifshitz transition and its possible impact on superconductivity in 112 compounds

In this chapter we present a detailed density functional theory based first principles electronic structure calculations on a series of 112 compounds $\text{Ca}_{1-x}\text{La}_x\text{Fe}_{1-y}\text{TM}_y(\text{As}_{1-p}\text{Sb}_p)_2$ for various values of x , y , p and transition metals ($\text{TM} = \text{Co}, \text{Ni}, \text{Mn}$). The possibility of Lifshitz like electronic topological transition in these doped 112 materials is investigated and its possible connection with the occurrence of superconductivity is also demonstrated. Our electronic structure investigations reveal that La doping at Ca site, Co or Ni doping at Fe site causes electron doping whereas Mn doping at Fe site causes hole doping. The hole bands gradually shift below the Fermi level causing Lifshitz transition with increased electron doping either through La or TM ($= \text{Ni}, \text{Co}$) doping. A merger of top of hole bands in the close vicinity of Fermi level *i.e.*, singular band structure (band edge van Hove singularity) are disclosed at around optimal doping on the verge of Lifshitz like topological transition. The optimal doping at which band edge van Hove singularities are observed, coincides with the experimental highest critical temperature (T_c) in the phase diagram.

Singular band structure occurs around 15% La doping, 0.5% Ni doping as well as 5% Co doping and respective highest T_c s are also observed at these optimal doping. In case of 25% La doping at Ca site, all the hole bands move below the Fermi level causing a topological modification in the hole Fermi surfaces, creating disconnected propeller like Fermi surfaces at the Γ point where superconductivity is predicted to cease. Mn doping has adverse effect on the electronic structure of 112 compounds. The hole like bands around the Fermi level starts shifting away above it barring any possibility of band edge singularity or Lifshitz transition. As a consequence superconductivity also ceases to exist in Mn doped 112 compounds. Our magnetic structure evaluation of these compounds reveal striped antiferromagnetism as magnetic ground state. A large reduction of Fe local magnetic moment (μ_{Fe}) and very low Co magnetic moment due to Co doping may be favourable to superconductivity, whereas very small reduction of μ_{Fe} and large μ_{Mn} may be the reason behind suppression of superconductivity due to Mn doping.

3.1 Theory and Computational Method

Our first-principles *ab-initio* simulations are performed using Cambridge Serial Total Energy Package (CASTEP), which exploits the plane-wave pseudo-potential method based on Density Functional Theory [128]. In our simulations the electronic exchange correlation is treated within the generalized gradient approximation (GGA) using Perdew-Burke-Enzerhof (PBE) functional [125]. Geometry optimization has been carried out using the Broyden-Fletcher-Goldfrab-Shanno (BFGS) scheme. In order to dope the system theoretically, we use Virtual Crystal Approximation (VCA) for small doping as well as supercell approaches [126, 129] for large doping respectively. Virtual crystal approximation is very effective for simulating disordered systems within primitive unit cell. In VCA method, we use the same atomic coordinates for Ca and La atoms. In VCA, in place of actual atoms fictitious virtual atoms are created for the doped system with the crystal having same periodicity [129]. We have used ultra-soft pseudopotential which are prone to generate ghost

states within VCA framework. There is a standard way for testing the applicability of the VCA approach for ghost states. One should always examine the value of the derivative of total energy w.r.t E_{cut} *i.e.*, the size of plane wave basis set, during finite basis set correction calculation. The derivative should be of the same order as that of the derivatives of the end member of the structures [130]. We have checked the validity of VCA for each of our calculations. Electronic structure studies using supercell method for 1111 system as well as a detailed comparison of that using both VCA and supercell methods for 122 FeSCs are available in literature [131, 132]. These studies suggest no appreciable modifications in the resulting electronic structures are expected in the low doping regime irrespective of VCA or supercell method. Non-spin-polarized as well as spin polarized single point energy calculations were carried out for monoclinic phase with space group symmetry $P2_1$ using ultrasoft pseudo-potentials and plane-wave basis set with energy cut off 600 eV. Brillouin zone (BZ) is sampled in the k space within the Monkhorst-Pack scheme [133, 134] and grid size for SCF calculation is $25 \times 26 \times 10$. All atoms were fully relaxed until the magnitude of the force on each atom converges to less than 0.01 eV/Å and the energy change per atom converged to less than 5×10^{-7} eV/atom, yielding optimized structures. Further, for checking the effect of Ni, Co and Mn doping at the Fe site we have performed spin polarized calculation with $2 \times 2 \times 1$ supercell. Spin-polarized single point energy calculations are performed on optimized structures using ultrasoft pseudopotentials and plane wave basis set with energy cut off 600 eV. The orbital projected band structure calculations of CaFeAs_2 is performed using QUANTUM ESPRESSO package [135] with ultrasoft pseudo-potential and PBE exchange correlation potential. After performing convergence test the energy cut off was set to 30 Rydberg and the grid size for SCF calculation was $16 \times 16 \times 6$.

3.2 Electronic structure of doped 112 materials

3.2.1 La doping at Ca site

We examine the effect of La doping on the electronic structure of CaFeAs_2 within Virtual Crystal Approximation (VCA). We have calculated the band structures (BNS), density of states (DOS) and Fermi Surfaces (FS) of CaFeAs_2 for various La doping values systematically. We have presented in this section calculated electronic structures in the monoclinic phase after geometry optimization in which experimentally measured lattice parameters [27] are used as starting input for our first principles calculations. In Fig. 3.1 we depict the FSs of CaFeAs_2 with various percentages of La doping. With La doping $x = 0.10$, there appears two electron like FSs around the BZ corners and three hole like FSs at the BZ centre which is consistent with the experimental observations [136, 79]. It is also evident from the FSs that with increasing La doping the hole like FSs shrink. One of our most important observations, is the occurrence of Lifshitz transition (LT) with increase of La doping. It has broadly following major manifestations: (i) appearance of new small to large FS around X-point, (ii) gradual disappearances of various hole FSs (hole bands drift below the Fermi level (E_F)), (iii) topological modifications of various FS sheets, namely, 2d to 3d like.

It is distinctly visible that with increasing percentage of La doping the resulting hole FSs actually become more 3D like. For illustrating the occurrence of Lifshitz transition, we have shown the calculated band structures (see Fig. 3.2) for La doping levels 0.10, 0.15, 0.20, 0.25, 0.30 at Ca-site respectively. Band structures around the high symmetry Γ and M points are shown particularly for illustrations of LT as well as for comparison with available ARPES results (see below). The calculated electronic band structures show features very similar to that observed in [143] where a singular electronic band structure is observed that can be fine tuned with doping. This is the situation here for doping values in between $x = 0.15$ to 0.2 where the highest superconducting transition occurs

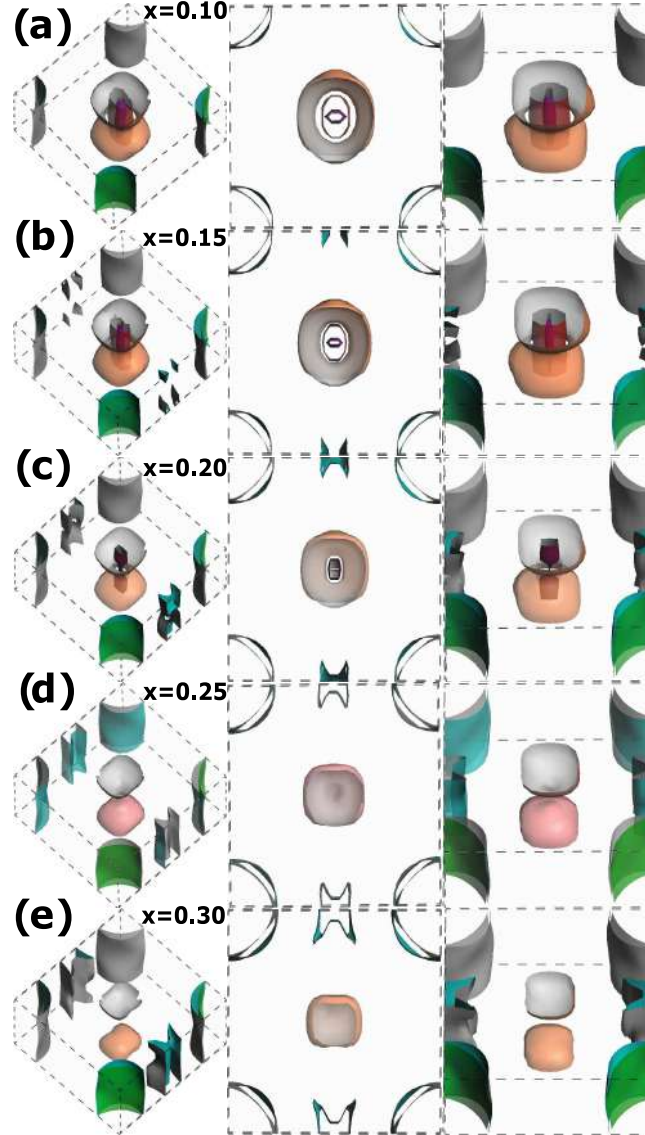


Figure 3.1: [137] Calculated Fermi surfaces of $\text{Ca}_{1-x}\text{La}_x\text{FeAs}_2$ system within VCA method. Doping levels (x) of La are (a) $x = 0.10$, (b) $x = 0.15$, (c) $x = 0.20$, (d) $x = 0.25$, and (e) $x = 0.30$ respectively. We have shown three different views of FSs in the same row for a particular value of doping. In middle and last column, FSs in 45° clockwise rotated BZ are shown. Upper view of the FSs is presented in the middle column.

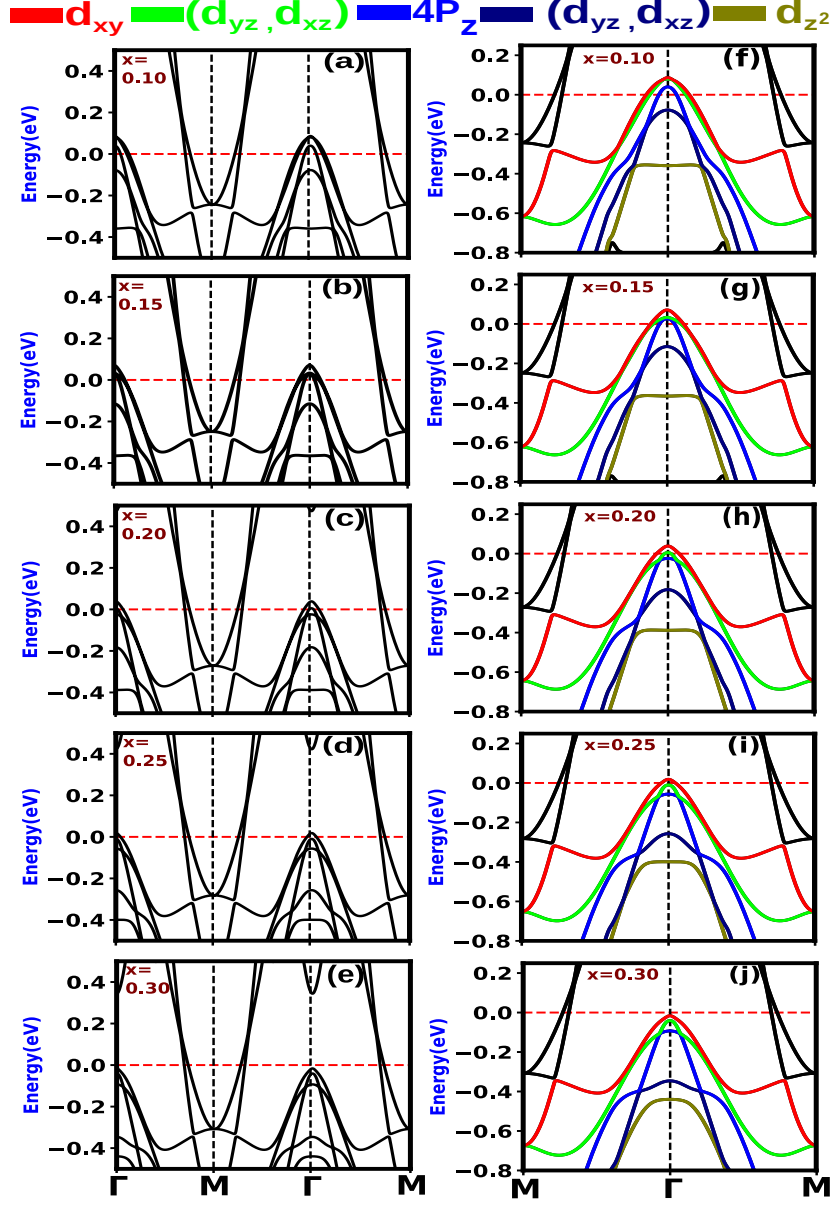


Figure 3.2: [137] Calculated band structures of $\text{Ca}_{1-x}\text{La}_x\text{FeAs}_2$ system within VCA method around high symmetry points. Doping levels are (a) $x = 0.10$, (b) $x = 0.15$, (c) $x = 0.20$, (d) $x = 0.25$, and (e) $x = 0.30$. The corresponding bands around Γ point for various doping values along with orbital natures are shown in (f), (g), (h), (i), (j). Fermi level is denoted by horizontal red line at zero energy.

in this system. This result may be compared with that of the Fig 1(i) of [143] where the top of the hole bands are in the close vicinity of E_F whereas the bottom electron bands are deep below the E_F . Singularities in the bulk low-energy electronic structure near the E_F found in our work has similarities with earlier such observations [144]. As the doping level is changed from $x = 0.10$ to $x = 0.15$, there appears small new Fermi surface around the X-point which grows with further La doping. This is an example of LT that were also predicted earlier in strongly correlated electron system like Na_xCoO_2 with x , where a small electron FS around the Γ point were predicted to appear but yet to be confirmed experimentally [145]. As the doping level is increased further to $x = 0.20$, there is a clear 2D to 3D crossover of the outer Fermi surfaces (FS) and the inner most FS vanishes at around Γ -point. This is also due to manifestation of Lifshitz transition. But the most remarkable change of FS occurs around La doping level 0.25 - a complete Lifshitz transition occurs. As a consequence of Lifshitz transition, hole like bands around Γ point from above E_F are pushed below the E_F . But there is no substantial modifications in the electron like bands around the M points. A remarkable topological modification of FSs takes place at around $x = 0.25$ resulting two separated hole FSs, which may be the main reason for appearance of superconductivity in CaFeAs_2 only below $x = 0.25$ of La doping. Disappearance of the centre of the propeller like structure at the M point of the Brillouin zone when going from $x = 0.4$ to $x = 0.6$ in doping in $\text{Ba}_{1-x}\text{K}_x\text{Fe}_2\text{As}_2$ lead to a complete suppression of the superconducting gap on the outer sheet of the Fermi surface centered at the Γ point [144]. Such topological modification of partially vanishing hole FS is also observed in BaRu_2As_2 where no superconductivity was found [146, 147].

We have shown the orbital characters of bands (Fig. 3.3) based on our calculations on undoped CaFeAs_2 performed using Quantum Espresso code. Fig. 3.3 presents the relative contribution of orbitals to different bands around high symmetry points. Differently coloured open circles are used to present different orbital characters to different bands and larger the size of the circle larger is its orbital weight. It is quiet clear from Fig. 3.3 that all the bands have mixed multi-orbital character. However a close look at the bands around

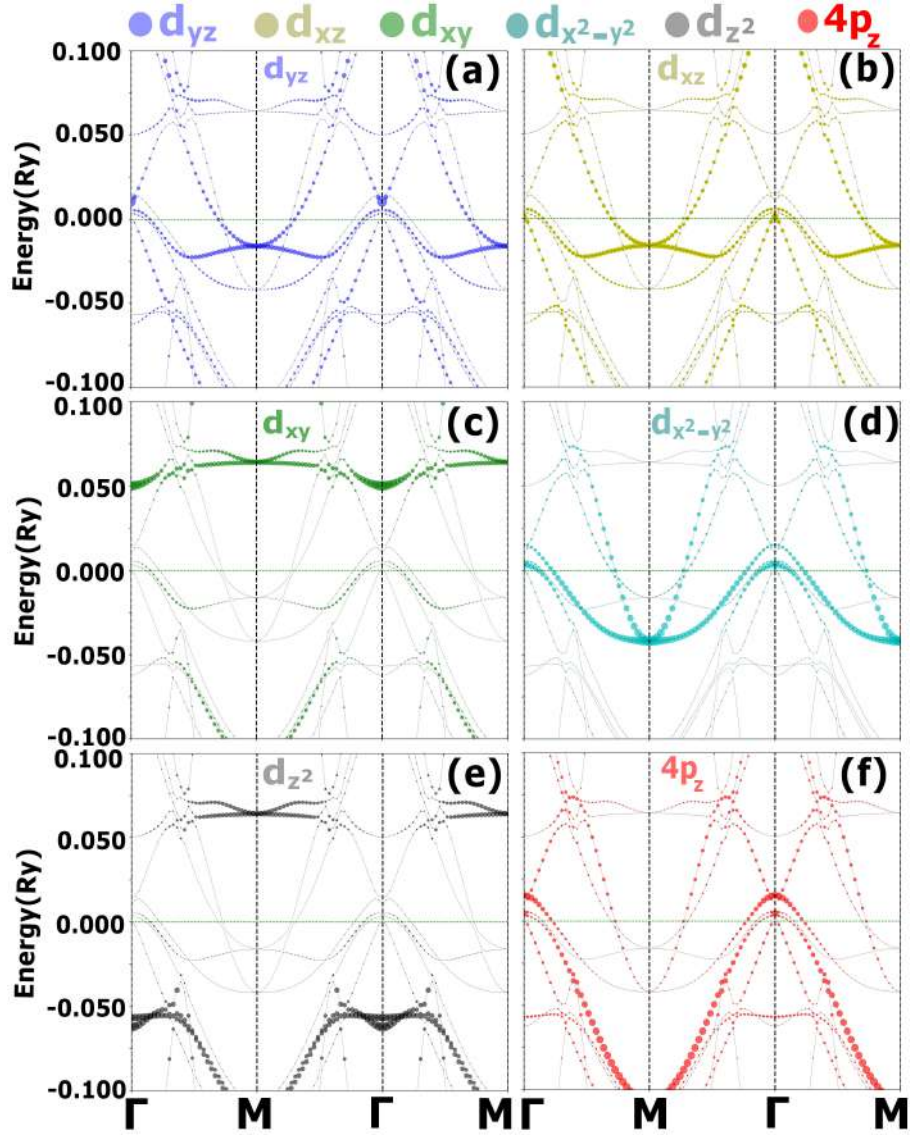


Figure 3.3: [137] Calculated orbital projected band structures of undoped CaFeAs_2 around high symmetry points. The weight of the different Fe 3d and As 4p orbitals for different bands is shown with varying sizes of the circles and colours - (a) d_{yz} , (b) d_{xz} , (c) $d_{x^2-y^2}$, (d) d_{xy} , (e) d_{z^2} , and (f) $4p_z$. Sizes of the circles correspond to the degree of relative contributions. Fermi level is denoted by horizontal dotted green line at zero energy.

the Γ -point reveals that the uppermost band near the E_F has $d_{x^2-y^2}$ as dominant orbital character (Fig. 3.3(d)). The next band have mixed (d_{xz}, d_{yz}) character (Fig. 3.3(a, b)). The band just above E_F for undoped CaFeAs_2 shows $4p_z$ orbital as dominant character coming from the As-chain (Fig. 3.3(f)). There exists also another band just touching the E_F having d_{xz} and p_z mixed character in undoped case. In La doped 112 materials this band is pushed below E_F . In the DFT calculation, the x and y directions are defined to be along the next nearest Fe-Fe bonds, and thus the Γ -M direction is parallel to the k_x (k_y) directions in the reciprocal space. This convention is same as that used in ref. [79]. This amounts to saying that the $d_{x^2-y^2}$ (in Fig. 3.3) is same as d_{xy} in the ARPES polarization (see for example Fig. 3 (a) in ref. [136]). Thus our band structure results agree quite well with earlier theoretical [79] as well as experimental results [136]. Making our results consistent with the ARPES measurements, we have shown that the uppermost orbital near E_F around Γ -point to be d_{xy} for doped cases. The shown orbital characters to bands for doped cases (as presented below and in Fig. 3.2) are dominant character around Γ -point only but mixed character otherwise.

Lifshitz transition plays an important role in understanding different properties of iron based superconductors. For La doped 112 system, hole like bands around Γ point are closed to the E_F . The As $4p_z$ band is very near to the E_F . The other two bands d_{xy} and (d_{yz}, d_{xz}) are slightly higher in energy than the $4p_z$ band. From Fig. 3.2(f), it is evident that at La doping level 0.10 all the three hole like bands are above E_F . Now as we increase the La doping level to 0.15, the hole bands start shifting towards the E_F (Fig. 3.2(g)); the $4p_z$ band just touches the E_F as well and a singular electronic band structure occurs. This may be the cause behind the highest T_C around doping 0.15 in these compounds. At La doping level 0.20 (Fig. 3.2(h)) the $4p_z$ band is pushed below the E_F . The Lifshitz transition occurs when the top of a hole like band drifts below the E_F because of increasing electron occupation. Thus there is a Lifshitz transition at this doping. Now as we increase La doping further the (d_{yz}, d_{xz}) and d_{xy} bands are also shifted below the Fermi level (Fig. 3.2(i), (j)). This is the cause of Lifshitz transition in the La

doped CaFeAs_2 compounds which might have great impact on superconductivity in these compounds. It has been observed that there should be a critical density of electrons at the Fermi level for the occurrence of superconductivity in high temperature superconductors [148]. We also know that superconductivity in iron based superconductors is due to intra as well as inter-band pairing of electrons from electron-like and hole-like bands. When Lifshitz like topological transitions come into play in these compounds, the interband pairing is affected. At La doping level 0.25, as the hole-like bands at Γ point disappears due to Lifshitz transition, the inter band pairing is diminished, the inter-band pair density decreases below certain critical density and as a result superconductivity would disappear.

3.2.2 Ni, Co and Mn doping at Fe site

Ni, Co and Mn doping at the iron site are proved to be very much impactful on superconductivity of 112 family of iron based superconductors. Recently, the phase diagram of CaFeAs_2 with Ni doping at Fe site for a fixed La doping at Ca site has been studied experimentally [40]. In order to make our studies impactful for such experimental observations, we have studied the electronic structure of $\text{Ca}_{1-x}\text{La}_x\text{Fe}_{1-y}\text{Ni}_y\text{As}_2$ using spin polarized virtual crystal approximation. Experimentally, it has also been observed that Co doping enhances superconductivity in CaFeAs_2 but Mn doping suppresses superconductivity [34]. To investigate the effect of Co and Mn doping at Fe site, we have studied the electronic structures in detail through evaluation of Fermi surface and band structures of $\text{Ca}_{1-x}\text{La}_x\text{Fe}_{1-y}\text{Co}_y\text{As}_2$ and $\text{Ca}_{1-x}\text{La}_x\text{Fe}_{1-y}\text{Mn}_y\text{As}_2$ respectively within non spin polarized as well as spin polarized VCA calculations. CaFeAs_2 shows striped antiferromagnetic phase as its ground state spin configuration. To check the effect of Co, Mn as well as Ni doping at Fe site on magnetic state of CaFeAs_2 , we have performed spin polarized calculations using supercell approach. Through magnetic calculations using supercell we extract changes in the density of states (DOSs), magnetic moments to validate the observed experimental facts.

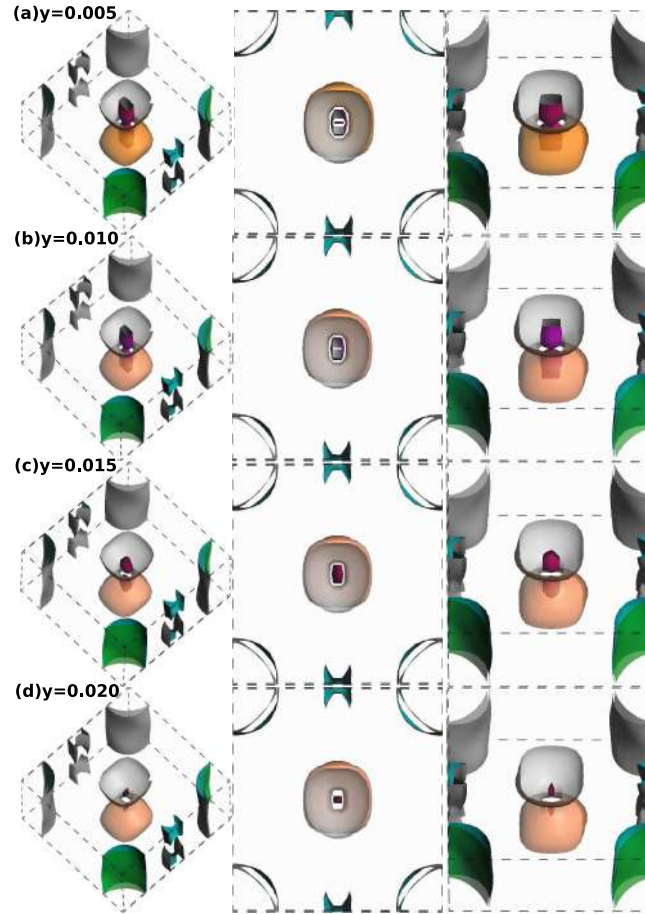


Figure 3.4: [137] Fermi surfaces of $\text{Ca}_{0.82}\text{La}_{0.18}\text{Fe}_{1-y}\text{Ni}_y\text{As}_2$ for doping levels (a) $y = 0.005$, (b) $y = 0.010$, (c) $y = 0.015$, and (d) $y = 0.020$. We have shown three different views of FSs in the same row for a particular value of doping. In middle and last column, FSs in 45°clockwise rotated BZ are shown. Upper view of the FSs is presented in the middle column.

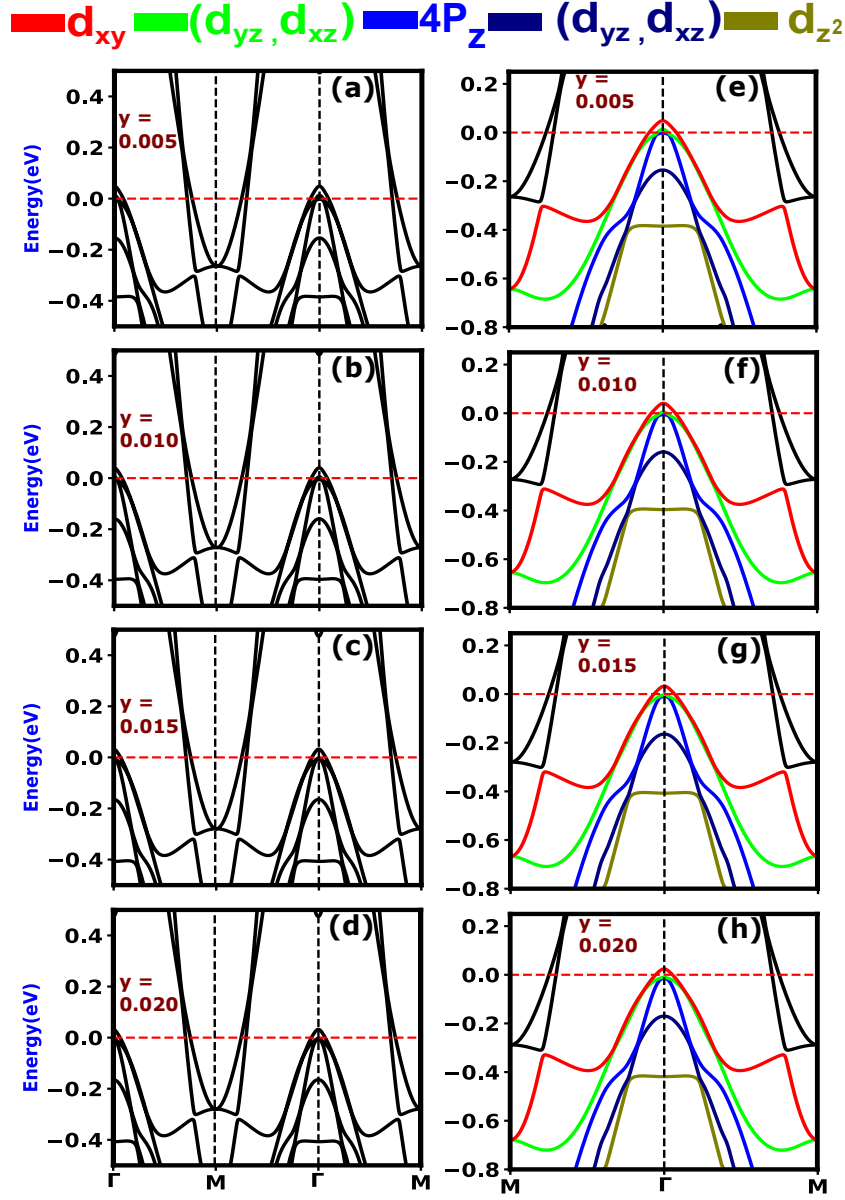


Figure 3.5: [137] Band structures of $\text{Ca}_{0.82}\text{La}_{0.18}\text{Fe}_{1-y}\text{Ni}_y\text{As}_2$ for doping levels (a) $y = 0.005$, (b) $y = 0.010$, (c) $y = 0.015$, and (d) $y = 0.020$. The corresponding bands around Γ point with the respective dopings along with orbital nature is shown in (e), (f), (g), (h). Fermi level is denoted by horizontal red line at zero energy.

We have studied the effect of Ni doping at Fe site of $\text{Ca}_{0.82}\text{La}_{0.18}\text{Fe}_{1-y}\text{Ni}_y\text{As}_2$ and $\text{Ca}_{0.76}\text{La}_{0.24}\text{Fe}_{1-y}\text{Ni}_y\text{As}_2$ on their electronic structures. La doping concentration 0.18 at Ca site is much below the concentration where superconductivity vanishes (*i.e.*, 0.25) in contrast to La doping concentration at Ca site 0.24 which is just about the concentration where superconductivity is at the verge of being vanished. In Fig. 3.4, we have presented the Fermi surfaces of Ni doped CaFeAs_2 *i.e.*, $\text{Ca}_{0.82}\text{La}_{0.18}\text{Fe}_{1-y}\text{Ni}_y\text{As}_2$ where y represent Ni content. From Fig. 3.4(a), it is clearly visible that there are three hole like FSs around the Brillouin zone centre and two electron like FSs around the Brillouin zone corners at Ni doping 0.005. The band structure at this doping (Fig. 3.5 (a)) reveals a singular band structure with two bands just touching the E_F . As we increase Ni doping slightly *i.e.*, $y = 0.010$ (Fig. 3.4(b)), the inner hole like Fermi surface at Γ point vanishes and a lower lying band that was just touching the E_F , is pushed below it (Fig. 3.5(b)). This is a clear occurrence of Lifshitz transition. The other two hole like FSs become more 3D like in nature. If we increase Ni doping further to 0.015, the hole like FSs shrink and the inner FS around the Γ point segregates into two parts causing Lifshitz transition once again (Fig. 3.4(c)). Another hole like band around the Γ point just crosses the FL (Fig. 3.5(c)). If doping is increased further, the outer most hole FS become more 3D like but there is not much modifications in the electron like FSs (Fig. 3.4(d)) around M point. So, the electronic band structure of $\text{Ca}_{0.82}\text{La}_{0.18}\text{Fe}_{1-y}\text{Ni}_y\text{As}_2$ depicts the occurrence of Lifshitz transition induced by Ni doping. We believe our results may be verified experimentally through ARPES studies in future.

At Ni doping 0.005, the hole like bands (d_{yz}, d_{xz}) and $4p_z$ seem to just touch the E_F , causing singular BNS. This may be the cause behind occurrence of the highest T_c about this doping in the phase diagram. As Ni doping is increased further the hole like $4p_z$ band is pushed below the E_F (Fig. 3.5(f)) *i.e.*, Lifshitz transition occurs. Eventually when $y = 0.015$, the hole like (d_{yz}, d_{xz}) band moves just below E_F and second Lifshitz transition occurs. If we further increase Ni doping, at $y = 0.020$ hole like (d_{yz}, d_{xz}) band is pushed below E_F further. Thus, it is evident that Ni doping induces Lifshitz transition in 18% La

co-doped CaFeAs_2 . When the doping concentration of Ni is 0.010, hole like bands around Γ point start moving below the Fermi level and this causes critical density available for interband electron pairing to reduce drastically. This may be the reason for the appearance of a very narrow experimentally observed phase diagram of $\text{Ca}_{1-x}\text{La}_x\text{Fe}_{1-y}\text{Ni}_y\text{As}_2$ in which superconductivity exists only within a very small concentration region of Ni doping [40]. At doping 0.015 the inner hole FSs become absent and the outer hole FS shrinks to an observable amount, causing only limited interband scattering, degraded nesting condition and appearance of extra electron like FSs around the X-point whereas the electron FSs surge but remain nearly 2D; points to the fact that for Ni doped superconductivity electron pockets have dominant role. This scenario is similar for Co-doping and as per with other Fe-based superconductors like $\text{K}_x\text{Fe}_{2-y}\text{As}_2$, single layer FeSe, the LiFeOHFeSe systems [85, 13, 78]. There is a distinct difference in 112 superconductors however, appearance of the electron like FS around X points of the BZ that consists of Fe-3d-As-p bands. So, our first principles DFT based results that qualifies experimental observation and predicts a connection between Lifshitz transition and superconductivity of 112 iron based superconductors calls for further ARPES as well as Hall measurements — appearance of electron FS at Lifshitz transition may show up unusual behaviour in Hall measurements.

In Fig. 3.6 we have presented the Fermi surfaces of Co doped CaFeAs_2 *i.e.*, $\text{Ca}_{0.90}\text{La}_{0.10}\text{Fe}_{1-y}\text{Co}_y\text{As}_2$ where y represents the percentage of Co doping. We have shown three different views of the Fermi surfaces in each row of Fig. 3.6 at a particular doping. We have performed calculations for four different Co doping levels *i.e.*, 0.03, 0.05, 0.10, 0.20 respectively with La co-doping level at Ca site 0.10. It is visible from Fig. 3.6(a) that there appears three hole like Fermi surfaces at the Brillouin zone centre and two electron like Fermi surfaces at the Brillouin zone corners, at Co doping level $y = 0.03$, it is more like the Fermi surface at La doping level 0.10 (Fig. 3.1(b)). But as we increase the level of Co doping further, the hole like Fermi surfaces start shrinking *i.e.*, the hole FSs become more 3D like. At Co doping level $y = 0.10$ the inner most FS around the BZ centre disappears and the outer two hole FSs around the Γ point also shrinks by an observable amount (Fig.

3.6(c)). At doping level $y = 0.10$, apart from the two electron like FSs at the BZ corners *i.e.*, at M points, two extra electron like FSs start appearing around the X-point. At $y = 0.20$ doping, the inner two hole like FSs disappear and the outer hole like FS shrinks at the Γ point further (Fig. 3.6(d)). The electron like FS at X point becomes more prominent. This is in contrast to Ni doping (Fig. 3.4). It appeared from Fig. 3.4 that the sizes of the FS at X point does not change with Ni-doping (y -value). However, with Co-doping this is not the case. From the band structures of the Co doped 112 material (Fig. 3.7), we can clearly see that there are three hole like bands at the Γ point and two electron like bands at around M point when the percentage of Co doping is relatively low, see Fig. 3.7(a), Fig. 3.7(b). But as we increase Co doping further, at $y = 0.10$, one of the hole like bands is pushed below the Fermi level (Fig. 3.7(c)) and at $y = 0.20$ another hole like band also moves below the Fermi level (Fig. 3.7(d)). Thus, only one hole like band remains just touching the Fermi level. Evidently these are the causes of Lifshitz transition.

From Fig. 3.7(e), it is clear that all the three hole like bands around Γ point *i.e.*, d_{xy} , (d_{yz} , d_{xz}), As $4p_z$ are above the Fermi level E_F at $y = 0.03$. If we further increase Co doping level, the $4p_z$ band starts shifting towards the Fermi level (Fig. 3.7(f)). At higher doping $y = 0.10$, $4p_z$ band is pushed below the E_F (Fig. 3.7(g)) *i.e.*, Lifshitz transition takes place. When the Co doping level is 0.20, the (d_{yz} , d_{xz}) band also moves below the Fermi level and the d_{xy} band just touches E_F (Fig. 3.7(h)) which is also a Lifshitz transition.

To investigate the effect of Mn doping, we have depicted the FSs (Fig. 3.8) and BNSs (Fig. 3.9) of $\text{Ca}_{0.90}\text{La}_{0.10}\text{Fe}_{1-y}\text{Mn}_y\text{As}_2$ with different Mn doping level at the Fe site. Here we have also shown three different views of FSs in a row at a particular Mn doping. At doping level $y = 0.03$ there are four hole like Fermi surfaces (this is in contrast to other TM doped FSs) at the Brillouin zone centre. Thus, there appears an extra hole like FS in Mn doping case in contrast to the La doped $\text{Ca}_{1-x}\text{La}_x\text{FeAs}_2$ with doping level $x = 0.10$ (Fig. 3.8(a)). There appears two electron like FSs at M point also. We can also visualize that with increasing Mn doping at Fe site, the FSs tend to become more 2D like

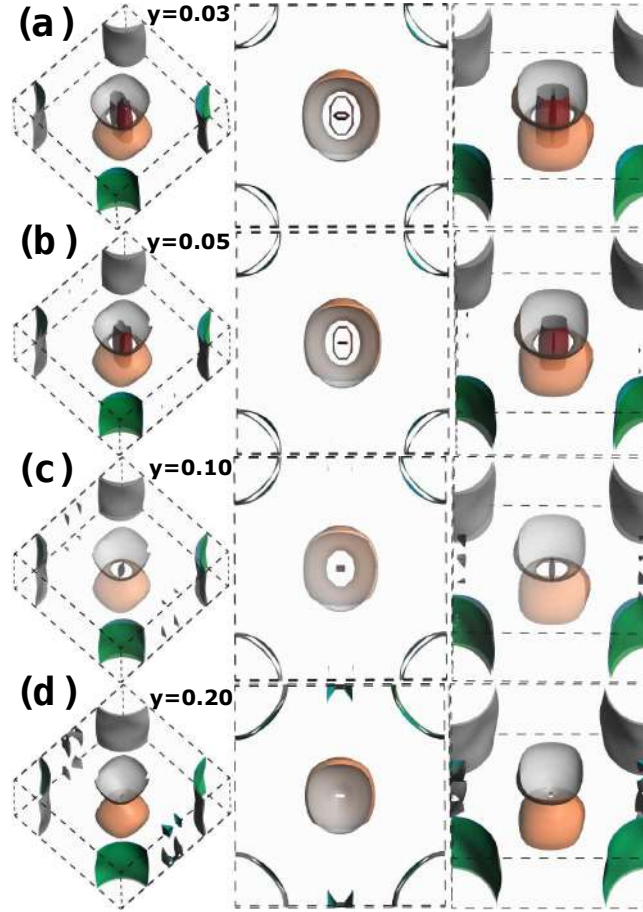


Figure 3.6: [137] Calculated Fermi surfaces of $\text{Ca}_{1-x}\text{La}_x\text{Fe}_{1-y}\text{Co}_y\text{As}_2$ system within VCA method. We have shown three different views of FSs in the same row for same doping. Doping levels are (a) $x = 0.10$, $y = 0.03$; (b) $x = 0.10$, $y = 0.05$; (c) $x = 0.10$, $y = 0.10$; and (d) $x = 0.10$, $y = 0.20$. We have shown three different views of FSs in the same row for a particular value of doping. In middle and last column, FSs in 45° clockwise rotated BZ are shown. Upper view of the FSs is presented in the middle column.

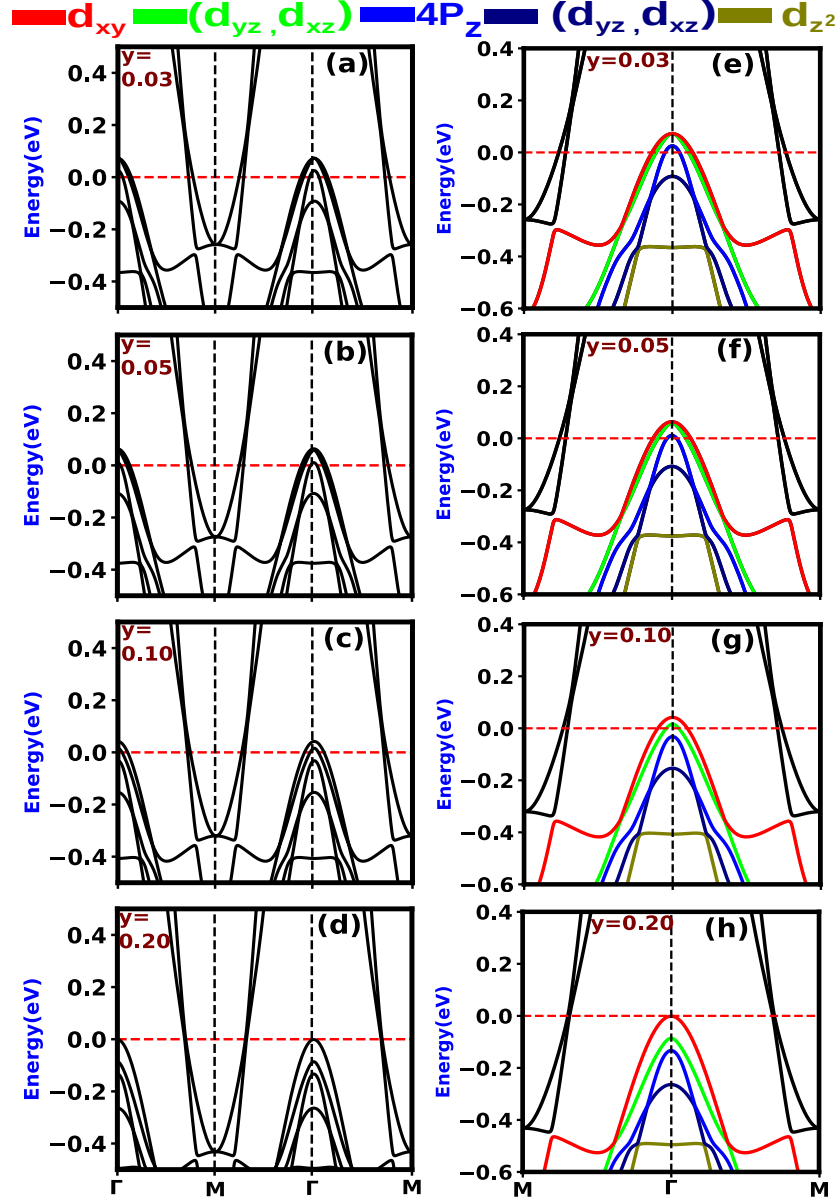


Figure 3.7: [137] Band structures of $\text{Ca}_{1-x}\text{La}_x\text{Fe}_{1-y}\text{Co}_y\text{As}_2$ for doping levels (a) $x = 0.10$, $y = 0.03$; (b) $x = 0.10$, $y = 0.05$; (c) $x = 0.10$, $y = 0.10$; and (d) $x = 0.10$, $y = 0.20$. The corresponding bands around Γ point with the respective dopings along with orbital nature is shown in (e), (f), (g), (h). Fermi level is denoted by horizontal red line at zero energy.

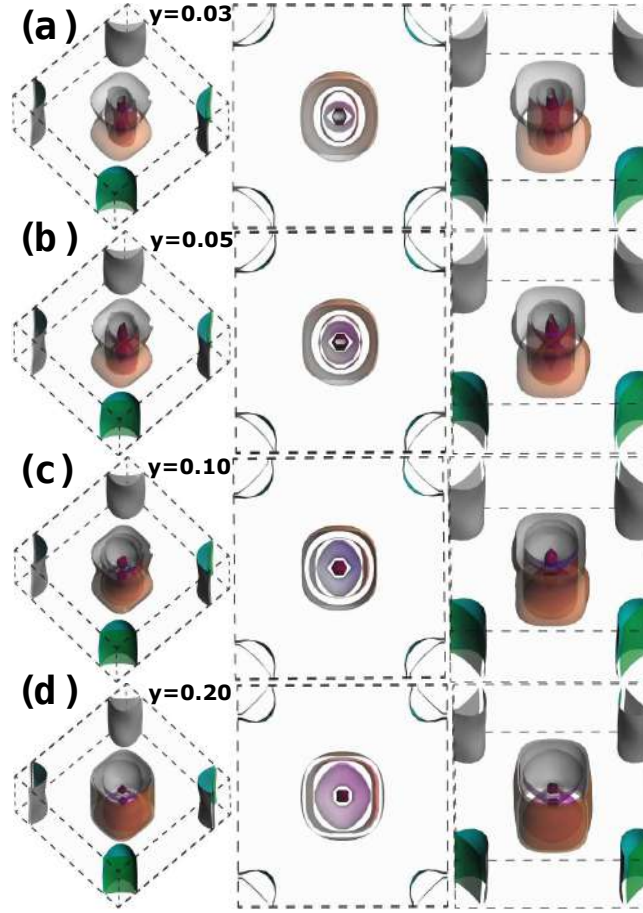


Figure 3.8: [137] Calculated Fermi surfaces of $\text{Ca}_{1-x}\text{La}_x\text{Fe}_{1-y}\text{Mn}_y\text{As}_2$ system within VCA method. We have shown three different views of FSs in the same row for same doping. Doping levels are (a) $x = 0.10$, $y = 0.03$; (b) $x = 0.10$, $y = 0.05$; (c) $x = 0.10$, $y = 0.10$; and (d) $x = 0.10$, $y = 0.20$. We have shown three different views of FSs in the same row for a particular value of doping. In middle and last column, FSs in 45° clockwise rotated BZ are shown. Upper view of the FSs is presented in the middle column.

as the dispersion along z direction decreases. The BNSs of Mn doped CaFeAs_2 show that there are four hole like bands at the Γ point and two electron like bands around M point (Fig. 3.9). With increasing doping level of Mn, the overlap between the hole like bands decreases and they move above the Fermi level. The hole like bands at the Γ point move above the E_F . So, Mn doping acts as hole doping in La doped 112 superconductors. There is no signature of Lifshitz transition in case of Mn doping at the Fe site.

To establish a direct correlation between superconductivity and Lifshitz transition (LT) we have plotted T_c with normalized doping for 112 compounds and compared them with the existing experimental phase diagram in Fig.3.10. Normalized doping is defined as

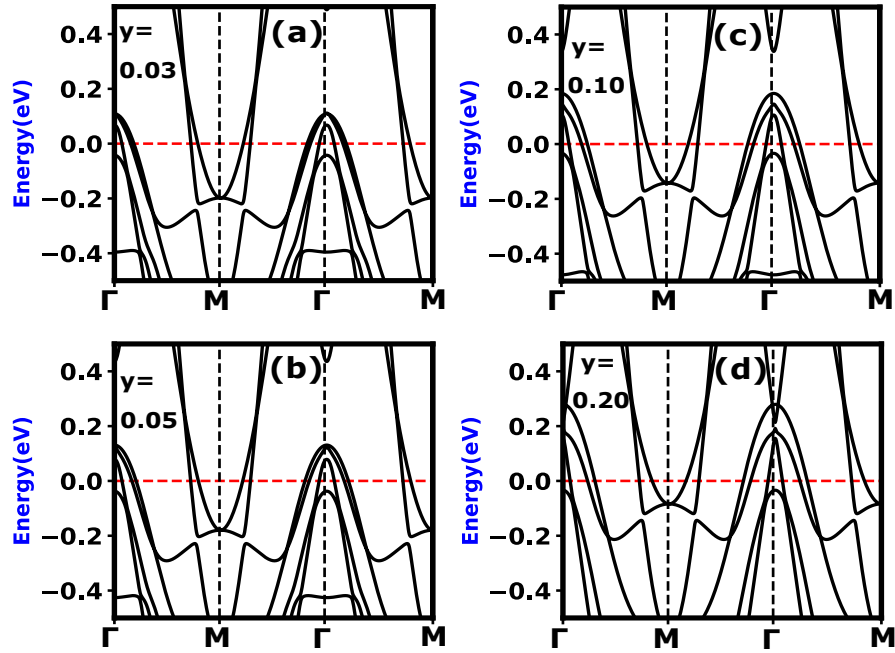


Figure 3.9: [137] Band structures of $\text{Ca}_{1-x}\text{La}_x\text{Fe}_{1-y}\text{Mn}_y\text{As}_2$ for doping levels (a) $x = 0.10$, $y = 0.03$; (b) $x = 0.10$, $y = 0.05$; (c) $x = 0.10$, $y = 0.10$; and (d) $x = 0.10$, $y = 0.20$. Fermi level is denoted by horizontal red line at zero energy.

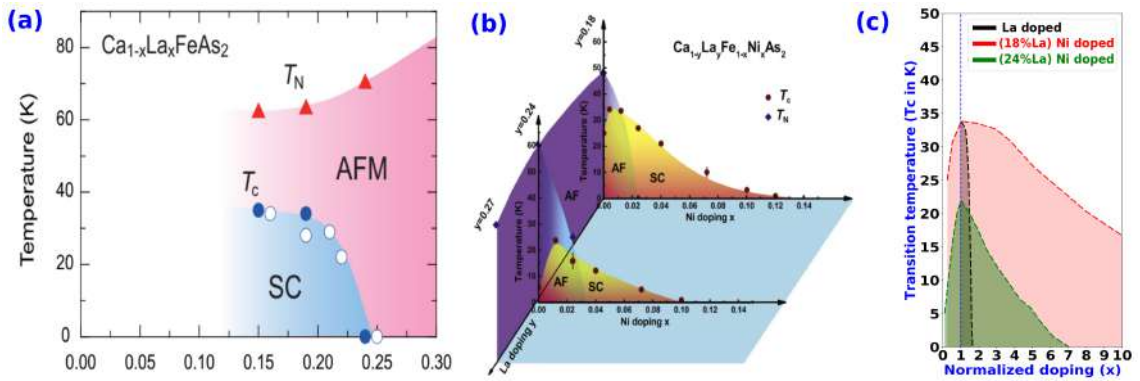


Figure 3.10: Phase diagram of 112 compounds with (a)[31] La-doping, (b)[40] Ni doping with La co-doping (c) doping normalized to Lifshitz transition.

(doping value/doping at which calculated first LT occurs). From Fig.3.10(c), it is evident that the phase diagrams of 112 compounds for La doping, Ni doping with 18% and 24% La co-doping, give rise to domes peaked at the normalized doping value 1. Therefore, the highest T_c is obtained at a fixed normalized doping value for all the three condition of doping. If we compare Fig.3.10(a,b) with (c), it is conspicuous that the nature of domes in the normalized phase diagram is very similar to the experimental phase diagrams with the highest T_c peaked at a particular doping value normalized to LT. This indicates a clear inter connection between superconductivity and LT in 112 Fe based superconductors.

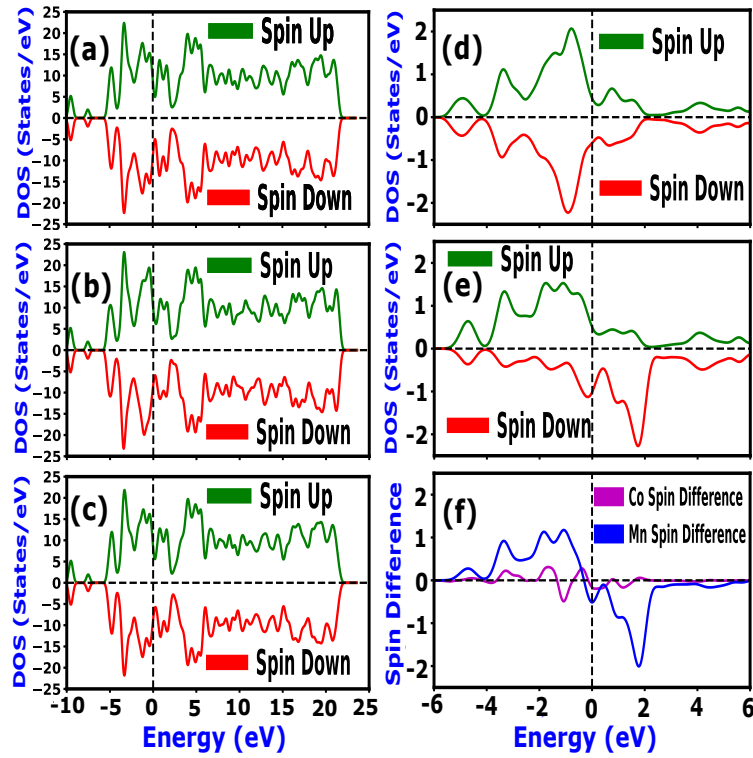


Figure 3.11: [137] (a) Total DOS of La doped ($x = 0.125$) 112, (b) total DOS of Co doped at Fe site 112 with doping level $x = 0.125$, $y = 0.125$; (c) total DOS of Mn doped at Fe site 112 with doping level $x = 0.125$, $y = 0.125$; (d) spin dependent partial DOS of Co in Co doped 112 with doping level $x = 0.125$, $y = 0.125$; (e) spin dependent partial DOS of Mn in Mn doped 112 with doping level $x = 0.125$, $y = 0.125$; and (f) difference in up and down spin density of states of Co and Mn in Co and Mn doped 112 respectively.

As La doped 112 superconductors show striped antiferromagnetism in its ground state, the interplay between magnetism and superconductivity can have an important effect on the superconducting properties of these superconductors [152]. Co and Mn doping at iron

site can affect the magnetic behaviour of the 112 superconductors. We have performed spin polarized calculation using supercell approach for different Co and Mn doping levels to check the effect of these doping on the striped anti-ferromagnetic ground state. Our spin polarized calculations of density of states show that the full DOS of undoped, Co and Mn doped case is symmetric (Fig. 3.11(a), (b), (c)) with respect to up or down spins. Further, we have shown that the partial spin DOS of Co (Fig. 3.11(d)) and Mn (Fig. 3.11(e)) with Co, Mn doping level $y = 0.125$. In both the cases, there is some amount of induced asymmetry in the partial spin DOS. Our calculation shows that the difference of the up and down spin density of states in Mn partial DOS is more than that for the Co spin density difference (Fig. 3.11(f)). In case of Ni doping spin density difference as well as magnetic moments reduce down to zero and not presented here. Calculated magnetic moments of Co, Mn and Fe has been depicted in TABLE I for transition metal (TM = Co, Mn) doping at Fe site of $\text{Ca}_{0.875}\text{La}_{0.125}\text{Fe}_{0.875}\text{TM}_{0.125}\text{As}_2$. From TABLE I, it may be observed that the magnetic moment of Fe (μ_{Fe}) is $1.91 \mu\text{B}$ in the undoped case which is greater than the magnetic moment of Fe in Co and Mn doped case. With Co doping magnetic moment of iron is reduced down to $0.8742 \mu\text{B}$ and induced magnetic moment in Co (μ_{Co}) is also very less $0.12 \mu\text{B}$. So, the reduced magnetic moment of iron may be the cause behind favourable condition of superconductivity in the Co, Ni doped cases. But in case of Mn doping, the magnetic moment of Fe is reduced only to $1.725 \mu\text{B}$. Thus the decrement of magnetic moment of iron is much less in Mn doped compound compared to the Co or Ni doped compounds. Also the local magnetic moment of Mn (μ_{Mn}) is $2.64 \mu\text{B}$ which is large and localized (*i.e.*, Fe and Mn states do not mix considerably) in contrast to that for Co-d and Fe-d. Our results are consistent with earlier experimental studies on Mn doped BaFe_2As_2 superconductors [149, 150]. The suppression of superconductivity in Fe based superconductors due to magnetic impurities like Mn has also been discussed theoretically with five band multi orbital Hubbard model [151]. In presence of Coulomb correlations both local and non local (inducing spin polarizations of the surrounding itinerant electrons) magnetic interactions generated by the magnetic impurity like Mn lead to

a fast suppression of superconductivity.

Table 3.1: Magnetic Moment (in μ_B)
on TM site of $\text{Ca}_{0.875}\text{La}_{0.125}\text{Fe}_{0.875}\text{TM}_{0.125}\text{As}_2$

Magnetic moment(μ)	Undoped	Co-doping	Mn-doping
$\mu_{\text{Fe}} \Rightarrow$	1.91	0.8742	1.725
$\mu_{\text{Co}} \Rightarrow$	-	0.12	-
$\mu_{\text{Mn}} \Rightarrow$	-	-	2.64

For theoretical investigation of doping effects, very common approximations in first principles calculations are supercell, rigid band model and the virtual crystal approximation (VCA). It is very difficult to simulate a crystal for a large range of doping (very low to high) with supercell approach because handling huge supercells are computationally very costly. In a rigid band approximation, there happens to be a simple shift of the Fermi energy that leaves the band curvatures unchanged. In VCA, on the other hand, the integer electron number of a given atom is changed to a non-integer one in order to represent doping or impurity effects in the crystal [153]. This works reasonably well as long as the core electrons of the original atom match with the core electrons of the substituting atom. As VCA also takes into account changes in the band structure apart from a simple shift of the filling, this method is clearly preferable over rigid band model. Also VCA results for Fe based superconducting compounds has been consistent with supercells in many cases [131]. In our previous work [132], we have shown that for BaFe_2As_2 at low doping VCA and SC calculated FSs differ only by a rigid band shift due to difference in effective chemical potential. Following earlier works [131, 132] and the fact that the 112 materials that we are dealing with have simultaneous more than one doping elements, size of the supercell is too large to make a systematic computational study to compare between VCA and supercell approaches in this work.

3.3 Discussions and Conclusions

A detailed density functional theory based first principles electronic structure calculations on $\text{Ca}_{1-x}\text{La}_x\text{Fe}_{1-y}\text{TM}_y(\text{As}_{1-p}\text{Sb}_p)_2$ for various values of x , y , p and transition metals (TM = Co, Ni, Mn) reveals many interesting feature of the electronic structure of 112 compound. Doping of La at Ca site of CaFeAs_2 has a great impact on its electronic structure. This systematic doping dependent evaluation of electronic structure for this family of materials is so far not available in literature. A common important feature of the electronic structure calculation is, merger of tops of a number of hole like bands near Fermi level which we call as singular band structure, with various doping where maximum T_c is observed. For example, Fig. 3.2 shows singular band structure accompanied by LT (appearance of new FS (Fig. 3.1 (b)) as well as topological modifications of inner hole FS (Fig. 3.1(c)) caused by movement of hole bands below E_F (Fig.3.2 (c))) at in between La doping of 0.15 to 0.20, around very close vicinity of the Fermi level. In contrast, experimentally the highest T_c achievable with La doping in this family of superconductors is 0.16 as may be found from the phase diagram [31]. Phase diagram of Ni doped 112 system with 18% La co-doping at Ca site shows the highest T_c between Ni doping level 0.005 and 0.010 [40]. Fig. 3.5 demonstrates singularity in band structure near E_F at around Ni doping 0.005 and 0.010 [155]. This coincidence also occurs for compounds with Co doping at Fe site having La co-doping at Ca site, for example, Fig. 3.7 shows that the band density is maximum in between Co doping 0.03 and 0.05. These features from the present work indicates that the highest T_c in 112 family of superconductors appear at the verge of Lifshitz transition. Due to Lifshitz like topological transitions in these compounds, the interband pairing is diminished and superconductivity also start getting affected. One of the unique features of 112 materials is the existence of electron like Fermi surface around X-points of the Brillouin zone.

Chapter 4

Effect of rare earth (*f*-atom) doping on 112 materials; orbital selectivity, bandwidth renormalization and Lifshitz transition

A density functional theory based first principles electronic structure study on $\text{Ca}_{1-x}\text{RE}_x\text{FeAs}_2$ for various values of x and different rare earth elements ($\text{RE} = \text{Ce}, \text{Pr}, \text{Nd}, \text{Sm}, \text{Gd}$) is presented in this chapter. It is disclosed through our electronic structure study that rare earth doping act as heavy electron doping in this compound. Due to heavy electron doping caused by rare earth doping hole bands drift below the Fermi level and the associated Fermi surfaces shrink leading to Lifshitz transition for each RE doping. But initialization of the Lifshitz transition depend highly on the optimal doping of the particular rare earth element. The general trend is as one moves from Ce to Gd in the periodic table optimal doping at which the transition occurs gradually decreases. We emphasize on the fact that rare earth doping causes significant modifications to the bandwidths of Fe derived bands that are known to be responsible for superconductivity. To emphasize the effect of

rare earth doping on electronic structure, we have calculated the bandwidth of the three holelike bands around the Γ -point that are known to be responsible for superconductivity. Our study on bandwidth disclose that evolution of bandwidth with rare earth doping is orbital selective. The variation in bandwidth derived from d_{xy} is quiet different from its variation in $d_{xz/yz}$. The variation of band renormalization ratio (which is defined as the ratio of bandwidth of d_{xy} with $d_{xz/yz}$) with increasing rare earth doping reveals a unique connection between orbital selectivity and Lifshitz transition in 112 iron pnictides.

4.1 Theory and Computational Method

Density Functional theory (DFT) based first principles calculations are performed using plane wave pseudo potential method implemented in Cambridge Serial Total Energy Package (CASTEP) [128] that is one of the software modules in Materials studio. The electronic exchange correlation is considered by generalized gradient approximation (GGA) with Perdew-Burke-Enzerhof (PBE) functional [125]. Geometry optimization is carried out using Broyden-Fletcher-Goldfrab-Shanno (BFGS) routine before calculating the electronic structure of the doped systems. In order to simulate the doped system theoretically, we have used Virtual Crystal Approximation (VCA) for different rare earth doping. The validity of VCA at each doping is checked under standard method described in Material Studio, CASTEP user guide [130]. Previous studies on IBSCs using both supercell and VCA suggest that there is no appreciable modifications in electronic structure in both the cases as far as low doping regime is concerned [131, 132]. For minimizing the number of plane wave basis, ultrasoft pseudopotential is used to describe the interactions between the ion core and the valence electrons in the Vanderbilt form. The f -orbitals are treated as core in the rare earth pseudopotentials used for the calculations. Non-spin-polarized as well as spin polarized single point energy calculations were carried out for monoclinic phase with space group symmetry $P2_1$ except for Pr doped case where we have taken monoclinic phase with space group symmetry $P2_1/m$. The cut-off energy for

plane wave expansion is set to 600 eV after convergence test. For the calculation of electronic properties Brillouin zone (BZ) is sampled in the k space within Monkhorst-Pack scheme [133, 134] with $26 \times 26 \times 10$ k-point mesh. All the atoms were fully relaxed until the energy change per atom is less than 5×10^{-7} eV and the Hellmann–Feynman force applied on each atom is less than 0.01 eV/Å. For calculating formation enthalpy with different rare earth doping, we have performed single point energy calculations with $2 \times 2 \times 1$ supercell with plane wave energy cut-off 400 eV. We resolved the orbital character of the bands performing simulations using QUANTUM ESPRESSO package [135] with ultrasoft pseudo-potential and PBE exchange correlation potential. The plane wave energy cut off and the grid size for SCF calculation was set to 30 Rydberg and $16 \times 16 \times 6$ respectively after performing convergence test.

4.2 Relative stability of rare earth doped 112 materials and Formation enthalpy

To check the relative stability of CaFeAs_2 with RE doping, we have calculated the energy of formation (ΔE) for different rare earth doping at Ca site. Formation enthalpy can be defined for these systems as difference in total energy of the sum of products minus the sum of the reactants -

$$\Delta E = E_{RE-doped} - E_{Pure} - \mu_{RE} + \mu_{Ca}$$

where E_{Pure} , $E_{RE-doped}$ are the total energies of the $2 \times 2 \times 1$ supercell (SC) of CaFeAs_2 and RE doped SC respectively and respectively μ_{RE} , μ_{Ca} are energies per atom of RE elements and Ca which are calculated from their respective bulk.

Table 4.1 lists the calculated values of formation enthalpy in which it is clear that as we move to the right of lanthanide series, ΔE changes from -1.012 eV for La doping to -2.208 eV for Gd. ΔE for Pr, Nd, Sm are -1.469 eV, -2.313 eV and -2.333 eV respectively. Thus

Table 4.1: Formation energy of $\text{Ca}_{0.875}\text{RE}_{0.125}\text{FeAs}_2$

RE element	Formation Enthalpy(in eV)
La	-1.012
Pr	-1.469
Nd	-2.313
Sm	-2.333
Gd	-2.208

there is a general trend of increasing thermodynamic stability with decreasing lanthanide radius. Thus the RE doped 112 compounds with different RE doping are predicted to be thermodynamically stable in agreement with experimental facts [28, 29].

4.3 Electronic structure of rare earth doped 112 materials

4.3.1 Ce doping at Ca site

Although superconductivity was not observed experimentally with only Ce doping at Ca site, we have presented the doping dependent electronic structure of $\text{Ca}_{1-x}\text{Ce}_x\text{FeAs}_2$ within VCA. We have calculated band structures (BNS), density of states (DOS) and Fermi surfaces (FS) at different Ce doping concentrations systematically. We have performed our first principles calculations after optimizing geometry taking experimental lattice parameters with monoclinic structure as initial input. In Fig. 4.1 we have shown the doping dependent FSs and BNSs of $\text{Ca}_{1-x}\text{Ce}_x\text{FeAs}_2$. It is conspicuous from Fig. 4.1 (a) that there are three hole like FSs around the Γ point at the brillouin zone centre and two electron like FSs around the M point at brillouin zone corner which is quite similar to the 10% La doped CaFeAs_2 . It is also evident from Fig. 4.1 that with increasing Ce doping, the hole like FSs at brillouin zone centre shrinks and gradually undergoes a 2D to 3D like crossover leading to Lifshitz like topological transition.

As Ce doping at Ca site is increased, a discernible change in the hole like FSs occurs – they become more 3D like. To illustrate the occurrence of Lifshitz transition, we have presented electronic structures with Ce doping level 0.01, 0.03, 0.05, 0.10, 0.15. At $x = 0.01$, there are three hole like bands at around the Γ -point and two electron like bands at around the M-point (Fig. 4.1(f)). From Fig. 4.1(g), (h) it is eloquent that further increase in Ce doping level pushes the hole like bands towards the Fermi level (E_F). Subsequently, from Fig. 4.1(b), (c), it is clearly visible that there occurs 2D to 3D crossover of the hole like FSs at the brillouin zone centre. But remarkable changes in FS occur only when the doping level is slightly higher *i.e.*, 0.10, 0.15. At $x = 0.10$ (Fig. 4.1(d)) the innermost hole like FS vanishes which is a consequence of Lifshitz transition. Also, significant quenching of the outer hole like FSs take place. Another notable change in the Fermi surface topology at this doping is the appearance of a new electron like FS at X-point as a consequence of Lifshitz transition. BNS at $x = 0.10$ (Fig. 4.1(i)) also shows that one hole like band is pushed just below the E_F and the other two hole like bands just touch it leading to “band edge van Hove singularity” (or singular band structure) at this particular doping. If we increase Ce doping further to $x = 0.15$, all the hole like bands are propelled below the E_F (Fig. 4.1(j)). Consequently, hole like FS at Γ -point vanishes which is due to occurrence of Lifshitz transition (Fig. 4.1(e)). The electron like FS at X-point also grows in size.

To have an insight into the orbital character of bands, we performed calculations using Quantum Espresso code. In Fig. 4.2 we have shown the relative contribution of different orbitals in different bands around the high symmetry points. Like other iron pnictides and chalcogenides compounds, CaFeAs_2 also shows mixed multi-orbital character in it's electronic structure. From Fig. 4.2 one can clearly visualize that the uppermost band near the E_F along M- Γ -M has $d_{x^2-y^2}$ as dominant orbital character. The band just next to $d_{x^2-y^2}$ has mixed (d_{xz}, d_{yz}) character. The band nearest to the E_F has dominant contribution from As-4 p_z orbital which is unique character of 112 iron pnictides. There is another band of mixed (d_{xz}, d_{yz}) and 4 p_z character around the Γ -point of the undoped compound that is

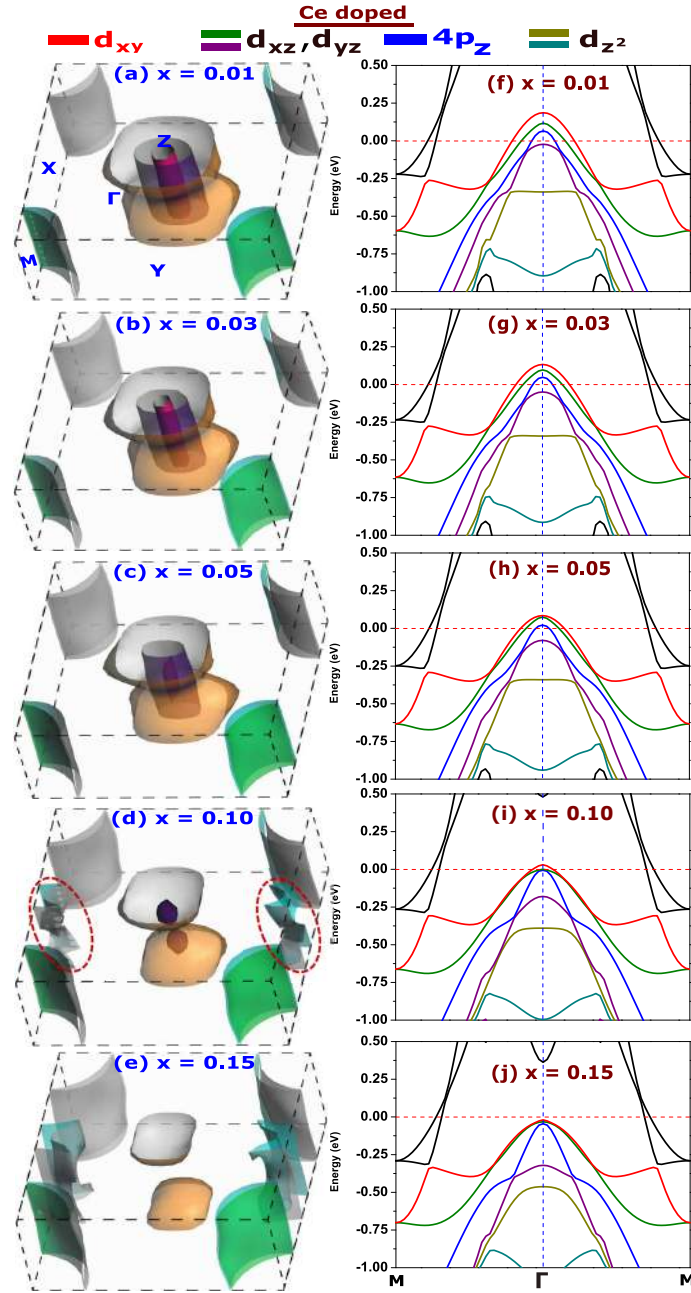


Figure 4.1: [138] Calculated Fermi surfaces (FSs) and band structures (BNSs) of $\text{Ca}_{1-x}\text{Ce}_x\text{FeAs}_2$ system within VCA method. We have shown the FS and BNS with same doping in the same row. Doping levels (x) of Ce are (a) $x = 0.01$, (b) $x = 0.03$, (c) $x = 0.05$, (d) $x = 0.10$ and (e) $x = 0.15$ respectively and (f), (g), (h), (i), (j) show BNSs with respective doping.

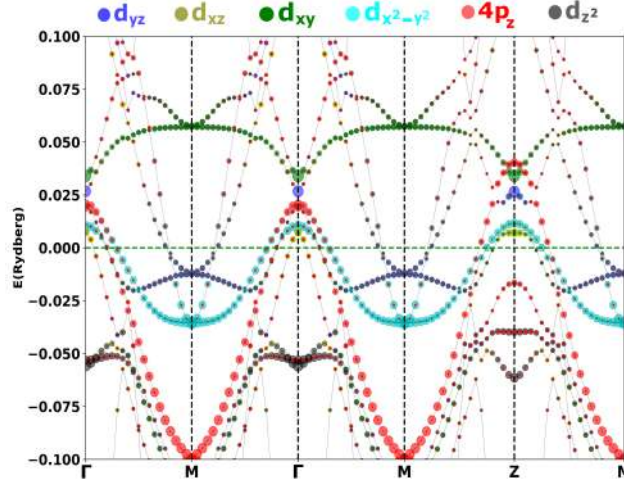


Figure 4.2: [138] Calculated orbital projected band structures of undoped CaFeAs_2 around the high symmetry points. The weight of the different Fe 3d and As 4p orbitals for different bands is shown with varying size of the circles and colours. Sizes of the circles correspond to degree of relative contribution. Fermi level is denoted by horizontal green line at zero energy.

pushed below the E_F with RE doping at Ca site. In our calculation, the x and y directions are defined to be along the next nearest Fe-Fe bonds, and thus the Γ -M direction is parallel to k_x (k_y) directions in the reciprocal space [79]. Thus band with the $d_{x^2-y^2}$ character (in Fig. 4.2) is equivalent to the band with d_{xy} orbital character in the ARPES polarization [136]. Following the notion of ARPES measurements, we have shown the uppermost orbital near E_F around the Γ -point to be d_{xy} for doped cases. Our shown orbital character of bands for doped cases is the character around the Γ -point near the E_F only and with mixed character otherwise.

A critical density of electrons is needed for the appearance of superconductivity in any material. It is known that intra as well as inter band pairing of electrons between electron and hole like bands play an important role behind superconductivity in iron based superconductors [156]. So, destruction of superconductivity may occur at $x = 0.15$ due to disappearance of hole bands at Γ -point. Although it is experimentally reported that superconductivity does not exist in Ce doped 112 [28, 39], our electronic structure calculation reveals that it may be due to large nominal doping of Ce at Ca site. At low doping there may be superconductivity in Ce doped 112 with highest critical temperature around $x =$

0.10 due to singular band structure near the E_F around this doping [157].

4.3.2 Pr doping at Ca site

Unlike Ce doping Pr doping induces superconductivity in 112 IBSC, as already been observed experimentally. It has a critical temperature (T_C) 24K which is less than the critical temperature with La doped 112. Here we present the electronic structure and FS of $\text{Ca}_{1-x}\text{Pr}_x\text{FeAs}_2$ within VCA taking monoclinic phase with P21/m symmetry as initial structure. We have shown our calculated band structures (BNS), density of states (DOS) and Fermi surfaces (FS) at different Pr doping systematically. We have performed our first principles calculations after optimizing geometry taking experimental lattice parameters as initial input. We have depicted the doping dependent FSs and BNSs of $\text{Ca}_{1-x}\text{Ce}_x\text{FeAs}_2$ in Fig. 4.3. Pr doped CaFeAs_2 posses three hole like FSs around the Γ point at the brillouin zone centre and two electron like FSs around the M point at brillouin zone corner at $x = 0.01$ (Fig. 4.3(a)). From Fig. 4.1 it is comprehensible that with increasing Pr doping, the hole like bands at around the Γ -point successively shift below E_F . As a consequence, the hole like FSs at brillouin zone centre shrinks leading to Lifshitz transitions.

We have presented BNSs and FSs with Pr doping level 0.01, 0.03, 0.05, 0.10. At Pr doping level $x = 0.01$, there are three hole like bands at around the Γ -point and two electron like bands at around the M-point (Fig. 4.3(e)) above the E_F . If we increase the doping slightly to $x = 0.03$ the lower most band starts shifting towards E_F . Hole like FS volumes also decrease with RE-doping. At $x = 0.05$, all the FSs shrink further and the outermost FS gets more 3D character (Fig. 4.3(g)). The bands around the Γ -point approach closer to E_F . An extra electron like FS appears at X-point. Such appearance of new FS indicate Lifshitz like topological transition. The most remarkable change in the electronic structure happens at Pr doping level $x = 0.10$. All the three hole like bands are pushed below the E_F (Fig. 4.3(h)). Significant changes in topology of Fermi surface also take place. The only remaining outermost hole like part of the FS is parted in two different

propeller like FSs having Z-dispersion with no dispersion at Γ -point (Fig. 4.3(d)). This is a situation observed earlier in La doped (with Ni co-doped at Fe-site) 112 superconductor [154]. Thus complete Lifshitz transition of the hole like FSs occurs at this doping. The electron like FSs at X-point also grow in size.

At doping 0.10 the hole FSs at Γ -point become absent causing only limited interband scattering, degraded nesting condition and appearance of extra electron like FSs around the X-point, whereas other electron FSs surge but remain nearly 2D. This points to the fact that for Pr doped superconductivity electron pockets have dominant role. In case of Pr doping singular band structure is observed in between Pr doping 0.05 to 0.10. Thus highest T_c would occur at a lower nominal doping in the appropriate phase diagram.

4.3.3 Nd doping at Ca site

The next compound in the lanthanide series showing superconductivity after being doped at Ca site of CaFeAs_2 is Nd. The doping dependent electronic structure of $\text{Ca}_{1-x}\text{Nd}_x\text{FeAs}_2$ has been depicted within VCA formalism. Calculated band structures (BNS), density of states (DOS) and Fermi surfaces (FS) at different Nd doping are presented systematically. Density functional theory based first principles calculations has been performed after optimizing geometry (taking experimental lattice parameters with monoclinic phase and space group symmetry P21 as initial input). In Fig. 4.4 we have shown the doping dependent FSs and BNSs of $\text{Ca}_{1-x}\text{Nd}_x\text{FeAs}_2$. Like La, Ce doped 112 compounds at lower doping, there are three hole like FSs around the Γ -point at the brillouin zone centre and two electron like FSs around the M point at brillouin zone corners (Fig. 4.4(a)). It is also evident from Fig. 4.4 that with increasing Nd doping, the hole like FSs at brillouin zone centre contracts leading to dimensional crossover of the FSs.

As Nd doping at Ca site is increased, the hole like FSs become more 3D like. We have shown electronic structures with Nd doping levels 0.01, 0.03, 0.05, 0.10 respectively. At

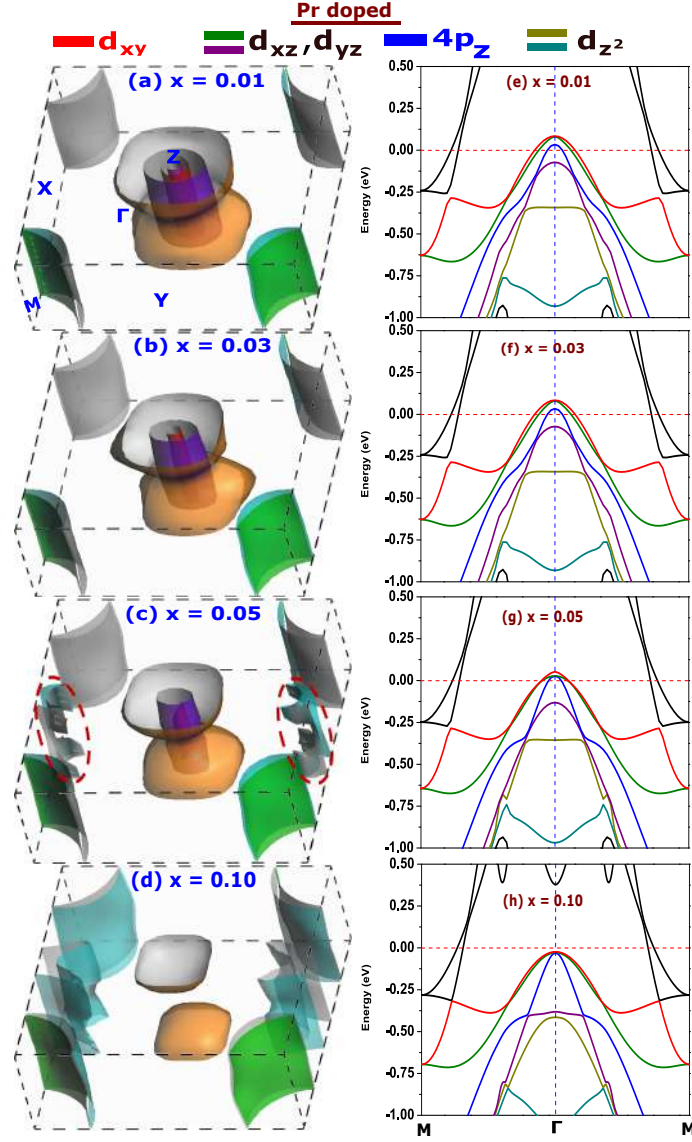


Figure 4.3: [138] Calculated Fermi surfaces (FSs) and band structures (BNSs) of $\text{Ca}_{1-x}\text{Pr}_x\text{FeAs}_2$ system within VCA method. We have shown the FS and BNS with same doping in the same row. Doping levels (x) of Pr are (a) $x = 0.01$, (b) $x = 0.03$, (c) $x = 0.05$, (d) $x = 0.10$ respectively and (e), (f), (g), (h) show BNSs with respective doping.

$x = 0.01$, there are three hole like bands at around the Γ -point and two electron like bands at around the M-point (Fig. 4.4(e)). From Fig. 4.4(f), (g) it is perceptible that further increase in Nd doping level pushes the hole like bands towards the E_F increasing band density at the E_F . The hole like FSs start shrinking and at $x = 0.05$ the inner most FS completely disappears which signifies Lifshitz transition. Another noticeable change in FS due to Lifshitz transition is the appearance of an electron like FS at X-point. At $x = 0.10$ (Fig. 4.4(h)) BNS shows that all the hole like bands are pushed just below the E_F leading to disappearance of the outermost hole like FS at Γ -point (Fig. 4.4(d)) indicating complete Lifshitz transition. The electron like FS at X-point also grows in size.

For Nd doping appearance of extra electron like FSs around the X-point raises further importance of the electron pockets that have contributions also from As atoms for occurrence of superconductivity in this compound. Singularity in electronic band structure happens to be in between doping 0.03 to 0.05.

4.3.4 Sm doping at Ca site

Now we are going to discuss about the effect of Sm doping on the electronic structure of CaFeAs_2 . Sm doped CaFeAs_2 shows superconductivity with critical temperature less than that of the Nd doped 112 compound. We have presented the results of electronic structure of $\text{Ca}_{1-x}\text{Sm}_x\text{FeAs}_2$ within VCA. We have performed our first principles calculations after optimizing geometry taking experimental lattice parameters with monoclinic phase having P21 symmetry as initial input to calculate BNS, DOS and FS. In Fig. 4.5 we have shown the doping dependent FSs and BNSs of $\text{Ca}_{1-x}\text{Sm}_x\text{FeAs}_2$. It is clear from Fig. 4.5(a) that there are three hole like FSs around the Γ -point at the brillouin zone centre and two electron like FSs around the M point at brillouin zone corner. To illustrate the occurrence of Lifshitz like topological transitions we have studied the electronic structure with gradually increased doping.

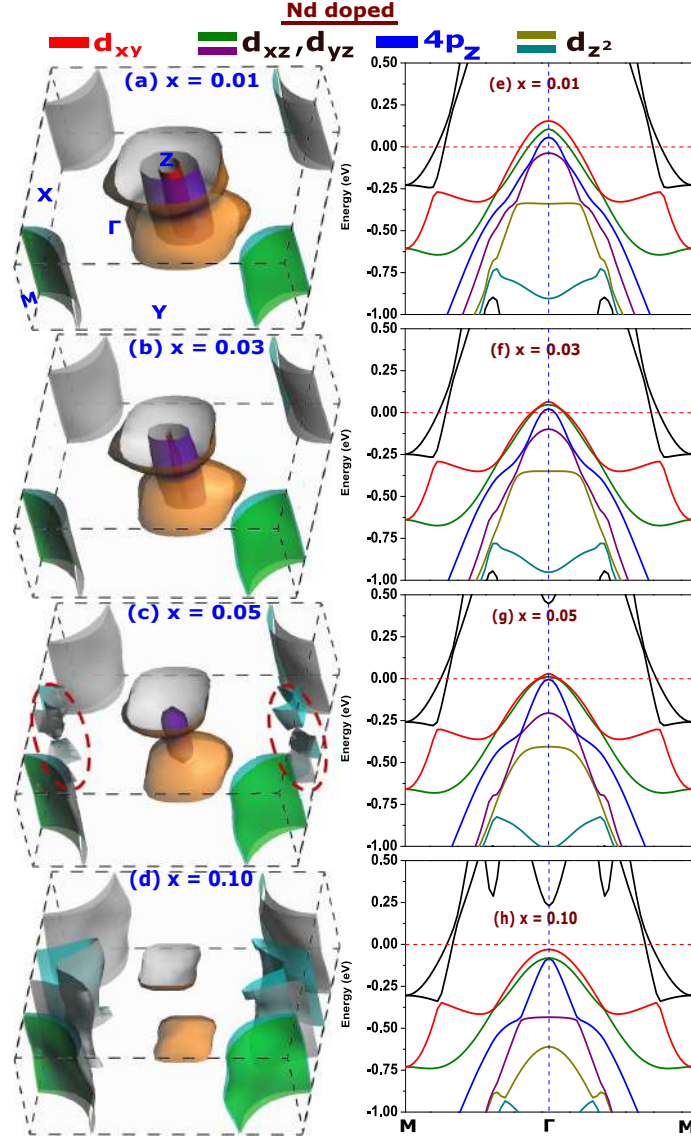


Figure 4.4: [138] Calculated Fermi surfaces (FSs) and band structures (BNSs) of $\text{Ca}_{1-x}\text{Nd}_x\text{FeAs}_2$ system within VCA method. We have shown the FS and BNS with same doping in the same row. Doping levels (x) of Nd are (a) $x = 0.01$, (b) $x = 0.03$, (c) $x = 0.05$, (d) $x = 0.10$ respectively and (e), (f), (g), (h) show BNSs with respective doping.

With increasing Sm doping the electronic structure of $\text{Ca}_{1-x}\text{Sm}_x\text{FeAs}_2$ evolve quite differently than other lanthanide doped 112 compound. At $x = 0.01$ there are three hole like bands at around the Γ -point and two electron like bands at around the M-point. If we increase the doping slightly to 0.03, one hole like band drifts below the E_F causing one hole like FS to vanish and Lifshitz transition occurs (Fig. 4.5(b)). Another significant change in the Fermi surface topology is the appearance of an extra electron like FS at around the X-point due to Lifshitz transition. So Sm doping act as heavy electron doping in CaFeAs_2 . At $x = 0.05$ another hole like band is pushed below the E_F causing the inner FS to vanish which signify Lifshitz transition (Fig. 4.5(c)). But it is quite surprising that with slight increase of Sm doping to 0.07, all the hole like bands around the Γ -point move below the E_F and consequently the hole like FS at Γ -point also vanishes leading to Lifshitz transition. Lifshitz transition leads to further topological modifications of the FSs. There appears new electron like FSs around the X-point as well as Y-point (Fig. 4.5(d)). The appearance of electron like FS around the Y-point is a unique feature of the electronic structure with Sm doping. Appearance of electron like bands both around the X and Y point due to Lifshitz transition signals toward important role of electron like bands in superconductivity. Band singularity in this compound arise at around Sm doping level 0.03.

4.3.5 Gd doping at Ca site

The last element of the lanthanide series to induce superconductivity in 112 iron pnictides is Gd. We have carried out Density Functional Theory based first principles calculations to simulate electronic structure and Fermi surfaces of $\text{Ca}_{1-x}\text{Gd}_x\text{FeAs}_2$ within virtual crystal approximation. We have presented BNSs, FSs of $\text{Ca}_{1-x}\text{Ce}_x\text{FeAs}_2$ to get insight into the phenomenon of superconductivity. It is discernible from Fig. 4.6(a) that $\text{Ca}_{0.99}\text{Gd}_{0.01}\text{FeAs}_2$ has three hole like FSs around the Γ point at the brillouin zone centre and two electron like FSs around the M point at brillouin zone corner, quite similar to

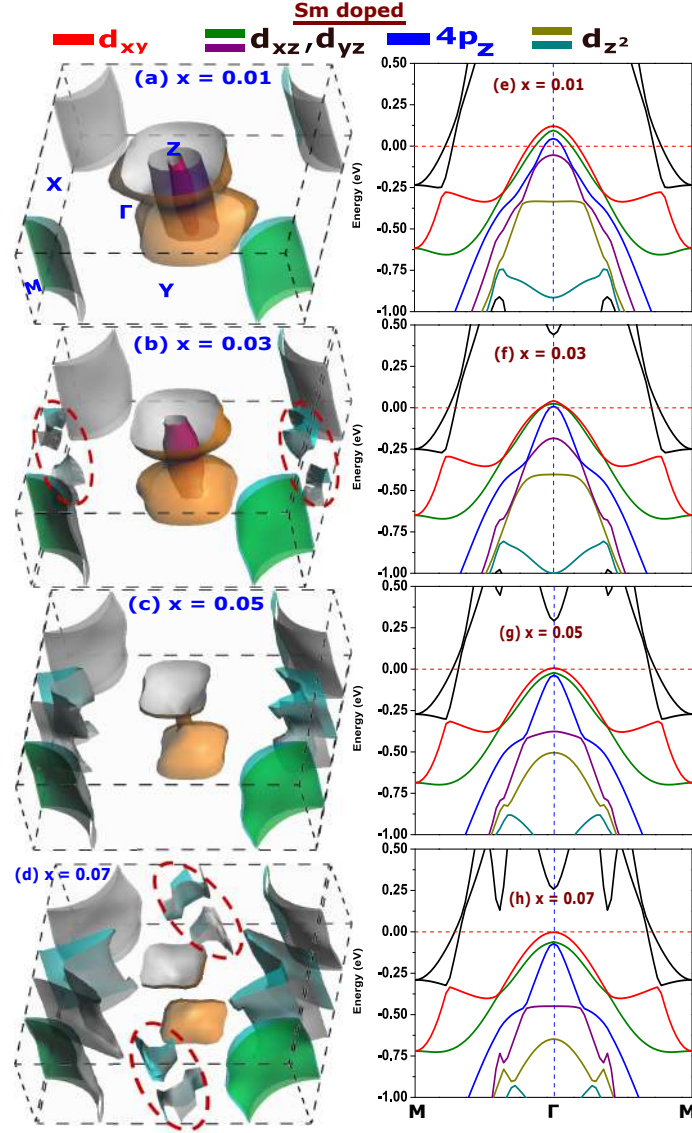


Figure 4.5: [138] Calculated Fermi surfaces (FSs) and band structures (BNSs) of $\text{Ca}_{1-x}\text{Sm}_x\text{FeAs}_2$ system within VCA method. We have shown the FS and BNS with same doping in the same row. Doping levels (x) of Sm are (a) $x = 0.01$, (b) $x = 0.03$, (c) $x = 0.05$, (d) $x = 0.10$ respectively and (e), (f), (g), (h) show BNSs with respective doping.

other lanthanide doped CaFeAs_2 . Still Lifshitz transition is the common phenomenon in all the lanthanide doping cases.

We have presented here electronic structures with Gd doping levels 0.01, 0.03, 0.05 respectively. At $x = 0.01$, there are three hole like bands at around the Γ -point and two electron like bands at around the M-point (Fig. 4.6(e)). If we increase the Gd doping slightly to $x = 0.03$, due to very heavy electron doping, two hole like bands at Γ -point are pushed below the Fermi level (Fig. 4.6(f)). Subsequently, two inner hole like FSs around the Γ -point vanish inducing Lifshitz transition. The outermost FS also becomes more 3D like. Another visible change in FS topology at this doping is the appearance of an extra electron FS at X-point (Fig. 4.6(b)) due to Lifshitz transition. At $x = 0.05$, the remaining band also shifts below the E_F causing complete disappearance of hole like bands at Γ -point as a manifestation of Lifshitz transition (Fig. 4.6(c), (f)). The electron like band at X-point also grows in size. There appears electron like bands for Gd doped compounds indicating the importance of electron like bands in superconductivity of these compounds. Around Gd doping level 0.03, singular BNS arise in this compound.

We have shown the evolution of orbital dependent BNSs for each rare earth doping. In Fig. 4.2 we have shown the relative contribution of different orbitals in different bands around the high symmetry points. Three hole like bands with orbital character – d_{xy} , (d_{yz}, d_{xz}) from Fe-3d and $4p_z$ from As cross the Fermi level at low rare earth doping. The $4p_z$ band is the lowest in energy and closer to the E_F (E_F). The bands with orbital character d_{xy} , (d_{yz}, d_{xz}) are visibly away from the E_F with d_{xy} band having higher energy at Γ -point. But as we start to increase the RE doping, all the three bands start moving towards the E_F and finally cause Lifshitz transitions at certain doping depending upon the RE element. For example, Fig. 4.1 shows that at lower doping *i.e.*, 0.01, 0.03, 0.05 all the three bands are above the E_F with FS having a 2D to 3D crossover. If we increase further doping to 0.10, (d_{yz}, d_{xz}) and $4p_z$ bands slide below the E_F and the two inner FSs at Γ -point vanish due to Lifshitz transition. On increasing doping further to 0.15,

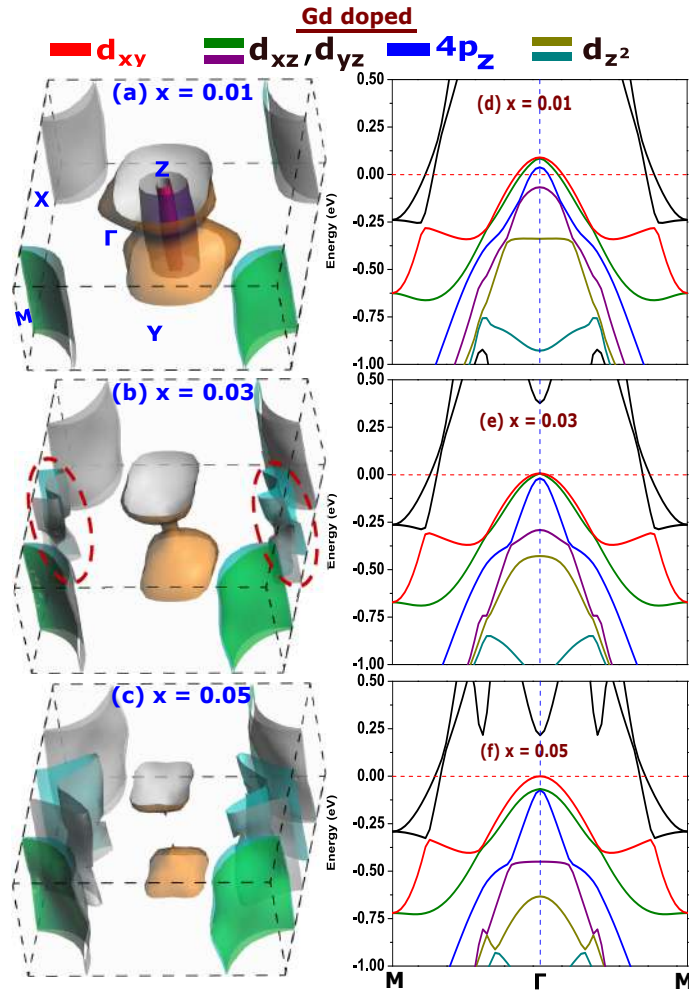


Figure 4.6: [138] Calculated Fermi surfaces (FSs) and band structures (BNSs) of $\text{Ca}_{1-x}\text{Gd}_x\text{FeAs}_2$ system within VCA method. We have shown the FS and BNS with same doping in the same row. Doping levels (x) of Gd are (a) $x = 0.01$, (b) $x = 0.03$, (c) $x = 0.05$, (d) $x = 0.10$ respectively and (e), (f), (g), (h) show BNSs with respective doping.

d_{xy} band also moves below the E_F causing LT at that doping. As we move to Pr doped CaFeAs_2 , it is clearly visible from Fig. 4.3 that the electronic structure remains almost same at lower doping but the Lifshitz transition start at doping 0.05. Due to Lifshitz transition there appears a new FS at the X-point. For further increase in Pr doping to 0.10 all the three bands above the E_F d_{xy} , (d_{yz}, d_{xz}) and $4p_z$ are pushed below the E_F and FSs at Γ -point vanish. These are the manifestations of Lifshitz transition. Fig. 4.4, 4.5, 4.6 reveal that the shift of the d_{xy} , (d_{yz}, d_{xz}) and $4p_z$ bands is higher with doping as we gradually move from Nd doping to Gd doping. In case of Nd doping with doping level 0.03, the $4p_z$ band just touches the E_F and d_{xy} , (d_{yz}, d_{xz}) bands are well above the E_F . But for Sm and Gd doped case, at doping level 0.03 the $4p_z$ band and (d_{yz}, d_{xz}) bands come below the E_F respectively inducing Lifshitz transition. As we increase the doping to 0.05, $4p_z$ band shifts below the E_F for Nd doped compound accompanying Lifshitz transition. The shifting of (d_{yz}, d_{xz}) and d_{xy} bands are the cause of respective Lifshitz transition in Sm and Gd doped compounds at doping concentration 0.05. Thus complete disappearance of FS at Γ -point occurs at around this doping for Gd. For Nd and Sm doped case complete removal of FS at Γ -point happens to be at around 0.10 and 0.07 respectively. Occurrence of band edge van Hove singularity prior to Lifshitz transition is thought to be an important factor in controlling highest critical temperature for IBSCs. Conversely, the occurrence of Lifshitz transition arrests the growth of T_c with doping as more number of hole bands do not participate in superconductivity. In this regard our observed electronic structure reveals a trend of occurrence of band edge van Hove singularity as well as Lifshitz transition at lower doping as we move from La to Gd doping. This indicates to the fact that there should be a decrement in T_c as we move from left to right in lanthanide series. This is in agreement with the experimental observations [28].

All the above DFT based electronic structure calculations are also performed using GGA+U method for various values of U, *e.g.*, 0.5 eV, 1 eV, 1.5 eV and 2 eV. However, the calculated electronic structures using GGA+U calculations do not match with the experimen-

tally observed ARPES band structure [136].

4.4 Bandwidth renormalization and orbital selectivity

We have already discussed about the importance of calculating bandwidth in section-I. To understand the effect of rare earth doping on bandwidths of different orbital derived bands and its possible connection to superconductivity, we have calculated bandwidths of the major hole like bands crossing the Fermi level around the Γ -point using our first principles calculations within GGA. We have calculated the bandwidth of different hole like bands by measuring the difference in energy between the top of the respective hole like band (at Γ -point) and first minima of the same band in Γ -M direction following the procedure adopted in [158]. This electronic bandwidth renormalization together with Fermi surface topology can provide useful insight about the phenomenon of superconductivity in these rare earth doped compounds. We have calculated the bandwidth of the three hole like bands mainly derived from $-d_{xy}$, (d_{yz}, d_{xz}) and $4p_z$ orbitals for RE doped materials and presented in TABLE-7.9. We have also presented c-axis length, distance between FeAs-layers and As-chain, pnictogen height (Z_{As}) in TABLE-4.3 to understand the inter relationship between the structural parameters and bandwidth renormalization of various orbital selective bands.

Table 4.2: Doping dependent bandwidth of $\text{Ca}_{1-x}\text{RE}_x\text{FeAs}_2$

RE element	Doping level (x)	Band-orbital	Bandwidth in meV
Ce	0.01	d_{xy}	527
		d_{yz}, d_{xz}	772
		$4p_z$	1596
	0.03	d_{xy}	488
		d_{yz}, d_{xz}	769

RE element	Doping level (x)	Band-orbital	Bandwidth in meV
	0.05	$4p_z$	1600
		d_{xy}	451
		d_{yz}, d_{xz}	768
		$4p_z$	1577
	0.10	d_{xy}	414
		d_{yz}, d_{xz}	708
		$4p_z$	1576
	0.15	d_{xy}	390
		d_{yz}, d_{xz}	699
		$4p_z$	1578
Pr	0.01	d_{xy}	506
		d_{yz}, d_{xz}	769
		$4p_z$	1616
	0.03	d_{xy}	449
		d_{yz}, d_{xz}	769
		$4p_z$	1596
	0.05	d_{xy}	427
		d_{yz}, d_{xz}	723
		$4p_z$	1603
	0.10	d_{xy}	382
		d_{yz}, d_{xz}	706
		$4p_z$	1582
Nd	0.01	d_{xy}	501
		d_{yz}, d_{xz}	768
		$4p_z$	1598
	0.03	d_{xy}	437

RE element	Doping level (x)	Band-orbital	Bandwidth in meV
	0.05	d_{yz}, d_{xz}	745
		$4p_z$	1589
		d_{xy}	415
	0.10	d_{yz}, d_{xz}	705
		$4p_z$	1589
		d_{xy}	409
		d_{yz}, d_{xz}	678
		$4p_z$	1564
Sm	0.01	d_{xy}	478
		d_{yz}, d_{xz}	772
		$4p_z$	1603
	0.03	d_{xy}	414
		d_{yz}, d_{xz}	719
		$4p_z$	1601
	0.05	d_{xy}	408
		d_{yz}, d_{xz}	697
		$4p_z$	1583
	0.07	d_{xy}	412
		d_{yz}, d_{xz}	685
		$4p_z$	1558
	0.10	d_{xy}	445
		d_{yz}, d_{xz}	670
		$4p_z$	1578
Gd	0.01	d_{xy}	451
		d_{yz}, d_{xz}	767
		$4p_z$	1593

RE element	Doping level (x)	Band-orbital	Bandwidth in meV
	0.03	d_{xy}	397
		d_{yz}, d_{xz}	713
		$4p_z$	1580
	0.05	d_{xy}	424
		d_{yz}, d_{xz}	678
		$4p_z$	1588
	0.10	d_{xy}	385
		d_{yz}, d_{xz}	641
		$4p_z$	1574

Table 4.3: Variation of c-axis and FeAs layer to As-chain distance of $\text{Ca}_{1-x}\text{RE}_x\text{FeAs}_2$

RE element	Doping	c-axis (Å)	Layer to chain distance (Å)	a-axis (Å)	b-axis (Å)	Z_{As} (Å)
Ce	0.01	10.025	4.986	3.926	3.868	1.251
	0.03	10.014	4.970	3.929	3.873	1.242
	0.05	9.981	4.949	3.940	3.876	1.240
	0.10	9.911	4.912	3.932	3.888	1.223
	0.15	9.867	4.890	3.926	3.891	1.232
Pr	0.01	10.024	5.015	3.911	3.867	1.232
	0.03	9.970	4.947	3.930	3.873	1.238
	0.05	9.901	4.945	3.912	3.882	1.235
	0.10	9.743	4.857	3.908	3.897	1.234
Nd	0.01	10.012	4.971	3.926	3.869	1.245
	0.03	9.923	4.922	3.928	3.874	1.239
	0.05	9.823	4.868	3.921	3.875	1.247
	0.10	9.593	4.771	3.899	3.895	1.245
Sm	0.01	9.986	4.956	3.928	3.870	1.241
	0.03	9.828	4.873	3.917	3.869	1.261
	0.05	9.662	4.772	3.905	3.878	1.246
	0.10	9.351	4.674	3.872	3.871	1.249
Gd	0.01	9.954	4.939	3.927	3.870	1.240
	0.03	9.722	4.817	3.912	3.873	1.251
	0.05	9.529	4.760	3.876	3.882	1.246
	0.10	9.179	4.591	3.850	3.849	1.266

A close look at the TABLE-7.9 indicates a trend of *decreasing* bandwidth with *increasing* rare earth doping. The same trend follows as we move from right to the left in the periodic

table containing lanthanide series. But all the three bands are not equally renormalized by the RE doping. For example, the bandwidth of d_{xy} derived band decreases from 527 meV to 414 meV, from 506 meV to 382 meV, from 501 meV to 409 meV, from 478 meV to 445 meV, from 451 meV to 385 meV for increasing Ce, Pr, Nd, Sm and Gd doping upto 10% respectively. On the other hand, the bandwidth of (d_{yz}, d_{xz}) derived band also decreases from 772 meV to 699 meV, from 769 meV to 706 meV, from 768 meV to 678 meV, from 772 meV to 699 meV, from 767 meV to 641 meV for increasing Ce, Pr, Nd, Sm and Gd doping upto 10% respectively. On the contrary, there is no such general trend of decreasing bandwidth for As $4p_z$ band and the value of bandwidth is also very large. This indicates to the fact that all the three bands crossing the E_F are not affected equally due to RE doping. Thus the RE doping to 112 compounds (which induces superconductivity) orbital selectively renormalizes different bands of different orbital weights – *e.g.*, it prominently effects the bandwidth of d_{xy} and (d_{yz}, d_{xz}) bands but not the As- $4p_z$ derived hole band. However, it is to be noted that in the superconducting phase only the bands having energy within 100-200 meV around E_F play key role. So, one should look into mass renormalization/Fermi velocity renormalization at the Fermi level for bands with different orbital weight to have a more rigorous idea about orbital selectivity and superconductivity.

From TABLE-4.3 we can see that with increasing doping the c-axis as well as FeAs to As-chain layer distance shrinks leading to decrease in bandwidth. Thus the bandwidth renormalization of RE doped 112 iron based superconductor are related to the modifications in structural parameters. However, the pnictogen height (Z_{As}) does not show any general trend of increase or decrease with RE doping. In case of $Ca_{1-x}RE_xFeAs_2$, the orbital selective bandwidth renormalization can tune the rare earth doping induced orbital selective superconductivity in it. However rare earth doping also has significant effect on the Fermi surface topology of these compounds. To investigate the connection between Lifshitz transition and bandwidth renormalization, we have shown the variation of bandwidth of different Fe-3d bands in Fig. 4.7 (a), (b) for different rare earth element doping.

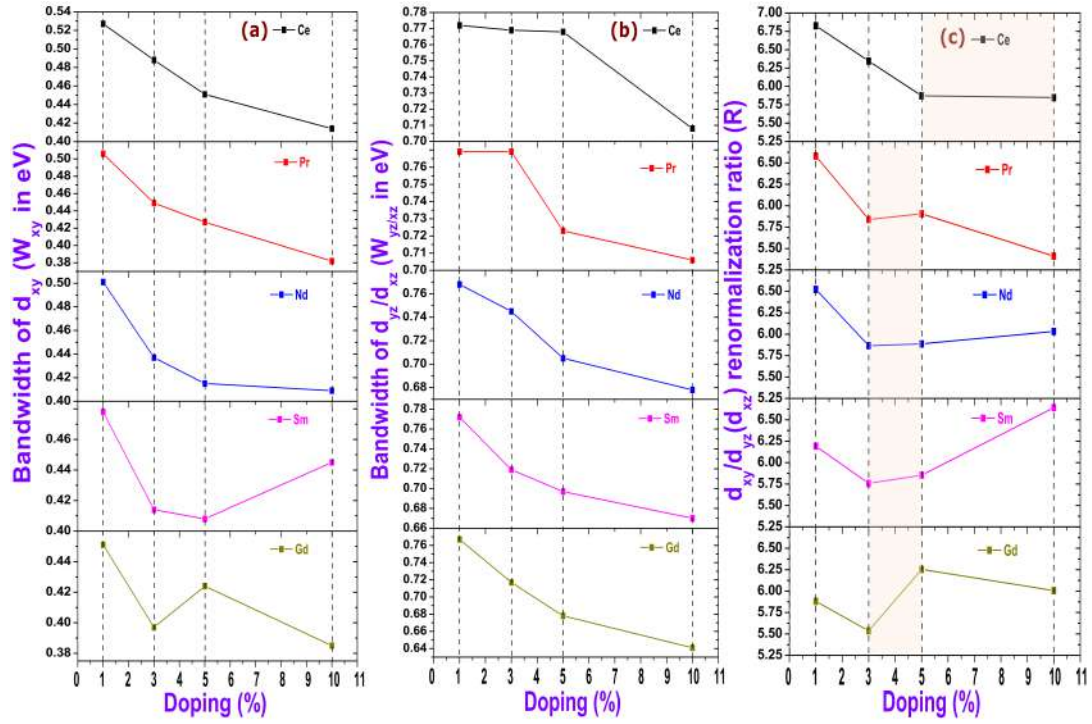


Figure 4.7: [138] (a) Variation of calculated bandwidth of d_{xy} band with doping for different rare earth elements, (b) variation of calculated bandwidth of (d_{yz}, d_{xz}) band with doping for different rare earth elements, and (c) variation of band renormalization ratio with doping for different rare earth elements. The shaded region in (c) is the region of onset of Lifshitz transition. The slope of R vs doping in (c) changes sign whenever there is onset of electronic topological transition.

Fig. 4.7 clearly shows that the change in the bandwidth of d_{xy} orbital (W_{xy}) is much more compared to that of (d_{yz}, d_{xz}) orbital ($W_{yz/xz}$). This again indicates to orbital selective band renormalization. Since reduction in bandwidth corresponds to some kind of localization due to possible manifestations of electron correlation effect, our results indicate a orbital selective band renormalization leading to orbital selective electron correlation induced by rare earth doping. Further the nature of variation of bandwidths depends on nature of rare earth doping. For Ce doping at Ca site, there is a trend of decreasing bandwidth of d_{xy} band-orbital. For Pr and Nd doped case, the trend is nearly similar except the fact that in case of Nd doping the change in bandwidth at higher doping is significantly small. For Sm and Gd doped case, the nature of variation of W_{xy} is very much different than the above mentioned cases. Fig. 4.7(a) clearly shows that in between 3% to 5% Sm doping W_{xy} changes a little but in between 5% to 10% doping there is a sudden increase. Such abrupt changes in bandwidth due to RE-doping are related to electronic topological changes in band structure and Fermi surfaces. This is also reflected in Fig. 4.5 (c, d) where appearance of some electron like FSs at around the X point is seen which is accompanied by the disappearance of some hole like Fermi surfaces. This electronic structure reconstruction is topological in nature, some d_{xy} derived hole like band transforms into electron like. This establishes a relationship between orbital selective nature of bandwidth renormalization as well as Lifshitz transition. For Gd doped case the change in W_{xy} is not following any particular trend. Thus the nature of variation of W_{xy} largely depend on the particular rare earth element doped at Ca site. Fig. 4.7 (b) gives us an idea about the variation of $W_{yz/xz}$ with different RE doping. For Ce doping there is a little change in $W_{yz/xz}$ for 1% to 5% doping. In Ce doping range 5%–10%, a sudden decrease of $W_{yz/xz}$ occurs. In case of Pr doping the bandwidth remains nearly constant for 1% to 3% doping. There is a sudden decrease in $W_{yz/xz}$ in between 3% to 5% doping. Further decrease in the value of bandwidth occurs upto 10% doping. Unlike Ce and Pr doped cases, there is a general trend of decreasing $W_{yz/xz}$ with increased doping for Nd, Sm and Gd doped cases. The above observations indicate to the fact that the nature of bandwidth renormalization is

quite different for d_{xy} and (d_{yz}, d_{xz}) derived bands in 112 IBSCs. To know about the orbital selectivity of the Fe-3d derived bands, we have calculated the renormalization ratio of d_{xy} and (d_{yz}, d_{xz}) bands and have shown their variation with different RE doping concentration in Fig. 4.7 (c). We have defined renormalization ratio (R) as $R = W_{xy}/W_{yz/xz} \times 10$. From Fig. 4.7 (c) it is clear that there is a trend of decreasing R for 1% to 5% doping in case of Ce doping. But R does not change much in between 5% to 10% Ce doping. For Pr doped case, R decreases as we increase the doping from 1% to 3%. In the doping range 3%–5%, a slight increase in the value of R is observed and R decreases again for further Pr doping in between 5%–10%. In case of Nd and Sm doping, there is decrement in the value of R at around 1%–3% doping. After that a general trend of increasing R with increased doping is observed upto 10% doping. The increase is larger in Sm doped case in comparison to Nd doped case. Thus bandwidth renormalization of d_{xy} band with respect to $d_{xz/yz}$ band is quite different for different RE doping. A close inspection and comparison of Fig. 4.7 (c) with the electronic structure of different RE doped 112 compounds (*i.e.*, Fig. 4.1, 4.3, 4.4, 4.5, 4.6) reveals a unique connection between bandwidth renormalization ratio (R) and Lifshitz transition. The change in sign of slope of the R Vs Doping plot (Fig. 4.7 (c)) may be associated with orbital selective Lifshitz transition. Fig. 4.1 shows that upto 5% doping there occurs no Lifshitz transition. If the Ce doping is increased further from 5% to 10% Lifshitz transition sets in and the slope of the Fig. 4.7 (c) also changes. For Pr doping sign of the slope changes as the doping changes from 3% to 5% and the subsequent Lifshitz transition also occurs. Above 5% Pr doping there is again a change in the slope of R Vs Doping plot which can be associated with Lifshitz transition in between 5% to 10% doping. For Nd and Sm doped case also the change in the slope of R Vs RE doping plot which is shown to be associated with Lifshitz transition at the respective doping. For example, around 5% of Nd doping one hole like band at around the Γ -point vanishes and one electron like band around the X-point appears. These indicate occurrence of Lifshitz transition at around that doping. Consequently, sign of slope of the R vs doping curve in Fig. 4.7 (c) also changes in between 3% to 5% Nd doping. The slope change between

5% to 10% Nd doping is also associated with the topological changes in the FS leading to Lifshitz transition. Similarly, in case of Sm doping, Lifshitz transition in between 1% to 3%, 3% to 5%, or 5% to 10% occur together with a change in slope of R Vs RE doping curve at around respective doping. Due to very high electron doping in case of Gd doped 112 compound the modification in the Fermi surface topology is very rapid with doping. Consequently, the change in the slope of R -Doping plot is also large. Fig. 4.6 and Fig. 4.7 clearly indicate a correspondence between bandwidth renormalization and Lifshitz transition. From the above discussion it is comprehensible that the rare earth doping do not affect all the Fe-3d bands equally. The effect is most prominent on d_{xy} orbital. Thus the variation of R with doping dictate the evolution of orbital selectivity. This indicates to the fact that RE doping influences electron correlation of the major bands orbital selectively and leads to orbital selective Lifshitz transition in RE doped 112 compounds.

4.5 Conclusions

We have presented a detailed DFT based first principles electronic structure study on $\text{Ca}_{1-x}\text{RE}_x\text{FeAs}_2$ for different rare earth (RE = Ce, Pr, Nd, Sm, Gd) elements. We have shown in details that doping by RE elements has a great impact on the electronic structure as well as Fermi surface topology of $\text{Ca}_{1-x}\text{RE}_x\text{FeAs}_2$. Doping is proved to modify electronic structure to a great extent for many other compounds also. For example, in [159], the effect of hydrogenation or fluorination on phagraphene is studied using DFT calculations. Adsorption-induced semimetal–semiconductor transition and semimetal–insulator transition in hydrogenated or fluorinated phagraphene is a direct evidence of prominent impact of doping on the electronic structure of this material. Similar studies on penta-silicene with fluorination reveals tunable electronic structure of penta-silicene depending on the fluorine concentration including a concentration-induced semiconductor to metal transition [160]. The studies on the effect of size of functional group in g- C_3N_4 [161] or nitrogenated holey graphene C_2N monolayer [162] also reveals the tunability of band gap

with enhanced electronic properties. Although $\text{Ca}_{1-x}\text{RE}_x\text{FeAs}_2$ remain metallic after rare earth doping, its electronic structure gets modified to an appreciable amount. A common characteristic in the electronic structure of all the RE doped 112 compound is gradual disappearance of hole like Fermi surface near Γ -point with increased doping leading to Lifshitz transition. This suggests that the RE doping acts as heavy electron doping. Our calculated electronic structure shows a trend of Lifshitz transition at lower doping as we gradually move from left to right of lanthanide series in the periodic table due to excess electron doping. Our detailed electronic structure results indicate delicate inter connection between bandwidth renormalization and Lifshitz transition where “orbital selectivity” is in built. The occurrence of low T_c to various RE doped 112 materials, our calculation attributes it to the occurrence of Lifshitz transition at very low doping. These suggest that “orbital selectivity” would also play a decisive role in the superconductivity of the RE doped 112 materials. To demonstrate the connection between bandwidth renormalization and Lifshitz transition and their implications on superconductivity of these compounds we have calculated the bandwidth of the hole like bands derived from d_{xy} , (d_{yz} , d_{xz}) and $4p_z$ orbitals. Rare earth doping does not affect all the bands equally. Bandwidth of d_{xy} -band only changes significantly. Thus RE doping at Ca site induces orbital selective electron correlation in this compound. The renormalization ratio (R) shed light on the orbital selectivity of the bands. The R vs doping plot clearly shows that the onset of Lifshitz transition corresponds to the change of sign of slope. The change in the slope continues for transitions at higher doping. This indicates to the fact that there is a connection between orbital selectivity and Lifshitz transition. The RE doping at Ca site renormalizes the bandwidth of the Fe-3d derived hole like bands around the Γ -point in such a way that it in turn influences the topological changes in FSs leading to orbital selective Lifshitz transition. A detailed ARPES study compared with first principles study might be very useful for further research in this direction.

Chapter 5

Doping As site sensitivity in 112 compounds

The effect of Sb doping in As-chain as well as FeAs-layer on the electronic structure of rare earth ($R = \text{La, Pr, Nd, Sm}$) co-doped $\text{Ca}_{1-x}\text{R}_x\text{FeAs}_2$, 112 compound is discussed in this chapter. Unique modifications in the electronic structures compared to other family of Fe based superconductors are obtained through Sb doping at As belonging to FeAs layers as well as that belonging to chains in between the layers. While Sb doping at the As site of FeAs layer causes enhancement of electronic Fermi arcs around the high symmetry X point of the Brillouin zone, the same on the chain As atom suppresses its formation at X. Contribution of chain As atoms and their role in Lifshitz transition are also demonstrated. Enhanced contribution to the density of states from chain atoms in comparison to that of the layers signify possible role of chain atoms in contributing to superconductivity in these materials. An increase in density of states at the Fermi level (E_F) indicates increased availability of electrons for Cooper pairing and hence possible enhancement of superconductivity. Our results predict preference of Sm doping over other rare earth elements as far as enhancement of superconductivity via Sb doping at As-chain is concerned.

5.1 Theory and Computational Method

We have performed first-principles simulations based on density functional theory using plane-wave pseudopotential method implemented in Cambridge Serial Total Energy Package (CASTEP) [128]. We have incorporated the generalized gradient approximation (GGA) with Perdew-BurkeEnzerhof (PBE) functional to tackle electronic exchange correlation [125]. For the doped systems, we have carried out geometry optimization using Broyden-Fletcher-Goldfrab-Shanno (BFGS) scheme. Virtual Crystal Approximation (VCA) is used to simulate defects in the crystal structure due to doping. In VCA, the defects in the crystal due to rare earth and Sb doping are incorporated considering fictitious virtual atoms in place of actual atoms [126]. In this approximation the periodicity of the crystal is considered to be unchanged. Any possible short range order is ignored in VCA. It is assumed that each potentially disordered site is filled with a virtual atom which interpolates between the behavior of the actual components. The ultrasoft pseudopotential which we have used for our electronic structure calculations, are vulnerable to the generation of ghost states within VCA framework. We have used the standard way to check the applicability of the VCA approach for ghost states [130]. The value of the derivative of the total energy during the finite basis set correction calculation is checked to be of the same order as that of the derivatives of the end member of the structures. Thus the validity of VCA holds for our Calculations. VCA is proved to be very effective to simulate the electronic structure of disordered systems like Fe based superconductors as far as small doping (like our case) is concerned [132]. To calculate electronic properties, Monkhorst-Pack scheme [133, 134] is implemented to sample the k space in Brillouin zone (BZ) with $26 \times 26 \times 10$ k-point mesh. To get the optimized structure, all atoms are fully relaxed until the magnitude of Hellmann-Feynman force on each atom is converged to less than 0.01 eV/\AA and the energy change per atom converged to less than $5 \times 10^{-7} \text{ eV/atom}$. To perform spin polarized single point energy calculations, we have taken CaFeAs_2 in monoclinic phase with space group symmetry P21 or P21/m. The interactions between the ion

core and the valence electrons is treated using ultrasoft pseudopotential and the cut-off energy for plane wave is set to 600 eV. To resolve the orbital character of the bands, we have performed simulations using QUANTUM ESPRESSO package [135] with ultrasoft pseudo-potential and PBE exchange correlation potential. The cut off energy of plane wave and the grid size for SCF calculation is 30 Rydberg and $16 \times 16 \times 6$ respectively, decided after performing rigorous convergence test.

5.2 Sb doping at As site - chain vs layer

Sb doping at the As site has remarkable effect on superconductivity of 112 iron based superconductors. It increases T_c upto 47 K which is the highest achievable so far for 112 family (in case of doping at the chain). There are two types of As in CaFeAs_2 - at As chain in between the FeAs layers with oxidation state -1 and at the FeAs layers with oxidation state -3. Furthermore, unlike other iron based superconductors the spacer layer is conducting in case of 112 superconductors. We have studied the effect of Sb doping at both the sites. Recently, theoretical as well as experimental studies have revealed that Sb doping at the As chain is more favourable than doping at FeAs layer [164, 165, 166]. We have studied the Fermi surface, band structure and density of states in both the doping cases. We present all the results obtained within virtual crystal approximation.

Fig. 5.1, 5.2 show that the calculated FSs of $\text{Ca}_{1-x}\text{La}_x\text{Fe}(\text{As}_{1-y}\text{Sb}_y)_2$ with different Sb doping concentrations as indicated in the Figure. This Fig. 5.1 should be contrasted with Fig. 3.1(b) and Fig. 3.1(c) respectively. In absence of Sb doping in the As chain, there are three hole like Fermi surfaces around the Brillouin zone centre (the two inner FSs being very narrow), two electron-like Fermi surfaces at the Brillouin zone corners (Fig. 3.1(b), Fig. 3.1(c)) along with small but finite electron like FSs at around the X point. When the system is further 0.10 Sb doped, one of the hole FSs as well as FSs at around the X point disappear. This clearly demonstrates the distinguishing influence of As chain atoms on

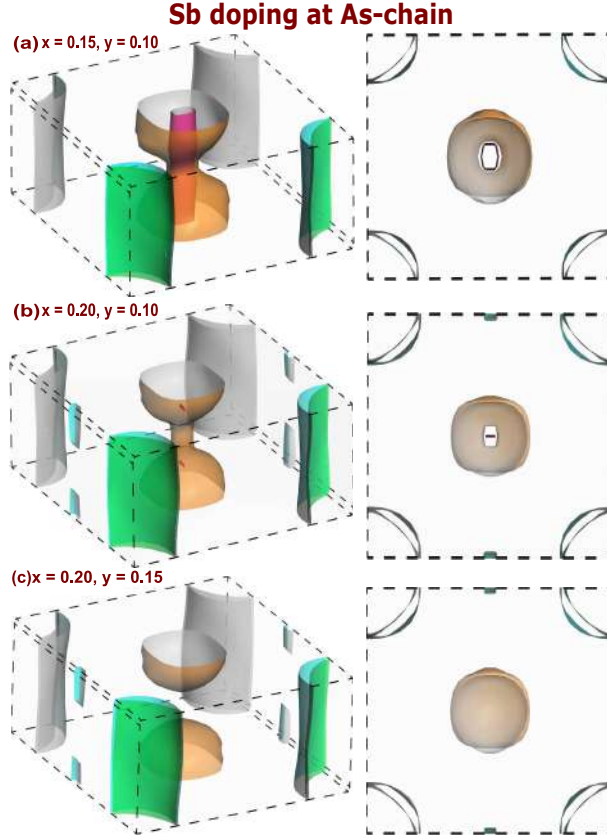


Figure 5.1: [137] Fermi surfaces of $\text{Ca}_{1-x}\text{La}_x\text{Fe}(\text{As}_{1-y}\text{Sb}_y)_2$ for Sb doping at As chain: (a) for $x = 0.15$, $y = 0.10$; (b) for $x = 0.20$, $y = 0.1$; and (c) for $x = 0.20$, $y = 0.15$. Two different views of FSs have been shown in the same row at a particular doping.

electronic structures. In Fig. 5.1(b) and Fig. 5.1(c) we increase the La doping at Ca site corresponding to that of Fig. 3.1(b), 3.1(c)) where two hole FSs as well as well-developed FS arcs at X-points are obtained. When 0.10 Sb is doped at the As chain, one of the inner hole FSs again disappears and size of the well-developed electron FS arcs at around X-points are diminished a lot. When the amount of Sb doping is further increased from 0.10 to 0.15, the single hole FS dis-integrates into two disconnected FSs at the Γ point. This should be contrasted with Sb doping at layered As atoms, see Fig. 5.2. A close comparison between Fig. 5.2 and Fig. 5.1 would indicate that Sb doping at the As site of FeAs layer causes enhancement of electronic Fermi arcs around the high symmetry X point of the Brillouin zone, whereas the same on the chain As atom suppresses its formation at X. From diminishing electron pocket around X-point due to Sb doping at As-chain it may be predicted that the nesting between only 3D hole like pockets around Γ /Z-point and 2D

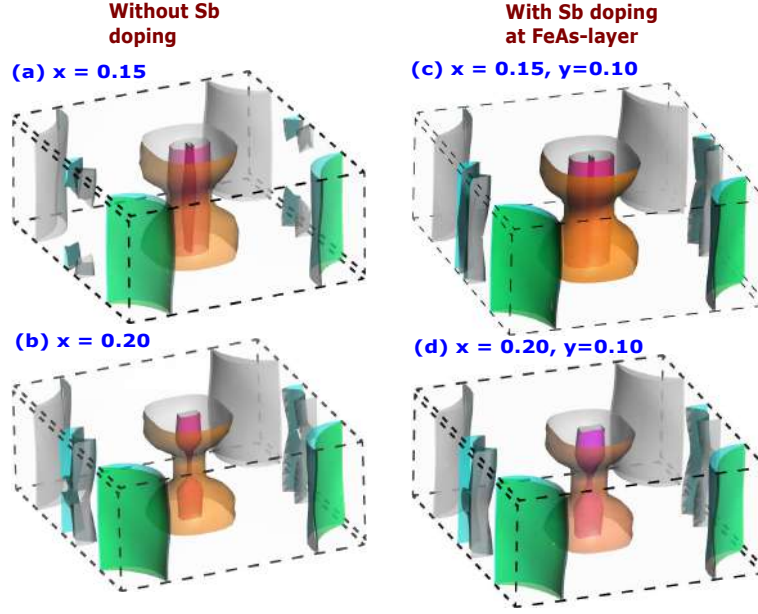


Figure 5.2: [137] Fermi surfaces of $\text{Ca}_{1-x}\text{La}_x\text{Fe}(\text{As}_{1-y}\text{Sb}_y)_2$ for Sb doping at FeAs layer: (a) $x = 0.15$ (b) $x = 0.20$; (c) $x = 0.15, y = 0.10$; and (d) for $x = 0.20, y = 0.10$.

electron like pockets around M-point is important to superconductivity (Fig. 5.11 c, d). This is confirmed by neutron spin resonance experiments for $\text{Ca}_{0.82}\text{La}_{0.18}\text{Fe}_{0.96}\text{Ni}_{0.04}\text{As}_2$, where only a 2D spin resonance around $Q = (1,0)$ corresponding to the wave vector Q from Γ/Z to M is found. These experimental observations supported our theoretical results lead to the conclusion that the s^\pm pairing only happens around the 3D hole pockets around Γ/Z -point and the 2D electron like pockets around M-point. There are however no visible effects on the hole FS topologies in case of Sb doping at layered As atoms (Fig. 5.2(b)). These modifications in the FS with Sb doping indicate influence of As-chain on electronic structure of 112 compounds that are absent in other classes of FeSC. This important electronic structure effect is at play for the rise of T_c in case of doping at As-chain, indicating the uniqueness of these particular family of materials.

A trend of c-axis lattice constant as well as the distance between chain and layer as a function of various doping as resulted from first principles density functional theory are presented in Table-5.1. Increasing La doping increases the separation between the layers, this makes the layers and chains more independent. So the Fermi surface of the conducting As -chain appears at the X -points more prominently and as La doping causes electron

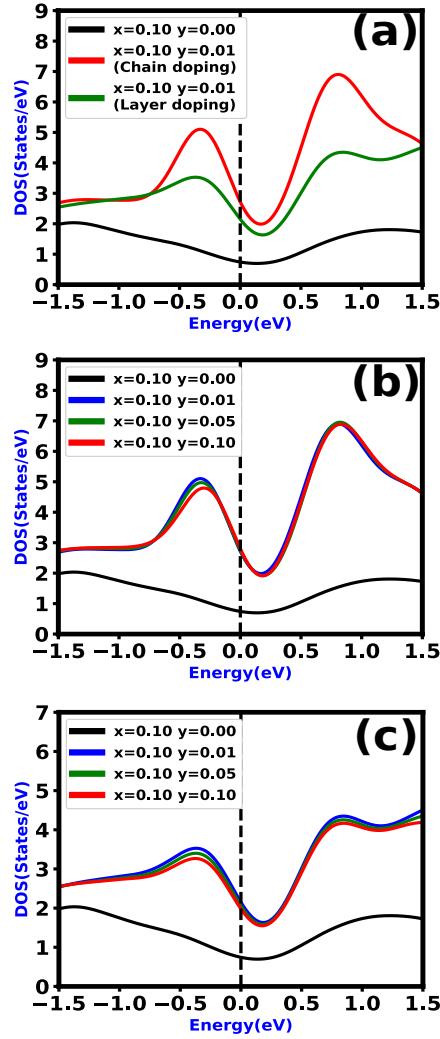


Figure 5.3: [137] Partial density of states of As for (a) undoped (without Sb doping) and Sb doping at two different sites (As-chain and FeAs layer), (b) Sb doping at As chain, and (c) Sb doping at FeAs layer of $\text{Ca}_{1-x}\text{La}_x\text{Fe}(\text{As}_{1-y}\text{Sb}_y)_2$. Fermi level is denoted by vertical black line at zero energy.

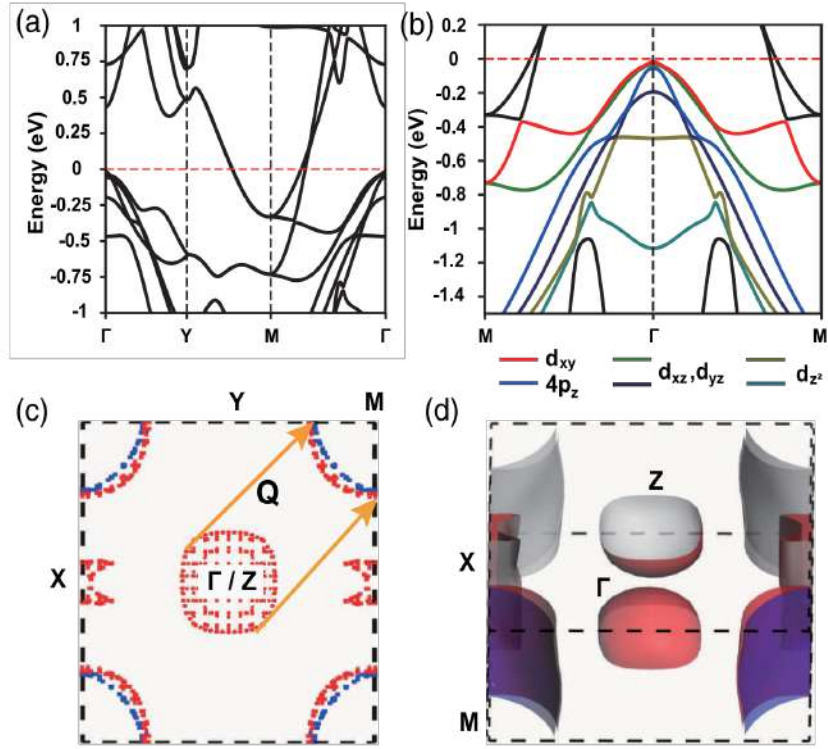


Figure 5.4: [139] Electronic structure of $\text{Ca}_{0.82}\text{La}_{0.18}\text{Fe}_{0.96}\text{Ni}_{0.04}\text{As}_2$; (a) band structure, (b) orbital projected band, (c) 2D Fermi surface, (d) 3D Fermi surface.

doping the electron FSs remain essentially 2-dimensional, whereas the hole FSs become very much 3-dimensional. Sb doping at the chain on La doped samples deteriorates the metallic property of the chain without causing much change in the layer-chain distance. As a result, FS of disordered chains appearing at the X-points become smaller. It also affects some of the hole FSs as it contains some contributions of chain As in it as evidenced through band structure results. In contrast, when Sb is doped at the layers the c-axis as well as chain-layer distance increases further and hence causes the conducting As-chain

Table 5.1: Variation of c-axis and FeAs layer to As-chain distance with different doping

Doping	c-axis (Å)	Layer to chain distance (Å)
10% La	10.088	5.012
15% La	10.101	5.018
20% La	10.112	5.024
15% La 10% Sb (chain)	10.105	5.019
20% La 10% Sb (chain)	10.090	5.015
20% La 15% Sb (chain)	10.100	5.034
15% La 10% Sb (layer)	10.184	5.084
20% La 10% Sb (layer)	10.170	5.051

FS appearing at the X-points again without much topological modifications of other FSs.

Fig. 5.3(a) displays atom projected partial density of states of As in case of Sb doping at As chain and Sb doping at FeAs layer for Sb doping $y = 0.01$. From Fig. 5.3(a) we see that the density of states of As atoms at the Fermi level is very less in La doped CaFeAs_2 . When we dope Sb, the partial density of states of As increases significantly. But the increase in density of states for doping at the As chain site is more than the doping at FeAs layer. A close inspection of the As partial DOS at the Fermi level also reveals that the DOS at the Fermi level remain same with further increase in Sb doping at As chain (Fig. 5.3(b)) as well as at FeAs layer (Fig. 5.3(c)).

5.3 Electronic structure of the Sb doped 112 compounds

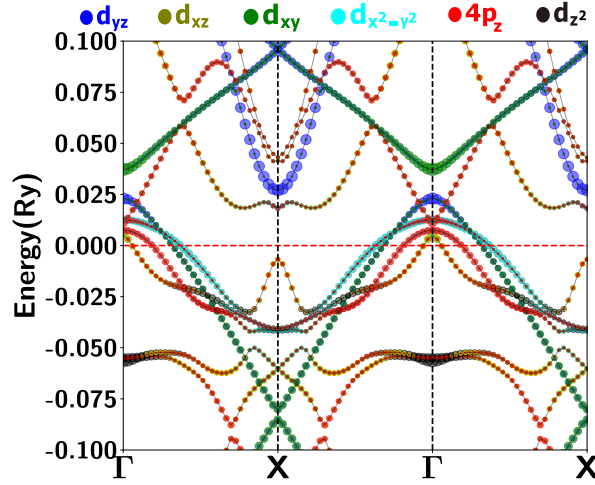


Figure 5.5: [140] Band structure of undoped CaFeAs_2 . The orbital weight of different bands is shown with circles of varying radius and designating a particular colour to a particular orbital (Fe-3d, As-4p).

We want to investigate the effect of Sb doping at As-chain site in the rare earth co-doped 112 compound. Experimentally it has been observed that in the range of 1% to 10% Sb doping, the transition temperature remain almost the same. Also, theoretical studies reveal that the partial density of states of As at the E_F does not change to a significant amount due to Sb doping [187]. Therefore, we have chosen 5% Sb doping for our calculations. The

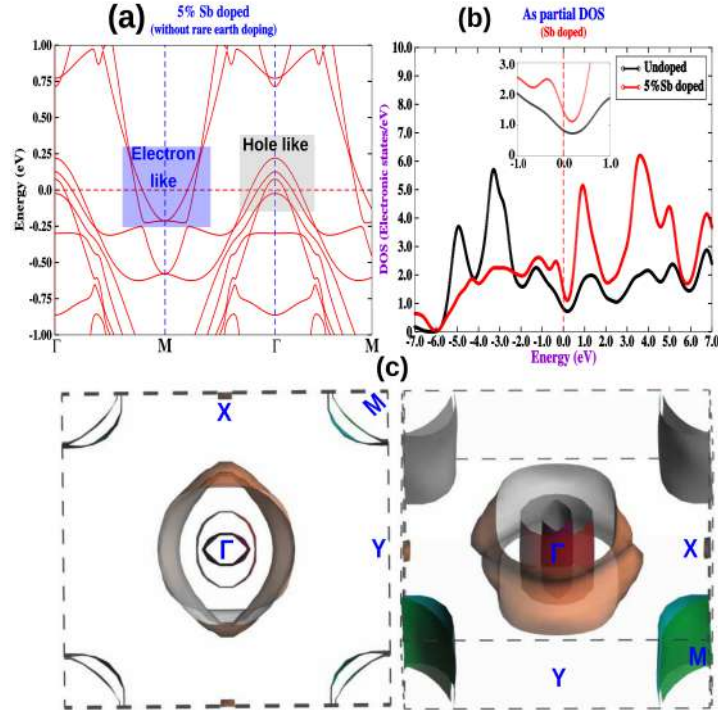


Figure 5.6: [140] Calculated (a) BNSs, (b) DOS, and (c) FSs of $\text{CaFe}(\text{As}_{0.95}\text{Sb}_{0.05})_2$ system within VCA method. In (c) two different view of the same FSs is presented.

calculations of the doped system are performed within Virtual Crystal Approximation. We have calculated the band structures (BNS), density of states (DOS) and Fermi Surfaces (FS) of CaFeAs_2 for various rare earth elements doping systematically. In this section the calculated electronic structures are presented. The calculations are performed in the monoclinic phase after geometry optimization. We have used experimentally measured lattice parameters [27] as starting input for our first principles calculations.

Table 5.2: Lattice parameters of the undoped and different doped 112 compounds

Doping	a (Å)	b (Å)	c (Å)
10% Pr [188]	3.908	3.897	9.743
10% Pr 5% Sb	3.899	3.895	9.593
10% Nd [188]	3.918	3.908	3.739
10% Nd 5% Sb	3.910	3.908	9.604
10% Sm [188]	3.872	3.871	9.351
10% Sm 5% Sb	3.882	3.882	9.351
5% Sb	3.939	3.879	10.046
undoped	3.926	3.865	10.054

In Fig.5.5 we depict the orbital projected BNS of undoped CaFeAs_2 along high symmetry

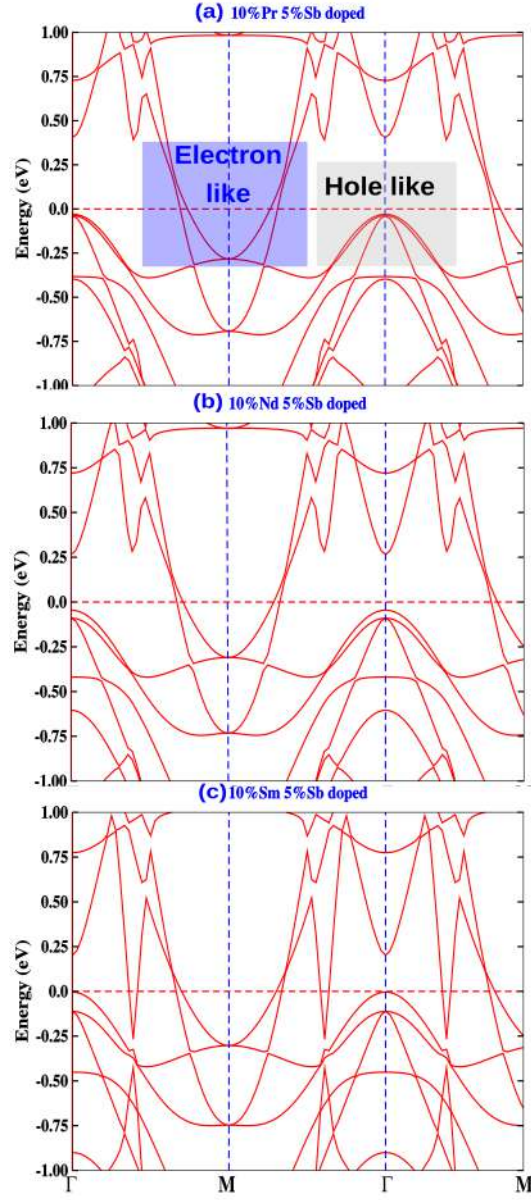


Figure 5.7: [140] Calculated BNSs of $\text{Ca}_{0.90}\text{R}_{0.10}\text{Fe}(\text{As}_{0.95}\text{Sb}_{0.05})_2$ system within VCA method for rare earth = (a) Pr, (b) Nd, (c) Sm.

directions. Like other IBSCs, the bands of 112 are also of multi-orbital multi-band character. Bands around the Fermi level are mostly derived from different Fe-3d orbitals. But unlike most of the IBSCs, there is a significant contribution from the As-4 p_z orbital which has been verified both theoretically as well as by ARPES measurements [168]. From Fig.5.5 it is conceivable that along Γ -X or X- Γ direction the As-4 p_z orbital mixes remarkably with Fe-3d orbitals. A closer look into the orbital projected band structure around the Γ -point near the E_F reveals Dirac cone like feature of bands which are primarily derived from As-4 p_z orbital. It is believed that bands near the E_F are mainly responsible for superconductivity in IBSCs. Thus the study on orbital character of the bands disclose that the As-4 p_z orbital might have a significant effect on the superconductivity of 112 Fe based superconductors which has been discussed in the following sections in detail.

In Table. 5.2 we have presented the lattice parameters of the optimized rare earth doped 112 compound with or without Sb doping. Comparison of the lattice parameters clearly show that a , b do not change much due to Sb doping in the rare earth doped 112 compounds. On the other hand there is a significant decrease in c . This might have a significant impact on the electronic structure of the 112 Fe based superconductors which we will discuss in the following sections. Fig.5.6 depicts the BNS, DOS and FS of $\text{CaFe}(\text{As}_{0.95}\text{Sb}_{0.05})_2$ which has not yet been synthesized experimentally. It is clear from Fig.5.6(a) that there are three hole like bands around the Γ -point and two electron like bands around the M-points. Consequently, three hole FSs and two electron FSs are observed around the Γ and the M-point (Fig.5.6(c)) respectively. A small FS around X-point also appears due to Sb doping. Three hole like bands around the Γ -point (crossing the E_F) remain separated from each other above the E_F . Thus, the band edge singularity which is observed to play an important role in the superconductivity of Fe based superconductors [170], does not exist. Fig.5.6(b) shows the partial density of states of As in undoped and 5% Sb doped CaFeAs_2 . It is conspicuous that there is very small enhancement in partial DOS of As at the E_F in comparison to the undoped 112 compound. We will compare this observation with the rare earth (RE)/Sb co-doped compounds in the following discussions.

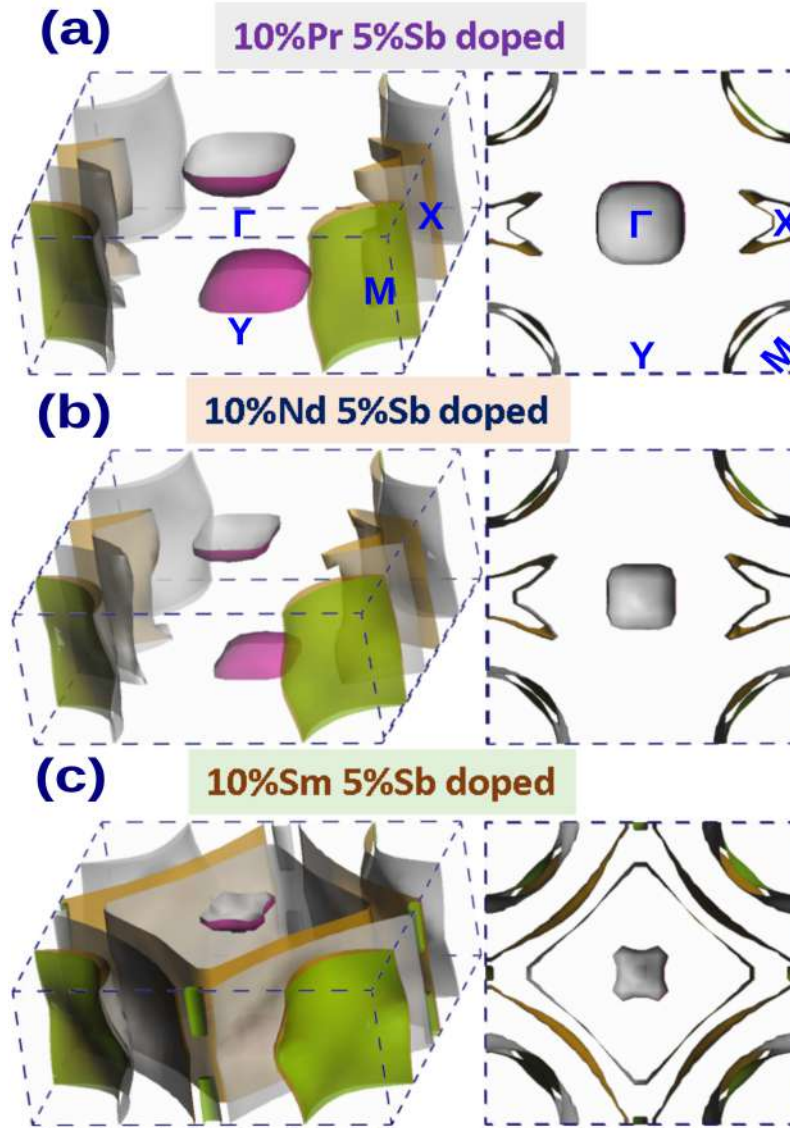


Figure 5.8: [140] Calculated FSs of $\text{Ca}_{0.90}\text{R}_{0.10}\text{Fe}(\text{As}_{0.95}\text{Sb}_{0.05})_2$ system for RE = (a) Pr, (b) Nd, (c) Sm. We have shown two different views of FS with same doping in a particular row.

In Fig.7.13(a),(b),(c), we have shown the band structures of $\text{Ca}_{0.90}\text{R}_{0.10}\text{Fe}(\text{As}_{0.95}\text{Sb}_{0.05})_2$ for RE = Pr, Nd, Sm respectively. We have discussed the electronic structure with only rare earth doping in [188]. From Fig.7.13(a) it is clearly visible that there are two electron like bands around M-point crossing the E_F , whereas three hole like bands near the E_F dip slightly below E_F in 10% Pr 5% Sb doped 112 compound. Consequently, the hole like FS at the Γ -point shown in Fig.7.14(a) vanishes and segregates into two parts. Theoretically, it has been shown that Sb doping at As-chain site act as low electron doping [187]. If we compare the FSs of the 10% Pr 5% Sb doped 112 compound with 10% Pr doped 112 IBSCs [188], it is visible that the FSs are quite similar *i.e.*, no hole like FS at the Γ -point and two electron like FSs around the M-point and one electron like FS around the X-point. Now if we look into the Fig.7.13(b), there are two electron like bands around the M-point crossing the E_F and three hole like bands slightly below the E_F . If we compare Fig.7.13(a) with Fig.7.13(b) three hole like bands are shifted slightly more away from the E_F in the later case. From Fig.7.14(a),(b) it is clear that the hole like FS around the Γ -point shrinks further and the electron like FSs around the M and X-point visibly grow in size in Nd/Sb doped compound in comparison to Pr/Sb doped cases. Fig.7.13(c) shows that the band structure of 112 compounds get modified by a large amount due to Sm/Sb doping. There are two electron like bands around the M-point crossing the E_F , but a new electron like band appears during Γ -M direction. One hole like band around Γ -point slightly touches the E_F giving rise to situation similar to a band edge van Hove singularity. From Fig.7.14(c) it is observable that the FSs also get largely modified due to Sm/Sb doping. The size of the electron like FSs around M-point surge further. Appearance of new electron FSs both at X-point and Y-point is visible. The hole like FS around the Γ -point shrinks further. So it is conspicuous that the modifications in the electronic structure in Sm/Sb doped case is quite distinct than other two cases. The nesting between the electron and hole like bands completely disappears, but substantial nesting between various electron FSs are possible.

From the above discussions it is palpable that RE/Sb doping has very prominent effect

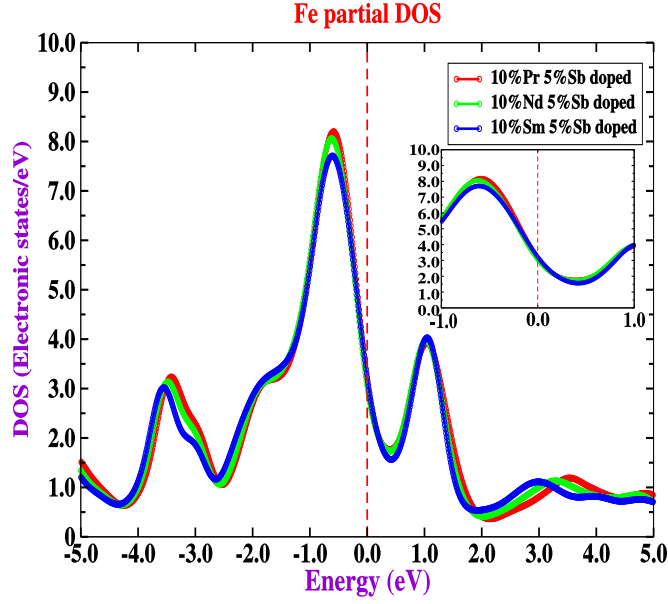


Figure 5.9: [140] Partial density of states of Fe with different RE/Sb doping at As chain. The magnified partial DOS of Fe at a smaller energy window is shown in the inset.

on the electronic structure of the 112 compounds which in turn should influence superconductivity. Although the modifications in the electronic structure are largely due to RE doping at the Ca site, Sb doping also plays a crucial role. We further continue our discussion about the effect of Sb doping on RE doped 112 compounds in the next section to verify its possible role in the enhancement of superconductivity.

5.4 Effect of RE/Sb doping on Fe partial DOS

While the phenomenon of superconductivity depends on many facts, the available electronic states at the E_F is one of the important one. Larger the DOS at the E_F , greater is the number of electronic states available for Cooper pairing. Therefore it is very important to look into the changes in DOS due to different doping. In Fig. 5.9 we have shown the atom projected partial DOS of Fe in $\text{Ca}_{1-x}\text{R}_x\text{Fe}(\text{As}_{1-y}\text{Sb}_y)_2$ for different RE/Sb co-doped 112. It is clear that the presence of different rare earth elements like Pr, Nd, Sm do not affect the Fe partial DOS. The value at the E_F remain almost same for all the RE doping. This signals to the fact that the electronic states derived from Fe, available for Cooper pairing

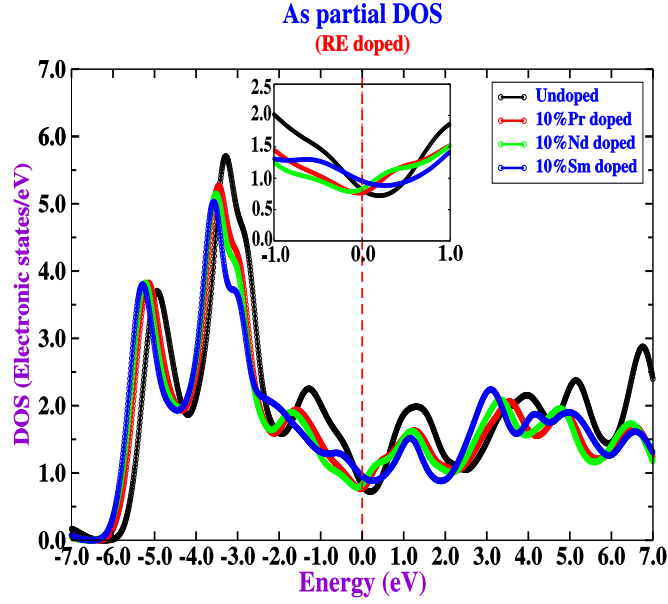


Figure 5.10: [140] Partial DOS of As in rare earth doped CaFeAs_2 . The magnified partial DOS of As at a smaller energy window is shown in the inset.

do not change due to Sb doping.

5.5 Effect of only RE or RE/Sb doping on As partial DOS

From the discussion about orbital projected band structure, it is clear that the bands near the E_F are not only derived from Fe-3d but also from As-4p orbitals. So we have investigated into the partial DOS of As. Fig.5.10 shows the change in partial DOS of As due to different RE doping at Ca site of CaFeAs_2 in absence of Sb doping at As-chain site. Value of partial DOS of As at the E_F does not change much due to different RE doping. Although the value is highest for Sm doping and lowest for Pr doping, but the net change is very small. For Nd doping As partial DOS at the E_F remain nearly same as undoped case. Thus it is perceptible that RE doping at Ca site rarely affects the electronic states at the E_F .

Now we will explore the effect of Sb doping on the partial DOS of As in different rare earth co-doped 112 compounds. It has been observed by experiments as well as theo-

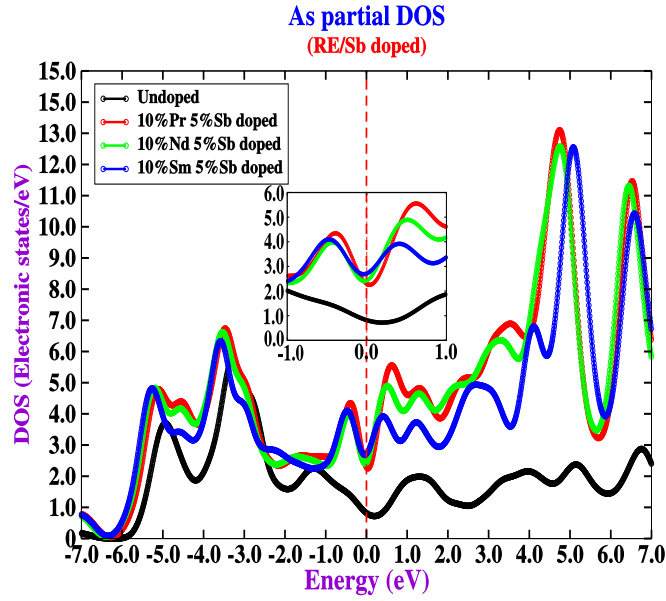


Figure 5.11: [140] Partial DOS of As in rare earth and Sb co-doped CaFeAs_2 . The magnified partial DOS of As at a smaller energy window is shown in the inset.

retically that Sb doping at As-chain is very effective in increasing critical temperature of La doped 112 compound even upto 47K. Therefore, it is very interesting to see if it can enhance the superconductivity in other rare earth doped compounds other than La. In Fig.5.11 we have shown the change in partial DOS of As due to Sb doping at As-chain in RE co-doped 112 Fe based superconductors. Sb doping at As-chain site clearly have a large impact on the partial DOS of As in 112 compounds. From Fig.5.11, it is evident that there is a surge in the value of As partial DOS at the E_F due to Sb doping. This implies that the increased As partial DOS at the E_F provides increased electronic states for Cooper pairing, enhancing the possibility of superconductivity in turn. Further, the surge in partial DOS of As is much greater in RE/Sb co-doped CaFeAs_2 than that of $\text{CaFe}(\text{As}_{0.95}\text{Sb}_{0.05})_2$ (Fig.5.6(b)). The atomic radius of Sb is 1.33\AA , higher than that of As 1.14\AA . This will cause chemical pressure on the FeAs-layer. The c-axis as well as distance between FeAs-layer and As-chain decrease significantly due to Sb doping. As a result of these effects the hybridization between different Fe-3d and As-4p orbitals increase to a significant amount. The Sb doping at As site of 112 compounds act as low electron doping [187]. As a consequence of these facts, the partial DOS of As at the

Fermi level increases. Another interesting fact is that the value of As partial DOS at E_F is maximum for Sm/Sb doped compound and minimum for Pr/Sb doped compound. The value for Nd/Sb doping remain intermediate. So there may be a possible preference of Sm doping over other RE doped compounds as far as the enhancement of superconductivity due to Sb doping is concerned.

Table 5.3: Variation of FeAs layer to As-chain distance, Z_{As} , and $\angle As - Fe - As$ with different doping

Doping	Layer to chain distance (Å)	Z_{As} (Å)	As-Fe-As angle (°)
10% Pr 5% Sb	4.866	1.239	106.76
10% Nd 5% Sb	4.788	1.232	106.578
10% Sm 5% Sb	4.676	1.243	107.109

We have also investigated the modifications in different structural parameters which are believed to impact superconductivity in iron based superconductors. A trend of FeAs layer to As-chain distance, anion height (Z_{As}) and As-Fe-As angle with RE/Sb doping calculated from the optimized structures are presented in Table.5.3. With the RE atom doping from Pr to Nd to Sm and Sb co-doping the layer to chain distance decreases from 4.866Å to 4.788Å to 4.676Å. Therefore, the overlap between Fe-3d and As-4p orbitals increases, making As-chain more conducting. The value of Z_{As} changes from 1.239Å to 1.232Å to 1.243Å for 112 compounds with Pr, Nd, Sm doping and Sb co-doping. Thus the value of Z_{As} is the highest for Sm/Sb doping. Although it is far from the optimal value (≈ 1.38 Å) for maximum T_c in IBSCs, it is closer than the other RE/Sb doped 112 compounds. Similarly, the As-Fe-As angle changes from 106.76° to 106.578° to 107.109° for Pr, Nd, Sm doped and Sb co-doped compounds respectively. The value of As-Fe-As angle in Sm/Sb doped 112 compound is closer to the optimal value ($\approx 109.47^\circ$) for maximum T_c in 1111 Fe based compounds [171]. Hence, Sm doping with Sb co-doping may be more favourable to superconductivity.

5.6 Discussions and Conclusions

We have systematically investigated the effect of rare earth and Sb co-doping on the electronic structure of 112 Fe based superconductors within density functional theory based first principles calculations. It is shown that if Sb is doped in place of As, then depending upon whether it is doped on chain or at the layer, the X-point electron FS diminishes or develops. There is no effect on the hole FS for Sb doping on FeAs layer but in contrary it is sensitive to Sb doping at chain. Our study on BNS and FS shows that the change in electronic structure due to Sm/Sb doping is more prominent than that for other two compounds. The hole like band around Γ -point show band edge van Hove singularity. The partial density of states of Fe at the E_F do not change significantly due to Sb doping. On the other hand, our calculations show a clear increase in the As partial density of states due to Sb doping at As-chain site of 112 iron pnictides. As increased partial DOS of As at E_F implies increased electronic states available for Cooper pairing, there may be an enhancement of superconductivity due to Sb doping in RE co-doped 112 compounds. From our results on density of states as well as different structural parameters it can be stipulated that there may be a possible preference of Sm doped 112 compounds over other rare earth doping for the enhanced superconductivity due to Sb doping.

Chapter 6

Chemical pressure induced orbital selective Lifshitz transition in hybrid 1144 compounds

In this chapter we have investigated the electronic structure of hybrid $\text{AeAFe}_4\text{As}_4$ known as, 1144 iron based superconductors (IBSC) for various $\text{Ae} = \text{Ca}, \text{Sr}, \text{Eu}$ and different alkali metals $\text{A} = \text{K}, \text{Rb}, \text{Cs}$. Like other iron based superconductors, these compounds are also found to be multi-orbital derived multi-band superconductors. But in contrast to the electronic structure of many of the Fe-based superconductors, significant contribution from $\text{As-}4p_z$ orbital and its mixing with $\text{Fe-}3d$ is revealed through our electronic structure investigations. Orbital selective electron/hole self-doping due to natural chemical pressure of higher/lower atomic (Ae/A) sizes of various members of 1144 family is very unique feature of the electronic structure of these compounds. It is disclosed that because of different chemical potential (self-doping) of different orbital derived electron/hole bands, some of them is pushed below the Fermi level (E_F), leading to orbital selective chemical pressure induced topological Lifshitz transition. This natural pressure induced orbital selective Lifshitz transition of hole bands is a distinctive characteristic of this family. The

effect of electron correlation (within DFT+U method) and spin-orbit coupling (incorporated using relativistic pseudopotentials) on the Lifshitz transition are also explored. The same conclusions as above about the Lifshitz like transition remains robust even in presence of moderate electron correlation and spin-orbit coupling. Bandwidths of different bands that crosses Fermi level around the Γ -point are evaluated. Different combinations of Ae and A in different 1144 materials cause changes in bandwidths to individual bands orbital selectively. A large value of bandwidths for most of the compounds including EuAF₄As₄ indicates weak correlation effect in these compounds.

6.1 Theory and Computational Method

We have performed calculations using plane wave pseudo potential method as implemented in Quantum Espresso [135], CASTEP [128] and VASP [172]. In our simulations the electronic exchange correlation is treated within the generalized gradient approximation (GGA) parametrized by Perdew-Burke-Enzerhof (PBE) functional [125]. Non-spin-polarized single point energy calculations were carried out for tetragonal phase with space group symmetry P4/mmm for all the 1144 iron based superconductors [41]. We have used experimentally available structures of the 1144 compounds to perform self consistent field calculations. The Kohn-Sham valence states are expanded in plane wave basis and kinetic energy is truncated at 45 Ry after performing rigorous convergence test. We also performed convergence test to sample the Brillouin zone (BZ) in k space and grid size for SCF calculation was set to $21 \times 21 \times 5$. The Convergence threshold on total energy (a.u) and forces (a.u) were fixed to 10^{-5} and 10^{-3} respectively for ionic minimization. Integration upto the Fermi surface has been made using the smearing technique with the smearing parameter 0.01 Ry. Results are verified using different numerical codes. The contribution of different orbitals onto FSs are shown using visualization tool Fermi surfer [173]. We have also incorporated both Hubbard parameter U and spin-orbit coupling (SO) in the calculations implemented in VASP, to take into account the electron correlation effect

(GGA+U) and the relativistic effect (GGA+U+SO) respectively.

6.2 Electronic structure of 1144 materials

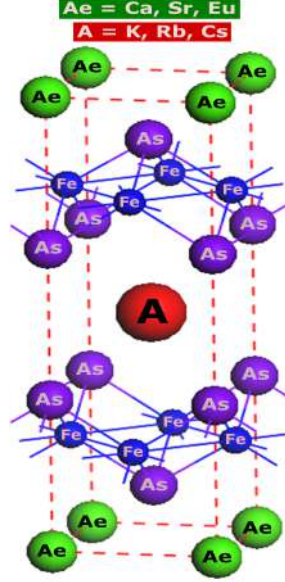


Figure 6.1: [141] Crystal structure of 1144 iron based superconducting materials.

We present the electronic structure of the undoped $\text{AeAFe}_4\text{As}_4$ ($\text{Ae} = \text{Ca}, \text{Sr}, \text{Eu}$) ($\text{A} = \text{K}, \text{Rb}, \text{Cs}$) materials to get an overall insight about the gradual modifications in the electronic structure of different members of 1144 family. From Fig.6.1 it is clearly visible that the A and Ae atoms are placed in the interstitial position between the FeAs layers alternately in case of 1144 compounds. If $\text{Ae} = \text{A}$, the crystal structure corresponds to that of the 122 family. The main aim in this section is to comprehensively demonstrate the orbital selective self doping and Lifshitz transition. This is achieved through three routes, demonstrating evolution of electronic band structure (BNS), Fermi surface (FS) and partial density of states (DOS), as one replaces K with Rb or Cs in various families of 1144 compounds. One of the most general and common features of electronic structure of all members of 1144 family are existence of six hole like bands around the zone centre Γ -point [174, 175] except for SrCs_{44} and EuCs_{44} compounds where five hole like bands and four electron like bands are found around zone corner M-point. Consequently six

hole like and four electron like FSs appear around the Γ -point and M-point respectively in most of the compounds. This should be contrasted with the same for 122 compounds [176]. The bands as well as FSs are of multiorbital character just like the constituent 122 compounds [177]. In case of EuCs44 and SrCs44 compounds the innermost hole like FS segregates into two parts leading to Lifshitz transition. Existence of different Ae and A makes two FeAs-layers inequivalent as well as there exists two inequivalent As-sites. One of the most striking difference in electronic structure of 1144 family in comparison to all other Fe-based materials except 112 family [178] is the existence of As states at the E_F and its hybridization with Fe-3d states.

6.2.1 $\text{CaAFe}_4\text{As}_4$ ($A = \text{K, Rb, Cs}$)

We present the electronic structure of the undoped $\text{CaAFe}_4\text{As}_4$ ($A = \text{K, Rb, Cs}$) to investigate the effect of substitution of alkali metal atoms of gradually increasing atomic radius on the electronic structure of these materials. All the calculations are performed using experimental lattice parameters with tetragonal structure [41, 42]. We have calculated detailed BNSs and FSs projected on different Fe-3d as well as As $4p_z$ orbitals to know the orbital nature of the bands and Fermi surfaces along major symmetric directions. We have also presented the partial density of electronic states to investigate the contributions of Fe-3d and As $4p_z$ orbitals to the electronic states at the E_F . Due to substitution of alkali metals in these compounds, a systematic modifications of the bands with an orbital selective shift near E_F takes place.

In Fig.6.2(a) we have shown the BNS of $\text{CaKFe}_4\text{As}_4$. We have resolved the orbital characters of different bands by projecting the atomic orbitals onto Kohn-Sham orbitals. In Fig.6.2(a) different colours and varying sizes of the circles are used to signify the orbital character and their weights respectively. Blue, olive, green, cyan, red and black colours have been assigned to signify the contribution of d_{yz} , d_{xz} , d_{xy} , $d_{x^2-y^2}$, $4p_z$ and d_{z^2} orbitals respectively. The colour scheme for different orbitals is kept same through out the paper.

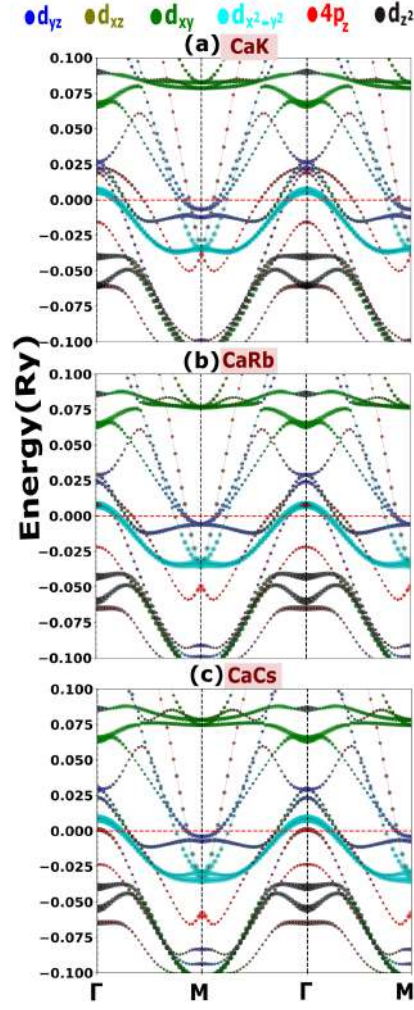


Figure 6.2: [141] Calculated orbital projected band structures of (a) $\text{CaKFe}_4\text{As}_4$, (b) $\text{CaRbFe}_4\text{As}_4$, and (c) $\text{CaCsFe}_4\text{As}_4$ around high symmetry points. The weight of the different Fe 3d and As 4p orbitals for different bands is shown with varying sizes of the circles and colours. Sizes of the circles correspond to degree of relative contributions. Fermi level is denoted by the horizontal green line at the zero energy.

Just like other iron based compounds, it is conspicuous that each band is of multi-orbital nature. We first describe the orbital characters of these hole like bands that cross the E_F around Γ point sequentially in energy from higher to lower. The top of the hole like bands that cross the E_F at around Γ -point with comparatively higher energies have very small energy differences between them (and are nearly energetically degenerate). The hole like bands around the Γ -point (top of which) having the highest energy is mainly derived from d_{z^2} , d_{yz} and $4p_z$ orbitals. The next two hole like bands (top of which are having sequentially lower energy) have mixed d_{xy} , d_{xz} character. There are two nearly degenerate hole

like bands close to the E_F , primarily derived from $d_{x^2-y^2}$ orbital. There exists another distinct hole like band near the higher energy band tops which is derived from the admixture of d_{z^2} and $4p_z$ orbitals. Now if we look at the electron like bands around the M-point that forms electron like FSs, it is quite clear that the two bands closest to the E_F have mixed $d_{x^2-y^2}$, d_{yz} and d_{z^2} character, bottom of which are energetically degenerate. The electron like band around the M-point, bottom of which is the farthest from E_F is primarily derived from $d_{x^2-y^2}$ orbital with very small contribution from As $4p_z$, whereas the band that forms the inner most electron FS around the M-point is mainly derived from $d_{x^2-y^2}$ as well as $4p_z$ orbitals. We have presented the electronic structure of the undoped $\text{CaRbFe}_4\text{As}_4$ which can be thought to be formed by replacing K with Rb in between the FeAs layers. We present the ensuing modifications in the electronic structure due to substitution of K by Rb. In Fig.6.2(b) we have presented the orbital resolved BNS of $\text{CaRbFe}_4\text{As}_4$. It is clearly visible that there are six hole like bands around Γ -point and four electron like bands at around M-points just like $\text{CaKFe}_4\text{As}_4$. Now we discuss about the effect of replacing alkali earth metals K or Rb with another element Cs. The BNS of $\text{CaCsFe}_4\text{As}_4$ is shown in Fig.6.2(c). Like the other two $\text{CaAFe}_4\text{As}_4$ (A= K, Rb) compounds, there are six hole like bands around Γ -point and four electron like bands at round M-points in this compound also. The multi-orbital nature of each band is clearly evident from BNS. The hole like band derived from d_{z^2} and $4p_z$ orbitals shifts below $d_{x^2-y^2}$ derived bands and its top almost touches the E_F . The lowest energy electron like bands around M-point has $d_{x^2-y^2}$ as the dominant orbital character with significant contributions from the d_{xz} , d_{yz} and $4p_z$ orbitals also.

One of the important significances of the change in size of electron or hole like FSs is that it denotes electron or hole doping. For example, a surge (decrease) in size (surface area) of hole like FS would indicate hole (electron) doping normally. The same for electron FS would correspond to electron (hole) doping. In this section, we shall establish that 1144 compounds are orbital selectively self-doped systems. Fig.6.3 provides overall nature of all FSs of 1144 family, contributions of different orbitals to the FSs are presented

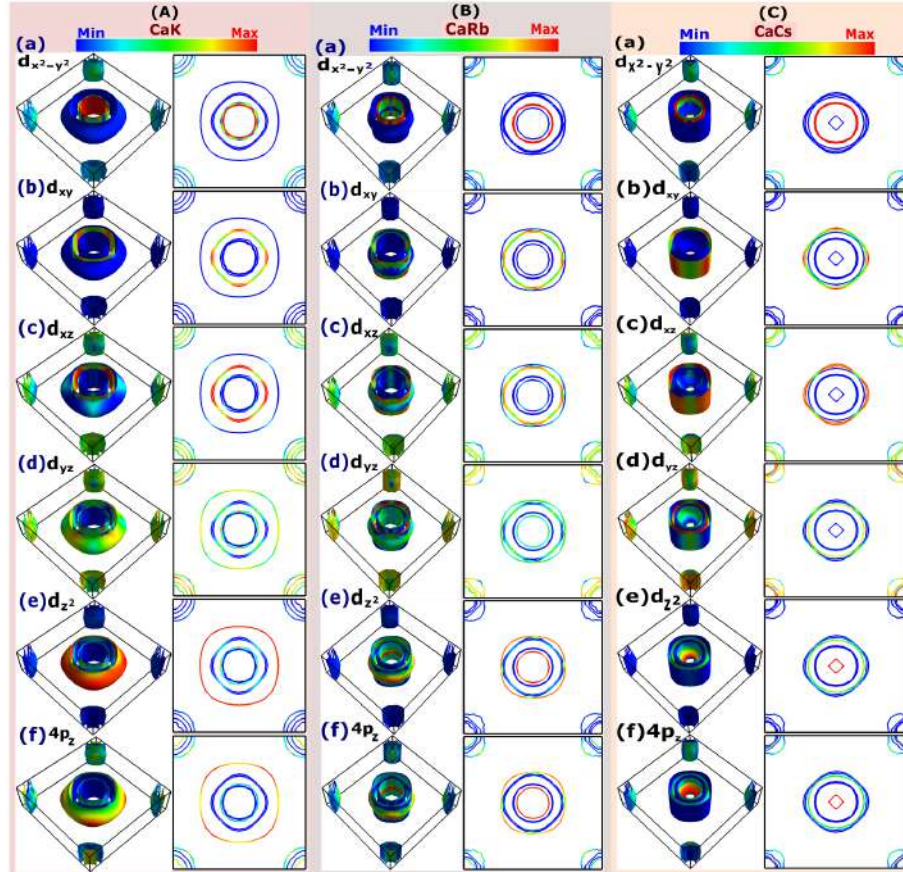


Figure 6.3: [141] Calculated orbital projected Fermi surfaces (FSs) on different Fe-3d and As- p_z orbitals for (A)CaKFe₄As₄, (B) CaRbFe₄As₄, and (C) CaCsFe₄As₄. The FSs are derived from (a) $d_{x^2-y^2}$, (b) d_{xy} , (c) d_{xz} , (d) d_{yz} , (e) d_{z^2} and (f) $4p_z$ orbitals. The colour scheme denotes increased contributions from different orbitals as we move from blue to red.

by colour intensity. The contributions of different orbitals to the FSs is denoted by the colour scheme where moving from blue region to red region indicates gradually increasing contributions of respective orbitals. The same colour scheme as above is used throughout the manuscript. In Fig.6.3(A) we have presented the orbital resolved FSs of CaKFe₄As₄. From Fig.6.3A(a), it is clearly visible that the $d_{x^2-y^2}$ orbital contributes mostly to the two innermost hole like FSs as well as substantially contributes to the third innermost hole like FS around the BZ centre. It also has substantial contribution to the outermost and innermost electron like FSs around the M-point. The contribution of d_{xy} and d_{xz} orbitals to the FSs are shown in Fig.6.3A(b) and Fig.6.3A(c) respectively. The electron like FSs seem to have a little contribution from d_{xy} orbitals whereas the d_{xz} orbital contributes significantly to them. The second outermost hole like FS around the BZ centre is mainly derived from d_{xz} and d_{xy} orbitals. The hole like FSs except the two innermost FSs as well as all the electron like FSs have significant amount of d_{yz} character (Fig.6.3A(d)). On the other hand, the d_{z^2} orbital contributes mostly to the outermost largest hole like FS (Fig.6.3A(e)). The $4p_z$ orbital contributes to the outermost hole like FS as well as to the innermost one and the outermost electron like FSs. The hole like bands around Γ -point are mainly concoction of d_{z^2} , d_{yz} , d_{xy} , d_{xz} , $d_{x^2-y^2}$ orbital derived bands with significant contribution from $4p_z$ orbital. The band with d_{z^2} and $4p_z$ orbital character lying between the lower and higher energy bands well above the E_F in case of CaRbFe₄As₄ shifts towards E_F when compared with that for CaK44. It now becomes almost degenerate with the $d_{x^2-y^2}$ derived bands lying near E_F . The electron like bands around M-point are mostly $d_{x^2-y^2}$, d_{yz} , d_{xz} , $4p_z$ derived with negligible contribution from d_{xy} and d_{z^2} orbitals. In Fig.6.3(B) we have presented FSs of CaRbFe₄As₄ with their respective orbital characters. The two dimensional (2d) cross section of the FSs clearly denote shrinkage of some of the hole like FSs while enhancement of others about BZ centre with respect to CaKFe₄As₄. The outermost larger hole FS shrinks in size. One or more electron like FS also shrinks. Thus, the topology of the FS changes significantly due to replacement of K by Rb that has higher ionic radius. Fig.6.3B(a) shows that the $d_{x^2-y^2}$ orbital mainly contributes to

the second and third innermost hole like FSs around the BZ centre. Like in $\text{CaKFe}_4\text{As}_4$ the $d_{x^2-y^2}$ orbital also has finite contribution to the outermost electron like FS around the BZ corner. The contributions of d_{xy} and d_{xz} orbitals to the FSs are shown in Fig.6.3B(b), (c) respectively. They contribute significantly to the second and third outermost hole like FSs. The electron like FSs seem to have a little contribution from the d_{xy} orbital whereas the d_{xz} orbital has finite contribution to them. Almost all the FSs except second and third innermost hole like FSs have significant amount of d_{yz} character (Fig.6.3B(d)). On the other hand, the d_{z^2} and $4p_z$ orbitals contribute mostly to the outermost and the innermost hole like FSs (Fig.6.3B(e),(f)). The innermost and the outermost electron FSs have significant $4p_z$ character. The orbital resolved FSs of $\text{CaCsFe}_4\text{As}_4$ are presented in Fig.6.3(C). The innermost and the outermost hole like FSs shrink while other FSs get bigger in size. Thus there is simultaneous orbital selective hole as well as electron self doping. One or more electron like FSs also shrink (and hence corresponds to hole-doping). Fig.6.3C(a) denotes that the $d_{x^2-y^2}$ orbital mainly contributes to the second and third inner hole like FSs around the BZ centre with significant contribution also to the outermost electron like FS around the BZ corners. Fig.6.3C(b), (c) show that the two outermost hole like FSs around the BZ centre are mainly derived from d_{xy} and d_{xz} orbitals. The d_{xz} orbital contributes significantly to the electron like FSs also. The third innermost hole like FS as well as almost all the electron like FSs have d_{yz} as dominant orbital character (Fig.6.3C(d)). On the other hand, d_{z^2} and $4p_z$ orbitals contribute mostly to the innermost hole like FS with finite contribution to the third outermost one (Fig.6.3C(e)). Further, the $4p_z$ orbital has significant contribution to the outermost electron like FS.

To investigate about the contributions of different Fe-3d orbitals to the electronic states at the E_F , we have also presented orbital projected partial density of states in Fig.6.4(a), (b), (c). It is quite distinct that the partial DOS of $d_{x^2-y^2}$ and d_{yz} orbitals are quite large as compared to other Fe-3d orbitals in all the three CaA44 compounds, whereas the As $4p_z$ and d_{xy} orbitals are having the lowest contribution at the E_F . The partial DOS of d_{yz} is found to be reduced as one substitutes K by Rb and then by Cs.

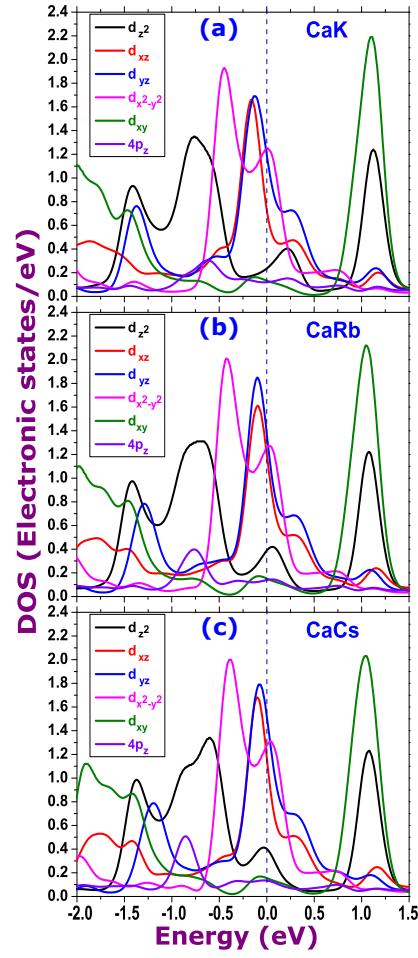


Figure 6.4: [141] Partial density of states of different Fe-3d and As-4p orbital derived states for (a) $\text{CaKFe}_4\text{As}_4$, (b) $\text{CaRbFe}_4\text{As}_4$, and (c) $\text{CaCsFe}_4\text{As}_4$. The Fermi level is denoted by the dotted blue vertical line at zero energy.

In this subsection we have discussed about the effect of replacing iso-electronic elements ($A = K [Ar]4s^1$, $Rb [Kr]5s^1$, $Cs [Xe]6s^1$) in between FeAs-layers of CaA44 compounds. Our studies on electronic structure reveal that the d_{z^2} and As- $4p_z$ derived hole like bands at around the Γ -point shifts towards the E_F (about to move below the E_F) as we replace alkali metals with higher atomic number and size (Fig.6.2). On the contrary, the two nearly degenerate bands derived from $d_{x^2-y^2}$ orbital shifts above the E_F towards higher energy. Thus, replacing K with Rb or Cs acts as electron self-doping for d_{z^2} and As- $4p_z$ derived band whereas hole doping for $d_{x^2-y^2}$ derived bands. Similar feature also emerges with the electron like bands around the M-point as well. The electron like bands shift towards E_F signifying hole doping for them. Thus the 1144 family of Fe based superconductors are rare examples of simultaneous orbital selective electron or hole self doped systems. This aspect of orbital selective self-doping, is further clarified by demonstrating the behavior of partial density of states of different orbitals at the E_F (Fig. 6.4) as one substitutes K with Rb or Cs. From the partial DOS of $d_{x^2-y^2}$ derived states, it appears as if the E_F shifted towards occupied states as K is replaced with Rb or Cs. This is thus example of hole self-doping as far as the $d_{x^2-y^2}$ - states are concerned. On the other hand, for the case of d_{xz} , d_{yz} , d_{z^2} partial DOS, it seems as if the E_F is moving towards unoccupied states as one replaces K with Rb or Cs, indicating electron doping to these orbital derived bands.

The evolution of orbital character of FSs is also very interesting. Due to orbital selective hole doping the two inner $d_{x^2-y^2}$ derived hole like FSs for CaK44 grow in size and contribute to the second and third inner hole FSs in case of CaRb44 and CaCs44 (Fig. 6.3A(a),B(a),C(a)). The innermost hole like band gets d_{z^2} and $4p_z$ character by virtue of orbital selective heavy electron doping to these bands. All the other orbital derived FSs shrink also along with modifications in orbital characters. Therefore, we have demonstrated an unique example of orbital selective electron/hole self-doping for 1144 family of Fe based superconductors. Most of the well established 122 Fe-based superconductors show superconductivity only after doping with certain amount of electron or hole. However, the 1144 (which are just mixtures of two 122 systems, in certain sense) fam-

ily superconductors show superconductivity without doping – this is probably because of the intrinsic nature of electronic structure of 1144 family that are orbital selectively self doped (OSSD) systems.

6.2.2 SrAFe₄As₄ (A = K, Rb, Cs)

Now we will look into another 1144 IBSC where the alkaline earth metal Ca is just replaced by another isovalent element Sr. First we will discuss about the electronic structure of SrKFe₄As₄ which is not still experimentally synthesized. However, it is predicted theoretically to be stable and a potential 1144 Fe based superconducting compound [179]. It is worth investigating the effect of different alkali metals (K, Rb, Cs) on electronic structure of these compounds that are predicted to be stable.

In Fig.6.5(a) we have shown the BNS of SrKFe₄As₄. We have resolved the orbital characters of different bands by projecting the atomic orbitals onto Kohn-Sham orbitals. It is conspicuous that the bands have multi-orbital character. The hole like bands around the Γ -point crossing the E_F are admixtures of different Fe-3d and As-4p orbitals. The contribution from $d_{x^2-y^2}$ orbital to the hole like bands is mainly to the lower energy bands just above the E_F . The hole like band primarily derived from d_{z^2} and $4p_z$ orbital is just below the $d_{x^2-y^2}$ derived bands nearest to the E_F . The upper lying flat bands in case of CaA44 compounds become sharper in SrK44 compound. Now analyzing the electron like bands around the M-point, $d_{x^2-y^2}$ seems to be the dominant orbital character of most of the bands with appreciable contributions from the d_{xz} and d_{yz} orbitals. But in comparison to CaK44 compounds, the inner most band around M-point mainly derived from $d_{x^2-y^2}$ and $4p_z$ orbitals shift towards the E_F . Also, the $d_{x^2-y^2}$, d_{z^2} , d_{yz} derived bands near E_F shift closer to the E_F . Now we investigate the effect of replacing alkali metal K with Rb in SrAFe₄As₄. In Fig.6.5(b) we have shown the BNS of SrRbFe₄As₄. Just like SrKFe₄As₄, there are six hole like bands around the Γ -point and four electron like bands at around the M-points with multi-orbital character. The hole like band derived from d_{z^2} and $4p_z$ orbitals touches

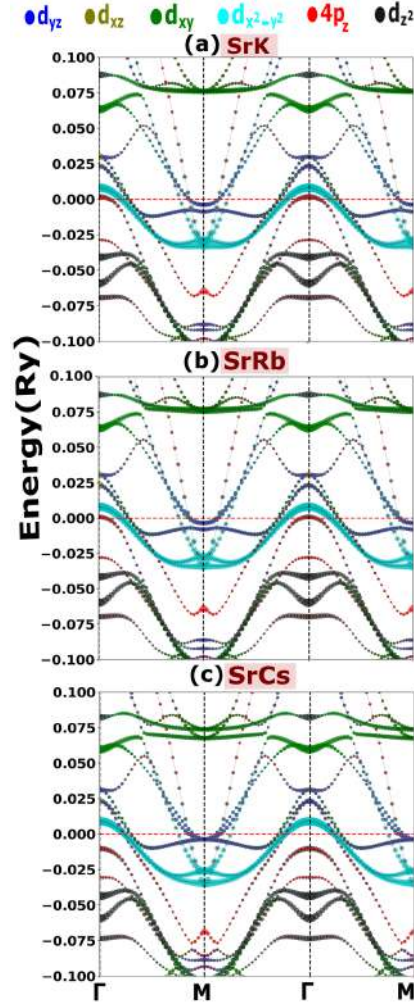


Figure 6.5: [141] Calculated orbital projected band structures of (a) $\text{SrKFe}_4\text{As}_4$, (b) $\text{SrRbFe}_4\text{As}_4$, and (c) $\text{SrCsFe}_4\text{As}_4$ around high symmetry points. The weight of the different Fe 3d and As 4p orbitals for different bands is shown with varying size of the circles and colours. Sizes of the circles correspond to degree of relative contribution. Fermi level is denoted by horizontal green line at zero energy.

the E_F . The $d_{x^2-y^2}$ orbital has emerged as one of the dominant characters of the electron like bands with significant contributions also from the d_{xz} and d_{yz} orbitals. But the inner most band around the M-point is mainly derived from $4p_z$ and $d_{x^2-y^2}$ orbitals. Now we will check the effect of replacing Rb with Cs in SrA44 compounds. In Fig. 6.5(c), we present the BNS of $\text{SrCsFe}_4\text{As}_4$. There are five (in contrast to six in other compounds) hole like bands around Γ -point and four electron like bands at round M-points crossing the E_F . This is because of orbital selective Lifshitz transition. The hole like band nearest to the E_F having $4p_z$ and d_{z^2} character in case of SrRb44 moves well below the E_F for

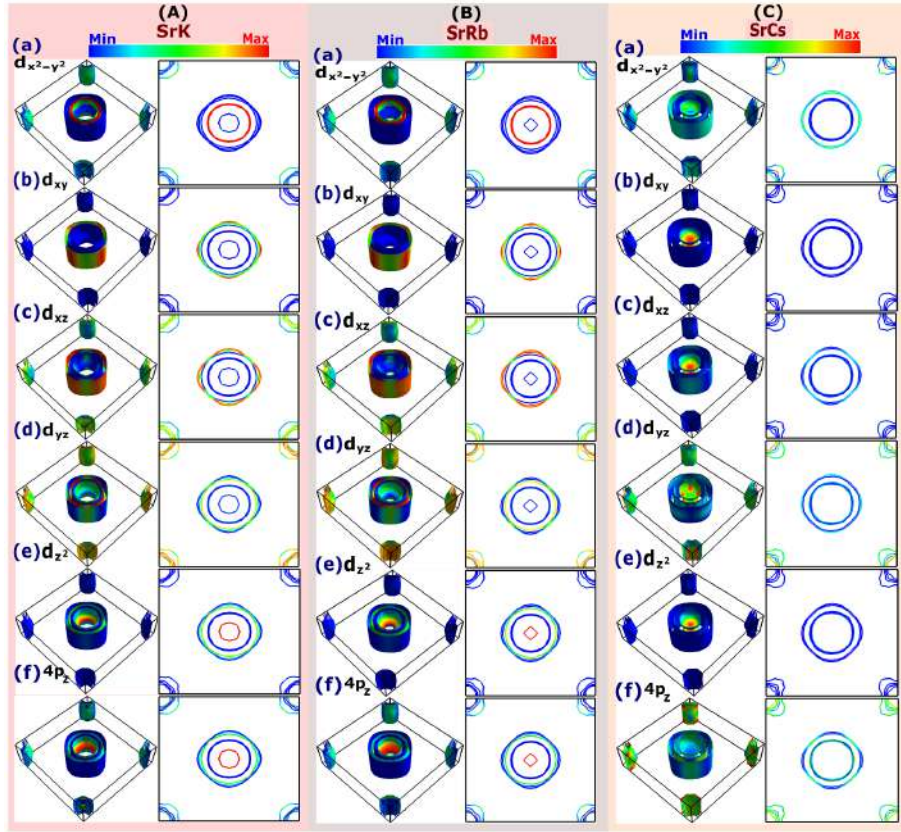


Figure 6.6: [141] Calculated projected Fermi surfaces (FSs) on different Fe-3d and As- p_z orbitals for (A) SrKFe₄As₄, (B) SrRbFe₄As₄, and (C) SrCsFe₄As₄. The FSs are derived from (a) $d_{x^2-y^2}$, (b) d_{xy} , (c) d_{xz} , (d) d_{yz} , (e) d_{z^2} , and (f) $4p_z$ orbitals. The colour scheme denotes increased contribution from different orbitals as we move from blue to red.

SrCs44. This corresponds to a Lifshitz like topological transition [180]. The bands having $d_{x^2-y^2}$ nature shift slightly away from the E_F . The contributions of d_{z^2} , d_{xy} , d_{xz} orbitals to the hole like bands remain very small. Another important modification to note is that the electron like bands near the E_F shift nearer to E_F .

In Fig.6.6(A) we present the angular momentum resolved FSs of SrKFe₄As₄. In comparison to the FSs of CaA44 compounds, there are distinctly visible changes in FS topology of SrKFe₄As₄. From the 2D cross section of the FSs through Γ and M-points, it is evident that the innermost hole like FS at the Γ -point comparatively shrinks in case of SrKFe₄As₄. The volume of the outermost hole like FS also decreases. The shape of the electron like FSs also undergoes changes significantly. From Fig.6.6A(a), it is evident that the second and third innermost hole like FSs around the BZ centre and the outermost electron like FSs are primarily derived from $d_{x^2-y^2}$ orbital. In contrast to the nature of orbital character in CaK44, the two outermost hole like FSs are derived from d_{xy} and d_{xz} (Fig.6.6A(b), (c)). The innermost and third outermost hole like FSs have mostly d_{z^2} and $4p_z$ orbital character (Fig.6.6A(e), (f)). The d_{yz} and d_{xz} orbitals contribute significantly to the electron like FSs (Fig.6.6A(c), (d)). The orbital character of FSs for SrRb44 is presented in Fig.6.6(B). All the hole like FSs around the Γ -point become almost cylindrical. If we compare the FS of this compound with CaRb44 compounds, it may be noted that the innermost hole like FS present at Γ point shrinks and become more 3d type (Fig.6.6A(a)). Fig.6.6B(a), clearly demonstrates that the $d_{x^2-y^2}$ orbital mainly contributes to the second and third innermost hole like FSs around the BZ centre with a small contribution to the electron like FSs. The contributions of d_{xy} and d_{xz} orbitals to the FSs are shown in Fig.6.6B(b), (c) respectively. Like SrK44 the two outermost hole like FSs around the BZ centre primarily have d_{xy} and d_{xz} orbital character. The d_{xz} orbital also have significant contribution to all electron like FSs. The third innermost and all the electron like FSs have d_{yz} as dominant orbital character (Fig.6.6B(d)). The innermost hole FS is mainly derived from d_{z^2} and $4p_z$ orbitals (Fig.6.6B(e), (f)). The hole FSs in SrCs44 become more cylindrical with reduction in FS volume (Fig.6.6C). Thus the change in the topology of the FSs is more prominent in

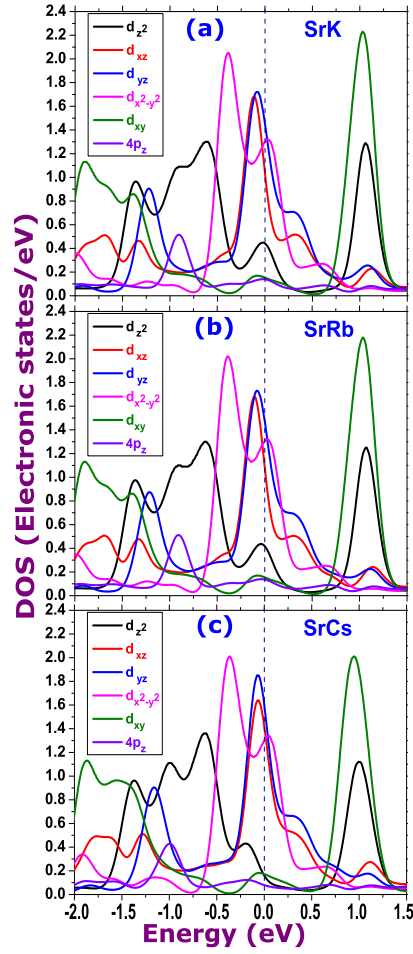


Figure 6.7: [141] Partial density of states of different Fe-3d and As-4p orbital derived states for (a) SrKFe₄As₄, (b) SrRbFe₄As₄, and (c) SrCsFe₄As₄. The Fermi level is denoted by dotted blue vertical line at zero energy.

comparison to SrRb44. The 2d cross section of FS in Fig.6.6C(a) clearly demonstrates that the innermost hole like FS around the Γ -point (in case of SrRb44) disappears. As one moves horizontally in Fig.6.6(C), there is topological modifications of FSs (inner most as well as outermost ones). The $d_{x^2-y^2}$ character of the hole FSs is reduced. The contributions of d_{xy} and d_{xz} orbitals to the FSs is reduced by a large amount (shown in Fig.6.6C(b), (c)) except for the innermost hole like FS. The d_{xz} character of electron like bands also drops down significantly. There exists finite d_{yz} character to the electron as well as hole like FSs (Fig.6.6C(d)). On the other hand, the contribution of d_{z^2} orbital to the FSs almost vanishes (Fig.6.6C(e)). But the $4p_z$ orbital character of the electron and hole FSs remain significant.

To investigate the contribution of different Fe-3d orbitals to the electronic states at the E_F , we present the partial density of states of various orbitals in Fig.6.7(a), (b), (c). The partial angular momentum-projected DOS for $d_{x^2-y^2}$ and d_{yz} , d_{xz} orbitals are substantially larger than that for other Fe-3d orbitals with d_{xy} and $4p_z$ having the lowest contribution at the E_F . This is also similar to the CaA44 compounds. Partial DOS of the d_{xz} orbital at the E_F is enhanced significantly in case of SrCs44 in comparison to that of the SrK44 or SrRb44 compounds. Another important observation is that the partial DOS of d_{z^2} orbital reduces significantly at the E_F as its peak shifts away from the E_F to the lower energy in SrCs44. This is also a signature of Lifshitz transition.

Above we have discussed mainly about the effect of replacing iso-electronic elements ($A = K [Ar]4s^1$, $Rb [Kr]5s^1$, $Cs [Xe]6s^1$) in between the FeAs-layers with further substitution of Ca ($[Ar]4s^2$) with Sr ($[Kr]5s^2$). Comparing Fig.6.2(a) with Fig.6.5(a), a shift of d_{z^2} and As- $4p_z$ derived bands around the Γ -point towards E_F and a shift of $d_{x^2-y^2}$ bands away from the E_F towards higher energy due to replacement of Ca with Sr are visible. From Fig.6.4(a) and Fig.6.7(a) it is clear that there is a visible decrement of $d_{x^2-y^2}$ partial DOS with its peak being shifted towards unoccupied states whereas the E_F shifts towards occupied states, hence corresponds to hole doping. The innermost d_{z^2} and As- $4p_z$ derived electron like band around the M-point also shifts below E_F whereas other electron like bands shift towards E_F (Fig.6.5). These clearly indicates orbital selective hole doping to $d_{x^2-y^2}$ bands and electron doping to d_{z^2} and As- $4p_z$ derived bands due to Sr substitution. This feature of orbital selective self-doping is further enhanced with substitution of K with Rb or Cs. Fig.6.5(b), (c) show that the d_{z^2} and As- $4p_z$ derived hole like band at around Γ -point shifts further towards E_F as we replace alkali metals with higher atomic numbers in between the FeAs-layers. On the contrary, the two nearly degenerate bands derived from $d_{x^2-y^2}$ orbital shifts slightly away from E_F . Thus, replacing K with Rb or Cs acts as electron doping for d_{z^2} and As- $4p_z$ derived bands whereas as hole doping for $d_{x^2-y^2}$ derived bands. Thus there is a clear indication of orbital selective electron/hole self-doping for 1144 compounds. If we look into the partial DOS of $d_{x^2-y^2}$ derived states, the

peak shifts towards the unoccupied states from E_F as K is replaced with Rb or Cs (Fig. 6.7). The decreasing partial DOS with E_F shift clearly signifies hole doping for $d_{x^2-y^2}$ derived bands. The trend in modifications of FSs also establish the same conclusion. The $d_{x^2-y^2}$ derived FSs grow in size whereas the volume of all other orbital derived FSs shrink (Fig. 6.6). Thus in this subsection we have demonstrated examples of orbital selective simultaneous electron or hole doping.

6.2.3 EuAFe₄As₄ (A = K, Rb, Cs)

We present the electronic structure of undoped EuAFe₄As₄ (A = K, Rb, Cs). This kind of 1144 family is basically quite different from other families because there is a rare earth element Eu instead of alkaline earth metals (Ca, Sr). We will investigate the modifications in electronic structure due to replacing alkaline earth with rare earth atom. The compound EuKFe₄As₄ is also not still experimentally synthesised, but theoretically predicted to be stable[179].

In Fig.6.8(a) we have shown the BNS of EuKFe₄As₄. Like other 1144 compounds the bands are of multi-orbital character. The BNS is nearly similar to other 1144 compounds. The two hole like bands with $d_{x^2-y^2}$ orbital character remain almost degenerate in this case also. The hole band with mixed d_{z^2} and $4p_z$ character remain just below the $d_{x^2-y^2}$ derived bands, closer to the E_F . Now if we look into the electron like bands around M-point, it is quite clear that the $d_{x^2-y^2}$ has the largest contribution to the bands with significant contributions from the d_{xz} , d_{yz} orbitals. We present the electronic structure of the undoped EuRbFe₄As₄ in Fig.6.8(b) which is formed by just replacing K with Rb. We will investigate the modifications in electronic structure by replacing K with Rb. A close look into the hole like bands reveals degenerate nature of the two $d_{x^2-y^2}$ derived bands. The band with d_{z^2} , $4p_z$ character shifts towards the E_F . The electron like bands near E_F are mainly derived from $d_{x^2-y^2}$, d_{yz} and d_{z^2} orbitals. They become more distinct and flat in comparison to other compounds. The $4p_z$ orbital mainly contribute to the inner most band

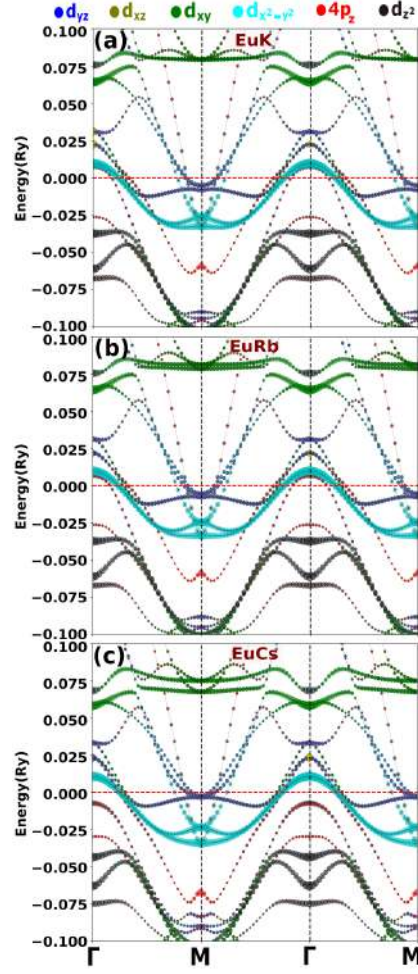


Figure 6.8: [141] Calculated orbital projected band structures of (a) $\text{EuKFe}_4\text{As}_4$, (b) $\text{EuRbFe}_4\text{As}_4$, and (c) $\text{EuCsFe}_4\text{As}_4$ around high symmetry points. The weight of the different Fe 3d and As 4p orbitals for different bands is shown with varying size of the circles and colours. Sizes of the circles correspond to degree of relative contribution. Fermi level is denoted by horizontal green line at zero energy.

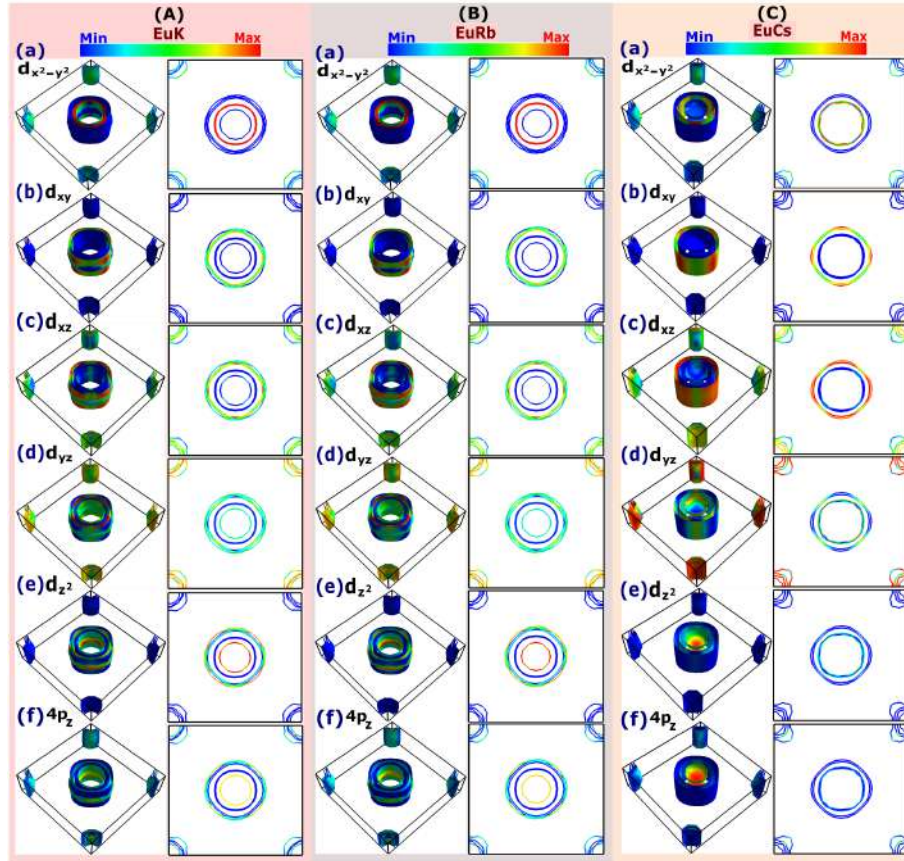


Figure 6.9: [141] Calculated projected Fermi surfaces (FSs) on different Fe-3d and As- p_z orbitals for (A) EuKFe₄As₄, (B) EuRbFe₄As₄, and (C) EuCsFe₄As₄. The FSs are derived from (a) $d_{x^2-y^2}$, (b) d_{xy} , (c) d_{xz} , (d) d_{yz} , (e) d_{z^2} , and (f) $4p_z$ orbitals. The colour scheme denotes increased contribution from different orbitals as we move from blue to red.

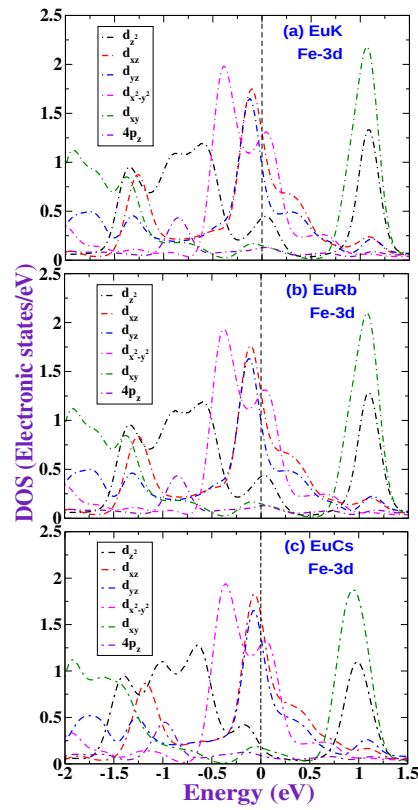


Figure 6.10: [141] Partial density of states of different Fe-3d and As-4p orbital derived states for (a) EuKFe₄As₄, (b) EuRbFe₄As₄, and (c) EuCsFe₄As₄. The Fermi level is denoted by dotted blue vertical line at zero energy.

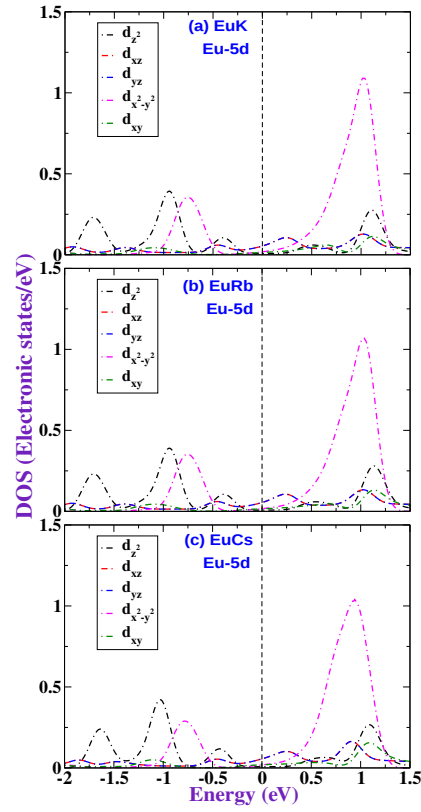


Figure 6.11: [141] Partial density of states of different Eu-5d orbital derived states for (a) $\text{EuKFe}_4\text{As}_4$, (b) $\text{EuRbFe}_4\text{As}_4$, and (c) $\text{EuCsFe}_4\text{As}_4$. The Fermi level is denoted by dotted blue vertical line at zero energy.

around M-point. The 4f bands/states are very much away from the E_F in agreement with earlier work [181]. Now we will discuss the electronic structure of undoped $\text{EuCsFe}_4\text{As}_4$ to investigate the effect of replacing Rb with isoelectronic Cs having higher atomic radius. In Fig.6.8(c) we have shown the BNS of $\text{EuCsFe}_4\text{As}_4$. Like other 1144 compounds the bands are of multi-orbital character. The hole like band around the Γ -point above E_F derived from d_{z^2} and $4p_z$ orbitals shifts below the E_F inducing Lifshitz transition. Now, if we look at the $d_{x^2-y^2}$ derived hole like bands both the bands slightly shifts towards higher energy above the E_F . It is quite clear that $d_{x^2-y^2}$ has large contribution to most of the electron like bands around M-point with some contributions from the d_{xz} , d_{yz} , d_{z^2} orbitals. Electron like bands with d_{yz} , d_{z^2} and $d_{x^2-y^2}$ character moves closer to the E_F .

The contributions of different Fe-3d and Eu-5d orbitals to the electronic states at E_F is also presented through the orbital projected partial density of states in Fig.6.10(a), (b), (c) and Fig.6.11(a), (b), (c). It is conceivable that the partial DOS of Fe-3d $d_{x^2-y^2}$ and d_{yz} , d_{xz} orbitals are quite large in comparison to that for the other Fe-3d orbitals and the As-4 p_z orbitals having the lowest contribution at the E_F . The partial DOS of Eu-5d states at the E_F is very small for these compounds (Fig.6.11(a)). Only Eu $d_{x^2-y^2}$ orbital have significant contribution to DOS at slightly above the E_F . The peak of $d_{x^2-y^2}$ partial DOS slides slightly towards the E_F for EuRb_4As_4 and EuCs_4As_4 in comparison to EuK_4As_4 . Fig.6.11(c) reveals an increased contribution of Fe-3d d_{xz} states to the partial DOS at E_F due to replacement of K or Rb with Cs.

The orbital resolved FSs of $\text{EuKFe}_4\text{As}_4$ is shown in Fig.6.9(A). The FS topology of this compound is just like other 1144 compounds. From Fig.6.9A(a), it is quite evident that the $d_{x^2-y^2}$ orbital mainly contributes to the second and third inner hole like FSs around the BZ centre, with finite contribution to all the electron like FSs around the BZ corner. The innermost hole like FS at around Γ -point are primarily derived from d_{z^2} and $4p_z$ orbitals with small contribution from d_{yz} also (Fig.6.9A(d), (e), (f)). The d_{xz} , d_{yz} orbitals contribute significantly to the electron like FSs around BZ corner with significant benefaction to

outer hole FSs. We present the orbital resolved FSs of $\text{EuRbFe}_4\text{As}_4$ in Fig.6.9(B). The FSs are very similar to that for EuK44 . The hole like FSs at around Γ -point are primarily derived from $d_{x^2-y^2}$, d_{xz} and d_{z^2} orbitals with a small d_{yz} orbital character (Fig.6.9B(a), (b), (c), (d)). The d_{yz} and d_{xz} are also the primary orbital characters of the electron FSs around M-point with a small contribution from $d_{x^2-y^2}$. The orbital resolved FSs of $\text{EuCsFe}_4\text{As}_4$ is shown in Fig.6.9(C). From 2d cross section of FSs along Γ and M-point, it is quite clear that the innermost hole like FS that are present in the previous cases around Γ -point, vanishes due to replacement of Rb with Cs leading to Lifshitz transition. From Fig.6.9C(a), (d), (e), it is distinct that the $d_{x^2-y^2}$, d_{yz} and d_{z^2} orbitals mainly contribute to the inner hole like FSs. The outer hole like FSs at around Γ -point are primarily derived from d_{xy} and d_{xz} orbitals (Fig.6.9C(b), (c)). The d_{xz} , d_{yz} orbitals contribute significantly to the electron like FSs around BZ corner also. The $4p_z$ orbital contribute to the inner most hole like FS.

In the previous two sub-sections we have mainly discussed in detail the electronic structures of various family members of 1144 Fe-based superconducting materials which is equivalent to discussing about the effect of substitution of isoelectronic elements on the electronic structure. Here we have also discussed about the modifications in electronic structure due to Eu ($[\text{Xe}]4f^76s^2$) which serves as more than isoelectronic substitution. Due to replacement of K with Rb or Cs, the d_{z^2} and As- $4p_z$ derived band around Γ -point is pushed towards E_F . Thus there is a clear signature of electron doping to the d_{z^2} and As- $4p_z$ derived band. The shift in the $d_{x^2-y^2}$ band is just opposite to that of d_{z^2} which means hole doping to $d_{x^2-y^2}$ derived bands. Modifications in the electronic structure due to substitution of K with Rb or Cs, discussed in Fig.6.8(b), (c) show that the d_{z^2} and As- $4p_z$ derived hole like band at around Γ -point shifts slightly towards E_F for EuRb44 . On the other hand, the electron like bands derived from d_{xz} and d_{yz} orbital below the E_F shifts slightly towards it. Fig.6.10 also shows that there is slight decrease in partial DOS of $d_{x^2-y^2}$. Substitution of K or Rb with Cs modifies the electronic structure to a large extent. The d_{z^2} and As- $4p_z$ derived hole like band is pushed far away from the E_F , whereas both

the $d_{x^2-y^2}$ derived band slightly shift towards higher energy. The electron like bands shift towards the E_F . A closer look at the partial DOS of $d_{x^2-y^2}$ derived states suggests that a clear visible peak shift with respect to the E_F as K is replaced with Rb or Cs (Fig. 6.10). On the contrary, there is an appreciable amount of reduction in the partial DOS of d_{z^2} for EuCs44. The volume of the $d_{x^2-y^2}$ derived hole like FSs grow whereas d_{z^2} and $4p_z$ derived FSs shrink. Therefore, there is orbital selective self-doping in 1144 compounds. It is self-doping because none of the compounds are actually doped, they all are parent compounds that are superconductors. It is 'orbital selective' because of two reasons; (i) amount of doping is different for different orbital derived bands, *e.g.*, d_{z^2} - $4p_z$ bands generally undergo Lifshitz transition (see also below) due to large electron doping, (ii) whereas $d_{x^2-y^2}$ bands get hole doped but with smaller movement with respect to the E_F . All the above calculations for EuA44 have also been performed within GGA+U, considering ferromagnetic arrangement of the Eu spins. The low energy band structures calculated using GGA+U do not alter to appreciable amount as compared to the GGA calculations. Recent calculations also indicate very small modifications in the low energy electronic structure due to very large U to Eu-4f [182]. We have discussed our calculations using GGA+U and spin orbit coupling in Section-V.

We discuss here general existence of orbital selective nesting. From Fig.6.3, 6.6, 6.9 it is clear that unlike many IBSCs where d_{xz} and d_{yz} contribute mostly to hole like FSs around Γ -point as well as electron like FSs around M-point, the contribution of $d_{x^2-y^2}$ or d_{z^2} orbital is also large. Thus intra-orbital nesting of these FSs will also play an important role to determine the gap symmetry. Both the d_{xz} and d_{yz} orbitals contribute strongly to the outer hole like FSs as well as all the electron like FSs (Fig.6.3,6.6,6.9). Therefore, it is conceivable that there exists a strong intra-orbital inter-band nesting between d_{xz} and d_{yz} orbital derived hole and electron like FSs. However, due to two nearly degenerate hole like bands with $d_{x^2-y^2}$ character, there exist a strong intra-orbital intra-band nesting also. The $d_{x^2-y^2}$ orbital derived FSs also show some amount of intra-orbital inter-band nesting. The nesting for d_{z^2} orbital derived FSs is predominantly intra-band type for all the

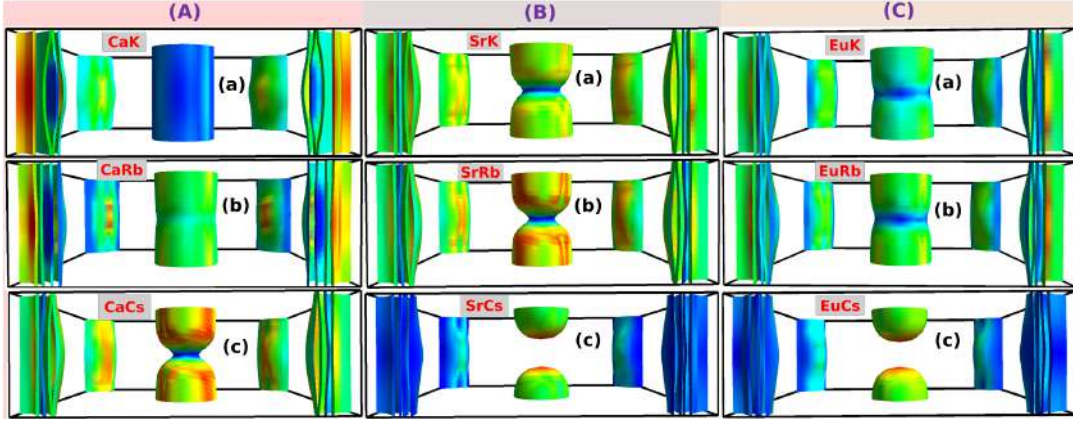


Figure 6.12: [141] The evolution of inner most hole-like Fermi surface and electron-like Fermi surfaces for different 1144 compounds - **A:** (a) $\text{CaKFe}_4\text{As}_4$, (b) $\text{CaRbFe}_4\text{As}_4$, (c) $\text{CaCsFe}_4\text{As}_4$, **B:** (a) $\text{SrKFe}_4\text{As}_4$, (b) $\text{SrRbFe}_4\text{As}_4$, (c) $\text{SrCsFe}_4\text{As}_4$, **C:** (a) $\text{EuKFe}_4\text{As}_4$, (b) $\text{EuRbFe}_4\text{As}_4$, and (c) $\text{EuCsFe}_4\text{As}_4$.

compounds as the contribution of this orbital to the electron like FS is almost negligible. As the nesting between the electron and hole like FSs enhance repulsive inter-band interaction, this might lead to s^\pm symmetry of the superconducting gap in all the 1144 compounds which is consistent with the experiments for CaK44 [183] but yet to be confirmed for all other compounds experimentally. The above discussion about the Fermi surface nesting gives us only a qualitative understanding about superconductivity. For better apprehension regarding superconductivity and pairing symmetry in Fe based compounds one should always look at multiorbital spin susceptibility and multiband version of the coupled linearized BCS equation to evaluate superconducting gap on the different Fermi surface pockets [184]. A detailed study examining the possibility of superconducting instability on these facts are already available in [185] and hence it is beyond the scope of our present paper.

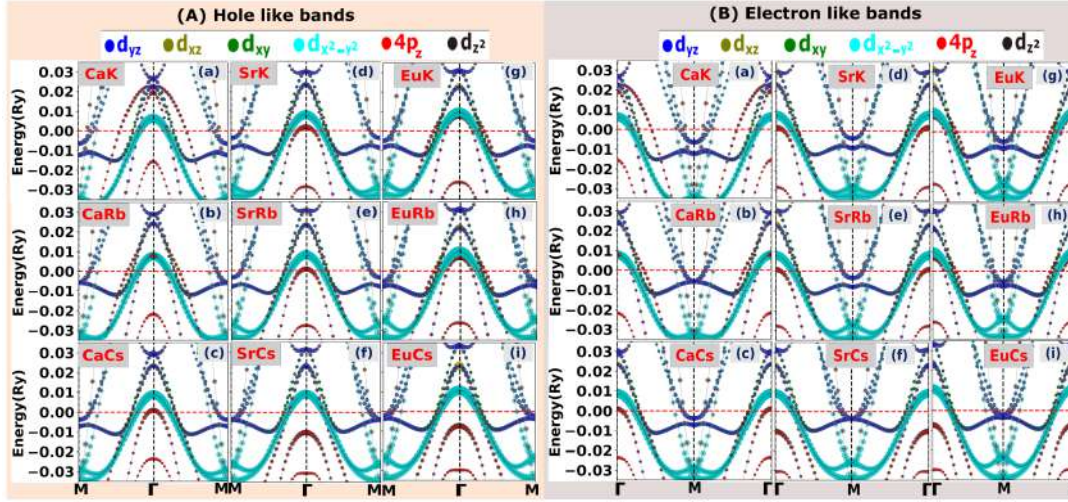


Figure 6.13: [141] The evolution of (A) hole-like bands around Γ -point and (B) electron-like bands around M-point for different 1144 compounds - (a) $\text{CaKFe}_4\text{As}_4$, (b) $\text{CaRbFe}_4\text{As}_4$, (c) $\text{CaCsFe}_4\text{As}_4$, (d) $\text{SrKFe}_4\text{As}_4$, (e) $\text{SrRbFe}_4\text{As}_4$, (f) $\text{SrCsFe}_4\text{As}_4$, (g) $\text{EuKFe}_4\text{As}_4$, (h) $\text{EuRbFe}_4\text{As}_4$, and (i) $\text{EuCsFe}_4\text{As}_4$.

6.3 Chemical pressure induced Orbital selective Lifshitz transition

The mechanism of superconductivity in Fe-based systems after eleven years of its discovery is still illusive and completely an open question. So in this work we have taken an observational route to the problem. In this section we illustrate through a number of detailed experimental and theoretical studies that a large number of systems exhibit Lifshitz transition where the highest T_c is achieved *i.e.*, Lifshitz transition somehow restricts T_c . Lifshitz transition (LT) is a common phenomena in many families of iron based superconductors [39, 186, 187, 188, 94]. It can be induced by chemical doping [189], external hydrostatic pressure [190] or even magnetic field [191]. Large topological modifications with appearance or destruction of new FSs are the primary signatures of Lifshitz transition. To discuss about the Lifshitz transition in 1144 compound we have presented the evolution of topology of innermost hole like FS around Γ -point as well as the electron like FSs around M-point in Fig.6.12. A closer view of the corresponding BNSs is also presented in Fig.6.13. The atomic radii of different substituted elements are presented in

Table-6.1.

Table 6.1: Atomic radius of different substituted elements

Element	Atomic radius (Å)
Ca([Ar]4s ²)	1.94
Sr([Kr]5s ²)	2.19
Eu([Xe]4f ⁷ 6s ²)	2.31
K ([Ar]4s ¹)	2.43
Rb([Kr]5s ¹)	2.65
Cs([Xe]6s ¹)	2.98

Table-6.1 provides the electronic configuration and atomic sizes of various substituted alkali metals (K, Rb, Cs) as well as alkaline earth metals (Ca, Sr) or rare earth (Eu) with increasing atomic radius. Fig.6.12 presents the evolution of the inner hole FS of 1144 compounds with a particular Ae for different A (K, Rb, Cs) column wise whereas compounds with different Ae (Ca, Sr, Eu) for a particular A row wise. From Fig.6.12A(a), (b), (c), it is visible that the inner hole like FS around BZ centre shrivel slightly in size as K is replaced by Rb whereas the shrinkage is large for Cs in CaA44 compounds. The hole like FS become more 3d like. The volume of the outer electron like FS also decreases. Fig.6.13A(a), (b), (c) show that the top of the hole like band with d_{z^2} and As-4 p_z character around Γ -point drifts from 0.02Ry to very close to the E_F as element with higher atomic radius is substituted. The nearly degenerate $d_{x^2-y^2}$ derived bands move in the opposite direction away from the E_F . Although the electron like bands around M-point remain below the E_F , they slightly shift toward E_F leading to reduction of volume of the electron FSs (Fig. 6.13B (a), (b), (c)). Therefore, it is clear that substitution of K by Rb or Cs brings about modifications in electronic structure but do not induce Lifshitz transition in CaA44 compounds. However, from Fig.6.12B(a), (b), (c) it is obvious that due to substitution of K by Rb, Cs there is a large topological modification of the inner hole like FS. Due to presence of Rb having larger radius than K and Sr having larger radius than Ca, the chemical pressure generated on the FeAs-layer which is equivalent to hydrostatic pressure leads to large modifications in the electronic structure. Both the hole as well as electron like FSs become more 3D like. If Rb is replaced by Cs, due to its larger size even larger

chemical pressure is generated on the FeAs-layer. As a result, modifications in electronic structure become more prominent. The hole like FS at Γ -point segregates into two parts leading to disappearance of FS at Γ -point (Fig.6.12B(c)). This is the manifestation of Lifshitz transition. The inner electron like FSs at M-point also become smaller in size. A close look at the Fig.6.13A (d), (e), (f) show that the d_{z^2} and As-4 p_z derived hole like band gradually shifts towards E_F and finally crosses below the E_F for SrCs44 compound. Following trends in Fig.6.13B (d), (e), (f) also dictate that the two electron like bands at M-point also shift closer to E_F . Thus it is an example of chemical pressure induced orbital selective Lifshitz transition in SrCs44 compounds. Due to larger radius of Eu than Ca or Sr, EuA44 compounds are able to generate larger chemical pressure on the FeAs-layer sandwiched between alkali metals (K, Rb, Cs) and Eu. Therefore, the presence of Eu in 1144 compounds is expected to produce larger modifications in the electronic structure. Gradually replacing K with Rb or Cs incite furthermore topological modifications to the inner FS. Due to large chemical pressure in presence of Eu as well as Cs, the d_{z^2} and As-4 p_z derived hole like band is also pushed below the E_F (Fig.6.13A(c)) inducing significant topological modification to the inner hole like FS. The FS at Γ -point vanishes as a result of Lifshitz transition. Therefore, it is very clear from the above discussions that the chemical pressure acts as equivalent to hydrostatic pressure that leads to orbital selective Lifshitz transition in 1144 compounds. Thus, 1144 Fe based superconductors which are thought to be just the sandwich of two different 122 superconductors might be different in many aspects (exotic phases like - SDW, nematicity are absent).

Table 6.2: Highest T_c and Lifshitz transition

IBSC	T_{cmax} in K	Doping(x) at T_{cmax}	LT at doping(x)
$Ba_{1-x}K_xFe_2As_2$	~ 38	~ 0.50	~ 0.50 [89, 90]
$Ba_{1-x}Na_xFe_2As_2$	~ 34	~ 0.50	~ 0.50 [89, 91]
$BaFe_{2-x}Co_xAs_2$	~ 26	~ 0.10	~ 0.10 [89, 92]
$BaFe_2(As_{1-x}P_x)_2$	~ 27	~ 0.35	~ 0.37 [89, 93]
$Ca_{1-x}La_xFe_2As_2$	~ 35	~ 0.16	~ 0.15 [94, 95]
$Ca_{0.82}La_{0.18}Fe_{1-x}Ni_xAs_2$	~ 35	~ 0.005	~ 0.005 [94, 96]

The 1144 materials were synthesized with a hope to raise T_c beyond that of 122 systems ($\sim 38K$). However as we have seen in Table.6.2, the highest T_c is always limited by LT.

This may be the reason that T_c could not be raised further due to occurrence of LT. Also recent studies have revealed strong evidence of orbital selective Cooper pairing in iron based superconductors [193, 198, 199]. Therefore, orbital selective Lifshitz transition might be proved to be an important phenomenon regarding superconductivity in 1144 compounds. Nevertheless, Lifshitz like topological transitions are robust in these compounds just like many other families of IBSCs. This indicates to a universal connection between superconductivity and orbital selective Lifshitz transition in Fe based superconductors.

6.4 Effect of electron correlation and spin orbit coupling on the electronic structure

So far we have discussed the electronic structure of 1144 superconducting materials based on DFT. As mentioned in the earlier section that upto moderate values of electron correlation low energy electronic structure only undergoes quantitative modifications. Overall qualitative nature of electronic structure, specially the occurrence of LT remain unaltered. However, some 1144 Fe based superconductors not only contain Fe-3d but also Eu-4f orbitals (for EuK44, EuRb44, EuCs44), therefore it is important to investigate the effect of electron correlation on the electronic structure of these compounds. There exist experimental as well as theoretical studies on a large number of iron pnictides and chalcogenides that suggest weak correlation effect in iron pnictide (but not in chalcogenide) supercon-

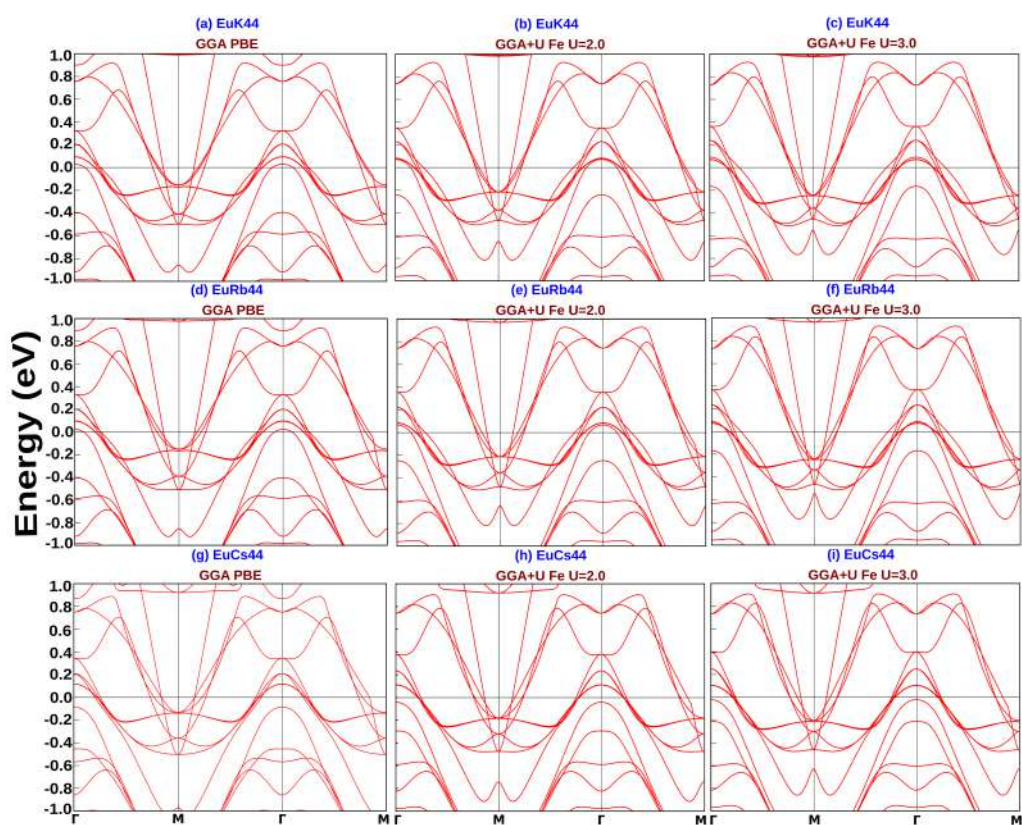


Figure 6.14: [141] Comparison of electronic band structure of EuA₄₄ compounds for various A within GGA and GGA+U methods. Indicated values of U are in eV.

ductors. For example, in [158] M. Yi *et. al.*, have performed quite elaborate experimental as well as theoretical studies on a large number of iron pnictides as well as chalcogenides. Their studies on a large number of doped and undoped 122 and 111 Fe pnictides revealed that the value of bandwidth renormalization ratio of d_{xy} and d_{yz} for most of the iron pnictide compounds are nearly equal to 1, indicating weak orbital selective bandwidth renormalization and hence electron correlation. On the other hand, the values of the renormalization ratio for doped as well as undoped Fe chalcogenides are 3 to 4 times larger which indicate strong bandwidth renormalization owing to orbital selective correlation. The above discussion is an indicator of possible weak electron correlation in 122 iron pnictides. As 1144 compounds are derived from two different 122 compounds, the electronic correlation is expected to be low to moderate which may not effect electronic structure of these compounds in a profound way. In this section we have investigated the impact of electronic correlation modeled by Hubbard U on Fe-3d as well as Eu-4f orbitals of 1144 compounds. We have carried out GGA+U calculation on all the 1144 compounds discussed in this paper, however to show the maximum effect of correlation (and for brevity), we have presented the results for EuA44 compounds.

In Fig.7.6, we have compared electronic band structure of EuA44 compounds evaluated within GGA and GGA+U methods for U=2, 3 eV, presented in first, second and third columns respectively. There is an overall upward shifts to all the bands with larger values of U. Now as Rb is replaced by Cs, the hole like band closest to the E_F shifts below the E_F (Fig.7.6(g)) due to chemical pressure inducing Lifshitz transition as discussed above. The orbital selective nature of the transition is discussed in the previous section. Now we will check the robustness of the Lifshitz like electronic topological transition in presence of electronic correlation. If we compare Fig.7.6(a) with Fig.7.6(b), it is conspicuous that the hole like band lying close to the E_F is slightly pushed away from it above the E_F in presence of on-site correlation U=2.0 eV and merges with the band just above it. Another band which was well below the E_F shifts appreciably towards the E_F . These movements of bands becomes more prominent if U is increased to 3.0 eV(Fig.7.6(c)).

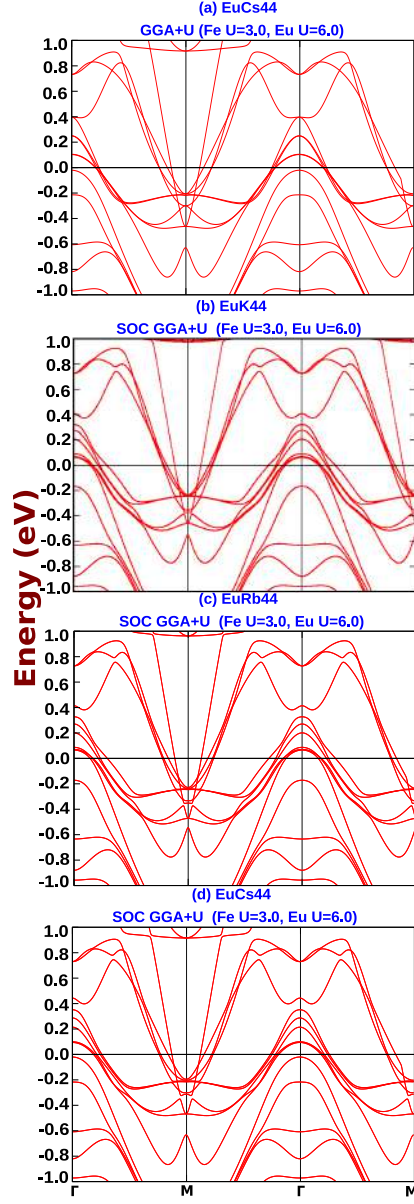


Figure 6.15: [141] Electronic structure within GGA+U method for – (a) EuCs44 with Fe U=3.0, Eu U=6.0 without spin orbit coupling (SOC), and (b) EuK44 with Fe U=3.0, Eu U=6.0, (c) EuRb44 with Fe U=3.0, Eu U=6.0, (d) EuCs44 with Fe U=3.0, Eu U=6.0 in presence of SOC. Indicated values of U are in eV.

Fig.7.6(d) shows the band structure of EuRb44 obtained within GGA PBE calculations, whereas Fig.7.6(e), (f) corresponds to the band structures within GGA+U for $U=2.0, 3.0$ eV respectively. The band nearest to the E_F is pushed away above the E_F and merges with another one due to U , just like the case in EuK44. Also the band well below the E_F moves towards E_F with increasing U . But the most prominent and interesting change in the electronic structure is observed in case of EuCs44. Due to chemical pressure induced by Cs, the band nearest to the E_F in case of EuK44 or EuRb44 is pushed below the E_F leading to Lifshitz transition. This is very much prominent from our GGA calculation (Fig.7.6(g)) as discussed in the previous sections. It is very important to verify whether the electronic topological transition is robust with respect to electron correlation or not. Our GGA+U calculations on EuCs44 shed a clear light on this question. From Fig.7.6(h), (i) it is visible that the band causing Lifshitz transition in GGA calculation, moves gradually closer to the E_F due to increasing U . Still it remains below the E_F for EuCs44 for $U=2.0, 3.0$ eV. Another noticeable fact is that the shift of the hole like band well below the E_F moving towards the E_F due to U is reduced in case of EuCs44. Its dispersion also becomes flat around Γ -point. Therefore, it is comprehensible that our discussion on orbital selective Lifshitz transition due to chemical pressure as described in Section-IV holds upto moderate values of electron correlation treated within GGA+U method for Hubbard U on Fe-3d bands.

We have also investigated the modifications in the electronic structure due to U on Eu-4f orbital in presence of $U=3.0$ eV on Fe-3d orbital in Fig.7.10(a). Comparing Fig.7.10(a) with Fig.7.6(i) it is plausible that strong electron correlation on Eu-4f *i.e.*, $U=6.0$ eV does not modify the electronic structure of 1144 compounds. This is due to the fact that the contribution of Eu-4f states to the low energy dispersion around the E_F is negligible. Further, with increasing U , Eu-4f states gradually shift away from the E_F . Therefore, the presence of U on Eu-4f does not affect Lifshitz like electronic topological transition due to chemical pressure in 1144 compounds. Spin orbit coupling (SOC) might be an important parameter which can tune the electronic structure of the compounds where specially

higher mass element like Eu is present. To have an idea about the effect of SOC on the electronic structure of 1144 compounds, we have presented the band structures of the EuA44 compounds which might have maximum effect of SOC on its electronic structure. Our GGA+U calculations incorporating SOC clearly shows that there are some quantitative modifications in the band structure of EuK44 (Fig.7.10(b)) due to spin orbit coupling. SOC lifts the degeneracy of the hole like bands around Γ -point crossing the E_F . The same kind of change is observed in EuRb44 and EuCs44. In case of EuCs44 the band which shifts below the E_F inducing Lifshitz transition in GGA as well as GGA+U calculations, remain still shifted below the E_F in presence of SOC too. Therefore, chemical pressure induced Lifshitz transition is expected to occur even in presence of moderate electron correlation and spin orbit coupling. As evident from the above discussion about electronic structure, the change in band structure of different 1144 compounds is only quantitative in presence of Hubbard U or SOC. Thus, the ensuing changes in the FSs are negligibly small in comparison to those in Fig.6.12. Therefore, we have not presented them for brevity.

6.5 Orbital Selective Bandwidth renormalization

To understand the effect of rare earth doping on bandwidths of different orbital derived bands, we present bandwidths of the hole like bands having different orbital characters. Bandwidth of different hole like bands is defined as the difference in energy between the top of the respective hole like band (at Γ -point) and the first minima of the same band in Γ -M direction [158]. Due to very much mixed character of the bands it is not reasonable to assign a single orbital character to any particular band. We assign five nomenclatures for the five visually distinct hole bands – α , β , γ , δ and ϵ that forms inner to outer FSs. The α , β , γ , δ and ϵ bands have mixed $d_{xy}/d_{yz}/d_{z^2}$, $d_{yz}/d_{xz}/d_{z^2}$, $d_{yz}/d_{xy}/4p_z$, $d_{x^2-y^2}$, $d_{x^2-y^2}/d_{z^2}/4p_z$ as dominant orbital characters of the hole like bands at around Γ -point. The values of bandwidths of different bands are presented in Table-7.9.

Table 6.3: Bandwidth of different 1144 IBSCs

1144 compound	Band (hole like)	Bandwidth (in meV)
CaKFe ₄ As ₄	α	566
	β	521
	γ	806
	δ	774
	ϵ	778
CaRbFe ₄ As ₄	α	562
	β	503
	γ	797
	δ	592
	ϵ	914
CaCsFe ₄ As ₄	α	558
	β	482
	γ	753
	δ	600
	ϵ	1020
SrKFe ₄ As ₄	α	576
	β	489
	γ	755
	δ	574
	ϵ	1046
SrRbFe ₄ As ₄	α	576
	β	480
	γ	747

1144 compound	Band (hole like)	Bandwidth (in meV)
	δ	583
	ϵ	1044
SrCsFe ₄ As ₄	α	566
	β	460
	γ	723
	δ	599
	ϵ	1173
EuKFe ₄ As ₄	α	590
	β	478
	γ	722
	δ	587
	ϵ	1344
EuRbFe ₄ As ₄	α	594
	β	475
	γ	716
	δ	590
	ϵ	1314
EuCsFe ₄ As ₄	α	576
	β	447
	γ	698
	δ	608
	ϵ	1078

In Table-7.9 we tabulate the change in bandwidth due to different combination of Ae (= Ca, Sr, Eu) or A (= K, Rb, Cs) in AeAFe₄As₄ compounds. For CaAFe₄As₄ compounds the

bandwidth of the α -band changes from 566 to 562 to 558 for A = K, Rb, Cs respectively. Thus there is not any significant change in the bandwidth of the α -band. The bandwidth of the β -band and γ -band gradually decreases for A = K, Rb, Cs respectively. The bandwidth of the δ -band varies from 774 to 592 to 600 for A = K, Rb, Cs respectively. For ϵ band it increases by a large amount for A = K, Rb, Cs respectively. Thus it is clear that with increasing the ionic radius of the alkali metals the bandwidths of β , γ , δ bands gradually decrease while bandwidth of ϵ band gradually increases for $\text{CaAFe}_4\text{As}_4$. Lowering of the value of bandwidths denote increased correlation. The bandwidth renormalization is significant for δ and ϵ bands which are primarily $d_{x^2-y^2}$ character at around Γ -point. Thus both the $d_{x^2-y^2}$ orbital derived bands are affected in a converse way. On the other hand as we go from K to Cs, the volume of the hole like FSs also decreases. Thus there might be a correlation between the bandwidth renormalization and FS volume. Like previous case, there is not any significant change in the bandwidth of the α -band for $\text{SrAFe}_4\text{As}_4$ compounds also. The bandwidth of the β -band and γ -band decreases for A = K, Rb, Cs respectively. The bandwidth of the δ -band increases by a small amount for A = K, Rb, Cs respectively. For ϵ band it changes from 1046 to 1044 to 1173 for A = K, Rb, Cs respectively. Thus it is clear that with increasing the ionic radius of the alkali metals the bandwidth of bands change in the same manner as $\text{CaAFe}_4\text{As}_4$ except δ bands where gradual increase is observed for $\text{SrAFe}_4\text{As}_4$. Now we will look into the change in bandwidth of $\text{EuAFe}_4\text{As}_4$. For $\text{EuAFe}_4\text{As}_4$ compounds the bandwidth of the α -band decreases in EuCs44 in comparison to EuK44 and EuRb44 . Like CaA44 and SrA44 compounds, the bandwidth of β and γ bands gradually decrease in EuA44 as K is replaced with Rb or Cs. An increasing trend is observed in the bandwidth of δ band in EuA44 compounds which is quiet similar to SrA44 compounds. Bandwidth of ϵ band decreases gradually for A = K, Rb, Cs respectively. But the reduction in bandwidth in case of EuCs44 compounds is very large. This is in contrary to CaCs44 and SrCs44 compounds where bandwidth increases in comparison to respective K or Rb based compounds. Thus it is clear that with increasing the ionic radius of the alkali metals the bandwidth of all the bands gradually

decreases for $\text{EuAFe}_4\text{As}_4$ except δ band for which there is gradual increase of bandwidth.

From the above discussion it is obviously clear that the bandwidth renormalization for different orbital derived bands are different. This indicates to the orbital selective bandwidth renormalization in 1144 family of IBSCs.

6.6 Conclusions

A comprehensive electronic structure study of a large number of 1144 compounds using DFT based first principles calculations disclose many important modifications of the BNSs as well as FSs. Comparative electronic structures of 1144 compounds reveal increasing atomic size of alkaline earth metal as well as alkali metals both have a significant impact on the electronic structure and FS topology of 1144 compounds. As we gradually increase the size of alkali metals ($A = \text{K, Rb, Cs}$) in a particular AeA44 ($\text{Ae} = \text{Ca, Sr, Eu}$) compounds, the $d_{x^2-y^2}$ derived hole like bands around Γ point start shifting to higher energy while the hole like band with d_{z^2} and $\text{As-}4p_z$ character shifts towards lower energy. These are indications of orbital selective self hole or electron doping due to chemical pressure of elements with higher atomic radius in between the FeAs -layers. In the discussed 1144 compounds two $d_{x^2-y^2}$ derived hole like bands are nearly degenerate. Due to increasing size of alkali metals as well as alkaline earth metals or Eu , a large chemical pressure equivalent to hydrostatic pressure is generated on the FeAs -layers. This natural chemical pressure modifies the electronic structure as well as the FS topology causing inner FS at Γ -point having $d_{z^2}/4p_z$ character to vanish in case of SrCs44 and EuCs44 compounds. This is a clear indication to the orbital selective Lifshitz transition. This natural chemical pressure induced orbital selective Lifshitz transition in newly discovered 1144 compounds is one of our most important results. Electronic correlation effects are treated within GGA+U method; for moderate values of U , electronic structure undergo only quantitative modification whereas inclusion of spin-orbit coupling to Eu based com-

pounds do not prohibit Lifshitz transitions. This orbital selective Lifshitz transition in 1144 IBSCs which do not show other exotic phases like nematicity, SDW *etc.* indicates possibility of orbital selective pairing in 1144 compounds and possibly restricts achieving higher superconducting transition temperature. Our studies on the bandwidth of different bands reveal a orbital selective modification of different orbital derived bands. This indicates orbital selective modifications in electron correlation in 1144 family.

Chapter 7

Correlation induced Lifshitz transition and nematicity in 12442 compounds

A systematic detailed electronic structure studies of the newly discovered $\text{ACa}_2\text{Fe}_4\text{As}_4\text{F}_2$ *i.e.*, 12442 iron based compounds (where $A = \text{K, Rb, Cs}$) within density functional theory (DFT) based first principles calculations is presented in this chapter. The orbital projected band structures (BNS) reveal mixed multi-orbital multi-band nature of the 12442 compounds having contributions mostly from Fe-3d orbitals. In contrast to other hybrid iron based superconductors, contribution of As-4 p_z orbital is negligible in these compounds. Substitution of alkali atoms of gradually higher atomic radii exert chemical pressure inside the compound and induce orbital selective evolution of band structure as well as density of states. Correlation induced orbital selective Lifshitz transition is revealed through GGA+U calculations. The tight binding band structure fitted with low energy DFT bands using maximally localized Wannier functions disclose a unique feature of the nearest neighbor hopping parameter. Unlike other compounds, intra-orbital hopping in d_{z^2} is larger than intra-orbital hopping in $d_{x^2-y^2}$. Orbital selective decrease in intra-orbital hopping of d_{xy} and d_{yz} due to change in chemical pressure induced by substitution of alkali atoms Rb or Cs in place of K is revealed in these compounds. The orbital anisotropy

of band structures as well as Fermi surfaces are discussed through electronic structure calculations. The degeneracy of d_{xz} and d_{yz} orbitals are lifted in 12442 compounds due to the reduction of symmetry D_{2d} to C_{2v} of local Fe-site. This degeneracy lifting of d_{xz} and d_{yz} causes band reconstruction which in turn induces emergence of nematic like splitting in these compounds. This splitting is maximum at the electron bands near the Brillouin zone corners. To verify the degeneracy lifting of $d_{xz/yz}$ level in 12442 compounds, crystal field splittings are calculated explicitly.

7.1 Theory and Computational Method

The Density Functional Theory (DFT) and plane wave pseudopotential based electronic structure calculations are performed using QUANTUM ESPRESSO code [135]. The electronic exchange correlation is considered within the generalized gradient approximation (GGA) with Perdew-Burke-Ernzerhof (PBE) functional [125]. Our non spin polarized single point energy calculations are performed using the experimental lattice parameters as input [200]. The plane wave cut off energy for the Kohn-Sham valence states is taken as 35 Ry after performing convergence test. The Brillouin zone (BZ) is sampled in k space with $8 \times 8 \times 8$ grid size to perform self consistent field (SCF) calculations in 12442 compounds. The geometry is optimized under Broyden-Fletcher-Goldfrab-Shanno (BFGS) scheme with 10^{-5} and 10^{-3} convergence threshold on total energy (a.u) and forces (a.u) respectively. The smearing technique with smearing parameter 0.01 Ry has been used to perform integration upto the Fermi surface. Visualization tool Fermi surfer [173] is used to show the contributions of different orbitals onto FSs. GGA+U calculations have been performed as implemented in QUANTUM ESPRESSO. We have employed Wannier 90 package [201] implemented in QUANTUM ESPRESSO to simulate the tight binding fitted band structure for 12442 compounds.

7.2 Electronic structure of 12442 compounds

Table 7.1: Comparison of theoretically calculated structural parameters with that of experimental results ([55])

Structural parameters	KCa ₂ Fe ₄ As ₄ F ₂			RbCa ₂ Fe ₄ As ₄ F ₂			CsCa ₂ Fe ₄ As ₄ F ₂		
	LDA	GGA	Expt.	LDA	GGA	Expt.	LDA	GGA	Expt.
$a = b$ (Å)	3.8647	3.8440	3.8684	3.8684	3.8422	3.8716	3.8778	3.8449	3.8807
c (Å)	31.0668	31.4012	31.0070	31.7194	32.1537	31.6670	32.4087	32.9687	32.3630
z_{As1} (Å)	1.3170	1.4046	1.405	1.3158	1.3875	1.403	1.3124	1.3910	1.401
z_{As2} (Å)	1.2924	1.4525	1.436	1.2910	1.4820	1.431	1.2854	1.4640	1.430
$\alpha_1(\angle As1 - Fe - As1^\circ)$	112.45	107.68	108.00	112.55	108.32	108.10	111.81	108.22	108.30
$\alpha_2(\angle As2 - Fe - As2^\circ)$	111.44	105.84	106.80	111.54	104.70	107.00	112.91	105.42	107.20
d_{inter} (Å)	8.5352	8.8031	8.6321	8.4926	8.6842	8.6132	8.4891	8.6524	8.5954
d_{intra} (Å)	7.0333	6.9596	6.8746	7.4483	7.2560	7.2211	7.8551	7.8420	7.5839

Fig.7.1 shows the crystal structure of 12442 compounds. The 12442 compounds crystallize in tetragonal phase with $I4/mmm$ space group symmetry. As mentioned earlier 12442 Fe based superconductors are mixture of 1111 and 122 Fe based compounds where one 122 compound is sandwiched in between two 1111 compounds forming conducting Fe_2As_2 double layers. It has been proposed from experimental observations that (like other iron based superconductors) different structural parameters like anion heights (*i.e.*, z_{As1} , z_{As2}), $\angle As - Fe - As$ (α_1 , α_2), distance between FeAs-layers belonging to 1111 and 122 blocks (d_{inter}), distance between FeAs-layers belonging to 122 block (d_{intra}) may affect the superconductivity of this compound to a large extent [55]. The structural parameter d_{inter} is exclusive to this family as 12442 compounds are mixture of two different iron based compounds belonging to two different families. There exists two anion heights and two $\angle As - Fe - As$ angles as well, due to presence of As in asymmetric environment (one As is closer to alkali metal, while the other is closer to Ca_2F_2 layer). We have calculated the structural parameters from DFT based first principles calculations with two different exchange correlation potentials – Local Density Approximation (LDA) and GGA and compared them with the experimental parameters to know the relative suitability of the respective potentials in electronic structure calculations. The results comparing structural parameters derived from theoretical investigations and experimental observations are presented in Table.7.1.

A close look into the Table.7.1 indicates that the lattice parameters *i.e.*, $a(= b)$, c are well

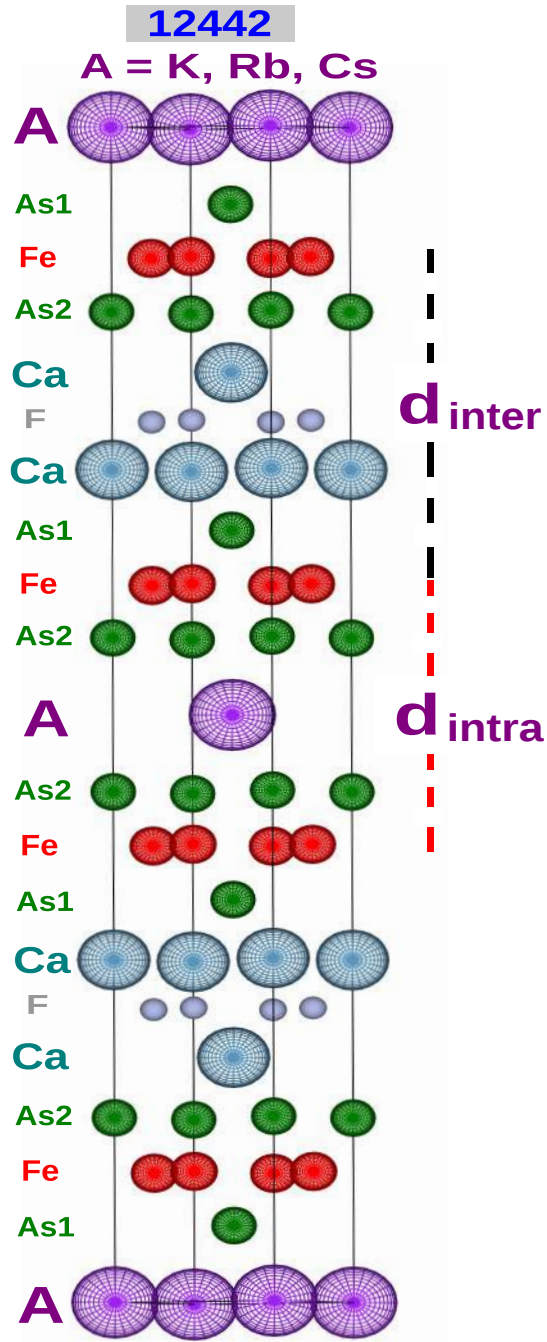


Figure 7.1: [142] Crystal structure of 12442 family of iron based superconductors.

estimated by LDA for all the three 12442 compounds. The values of the lattice parameter a obtained from LDA calculations are 3.8647 Å, 3.8684 Å, 3.8778 Å for $\text{KCa}_2\text{Fe}_4\text{As}_4\text{F}_2$, $\text{RbCa}_2\text{Fe}_4\text{As}_4\text{F}_2$ and $\text{CsCa}_2\text{Fe}_4\text{As}_4\text{F}_2$ respectively. These values are quiet close to the experimental values (of Table.7.1). On the other hand, the values of a lattice parameter obtained within GGA are 3.8440 Å, 3.8422 Å, 3.8449 Å respectively for the three 12442 compounds. The GGA slightly underestimates the values of both the lattice parameters (a, b). The same trend is also observed in case of lattice parameter c where the LDA calculated values are closer to the experimental values than GGA results. Thus, LDA describes the lattice parameters of 12442 compounds better than the GGA. Now we will investigate into the structural parameters which are known to impact both magnetism and superconductivity in Fe based compounds to a large extent. From Table.7.1 it is clearly visible that the GGA calculated values of $z_{\text{As}1}$ for the three 12442 compounds are 1.4046 Å, 1.3875 Å, 1.3910 Å respectively. These GGA calculated $z_{\text{As}1}$ are closer to the respective experimental values than that from the LDA calculated results. GGA and LDA results follow very similar trend in case of $z_{\text{As}2}$ also. LDA largely underestimates the anion heights while GGA results are quiet reasonable. α_1 and α_2 are also two very important structural parameters for 12442 compounds. The GGA derived values of α_1 (107.68°, 108.32°, 108.22°) are equitable with the experimental measurements (108.00°, 108.10°, 108.30°). The values are highly overestimated by LDA. While the values of α_2 are slightly underestimated by GGA, the trend of overestimation continues to remain for LDA. The d_{intra} and d_{inter} are measure of intra and inter Fe_2As_2 bilayer coupling in hybrid 12442 materials. These quantities are known to play important role in controlling superconducting transition temperature. From Table.7.1 it is visible that there is a clear trend of underestimation in the values of d_{inter} by LDA in comparison to experiments. On the contrary, GGA slightly overestimates d_{inter} , although the values are comparatively closer to experiments than that of the LDA. The GGA values tend to shift closer to the experimental values as K is replaced by alkali metals with higher radii – Rb, Cs. In case of d_{intra} , LDA overestimates to a visible amount, whereas the calculated values by

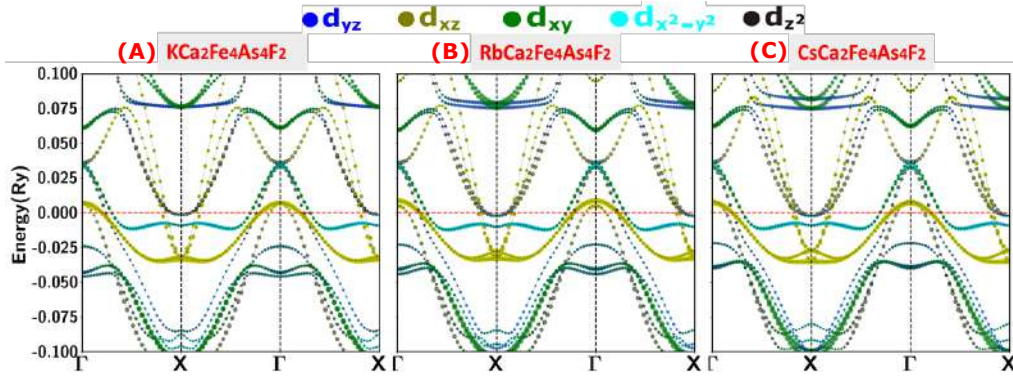


Figure 7.2: [142] Calculated orbital projected band structures (BNSs) on different Fe-3d orbitals for (A) $\text{KCa}_2\text{Fe}_4\text{As}_4\text{F}_2$, (B) $\text{RbCa}_2\text{Fe}_4\text{As}_4\text{F}_2$, and (C) $\text{CsCa}_2\text{Fe}_4\text{As}_4\text{F}_2$ around high symmetry points. Individual orbital contribution is shown with individual colours and the size of the circles are proportional to orbital weight. The Fermi level is denoted by dashed red horizontal line at zero energy.

GGA are very close (slight overestimation) to the experimental values. From the above discussions it is conceivable that GGA performs very well as long as we are interested in the crucial crystal parameters like $z_{\text{As}1}$, $z_{\text{As}2}$, α_1 , α_2 , d_{intra} , d_{inter} etc. which are known to be directly linked with the superconductivity in Fe based superconductors. Therefore, we have chosen GGA-PBE exchange correlation functional for our electronic structure calculations.

The orbital projected BNSs of the three 12442 compounds are presented in Fig.7.13. The contribution of different orbitals is denoted by assigning a colour to each orbital involved in band formation. The weight of the orbitals to the bands is proportional to the size of the circle. Blue, olive, green, cyan, and black colours are assigned to signify d_{yz} , d_{xz} , d_{xy} , $d_{x^2-y^2}$, d_{z^2} orbitals respectively. The same colour scheme is followed throughout the work. Just like in 1144 compounds, 12442 family also posses six hole like bands around the Γ -point and four electron like bands around the X-point [68, 203]. In the electronic structure of the respective constituent 1111 or 122 compounds (which makes up 12442 or 1144) three hole like bands around Γ -point and two electron like bands around X-point is observed [204, 205]. Thus the number of bands are just the double in the hybrid superconductors in comparison to that of the constituent Fe based compounds.

We have calculated the projection of different atomic orbitals onto different Kohn-Sham states to know about the orbital nature of different bands and Fermi surfaces. The orbital projected BNS reveals mixed multi-orbital multi-band nature of all the three compounds – $\text{KCa}_2\text{Fe}_4\text{As}_4\text{F}_2$, $\text{RbCa}_2\text{Fe}_4\text{As}_4\text{F}_2$, $\text{CsCa}_2\text{Fe}_4\text{As}_4\text{F}_2$. In Fig.7.13(A), we have presented the electronic structure of $\text{KCa}_2\text{Fe}_4\text{As}_4\text{F}_2$ around high symmetry points. There are six hole like bands around Γ -point crossing the Fermi level (E_F), of which three lie close to the E_F and the other three away from the E_F . Among the three upper lying bands two are almost degenerate and mostly of mixed d_{xy} , $d_{x^2-y^2}$ character. The third one is primarily of d_{z^2} and d_{yz} orbitals derived. Now, if we look into the three lower lying bands around the Γ -point close to the E_F , the two degenerate bands are mostly derived from d_{xz} orbital with a small contribution from d_{xy} . The innermost lower lying band is of mixed d_{xy} , d_{xz} , d_{yz} characters. There are four electron like bands around X-point crossing the E_F . The two lower lying electron like bands are multi-orbital in nature having mixed d_{xy} , d_{xz} , d_{yz} characters. Two almost degenerate upper lying electron bands closer to the E_F are mostly derived from d_{xz} , d_{yz} orbitals. It is interesting to note that the electron bands do not have contribution from d_{z^2} orbital, although a very small contribution from $d_{x^2-y^2}$ is visible. These two nearly degenerate upper lying bands are at the verge of Lifshitz transition. Thus very small electron FSs corresponding to these bands are expected. The alkali metal K ($[\text{Ar}]4s^1$) with atomic radius 2.43 Å is replaced with Rb ($[\text{Kr}]5s^1$) or Cs($[\text{Xe}]6s^1$) having atomic radius 2.65 Å and 2.98 Å in case of $\text{RbCa}_2\text{Fe}_4\text{As}_4\text{F}_2$ and $\text{CsCa}_2\text{Fe}_4\text{As}_4\text{F}_2$ respectively. Thus as one synthesizes $\text{KCa}_2\text{Fe}_4\text{As}_4\text{F}_2$ to $\text{RbCa}_2\text{Fe}_4\text{As}_4\text{F}_2$ to $\text{CsCa}_2\text{Fe}_4\text{As}_4\text{F}_2$ compounds by replacing $\text{K} \rightarrow \text{Rb} \rightarrow \text{Cs}$, it should be subjected to different chemical pressures. The reduced values of z_{As1} and z_{As2} (as well as larger values of $\angle \text{As} - \text{Fe} - \text{As}$) in Table.7.1 also indicates to the increased chemical pressure due to substitution of alkali metals with higher atomic radius. Fig.7.13(B) clearly shows that the degeneracies of the bands (in Fig.7.13(A)) are mostly lifted due to chemical pressure induced by Rb. The upper lying bands above the E_F are more affected than the bands below the E_F . A close inspection of the bands at Γ -point reveals appearance of a new small electron like band near 0.10

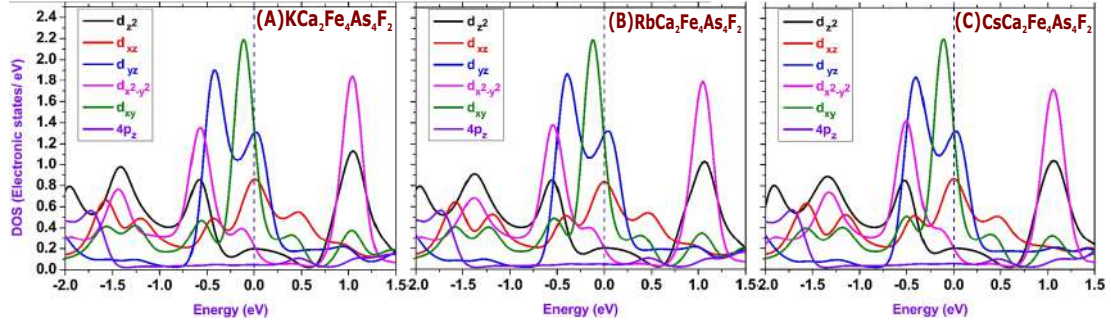


Figure 7.3: [142] Partial density of states of different Fe-3d and As-4p orbital derived states for (A) $\text{KCa}_2\text{Fe}_4\text{As}_4\text{F}_2$, (B) $\text{RbCa}_2\text{Fe}_4\text{As}_4\text{F}_2$, and (C) $\text{CsCa}_2\text{Fe}_4\text{As}_4\text{F}_2$. The Fermi level is denoted by dotted blue vertical line at zero energy.

Ry energy above the E_F . The innermost hole like band with d_{xy} , d_{xz} , d_{yz} character shifts slightly below the degenerate bands with d_{xz} orbital character. In that way the innermost hole like band become closest to the E_F . The two degenerate bands with d_{xz} orbital shift slightly away from the E_F . Thus there is an orbital selective self hole doping to the bands. The electron like bands around X-point in $\text{RbCa}_2\text{Fe}_4\text{As}_4\text{F}_2$ seems to be very similar to that of the $\text{KCa}_2\text{Fe}_4\text{As}_4\text{F}_2$. Although the degeneracy of the bands near the E_F with mixed d_{xz} , d_{yz} orbital characters is lifted. The degeneracy of the bands lying well above the E_F is lifted further due to substitution of K by Cs in $\text{CsCa}_2\text{Fe}_4\text{As}_4\text{F}_2$ (Fig.7.13(C)). The new small band around the Γ -point above the E_F which appeared in $\text{RbCa}_2\text{Fe}_4\text{As}_4\text{F}_2$ grows further in size due to replacement of Rb with Cs. The degeneracy of the two hole like bands with d_{xz} orbital character is slightly lifted in such a way that one of the bands is slightly pushed away from the E_F and the other one is pushed slightly towards the E_F . The electron like bands near E_F become more distinct in $\text{CsCa}_2\text{Fe}_4\text{As}_4\text{F}_2$ due to degeneracy lifting. From the above discussions we get a clear picture about the band structure of 12442 compounds and its modifications due to chemical pressure induced by replacement of alkali metal with higher atomic radius. Chemical pressure induced modifications in the BNS of 12442 compounds is milder in comparison to that for the 1144 compounds where orbital selective Lifshitz transition occurs due to this chemical pressure (discussed in chapter 6). Similar conclusions regarding 1144 compounds are revealed in an another study by us [141].

In Fig.7.3 the partial DOS of different Fe-3d and As-4 p_z orbitals of different 12442 compounds are presented. It is evident that unlike in 1144 and 112 compounds where there is a significant contribution of As-4 p_z orbital to the DOS at the E_F , the contribution of As-4 p_z orbital at around the E_F is negligible in case of 12442 compounds [137, 140, 141]. The dominant contribution in the DOS at around the E_F comes from different Fe-3d orbitals. Out of the five Fe-3d orbitals the maximum contribution to the DOS at the E_F arises from d_{xy} and d_{yz} orbitals. One of the peaks in the partial DOS of d_{yz} remain at the E_F , whereas the peak of d_{xy} orbital partial DOS is slightly shifted to the lower energy below the E_F in case of $\text{KCa}_2\text{Fe}_4\text{As}_4\text{F}_2$ (Fig.7.3(A)). The partial DOS of d_{xz} orbital at the E_F lie just below that of d_{xy} and d_{yz} with its peak at the E_F . The contributions of $d_{x^2-y^2}$ and d_{z^2} orbitals to the DOS at the E_F are the lowest. The peak of $d_{x^2-y^2}$ partial DOS is slightly shifted below the E_F , whereas the nature of d_{z^2} partial DOS is flat at the E_F . It is distinguishable from the Fig.7.3(B),(C), that the peak of d_{xy} partial DOS shifts towards E_F , whereas the d_{yz} partial DOS peak displaces away from the E_F towards higher energy as K is replaced by Rb or Cs respectively. There is no such visible effect on the d_{xz} or d_{z^2} peak in $\text{RbCa}_2\text{Fe}_4\text{As}_4\text{F}_2$ (Fig.7.3(b)) and $\text{CsCa}_2\text{Fe}_4\text{As}_4\text{F}_2$ (Fig.7.3(c)). A gradual flattening of peak in partial DOS (slightly away from the E_F) is observed in case of $d_{x^2-y^2}$ derived states. Therefore, discussion on partial DOS of different Fe-3d orbitals signals to the fact that although the overall nature of partial DOS variation is nearly similar in all the 12442 compounds, individual Fe-3d states are affected differently due to presence of Rb or Cs in the compound. The above mentioned behaviour of different partial DOS (which are different orbital derived) demonstrates that these materials are example of orbital selective self doped systems.

The discussions regarding topology of Fermi surface (FS) is very much important in case of iron based superconductors. It may reveal various important informations like nesting condition, possibility of Lifshitz like topological transitions *etc.* Now, we will discuss about the evolution of FSs in 12442 family of iron based superconductors. The projection of Kohn-Sham states on atomic orbitals also reveal the orbital character of different FSs. Gradually moving from red towards blue signify decreasing contribution of any in-

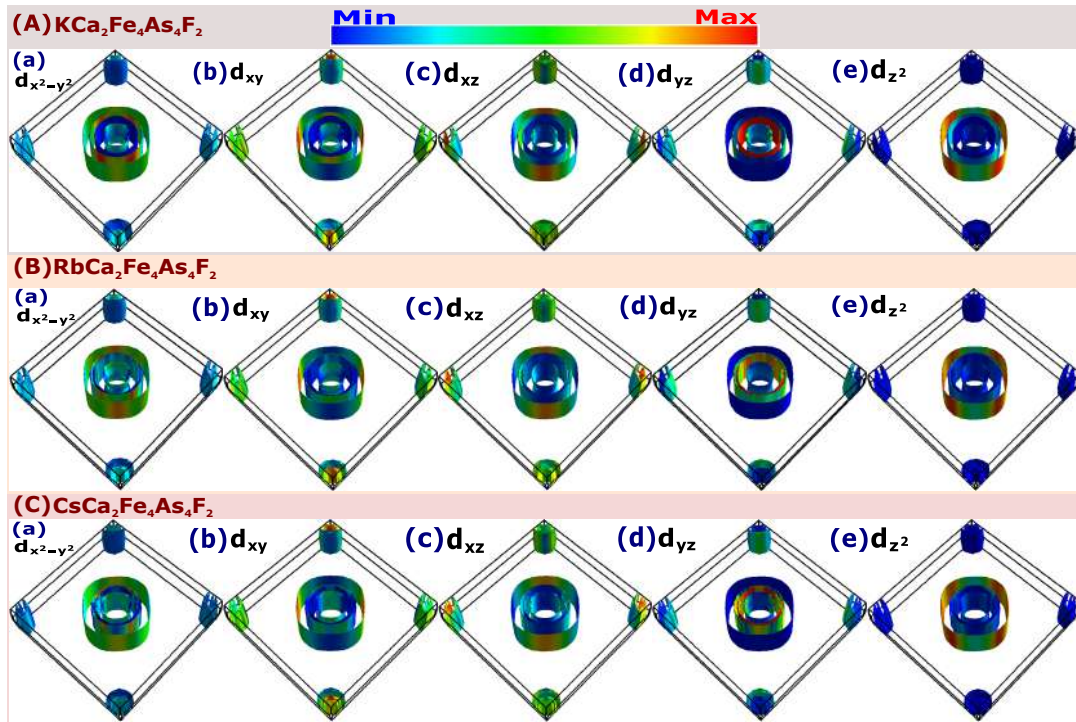


Figure 7.4: [142] Calculated orbital projected Fermi surfaces (FSs) of (A) $\text{KCa}_2\text{Fe}_4\text{As}_4\text{F}_2$, (B) $\text{RbCa}_2\text{Fe}_4\text{As}_4\text{F}_2$, and (C) $\text{CsCa}_2\text{Fe}_4\text{As}_4\text{F}_2$. Weights of the different Fe 3d orbitals for different FSs are shown using varying colours. The "red" colour denotes 'maximum' contribution while "blue" denotes 'minimum' contribution.

dividual orbital. Same colour scheme is followed throughout the current chapter. From Fig.7.14 it is conspicuous that there are six hole like FSs around Γ -point at the Brillouin zone centre whereas there are four electron like FSs around X-point at the Brillouin zone corner. Thus the number of FSs in these hybrid Fe based compounds is just the double in comparison to the constituent 1111 and 122 Fe based superconductors [204, 205]. The FSs look like concentric cylinders with centre at the Γ -point. The outer two hole like FSs and inner second and third hole like FSs are nearly degenerate. In the Fig.7.14(A)a, (B)a, (C)a, we have presented the $d_{x^2-y^2}$ orbital resolved FSs of $\text{KCa}_2\text{Fe}_4\text{As}_4\text{F}_2$, $\text{RbCa}_2\text{Fe}_4\text{As}_4\text{F}_2$ and $\text{CsCa}_2\text{Fe}_4\text{As}_4\text{F}_2$ respectively. In case of $\text{KCa}_2\text{Fe}_4\text{As}_4\text{F}_2$, the outer three hole like FSs (of them the two outermost FSs are nearly degenerate) have large contribution from $d_{x^2-y^2}$ orbital. The innermost FS has also small but finite contribution from $d_{x^2-y^2}$. When K is replaced by Rb or Cs, orbital contribution of $d_{x^2-y^2}$ to the innermost as well as to the second inner FS increases. The electron like FSs have very little $d_{x^2-y^2}$ orbital character. The orbital evolution of d_{xy} in the FSs is shown in Fig.7.14(A)b, (B)b, (C)c. The contribution of d_{xy} orbital to the hole like FSs is almost similar to that of the $d_{x^2-y^2}$, with its contribution being smaller than it. But its orbital weight in the innermost as well as outermost electron like FSs is remarkable. Fig.7.14(A)c, (B)c, (C)c, express the orbital weight of d_{xz} onto different FSs. It has significant contribution to the outer three hole like FSs and to all the four electron like FSs. Specifically, d_{xz} has dominant orbital contribution in those FSs where the contribution from d_{xy} is weak. The d_{yz} orbital chip in mostly to the inner second, third degenerate FSs in case of $\text{KCa}_2\text{Fe}_4\text{As}_4\text{F}_2$ (Fig.7.14(A)d). When K is replaced by Rb or Cs, the contribution of d_{yz} extends upto the fourth hole like FS, although its contribution to the second, third degenerate FSs decrease (Fig.7.14(B)d, (C)d). The d_{yz} orbital has a small contribution to the electron like FSs. Orbital contribution of the d_{z^2} to the FSs is shown in Fig.7.14(A)e, (B)e, (C)e. It has primary contribution to the two degenerate outermost FSs and a small contribution to the third outer FS for $\text{KCa}_2\text{Fe}_4\text{As}_4\text{F}_2$ which diminishes when K is replaced by Rb or Cs. From the above discussions the multi-orbital nature of the FSs is palpable. Unlike the parent 1111 and 122 compounds, in 12442 com-

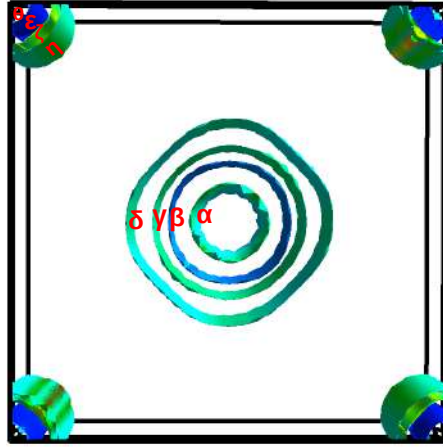


Figure 7.5: [142] Upper view of the Fermi surfaces. Each hole and electron pocket is designated with different names – $\alpha, \beta, \gamma, \delta$ and $\theta, \epsilon, \zeta, \eta$ respectively.

pounds the hole and electron like FSs not only possess $d_{xz/yz}$ orbital character, but also the contribution from $d_{x^2-y^2}/d_{z^2}$ orbital are very prominent like that in 1144 compounds [209]. From Fig.7.14(A), (B), (C), it is very clear that the nesting between hole like FSs around Γ -point and electron like FSs around M-point is negligible. This indicates to the reduced possibility of repulsive interband pairing interaction between electron and hole like FSs which may oppose s^\pm symmetry of the superconducting gap.

On the otherhand, the two outer hole like FSs and inner second, third FSs are degenerate to each other with similar orbital characters. Thus intra-orbital interband nesting between hole like bands is possible. Careful observation of the hole like FSs reveal that there might be strong intra orbital intra band nesting among outer hole like FSs having mostly $d_{x^2-y^2}/d_{z^2}$ character. Thus, this attraction within $d_{x^2-y^2}/d_{z^2}$ derived hole pocket may support the scenario of d -wave pairing in these self hole doped compounds [210]. On the contrary, the intra-orbital interband interaction between $d_{xz/yz}$ orbital derived electron and hole FSs may favour sign changing s -wave pairing [210]. From Fig.7.14(A), (B), (C), it is observable that d_{xy} , d_{xz} , and d_{yz} orbitals have significant contributions to both electron and hole FSs. This intra-orbital nesting between $d_{xz/yz}$ derived electron and hole FSs, enhances repulsive interband interaction leading to s -wave pairing. Thus there is a possibility of s -wave pairing also. These discussions may justify the observation of mixed

Table 7.2: Pocket size of electron and hole like FSs

12442 compound	Pocket type	Pocket name	Radius (in π/a)
$\text{KCa}_2\text{Fe}_4\text{As}_4\text{F}_2$	Hole	α	0.1404
		β	0.2886
		γ	0.3439
		δ	0.4379
	Electron	ϵ	0.0897
		ζ	0.1663
		η	0.2277
$\text{RbCa}_2\text{Fe}_4\text{As}_4\text{F}_2$	Hole	α	0.1286
		β	0.2812
		γ	0.3160
		δ	0.4164
	Electron	θ	0.1059
		ϵ	0.1466
		ζ	0.2080
		η	0.2557
$\text{CsCa}_2\text{Fe}_4\text{As}_4\text{F}_2$	Hole	α	0.2178
		β	0.2974
		γ	0.3298
		δ	0.4589
	Electron	θ	0.0932
		ϵ	0.1371
		ζ	0.1883
		η	0.2370

s and *d* wave gap experimentally [62, 63] in 12442 compounds.

To have an idea about nesting between different electron and hole pockets, we present sizes of the FSs in the Table. 7.2. The upper view of the FSs is presented in the Fig.7.5. Different hole pockets with gradually increasing radius are named as α , β , γ and δ , whereas the electron pockets are designated with θ , ϵ , ζ and η . From Table.7.2, it is visible that the size of the hole pockets are mostly larger than the electron pockets for all the three compounds. The only exception is the inner hole and electron pockets. Sizes of the calculated hole pockets are in well agreement with experiments [211]. In case of $\text{KCa}_2\text{Fe}_4\text{As}_4\text{F}_2$, ϵ electron pocket is very small (radius $0.0897 \pi/a$) in comparison to the outer hole pockets. But the α hole pocket which has a radius of $0.1404 \pi/a$, may show weak inter band nesting with ϵ . The inner most two degenerate electron pockets in $\text{KCa}_2\text{Fe}_4\text{As}_4\text{F}_2$, become distinct in case of $\text{RbCa}_2\text{Fe}_4\text{As}_4\text{F}_2$ and $\text{CsCa}_2\text{Fe}_4\text{As}_4\text{F}_2$. The α pocket (radius $0.1286 \pi/a$) may be weakly nested with θ (radius $0.1059 \pi/a$) or ϵ (radius $0.1466 \pi/a$) in $\text{RbCa}_2\text{Fe}_4\text{As}_4\text{F}_2$ due to their comparable radius. The situation is slightly different in $\text{CsCa}_2\text{Fe}_4\text{As}_4\text{F}_2$ where the size of α hole pocket (radius $0.2178 \pi/a$) is comparable with the outer electron pockets ζ (radius $0.1883 \pi/a$) and η (radius $0.2370 \pi/a$). So there may exist interband nesting between α and ζ or η in $\text{CsCa}_2\text{Fe}_4\text{As}_4\text{F}_2$. It is clear from the above discussion that the possibility of nesting between the hole and electron pockets is weak as the inner electron pockets are on the verge of Lifshitz transition. Our discussion about the nesting from the orbital character of FSs is qualitative only. One should always look into the spin susceptibility or nesting function to comment about nesting in Fe based compounds rigorously and quantitatively [184].

7.3 Effect of electron correlation and Spin Orbit Coupling (SOC) on the electronic structure of 12442 compounds

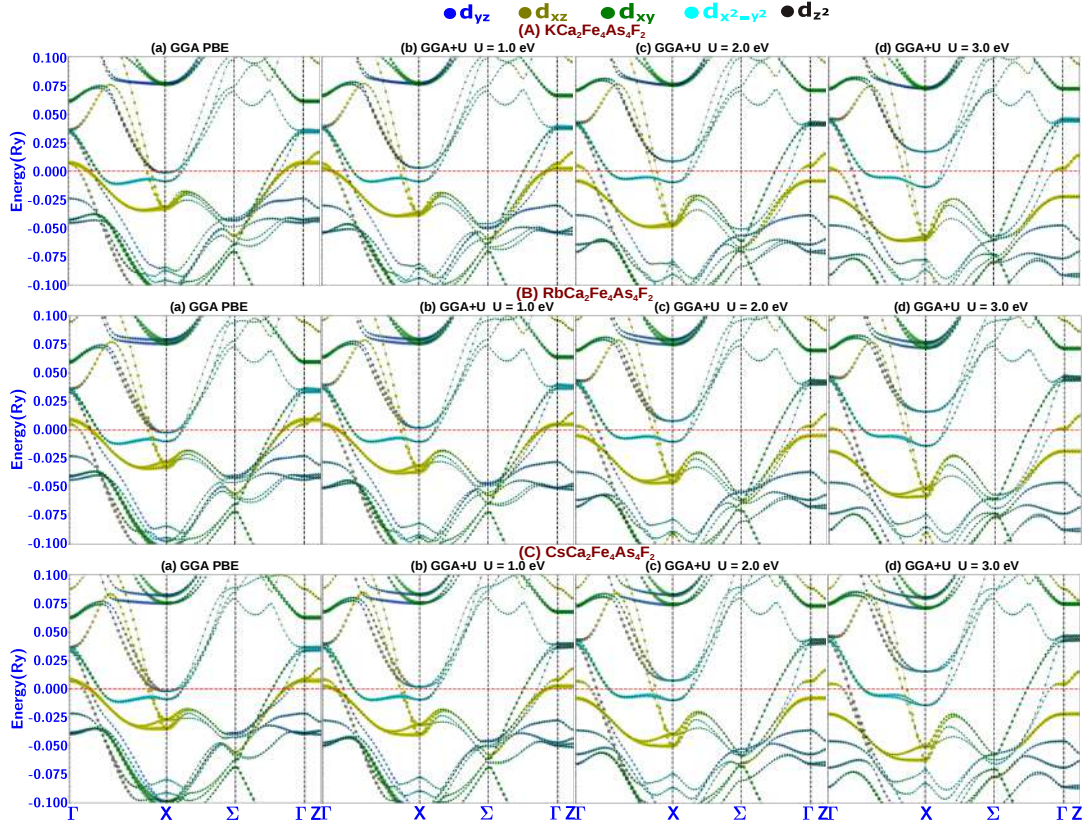


Figure 7.6: [142] Comparison of calculated band structures using GGA and GGA+U methods respectively for (A) $\text{KCa}_2\text{Fe}_4\text{As}_4\text{F}_2$, (B) $\text{RbCa}_2\text{Fe}_4\text{As}_4\text{F}_2$, and (C) $\text{CsCa}_2\text{Fe}_4\text{As}_4\text{F}_2$.

The effect of electron correlation on the electronic structures of the hybrid 12442 compounds within GGA+U method is investigated in this section. In Fig. 7.6 the evolution of electronic band structure of three 12442 compounds with different onsite Hubbard correlation (U) are presented. From Fig. 7.6(A) (a), (b) it is conspicuous that as $U = 1.0$ eV is incorporated, two nearly degenerate electron like bands around X-point from GGA calculation having mostly d_{yz} character which were previously below E_F , shifts just above the E_F leading to Lifshitz transition due to electron correlation. On the other hand, two nearly degenerate hole like bands with dominant d_{xz} character around Γ -point shifts towards the

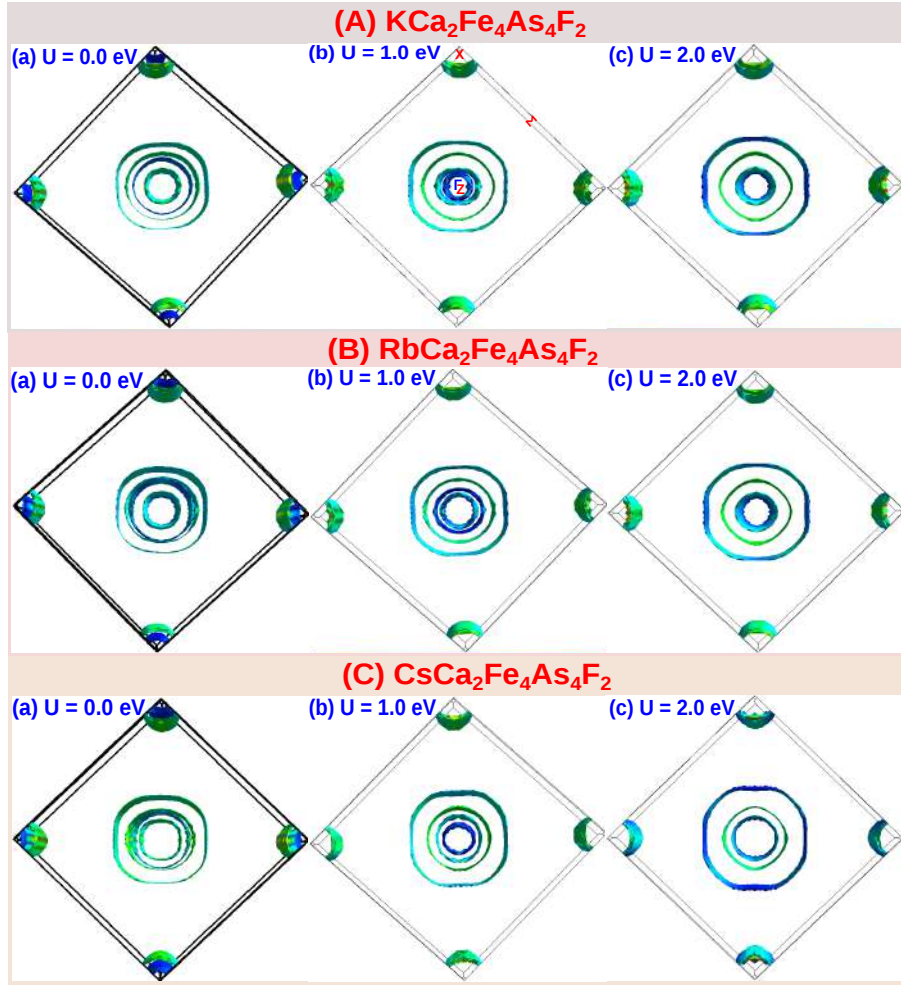


Figure 7.7: [142] Comparison of calculated Fermi surfaces using GGA and GGA+U methods respectively for (A) $\text{KCa}_2\text{Fe}_4\text{As}_4\text{F}_2$, (B) $\text{RbCa}_2\text{Fe}_4\text{As}_4\text{F}_2$, and (C) $\text{CsCa}_2\text{Fe}_4\text{As}_4\text{F}_2$ for different U (in eV).

E_F . If the Hubbard U is further increased to 2.0 eV the shifted electron like bands around X-point is displaced further away above the E_F (Fig.7.6(A)(c)). The degenerate hole like bands around Γ -point which was just above the E_F for $U = 1.0$ eV, are displaced below E_F leading to Lifshitz transition of the hole like bands. Increasing U to 3.0 eV only further shifts the respective electron or hole like bands towards or away from the E_F . Movement of the other electron or hole bands away from the E_F , is much smaller due to electron correlation. Now if we look into Fig. 7.6 (B) and (C), it is visible that the trend of shifting electron as well as hole like bands above and below the E_F respectively due to correlation remain same as that in $\text{RbCa}_2\text{Fe}_4\text{As}_4\text{F}_2$ and $\text{CsCa}_2\text{Fe}_4\text{As}_4\text{F}_2$. Correlation induced Lifshitz transition of the electron like bands having d_{yz} character and hole like bands of d_{xz} character is common in all the three hybrid 12442 compounds. One important aspect of the correlation induced modifications in the electronic structure is that it's orbital selective in nature. It is to be noted that only the two degenerate electron (hole) like bands around X (Γ) point having d_{yz} (d_{xz}) character shift above (below) the E_F inducing Lifshitz transition. Thus, the effect of onsite electron repulsion in creating separation between orbital selective hole and electron bands with dominant d_{yz} character and d_{xz} characters respectively is very similar to what happens in between the upper and lower Hubbard bands in case of Mott-Hubbard insulators. This is a signature of orbital selective Mottness. Furthermore, the onsite correlation induced modifications in the bandwidths of different bands are also orbital selective. We have explored the bandwidths of the hole like bands with different orbital characters to understand the effect of onsite correlation on the bandwidth renormalization. The hole like bands around Γ -point are named as α , β , γ and δ as shown in Fig.7.9. The dominant orbital characters of the α and β bands near Γ -point are mixed $d_{xy}/d_{x^2-y^2}$ nature, whereas γ and δ have mixed d_{z^2}/d_{yz} and d_{xz}/d_{xy} character. The Hubbard U dependent bandwidths of different bands for the three 12442 compounds are presented in the Table.7.3. It is evident from Table.7.3 that the bandwidths of the three bands α , β and γ gradually increases as onsite electron correlation is increased. On the other hand bandwidth of the δ band gradually decreases due to increased correlation for all the three

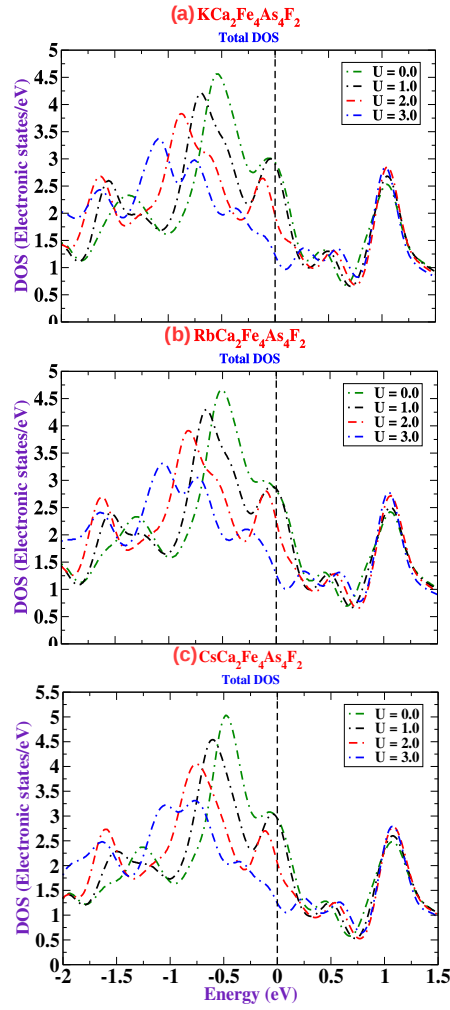


Figure 7.8: [142] Change in total density of states of (a) $\text{KCa}_2\text{Fe}_4\text{As}_4\text{F}_2$, (b) $\text{RbCa}_2\text{Fe}_4\text{As}_4\text{F}_2$, and (c) $\text{CsCa}_2\text{Fe}_4\text{As}_4\text{F}_2$ with different U values in eV.

compounds. The δ band has mostly d_{xz} character with small contribution from d_{xy} . It is the δ band which is pushed below the E_F due to increased correlation leading to orbital selective correlation induced Lifshitz transition. Therefore, the orbital selective bandwidth renormalization is very much apparent in these compounds. This orbital selective manifestation of electron correlation is supportive of orbital selective pairing [212, 213, 214] in 12442 compounds. All the results of this section is verified through various pseudopotentials as well as other numerical code like CASTEP.

Table 7.3: Bandwidth of different 12442 IBSCs

12442 compound	Hubbard U U in eV	Band (hole like)	Bandwidth (in meV)
KCa ₂ Fe ₄ As ₄ F ₂	0.0	α	639
		β	618
		γ	1628
		δ	573
	1.0	α	664
		β	639
		γ	1647
		δ	573
	2.0	α	674
		β	650
		γ	1663
		δ	555
RbCa ₂ Fe ₄ As ₄ F ₂	0.0	α	660
		β	618
		γ	1631
		δ	580
	1.0	α	678
		β	643
		γ	1667
		δ	583
	2.0	α	692
		β	650
		γ	1681

12442 compound	Hubbard U U in eV	Band (hole like)	Bandwidth (in meV)
		δ	562
CsCa ₂ Fe ₄ As ₄ F ₂	0.0	α	653
		β	608
		γ	1600
		δ	573
	1.0	α	667
		β	625
		γ	1633
		δ	573
	2.0	α	684
		β	643
		γ	1666
		δ	559

Fig.7.7 shows evolution of FSs with Hubbard U for the three different 12442 compounds. It is apparent from Fig.7.7(A)a, b that due to electron correlation two innermost nearly degenerate electron like FSs around Γ -point vanish for $U = 1.0$ eV which is a signature of correlation induced Lifshitz transition. On the other hand, the inner two hole like FSs shrink. Therefore, there is simultaneous electron as well as hole band renormalization induced by Hubbard correlation. Now as U is increased to 2.0 eV, two inner nearly degenerate hole like FSs around Γ -point vanish leading to topological transition again. Similar kind of correlation induced Lifshitz like topological transition is revealed from investigation of FS in RbCa₂Fe₄As₄F₂ (Fig.7.7(B)) and CsCa₂Fe₄As₄F₂ (Fig.7.7(C)) also. In Fig.7.8(a), (b), (c) we have presented change in the total density of states with Hubbard correlation in KCa₂Fe₄As₄F₂, RbCa₂Fe₄As₄F₂ and CsCa₂Fe₄As₄F₂ respectively. It

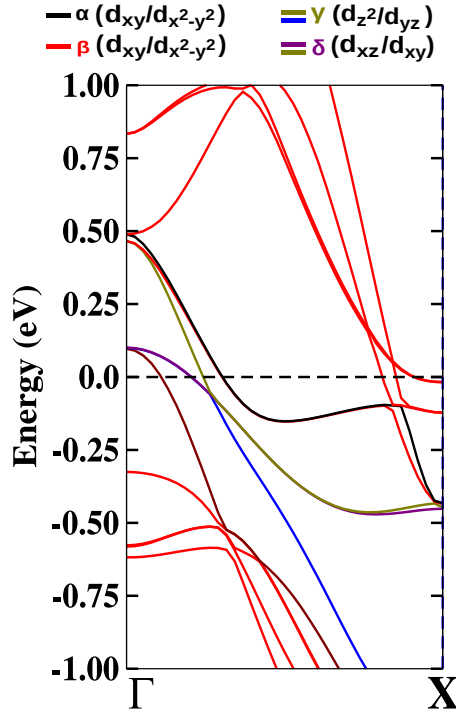


Figure 7.9: [142] Band structure along Γ -X direction used to measure bandwidth. Hole like bands with different orbital characters around Γ -point are marked as α , β , γ , and δ .

is clear that there is a continuous peak shift of the total DOS towards the occupied states below the E_F with increasing correlation. At $U = 1.0$ eV the peak shifts very slightly below the E_F . If the U is increased further to 2.0 eV, there is a visible decrease in DOS at E_F due to correlation induced Lifshitz transition of both the electron as well as hole like bands. This decrement in DOS at E_F becomes further prominent at $U = 3.0$ eV. Therefore, total DOS also divulge the signature of correlation induced Lifshitz transition. This may be one of the reasons as to why T_c decreases at or above Lifshitz transition.

Fig.7.10 depicts the comparative bandstructures of various 12442 compounds within GGA and GGA+SOC calculations. It is very much clear that there is only a little quantitative modifications in the electronic structure due to incorporation of SOC for all the three 12442 compounds. If we look at the bandstructure around Γ -point along the Γ -X direction, the degeneracy of the upper lying degenerate hole like bands is lifted. Energy of one of the bands is lowered and the other one remains same. Degeneracy of the two lower lying degenerate bands are also lifted. Therefore, SOC leads to band splitting of the degenerate

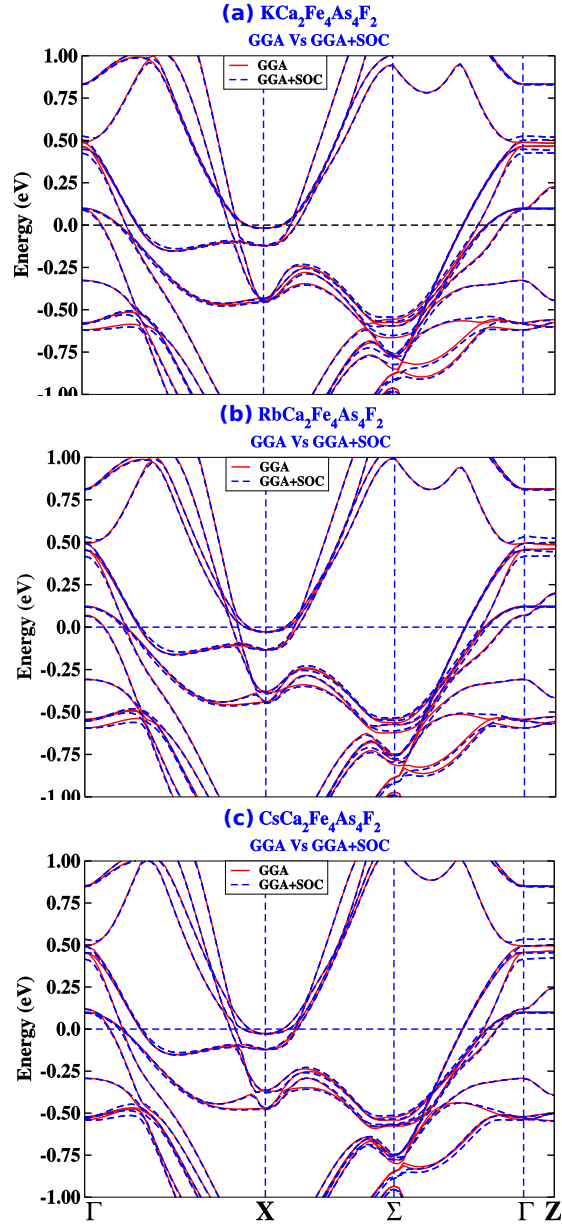


Figure 7.10: [142] Comparison of calculated band structures within GGA and GGA + Spin Orbit Coupling (SOC) for (a) $\text{KCa}_2\text{Fe}_4\text{As}_4\text{F}_2$, (b) $\text{RbCa}_2\text{Fe}_4\text{As}_4\text{F}_2$, and (c) $\text{CsCa}_2\text{Fe}_4\text{As}_4\text{F}_2$ respectively.

bands in these compounds. The band splitting due to SOC becomes more prominent in $\text{RbCa}_2\text{Fe}_4\text{As}_4\text{F}_2$ and $\text{CsCa}_2\text{Fe}_4\text{As}_4\text{F}_2$ than $\text{KCa}_2\text{Fe}_4\text{As}_4\text{F}_2$. On the other hand, degeneracy of the hole like bands along Γ -Z direction is also heaved. There is no appreciable changes in the electron like bands due to SOC.

7.4 Wannier fitted band structure of 12442 compounds

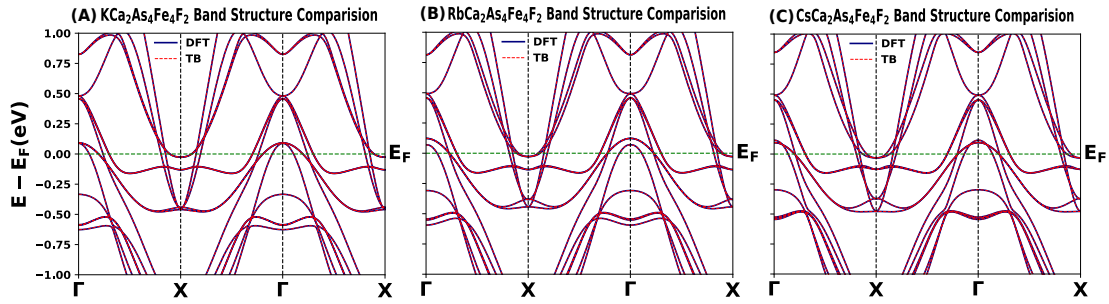


Figure 7.11: [142] Tight binding fitted band structures of (A) $\text{KCa}_2\text{Fe}_4\text{As}_4\text{F}_2$, (B) $\text{RbCa}_2\text{Fe}_4\text{As}_4\text{F}_2$, and (C) $\text{CsCa}_2\text{Fe}_4\text{As}_4\text{F}_2$.

We have used the Wannier function technique [215, 216, 217, 218] to construct the maximally localized Wannier functions (MLWF) from twenty Fe-3d orbitals and obtained the tight binding fitted low energy band structure for the three 12442 compounds. The transfer integrals $-t_{ij}(\mathbf{R}) = \langle \phi_{i0} | H_{KS} | \phi_{j\mathbf{R}} \rangle$, are also calculated from the maximally localized Wannier basis and Kohn-Sham Hamiltonian.

In Fig.7.18 we present the comparison of DFT calculated BNS with the Wannier fitted tight binding (TB) band structure. We have analyzed the electronic structure of the 12442 compounds by performing TB parametrization of Kohn-Sham Hamiltonian by considering the following five band model –

$$H = \sum_i n_i \epsilon_i + \sum_{i \neq j} t_{ij} c_i^\dagger c_j \quad (1)$$

where ϵ_i represents the site energy of an electron at site i , t_{ij} represents the hopping pa-

parameter between the i th and j th sites, c_i^\dagger and c_j are the creation and annihilation operators at the respective sites. We get an effective Hamiltonian like Eq.(1) by constructing twenty maximally localized Wannier functions freezing states in finite energy window above and below the E_F . The matrix elements of the original Kohn-Sham Hamiltonians are derived in the Wannier basis which can be directly linked to ϵ_i and t_{ij} parameters. It is very clear from Fig.7.18 (A),(B),(C) that we have achieved a perfect fitting between the DFT and TB band structure in a low energy window (-1 eV to 1 eV) around the E_F with the constructed MLWFs for the three 12442 compounds.

Table 7.4: Nearest neighbor (NN) hoppings t_{ij} (in eV) from maximally projected Wannier function calculation

KCa ₂ Fe ₄ As ₄ F ₂					
t_{ij} in eV	d_{z^2}	d_{xz}	d_{yz}	$d_{x^2-y^2}$	d_{xy}
d_{z^2}	-0.487	-0.014	-0.070	-0.132	0.395
d_{xz}	0.014	0.049	-0.232	0.017	0.005
d_{yz}	0.070	-0.232	-0.248	-0.011	0.055
$d_{x^2-y^2}$	-0.132	-0.017	0.011	0.093	0.240
d_{xy}	0.395	-0.005	0.055	0.240	-0.249
RbCa ₂ Fe ₄ As ₄ F ₂					
d_{z^2}	-0.528	-0.023	-0.031	-0.136	0.397
d_{xz}	-0.023	0.033	-0.249	0.038	0.001
d_{yz}	-0.031	-0.249	-0.247	-0.010	-0.023
$d_{x^2-y^2}$	-0.136	-0.038	-0.010	0.102	0.224
d_{xy}	-0.397	-0.001	-0.023	-0.224	-0.233
CsCa ₂ Fe ₄ As ₄ F ₂					
d_{z^2}	-0.528	-0.005	0.010	-0.128	0.390
d_{xz}	0.005	0.044	-0.248	0.066	0.004
d_{yz}	-0.010	-0.248	-0.241	0.016	-0.010
$d_{x^2-y^2}$	-0.128	-0.066	-0.016	0.113	0.208
d_{xy}	0.390	-0.004	0.010	0.208	-0.223

We have presented the main diagonal nearest neighbor (NN) in plane intra as well as inter orbital hopping parameters (t_{ij}) in the Table - 7.4. The intra (inter) orbital NN hoppings have been calculated by projecting the MLWFs to the atomic orbitals. From Table - 7.4 it is evident that the NN intra-orbital hopping is maximum in d_{z^2} orbitals, whereas it is minimum in d_{xz} orbitals. The value of t_{ij} increases from 0.487 eV (sign neglected) to 0.528 eV as K is replaced by Rb or Cs. The inter-orbital hopping of d_{z^2} is maximum

with d_{xy} , also having moderate value with $d_{x^2-y^2}$. The value does not vary much due to replacement of K with Rb or Cs. Now if we look into the d_{xz} orbitals, their intra-orbital hopping is very small, whereas its inter orbital hopping with d_{yz} is quite large. The intra-orbital hopping of d_{xz} remains small in all the compounds. It is notable that intra-orbital hopping in $d_{x^2-y^2}$ is small (0.093 eV) in $\text{KCa}_2\text{Fe}_4\text{As}_4\text{F}_2$ which increases gradually in $\text{RbCa}_2\text{Fe}_4\text{As}_4\text{F}_2$ (0.102 eV) and $\text{CsCa}_2\text{Fe}_4\text{As}_4\text{F}_2$ (0.113 eV). The inter-orbital hopping of $d_{x^2-y^2}$ with d_{xy} is quite large and a decreasing trend is noticed as K is replaced with Rb or Cs. Intra orbital hopping in d_{xy} decreases gradually with respect to $\text{KCa}_2\text{Fe}_4\text{As}_4\text{F}_2$ in Rb or Cs based 12442 compounds. Therefore, the main features observed in intra as well as inter-orbitals hopping may be summarized as below –

- i) unlike many of the iron based superconductors like LaFeAsO , BaFe_2As_2 , KFe_2As_2 , FeSe , FeTe [219], intra-orbital hopping in d_{z^2} is much larger than in $d_{x^2-y^2}$ and inter-orbital hopping of d_{z^2} with other orbitals is also significant.
- ii) The intra-orbital inplane hopping of d_{yz} is nearly equal to that of d_{xy} in $\text{KCa}_2\text{Fe}_4\text{As}_4\text{F}_2$, but it becomes higher in case of $\text{RbCa}_2\text{Fe}_4\text{As}_4\text{F}_2$ and $\text{CsCa}_2\text{Fe}_4\text{As}_4\text{F}_2$. There is significant amount of inter-orbital hopping in both d_{yz} and d_{xy} .
- iii) The intra-orbital hopping of d_{xy} and d_{yz} which have higher partial DOS at the E_F than other orbitals, decreases gradually as K is substituted with Rb or Cs. This might be related to the gradual reduction of superconducting transition temperature in $\text{RbCa}_2\text{Fe}_4\text{As}_4\text{F}_2$ and $\text{CsCa}_2\text{Fe}_4\text{As}_4\text{F}_2$. The chemical pressure induced by Rb, Cs affects the hopping as well as orbital selective superconductivity. Thus, the superconductivity in these compounds might be tuned by influencing intra orbital hopping orbital selectively, inducing chemical pressure on FeAs layers.

7.5 Orbital Anisotropy

To understand the general features of electronic structure we present density of states (DOS), band structure (BS) and orbital projected Fermi surface (FS) of the three 12442

compounds in this section. To resolve the orbital character of the electronic structure, we have used the default representation implemented in *ab initio* calculations where the x and y directions are defined to be along the next nearest Fe-Fe bonds and x, y axes are 45° rotated with respect to conventional axes along nearest neighbor Fe-Fe bonds. Therefore, Γ -M direction is parallel to the $k_x(k_y)$ directions in the reciprocal space. In Fig.7.12, the orbital contribution of different Fe-3d orbitals to DOS is presented. From Fig.7.12(a), it is noted that although all the five Fe-3d orbitals have finite contribution to the partial DOS at the Fermi level (Fl), three orbitals *i.e.*, d_{xy} , d_{xz} , d_{yz} have significantly greater contribution in comparison to $d_{x^2-y^2}$ and d_{z^2} in case of K12442. This feature of orbital resolved partial DOS is very similar in other two compounds *i.e.*, Rb12442 (Fig.7.12(b)) and Cs12442 (Fig.7.12(c)). Only slight peak shift of partial DOS is observed in the later two compounds. Therefore, we have chosen d_{xy} , d_{xz} , d_{yz} which would have higher impact on physical properties due to larger partial DOS at the Fl, to discuss the orbital evolution of BS and FS.

12442 Fe based compounds have six hole like bands around Brillouin zone (BZ) centre and four electron like bands around BZ corner having mixed multiorbital character [142]. Of the hole like bands, two higher energy and two lower energy bands are nearly degenerate. The orbital evolution of BS has been presented in Fig.7.13 along two different directions of BZ (*i.e.*, M_X & M_Y) from BZ centre (*i.e.*, Γ -point). The M_X and M_Y points are crystallographically symmetric due to tetragonal symmetry of the 12442 compounds. The BS of all the three compounds presented in Fig.7.13(a, b, c) reveal direction dependent orbital evolution of most of the bands along crystallographically high symmetry directions. For the upper lying three hole bands, as one moves along Γ - M_X direction, the d_{xy} orbital character gradually transforms into d_{yz} . The lower lying two nearly degenerate bands dominantly remain of d_{xz} character along Γ - M_X , although contribution from d_{xy} starts becoming significant. Another lower band which is mostly d_{xz} in nature around the Γ -point, starts showing increased d_{yz} contribution along M_X . In contrast, along the Γ - M_Y direction, it is very much clear that orbital evolution of bands is quite different in compar-

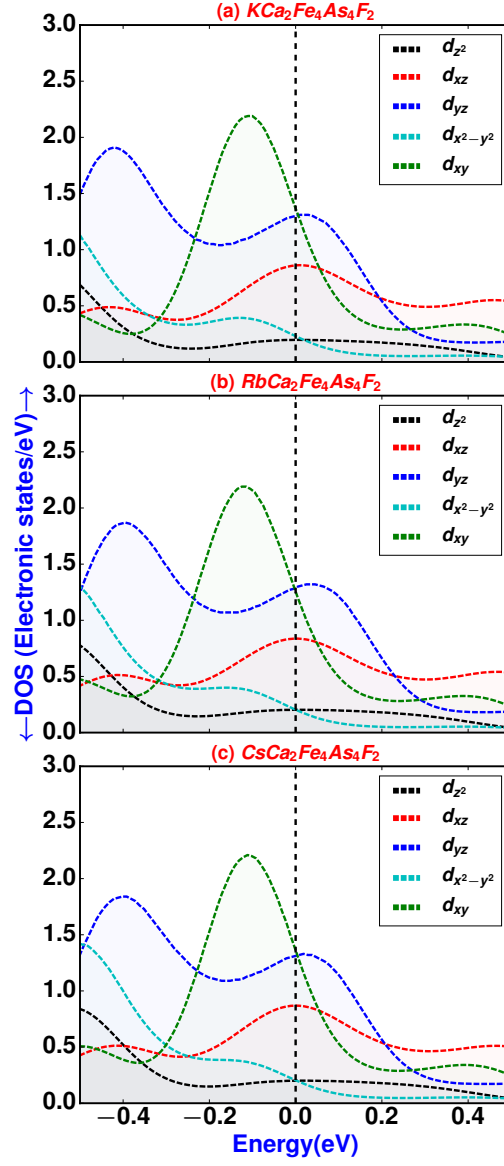


Figure 7.12: (Colour online) Partial density of states of different Fe-3d orbitals for (a) $\text{KCa}_2\text{Fe}_4\text{As}_4\text{F}_2$, (b) $\text{RbCa}_2\text{Fe}_4\text{As}_4\text{F}_2$, and (c) $\text{CsCa}_2\text{Fe}_4\text{As}_4\text{F}_2$.

ison to its evolution along Γ - M_X . The upper three hole bands around Γ -point, transforms from d_{yz} to d_{xy} before turning into d_{yz} again at around M_Y along Γ - M_Y . On the otherhand, the two degenerate bands around the FI with mostly d_{xz} character (around Γ) start showing increased d_{yz} nature (around M_Y). Another low lying band near FI, which is dominantly d_{xz} around Γ -point transform into d_{yz} along Γ - M_Y direction. Therefore, the orbital anisotropy of bands is a common feature of the electronic structure of all the three 12442 compounds. This orbital anisotropy is also reflected in the FSs of these compounds.

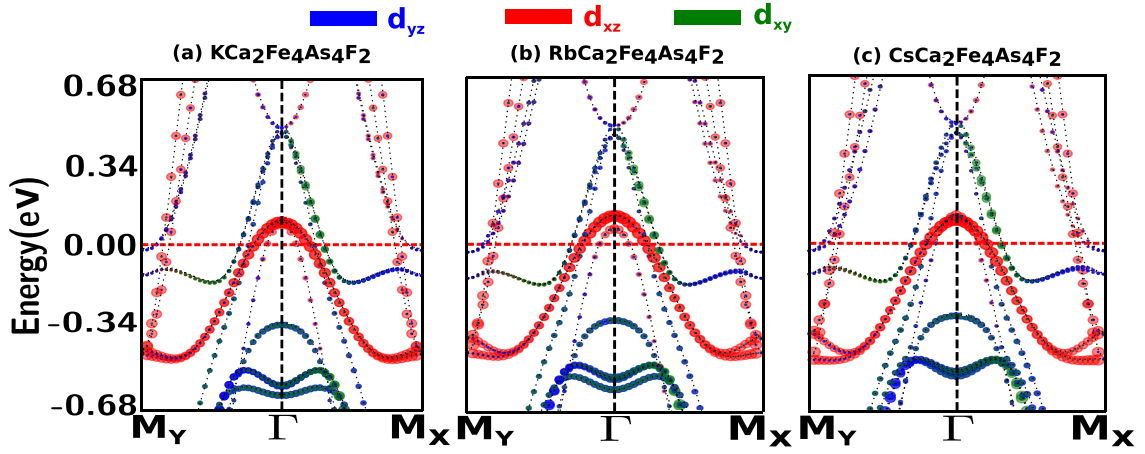


Figure 7.13: (Colour online) Orbital character of different bands for (a) $\text{KCa}_2\text{Fe}_4\text{As}_4\text{F}_2$, (b) $\text{RbCa}_2\text{Fe}_4\text{As}_4\text{F}_2$, and (c) $\text{CsCa}_2\text{Fe}_4\text{As}_4\text{F}_2$. The contribution from each orbital is shown with individual colour and orbital weight are proportional to size of the circles.

The orbital evolution of FSs is presented in Fig. 7.14. Theoretical studies reveal that the 12442 compounds have six hole pockets around Γ -point, of which outer two outermost and two second-third inner most FSs are degenerate leading to four distinct hole pockets [142]. There exists four electron pockets around the M-point out of which the two innermost are degenerate in case of $\text{KCa}_2\text{Fe}_4\text{As}_4\text{F}_2$. The experimental ARPES measurement shows five distinct hole pockets and one small electron pocket [220]. In Fig. 7.14, the 2d cross section of the FSs along Γ -M with relative contributions from different orbitals for the three compounds are shown. The outer two hole pockets are mostly d_{xy}/d_{yz} character. The second innermost hole pocket have dominant d_{xz} character, whereas the innermost hole pocket is d_{xy}/d_{yz} in nature. Now if we look into the evolution of orbital character of electron pockets along Γ - M_X , the two innermost pockets have dominant d_{yz} character.

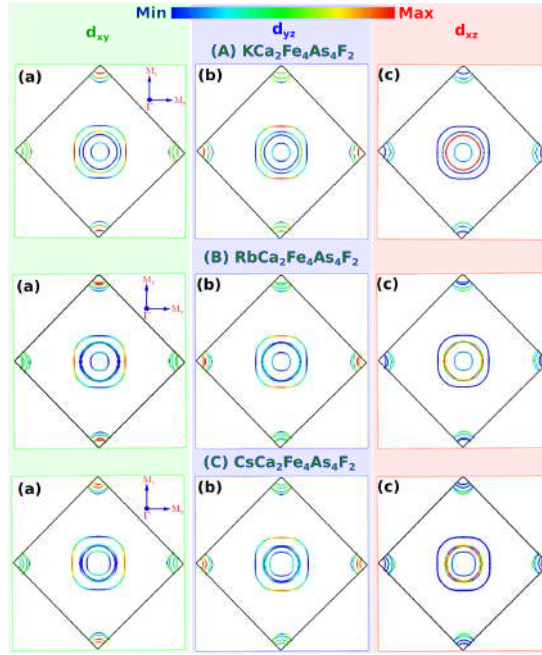


Figure 7.14: (Colour online) Calculated orbital character of the Fermi surfaces for (A) $\text{KCa}_2\text{Fe}_4\text{As}_4\text{F}_2$, (B) $\text{RbCa}_2\text{Fe}_4\text{As}_4\text{F}_2$, and (C) $\text{CsCa}_2\text{Fe}_4\text{As}_4\text{F}_2$. The orbital nature d_{xy} , d_{yz} and d_{xz} are shown in column (a), (b) and (c) respectively. The relative contribution of the different Fe 3d orbitals for different FSs are shown using varying colours. The "red" colour denotes 'maximum' contribution while "blue" colour denotes 'minimum' contribution.

On the other hand if the orbital character along Γ -M_Y is looked into, the two innermost electron FSs are dominantly d_{xy} nature. Thus, the orbital anisotropy of the BS and Fermi pockets is very much clear from our discussions.

These kinds of orbital anisotropy on Fermi pockets may raise the possibility of anisotropy in superconducting gap on the hole and electron like pockets. ARPES measurements have shown Fermi surface dependent superconducting gaps [220]. A more detailed study is necessary to detect anisotropy in superconducting gap. It is very important to note that the orbital selective anisotropic electronic structure has been observed to lead to band reconstruction and nematic splitting in previously existing families of iron based superconductors like $\text{Ca}(\text{Fe}_{1-x}\text{Co}_x)_2\text{As}_2$ [203], BaFe_2As_2 [204], FeSe [205] *etc.* In both the systems due to transition from tetragonal to orthorhombic phase, the C_4 symmetry is broken which finally leads to degeneracy lifting of d_{xz} and d_{yz} orbital. This degeneracy lifting in turn leads to band reconstruction and nematic like splitting of bands. As the hybrid 12442 compounds don't show any structural transition, it is very important to investigate the effect of its orbital selective anisotropy on the electronic properties. These compounds gives us a unique opportunity to explore orbital anisotropy and nematic like band splitting in tetragonal phase without any structural transition.

7.6 Intrinsic band splitting

Nematic like band splitting is induced in 12442 compounds due to C_{2v} ($m2m$) local Fe-site symmetry in tetragonal phase. In its constituents 122 and 1111 compounds Fe atom sits at $4d$ site, therefore local point group symmetry is D_{2d} ($\bar{4}m2$) because Fe layers are at $z = 1/4$ and $z_{As1} = z_{As2}$ (Fig.7.1). On the other hand, in case of hybrid 12442 compounds Fe sits at the $8g$ site, whose local symmetry is $m2m$ *i.e.*, C_{2v} as the Fe layers are displaced from $z = 1/4$ and $z_{As1} \neq z_{As2}$ (Fig.7.1) [207]. This symmetry lowering lifts degeneracy of d_{xz} and d_{yz} in tetragonal phase which in turn induce intrinsic band splitting in 12442

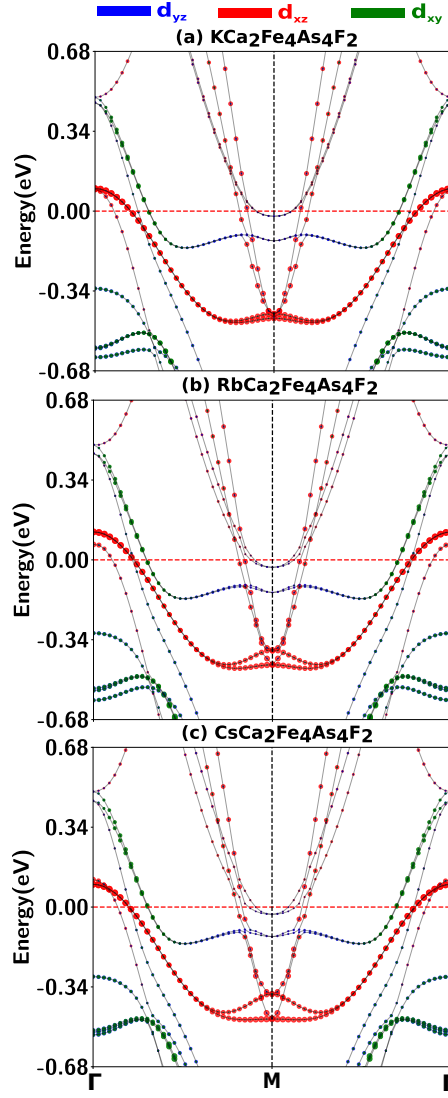


Figure 7.15: (Colour online) Orbital character of different bands for (a) $\text{KCa}_2\text{Fe}_4\text{As}_4\text{F}_2$, (b) $\text{RbCa}_2\text{Fe}_4\text{As}_4\text{F}_2$, and (c) $\text{CsCa}_2\text{Fe}_4\text{As}_4\text{F}_2$. The contribution from each orbital is shown with individual colour and orbital weight are proportional to size of the circles.

compounds.

In case of other IBSCs, it has been observed that the effect of nematic splitting (NS) of d_{xz} and d_{yz} orbitals is maximum at the electron like bands around the BZ corner (M-point) [209]. To show the nature of orbital character of the electron like bands around the M-point, we have presented orbital resolved BS for all the three 12442 compounds in Fig.7.16. It is conspicuous that the four electron bands crossing the FI mostly have d_{xz} character. One hole like band coming from Γ -point having d_{yz} character merges with

the electron band. This kind of orbital anisotropy induces orbital selective reconstruction of bands and band splitting. To discuss the splitting of bands, we have presented the calculated BS within GGA around the M-point of the Brillouin zone for hybrid 12442 compounds in Fig.7.16. To observe detailed splitting of the bands, zoomed BS in a narrow energy window is depicted in the inset. We have marked the bands having mostly d_{xz} character with "red" colour and d_{yz} character with "blue". Fig.7.16(a) clearly depicts that there are two nematic like splitting of the electron bands – one near the FI, other away from it. We have marked the two splittings as BS1 and BS2. In case of BS2, the reconstructed upper lying electron band is denoted with black colour as it has mixed $d_{xz/yz}$ nature, whereas the lower energy band is marked with red colour (zoomed inset) as it is mostly of d_{xz} nature. Our calculated electronic structure within GGA shows that there is no splitting of the band near FI (*i.e.*, BS1 = 0.0) for K12442. But there is finite splitting for the bands away from FI and BS2 = 8.6 meV. In case of Rb12442 (Fig.7.16(b)), a finite gap of 5.0 meV opens up at the electron bands. The gap BS2 around is 6.5 meV for Rb12442. Thus as one moves from K12442 to Rb12442, BS1 increases, but BS2 decreases. Band splittings BS1 and BS2 are 10.5 meV and 5.2 meV respectively for Cs12442. So our discussions on calculated BS within GGA reveal gradual increase in BS1 for K→Rb→Cs12442. On the otherhand, a gradual reduction in BS2 is found for K→Rb→Cs12442. This feature of splitting can be attributed to chemical pressure induced orbital selective evolution of electronic structure in hybrid 12442 compounds as discussed already in this chapter.

Spin orbit coupling (SOC) induced splitting has been demonstrated in all the Fe based superconductors [210]. Therefore, it is necessary to include SOC for extracting the fine features of the band reconstruction [215]. To get more detailed electronic structure which includes SOC, fully relativistic band calculation have been performed. The results are presented in Fig.7.17. It is quite evident Fig.7.17(a), that the introduction of SOC opens up gap (BS1) of 14.4 meV in K12442. BS2 is also increased to 10.0 meV. Therefore, SOC largely impacts nematic band reconstruction in K12442. In case of Rb12442, both BS1

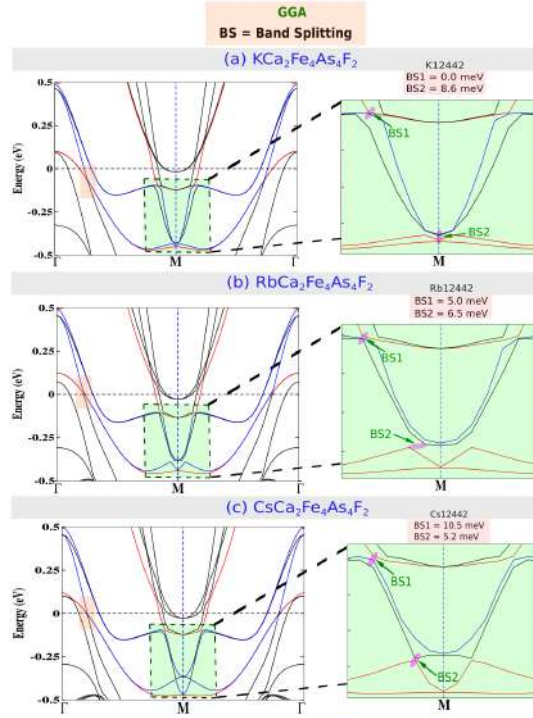


Figure 7.16: (Colour online) Splitting of bands around Brillouin zone corner for (a) $\text{KCa}_2\text{Fe}_4\text{As}_4\text{F}_2$, (b) $\text{RbCa}_2\text{Fe}_4\text{As}_4\text{F}_2$, and (c) $\text{CsCa}_2\text{Fe}_4\text{As}_4\text{F}_2$ calculated with GGA.

Table 7.5: Band splitting (BS) of d_{xz} & d_{yz}

$\text{KCa}_2\text{Fe}_4\text{As}_4\text{F}_2$		
BS in meV	GGA	GGA+SOC
BS1	0.00	14.4
BS2	8.6	10.0
$\text{RbCa}_2\text{Fe}_4\text{As}_4\text{F}_2$		
BS in meV	GGA	GGA+SOC
BS1	5.0	6.0
BS2	6.5	10.0
$\text{CsCa}_2\text{Fe}_4\text{As}_4\text{F}_2$		
BS in meV	GGA	GGA+SOC
BS1	10.5	13.0
BS2	5.2	24.0

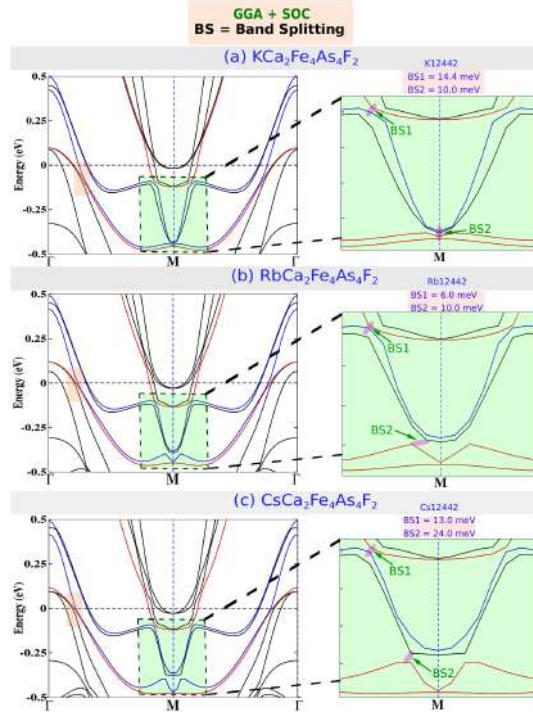


Figure 7.17: (Colour online) Splitting of bands around brillouin zone corner for (a) $\text{KCa}_2\text{Fe}_4\text{As}_4\text{F}_2$, (b) $\text{RbCa}_2\text{Fe}_4\text{As}_4\text{F}_2$, and (c) $\text{CsCa}_2\text{Fe}_4\text{As}_4\text{F}_2$ calculated with GGA + spin orbit coupling (SOC).

and BS2 increases to 6.0 meV and 10.0 meV respectively due to SOC (Fig.7.17(b)). The values of band splitting is enhanced very much in GGA+SOC calculation for Cs12442 (Fig.7.17(c)). BS1 and BS2 become 13.0 meV and 24.0 meV respectively. Therefore, the band splitting is inflated in all the three compounds due to SOC. Another feature worth noting is that the hole like bands around Γ -point having d_{xz}/d_{yz} character (pink shaded) which touches each other around the FI in GGA calculations (Fig.7.16), are splitted in GGA+SOC calculations. We have tabulated the GGA as well as GGA+SOC calculated values of BS1 and BS2 for all the three compounds in Table.7.5. From the above discussions it is conspicuous that there appears finite nematic like band splitting in 12442 family of Fe based superconductors. The recently observed enhanced electroresistance in K12442 compounds may be attributed to the nematic like fluctuations present in the compound [207]. For a rigorous conclusion, same kind of experiments should be performed on other 12442 compounds.

7.7 Crystal field splitting

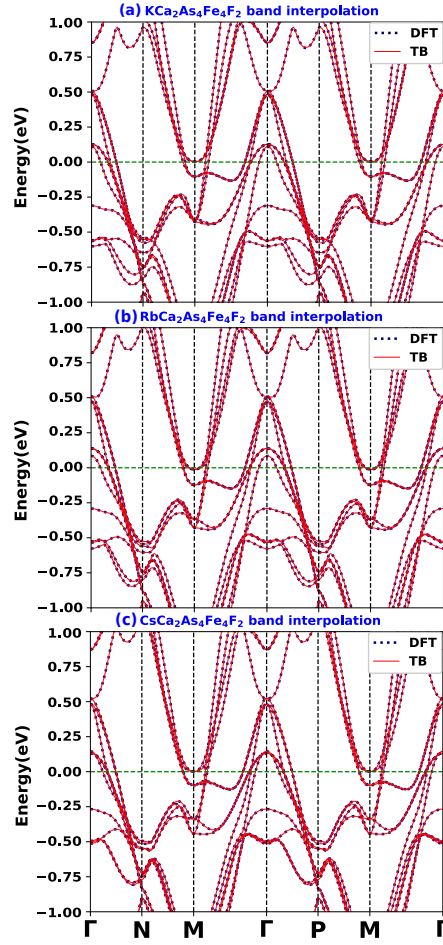


Figure 7.18: Tight binding fitted band structure of (a) $\text{KCa}_2\text{Fe}_4\text{As}_4\text{F}_2$, (b) $\text{RbCa}_2\text{Fe}_4\text{As}_4\text{F}_2$, and (c) $\text{CsCa}_2\text{Fe}_4\text{As}_4\text{F}_2$.

Perfect fitting of the DFT and TB electronic structure has been achieved for a low energy window with the constructed MLWFs (Fig.7.18 (a),(b),(c)).

We have investigated the crystal field splitting of the Fe-3d orbitals in the three 12442 compounds from the Wannier fitted DFT band structures. Twenty Fe-3d orbitals are used to describe the low energy physics of the system which might be useful to understand nematicity in these family of iron based superconductors. The electronic bands around the E_F in Fe based superconductors are mainly derived from the five Fe-3d orbitals with mixed multi-orbital character. The FeAs layer which is common in all the families of iron based superconductors, has tetrahedral symmetry. In general tetrahedral crystal field splits

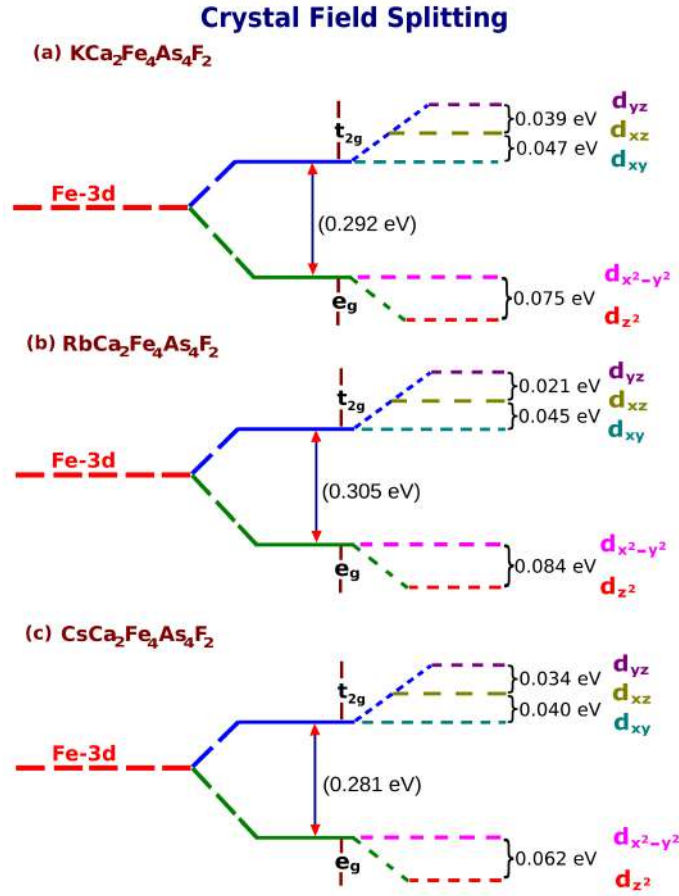


Figure 7.19: Calculated crystal field splitting of Fe-3d orbitals in the tight binding parametrization for (a) $\text{KCa}_2\text{Fe}_4\text{As}_4\text{F}_2$, (b) $\text{RbCa}_2\text{Fe}_4\text{As}_4\text{F}_2$, (c) $\text{CsCa}_2\text{Fe}_4\text{As}_4\text{F}_2$.

the d -orbitals into triply degenerate t_{2g} level consisting d_{xy} , d_{xz} , d_{yz} orbitals having higher energy and doubly degenerate e_g level consisting $d_{x^2-y^2}$, d_{z^2} orbitals with lower energy. In Fe based compounds due to the combined effect of anion crystal field and surrounding cations, the t_{2g} as well as e_g level splits further.

In Fig.7.19 we have presented a pictorial representation of the crystal field splitting in the three 12442 compounds with energy difference between orbitals. From Fig.7.19(a) it is conspicuous that the five fold degenerate atomic Fe-3d orbitals split into t_{2g} having higher energy and e_g level having lower energy due to tetrahedral symmetry of the FeAs layers. The t_{2g} level splits further with d_{yz} having the highest energy and d_{xy} having the lowest energy. The e_g level also splits into $d_{x^2-y^2}$ and d_{z^2} with the later having energy lower than the former. In case of $\text{KCa}_2\text{Fe}_4\text{As}_4\text{F}_2$, the degeneracy of d_{yz} and d_{xz} is lifted, with d_{yz} hav-

ing energy slightly higher than d_{xz} due to C_{2v} symmetry of Fe atoms in the compound as discussed earlier. There exist a splitting of 0.039 eV between d_{yz} and d_{xz} . Now if we look into Fig. 7.19(b),(c), it is very much evident that the d_{yz} orbital is elevated in energy with respect to d_{xz} orbital. The energy splitting between d_{yz} & d_{xz} is 0.021 eV and 0.034 eV respectively for Rb12442 and Cs12442. The energy difference between d_{xz} and d_{xy} decreases gradually: 0.047 eV, 0.045 eV, 0.040 eV for K12442, Rb12442 and Cs12442 respectively. These values of splitting are much lower than that in 1111 compounds like LaFeAsO and comparable to 122 compounds like KFe₂As₂ [208]. Now if we examine e_g levels, the splitting between $d_{x^2-y^2}$ and d_{z^2} levels are quite large for all the three compounds: 0.075 eV, 0.084 eV, 0.062 eV for K12442, Rb12442 and Cs12442 respectively. This splitting is quite large in comparison to the constituent 122 compounds, but comparable to the 1111 compounds. It is apparent that the crystal field splitting between the t_{2g} and e_g multiplet is quite significant – 0.292 eV in KCa₂Fe₄As₄F₂ which increases further to 0.305 eV in RbCa₂Fe₄As₄F₂ and 0.281 eV in CsCa₂Fe₄As₄F₂. These values are higher than the crystal field splitting in 1111 compound, whereas significantly lower than the splitting in 122 compounds. Therefore, the effect of alkali metal ion like K, Rb, Cs on the crystal field splitting of Fe-3d orbitals is reduced in 12442 compounds in comparison to that in 122 compounds.

7.8 Conclusions

We have presented a detailed electronic structure results on the three newly discovered 12442 compounds using DFT based first principles calculations. Our study reveals possible preference of GGA functionals over LDA functionals as far as the study of the effect of electronic structure on superconductivity in these compounds is concerned. The mixed multi-orbital multi-band nature of bands in all the three 12442 compounds with most contribution from Fe-3d orbitals is evident from band structures as well density of states. Unlike 1144 hybrid iron based superconductors, 12442 compounds have negligi-

ble contributions from As-4 p_z to its electronic structure as well as density of states at the Fermi level. Due to chemical pressure induced by replacement of K with atoms of higher atomic radius like Rb or Cs, there is an orbital selective shift of bands and the degeneracy of the bands lying away from the E_F are lifted. Appearance of a new band around Γ -point near 0.10 Ry energy above E_F due to chemical pressure induced by Rb, Cs is perceived. Peak shift in partial DOS of d_{xy} (d_{xz}) towards (away) from the E_F in presence of Rb or Cs signify orbital selective doping effect of chemical pressure in 12442 compounds. The orbital projected FSs reveal multi-orbital character of the six hole like FSs around zone centre and four electron like FSs around zone corner. Our results are consistent with the electronic structure observed by recent ARPES studies [211] where large hole pockets and comparatively smaller electron pockets due to the electron bands on the verge of Lifshitz transition, are clearly visible for $\text{KCa}_2\text{Fe}_4\text{As}_4\text{F}_2$. Contrary to most of the Fe based superconductors very poor nesting between the electron and hole like FSs which is evident from our theoretical as well as experimental study, lead to an in-commensurate neutron spin resonance mode. Effect of electronic correlation treated within GGA+U shows orbital selective evolution of electronic structure, leading to orbital selective Lifshitz transition. The studies on MLWF projected, tight binding fitted band structure reveal unique feature of intra orbital hopping. The intra orbital hopping in d_{z^2} orbital is larger than hopping in $d_{x^2-y^2}$ orbital. This is in sharp contrast with other iron based compounds where larger hopping in $d_{x^2-y^2}$ orbital than d_{z^2} is observed. The gradual reduction in superconducting transition temperature in $\text{RbCa}_2\text{Fe}_4\text{As}_4\text{F}_2$ and $\text{CsCa}_2\text{Fe}_4\text{As}_4\text{F}_2$ in comparison to $\text{KCa}_2\text{Fe}_4\text{As}_4\text{F}_2$ may be associated with decreased intra orbital hopping of d_{xy} and d_{yz} caused by the gradual increase in chemical pressure due to Rb and Cs. Orbital anisotropy and nematic like splitting in three newly discovered 12442 compounds are also explored. Direction dependent evolution of orbital character for different bands as well as Fermi pockets are direct reflection of orbital anisotropy in these compounds. Degeneracy of $d_{xz/yz}$ is heaved due to changes in local Fe-site symmetry from D_{2d} in parent 1111 and 122 compounds to C_{2v} in hybrid 12442 compounds. This induces orbital selective band recon-

struction and nematic like band splitting in the tetragonal phase. Values of the splittings are enhanced in GGA+SOC calculations in comparison to that of the GGA calculations. More experiments are needed to confirm this for Rb12442 and Cs12442. Nematic like splitting driven by orbital reconstruction hints towards the fact that orbital degrees of freedom are very important in 12442 compounds. The quantitative splitting of $d_{xz/yz}$ is calculated with our crystal field calculations using tight binding fitted band structure with MLWF. The splitting is nearly equal in K12442 and Cs12442, whereas slightly smaller splitting is observed in Rb12442. The splitting between t_{2g} and e_g multiplet have intermediate values in comparison to parent 1111 and 122 compounds. Therefore, from our discussions about crystal field splitting, it may be concluded that nematic like splitting is inherently present in 12442 compounds due to its local structural restriction.

Bibliography

- [1] Y. Kamihara, T. Watanabe, M. Hirano, and H. Hosono, J. Am. Chem. Soc. **130**, 3296 (2008).
- [2] Z. A. Ren, W. Lu, J. Yang, W. Yi, X. L. Shen, Z. C. Li, G.C. Che, X. L. Dong, L. L. Sun, F. Zhou and Z. X. Zhao, Chin. Phys. Lett. **25**, 2215 (2008).
- [3] S. Matsuishi, Y. Inoue, T. Nomura, T. Yanagi, M. Hirano, and H. Hosono, J. Am. Chem. Soc. **130**, 14428 (2008).
- [4] M. Fujioka, S. J. Denholme, M. Tanaka, H. Takeya, T. Yamaguchi and Y. Takano, Appl. Phys. Lett. **105**, 102602 (2014).
- [5] M. Rotter, M. Tegel, and D. Johrendt, Phys. Rev. Lett. **101**, 107006 (2008).
- [6] K. Kudo, K. Iba, M. Takasuga, Y. Kitahama, J. Matsumura, M. Danura, Y. Nogami and M. Nohara, Sci. Rep. **3**, 1478 (2013).
- [7] F. C. Hsu, J. Y. Luo, K. W. Yeh, T. K. Chen, T. W. Huang, P. M. Wu, Y. C. Lee, Y. L. Huang, Y. Y. Chu, D. C. Yan, M. -K. Wu, Proc. Nation. Acad. Sci. **105**, 14262 (2008).
- [8] J. H. Tapp, Z. Tang, B. Lv, K. Sasmal, B. Lorenz, P. C. W. Chu and A. M. Guloy, Phys. Rev. B **78**, 060505 (2008).
- [9] X. Wang, Q. Liu, Y. Lv, W. Gao, L. Yang, R. Yu, F. Li and C. Jin, Sol. Stat. Commun. **148**, 538 (2008), ISSN 0038-1098.
- [10] M. J. Pitcher, D. R. Parker, P. Adamson, S. J. C. Herkelrath, A. T. Boothroyd, R. M. Ibberson, M. Brunelli and S. J. Clarke, Chem. Commun. pp. **2008**, 5918-5920 (2008).
- [11] C. de la Cruz, Q. Huang, J. W. Lynn, J. Li, W. Ratcliff, J. L. Zarestky, H. A. Mook, G. F. Chen, J. L. Luo, N. L. Wang and P. Dai, Nature **453**, 899-902 (2008).
- [12] F. Chen, M. Xu, Q. Q. Ge, Y. Zhang, Z. R. Ye, L. X. Yang, Juan Jiang, B. P. Xie, R. C. Che, M. Zhang, A. F. Wang, X. H. Chen, D. W. Shen, J. P. Hu and D. L. Feng, Phys. Rev. X **1**, 021020 (2011).

- [13] X. H. Chen, T. Wu, G. Wu, R. H. Liu, H. Chen, D. F. Fang, *Nature* **453**, 761–762 (2008).
- [14] J. Zhao, Q. Huang, C. de la Cruz, S. Li, J. W. Lynn, Y. Chen, M. A. Green, G. F. Chen, G. Li, Z. Li, J. L. Luo, N. L. Wang and P. Dai, *Nat. Mater.* **7**, 953–959 (2008).
- [15] Villars, P., and L. D. Calvert, 1985, *Pearson’s Handbook of Crystallographic Data for Intermetallic Phases* (American Society for Metals, Metals Park, Ohio).
- [16] J. L. Niedziela, D. Parshall, K. A. Lokshin, A. S. Sefat, A. Alatas, and T. Egami, *Phys. Rev. B* **84**, 224305 (2011).
- [17] M. Rotter, M. Tegel, D. Johrendt, *Phys. Rev. Lett.* **101**, 107006 (2008).
- [18] L. Wang, Y. Qi, Z. Zhang, D. Wang, X. Zhang, Z. Gao, C. Yao and Y. Ma, *Supercond. Sci. Technol.* **23**, 054010 (2010).
- [19] P. M. Shirage, K. Miyazawa, H. Kito, H. Esaki and A. Iyo, *Appl. Phys. Express* **1**, 081702 (2008).
- [20] M. Yi, D. H. Lu, R. G. Moore, K. Kihou, C.-H. Lee, A. Iyo, H. Eisaki, T. Yoshida, A. Fujimori and Z.-X. Shen, *New J. Phys.* **14**, 073019 (2012).
- [21] X. C. Wang, Q. Q. Liu, Y. X. Lv, W. B. Gao, L. X. Yang, R. C. Yu, F. Y. Li, C. Q. Jin, *Solid State Communications* **148**, 538–540 (2008).
- [22] D. R. Parker, M. J. Pitcher, P. J. Baker, I. Franke, T. Lancaster, S. J. Blundell and S. J. Clark *Chem. Commun.*, **2009**, 2189–2191 (2009).
- [23] T. M. McQueen, A. J. Williams, P. W. Stephens, J. Tao, Y. Zhu, V. Ksenofontov, F. Casper, C. Felser and R. J. Cava, *Phys. Rev. Lett.* **103**, 057002 (2009).
- [24] D. Braithwaite, B. Salce, G. Lapertot, F. Bourdarot, C. Marin, D. Aoki and M. Hanfland, *J. Phys. Condens. Matter* **21**, 232202 (2009).

- [25] R. A. Zargar, A. Pal, A. K. Hafiz and V. P. S. Awana, *Journal of Superconductivity and Novel Magnetism* **27**, 897–901 (2014).
- [26] R. Hu, E. S. Bozin, J. B. Warren, and C. Petrovic, *Phys. Rev. B.* **80**, 214514 (2009).
- [27] N. Katayama, K. Kudo, S. Onari, T. Mizukami, K. Sugawara, Y. Sugiyama, Y. Kitahama, K. Iba, K. Fujimura, N. Nishimoto, M. Nohara and H. Sawa, *J. Phys. Soc. of Jap.* **82**, 123702 (2013).
- [28] A. Sala, H. Yakita, H. Ogino, T. Okada, A. Yamamoto, K. Kishio, S. Ishida, A. Iyo, H. Eisaki, M. Fujioka, Y. Takano, M. Putti and J.-i Shimoyama, *APEX* **7**, 073102 (2014).
- [29] H. Yakita, H. Ogino, T. Okada, A. Yamamoto, K. Kishio, T. Tohei, Y. Ikuhara, Y. Gotoh, H. Fujihisa, K. Kataoka, H. Eisaki and J.-ichi Shimoyama, *J. Am. Chem. Soc.* **136**, 846 (2014).
- [30] X. Wu, C. Le, Y. Liang, S. Qin, H. Fan and J. Hu, *Phys. Rev. B* **89**, 205102 (2014).
- [31] S. Kawasaki, T. Mabuchi, S. Maeda, T. Adachi, T. Mizukami, K. Kudo, M. Nohara and G.Q. Zheng, *Phys. Rev. B* **92**, 180508 (2015).
- [32] J. M. Tranquada, *Physics* **3**, 41 (2010).
- [33] S. Jiang, C. Liu, H. Cao, T. Birol, J. M. Allred, W. Tian, L. Liu, K. Cho, M. J. Krogstad, J. Ma, K. M. Taddei, M. A. Tanatar, M. Hoesch, R. Prozorov, S. Rosenkranz, Y. J. Uemura, G. Kotliar and N. Ni, *Phys. Rev. B* **93**, 054522 (2016).
- [34] H. Yakita, H. Ogino, A. Sala, T. Okada, A. Yamamoto, K. Kishio, A. Iyo, H. Eisaki and J. Shimoyama, *Supercond. Sci. Technol.* **28**, 065001 (2015) (6pp).
- [35] K. Kudo, Y. Kitahama, K. Fujimura, T. Mizukami, H. Ota and M. Nohara, *J. Phys. Soc. Jap.* **83**, 093705 (2014).
- [36] S. Fujitsu, S. Matsuishi and H. Hosono, *Int. Mater. Rev.* **57** 311 (2012).

- [37] K. Kudo, T. Mizukami, Y. Kitahama, D. Mitsuoka, K. Iba, K. Fujimura, N. Nishimoto, Y. Hiraoka and M. Nohara, J. Phys. Soc. Jap. **83**, 025001 (2014).
- [38] K. Kudo, Y. Kitahama, K. Fujimura, T. Mizukami, H. Ota, and M. Nohara, J. Phys. Soc. Jap. **83**, 093705 (2014).
- [39] T. Okada, H. Ogino, H. Yakita, A. Yamamoto, K. Kishio and J. Shimoyama, Physica C **505**, 1 (2014).
- [40] T. Xie, D. Gong, W. Zhang, Y. Gu, Z. Husges, D. Chen, Y. Liu, L. Hao, S. Meng, Z. Lu, S. Li and H. Luo, Supercond. Sci. Technol. **30**, 095002 (2017).
- [41] A. Iyo, K. Kawashima, T. Kinjo, T. Nishio, S. Ishida, H. Fujihisa, Y. Gotoh, K. Kihou, H. Eisaki and Y. Yoshida, J. Am. Chem. Soc. **138**, 3410–3415 (2016).
- [42] K. Kawashima, T. Kinjo, T. Nishio, S. Ishida, H. Fujihisa, Y. Gotoh, K. Kihou, H. Eisaki, Y. Yoshida and A. Iyo, J. Phys. Soc. of Jap. **85**, 064710 (2016).
- [43] W. Cheng, H. Lin, B. Shen and H.-H. Wen, Sci. Bull. **64**, 81–90 (2019).
- [44] J. M. Allred, K. M. Taddei, D. E. Bugaris, M. J. Krogstad, S. H. Lapidus, D. Y. Chung, H. Claus, M. G. Kanatzidis, D. E. Brown, J. Kang, R. M. Fernandes, I. Eremin, S. Rosenkranz, O. Chmaissem and R. Osborn Nat. Phys. **12**, 493–498 (2016).
- [45] E. Hassinger, G. Gredat, F. Valade, S. Rene de Cotret, O. Cyr-Choiniere, A. Juneau-Fecteau, J.-Ph. Reid, H. Kim, M. A. Tanatar, R. Prozorov, B. Shen, H. -H. Wen, N. D. Leyraud and L. Taillefer, Phys. Rev. B **93**, 144401 (2016).
- [46] W. R. Meier, T. Kong, U. S. Kaluarachchi, V. Taufour, N. H. Jo, G. Drachuck, A. E. Bohmer, S. M. Saunders, A. Sapkota, A. Kreyssig, M. A. Tanatar, R. Prozorov, A. I. Goldman, F. F. Balakirev, A. Gurevich, S. L. Budko and P. C. Canfield, Phys. Rev. B **94**, 064501 (2016).

- [47] A. Kreyssig, J. M. Wilde, A. E., Bohmer, W. Tian, W. R. Meier, B. Li, B. G. Ueland, M. Xu, S. L. Budko, P. C. Canfield, R. J. McQueeney and A. I. Goldman, Phys. Rev. B **97**, 224521 (2018).
- [48] W. Q. Meier, Q. -P. Ding, A. Kreyssig, S. L. Budko, A. Sapkota, K. Kothapalli, V. Borisov, R. Valentí, C. D. Batista, P. P. Orth, R. M. Fernandes, A. I. Goldman, Y. Furukawa, A. E. Böhmer and Paul C. Canfield, npj Q. Mat. **3**, 5 (2018).
- [49] A. Kreyssig, M. A. Green, Y. Lee, G. D. Samolyuk, P. Zajdel, J. W. Lynn, S. L. Bud'ko, M. S. Torikachvili, N. Ni, S. Nandi, J. B. Leao, S. J. Poulton, D. N. Argyriou, B. N. Harmon, R. J. McQueeney, P. C. Canfield and A. I. Goldman, Phys. Rev. B **78**, 184517 (2008).
- [50] U. S. Kaluarachchi, V. Taufour, A. Sapkota, V. Borisov, T. Kong, W. R. Meier, K. Kothapalli, B. G. Ueland, A. Kreyssig, R. Valentí, R. J. McQueeney, A. I. Goldman, S. L. Bud'ko, and P. C. Canfield, Phys. Rev. B **96**, 140501 (2017).
- [51] V. Borisov, P. C. Canfield and R. Valentí, Phys. Rev. B **98**, 064104 (2018).
- [52] Y. Liu, Y.-B. Liu, Z.-T. Tang, H. Jiang, Z.-C. Wang, A. Ablimit, W.-H. Jiao, Q. Tao, C.-M. Feng, Z.-A. Xu and G.-H. Cao, Phys. Rev. B **93**, 214503 (2016).
- [53] Y. Liu, Y.-B. Liu, Q. Chen, Z.-T. Tang, W.-H. Jiao, Q. Tao, Z.-A. Xu, G.-H. Cao, Sci. Bull. **61**(15), 1213–1220 (2016).
- [54] Y. Liu, Y.-B. Liu, Y.-L. Yu, Q. Tao, C.-M. Feng and G.-H. Cao, Phys. Rev. B **96**, 224510 (2017).
- [55] Z.-C. Wang, C.-Y. He, S.-Q. Wu, Z.-T. Tang, Y. Liu, A. Ablimit, C.-M. Feng, and G.-H. Cao, J. Am. Chem. Soc. **138**, 7856-7859 (2016).
- [56] T. Wang, J. Chu, H. Jin, J. Feng, L. Wang, Y. Song, C. Zhang, X. Xu, W. Li, Z. Li, T. Hu, D. Jiang, W. Peng, X. Liu, and G. Mu, J. Phys. Chem. C. **123**, 13925-13929 (2019).

- [57] C. de la Cruz, Q. Huang, J. W. Lynn, J. Li, W. Ratcliff, J. L. Zarestky, H. A. Mook, G. F. Chen, J. L. Luo, N. L. Wang and P. Da, *Nature* **453**, 899 (2008).
- [58] J. Dong, H.J. Zhang, G. Xu, Z. Li, G. Li, W.Z. Hu, D. Wu, G.F. Chen, X. Dai, J.L. Luo, *Europhys. Lett.* **83**, 27006 (2008).
- [59] C.-C. Chen, J. Maciejko, A. P. Sorini, B. Moritz, R. R. P. Singh, and T. P. Devereaux, *Phys. Rev. B* **82**, 100504 (2010).
- [60] S. Sen, H. Ghosh, A. K. Sinha, A. Bharathi, *Supercond. Sci. Technol.* **27**, 122003 (2014).
- [61] K. Sasmal, B. Lv, B. Lorenz, A. M. Guloy, F. Chen, Y.-Y. Xue, and C.-W. Chu, *Phys. Rev. Lett.* **101**, 107007 (2008).
- [62] F. K. K. Kirschner, D. T. Adroja, Z.-C. Wang, F. Lang, M. Smidman, P. J. Baker, G.-H. Cao, and S. J. Blundell, *Phys. Rev. B* **97**, 060506(R) (2018).
- [63] M. Smidman, F. K. K. Kirschner, D. T. Adroja, A. D. Hillier, F. Lang, Z. C. Wang, G. H. Cao, and S. J. Blundell, *Phys. Rev. B* **97**, 060509(R)(2018).
- [64] T. Xie, Y. Wei, D. Gong, T. Fennell, U. Stuhr, R. Kajimoto, K. Ikeuchi, S. Li, J. Hu, and H. Luo, *Phys. Rev. Lett.* **120**, 267003 (2018).
- [65] T. Xie, D. Gong, H. Ghosh, A. Ghosh, M. Soda, T. Masuda, S. Itoh, F. Bourdarot, L.-P. Regnault, S. Danilkin, S. Li and H.. Luo, *Phys. Rev. Lett.* **120**, 137001 (2018).
- [66] Y. Y. Huang, Z. C. Wang, Y. J. Yu, J. M. Ni, Q. Li, E. J. Cheng, G. H. Cao, and S. Y. Li, *Phys. Rev. B* **99**, 020502(R) (2019).
- [67] J. Ishida, S. Iimura, and H. Hosono, *Phys. Rev. B* **96** 174522 (2017).
- [68] G. Wang, Z. Wang and X. Shi, *EPL* **116**, 37003 (2016).

- [69] W. R. Meier, Q.-P. Ding, A. Kreyssig, S. L. Bud'ko, A. Sapkota, K. Kothapalli, V. Borisov, R. Valentí, C. D. Batista, P. P. Orth, R. M. Fernandes, A. I. Goldman, Y. Furukawa, A. E. Böhmer, and P. C. Canfield, *npj Q. Mat.* **3**, 5 (2018).
- [70] S. Benhabib, A. Sacuto, M. Civelli, I. Paul, M. Cazayous, Y. Gallais, M.-A. Masson, R.D. Zhong, J. Schneeloch, G.D. Gu, D. Colson, and A. Forget, *Phys. Rev. Lett.* **114**, 147001 (2015).
- [71] S.-Y. Xu, C. Liu, I. Belopolski, S. K. Kushwaha, R. Sankar, J. W. Krizan, T.-R. Chang, C. M. Polley, J. Adell, T. Balasubramanian, K. Miyamoto, N. Alidoust, Guang Bian, M. Neupane, H.-T. Jeng, C.-Y. Huang, W.-F. Tsai, T. Okuda, A. Bansil, F. C. Chou, R. J. Cava, H. Lin, and M. Z. Hasan, *Phys. Rev. B* **92**, 075115 (2015).
- [72] Y. Lemonik, I. L. Aleiner, C. Toke and V. I. Fal'ko, *Phys. Rev. B* **82** 201408(R) (2010).
- [73] A. Varlet, D. Bischoff, P. Simonet, K. Watanabe, T. Taniguchi, T. Ihn, K. Ensslin, M. M.-Kruczynski, and V. I. Falko, *Phys. Rev. Lett.* **113**, 116602 (2014).
- [74] N. Xu, P. Richard, X. Shi, A. van Rooykeghem, T. Qian, E. Razzoli, E. Rienks, G.-F. Chen, E. Ieki, K. Nakayama, T. Sato, T. Takahashi, M. Shi and H. Ding, *Phys. Rev. B* **88**, 220508 (2013).
- [75] H. Miao, T. Qian, X. Shi, P. Richard, T. K. Kim, M. Hoesch, L. Y. Xing, X. C. Wang, C. Q. Jin, J. P. Hu and H. Ding, *Nat. Commun.* **6**, 6056 (2015).
- [76] D. Liu, W. Zhang, D. Mou, J. He, Y.-B. Ou, Q.-Y. Wang, Z. Li, L. Wang, L. Zhao, S. He, Y. Peng, X. Liu, C. Chen, L. Yu, G. Liu, X. Dong, J. Zhang, C. Chen, Z. Xu, J. Hu, X. Chen, X. Ma, Q. Xue and X. J. Zhou, *Nat. Commun.* **3**, 931 (2012).
- [77] C. H. P. Wen, H. C. Xu, C. Chen, Z. C. Huang, X. Lou, Y. J. Pu, Q. Song, B. P. Xie, M. Abdel-Hafez, D. A. Chareev, A. N. Vasiliev, R. Peng and D. L. Feng, *Nat. Commun.* **7**, 10840 (2016).

- [78] B. Lei, J. H. Cui, Z. H. Xiang, C. Shang, N. Z. Wang, G. J. Ye, X. G. Luo, T. Wu, Z. Sun and X. H. Chen, Phys. Rev. Lett. **116**, 077002.
- [79] X. H. Niu, R. Peng, H. C. Xu, Y. J. Yan, J. Jiang, D. F. Xu, T. L. Yu, Q. Song, Z. C. Huang, Y. X. Wang, B. P. Xie, X. F. Lu, N. Z. Wang, X. H. Chen, Z. Sun and D. L. Feng, Phys. Rev. B **92**, 060504 (2015).
- [80] N. Xu, P. Richard, X. Shi, A. van Roekeghem, T. Qian, E. Razzoli, E. Rienks, G.-F. Chen, E. Ieki, K. Nakayama, T. Sato, T. Takahashi, M. Shi and H. Ding, Phys. Rev. B **88**, 220508 (2013).
- [81] S. N. Gupta, A. Singh, K. Pal, D. V. S. Muthu, C. Shekhar, M. A. Elghazali, P. G. Naumov, S. A. Medvedev, C. Felser, U. V. Waghmare, J. Phys. Condens. Matter. **30**, 185401 (2018).
- [82] A. Ptok, K. J. Kapcia, A. Cichy, A. M. Oles and P. Piekarczyk, Sci. Rep. **7**, 41979; doi: 10.1038/srep41979 (2017).
- [83] S. Mukherjee, A. Kreisel, P. J. Hirschfeld, and B. M. Andersen, Phys. Rev. Lett. **115**, 026402 (2015).
- [84] D. V. Chichinadze and A. V. Chubukov, Phys. Rev. B **97**, 094501 (2018).
- [85] S. Iimura, S. Matsuishi, H. Sato, T. Hanna, Y. Muraba, S. W. Kim, J. E. Kim, M. Takata, and H. Hosono, Nat. Comm. **3** 943 (2012).
- [86] M. Ren, Y. Yan, X. Niu, R. Tao, D. Hu, R. Peng, B. Xie, J. Zhao, T. Zhang, and D.-L. Feng, Sci. Adv. **3**, 7 (2017).
- [87] Y. Yamamoto, H. Yamaoka, M. Tanaka, H. Okazaki, T. Ozaki, Y. Takano, J.-F. Lin, H. Fujita, T. Kagayama, K. Shimizu, N. Hiraoka, H. Ishii, Y.-F. Liao, K.-D. Tsuei and J. Mizuki, Sci. Rep. **6**, 30946 (2016).
- [88] X. Shi, Z.-Q. Han, X.-L. Peng, P. Richard, T. Qian, X.-X. Wu, M.-W. Qiu, S. C. Wang, J. P. Hu, Y.-J. Sun, and H. Ding. Nat. Comm. **8**, 14988 (2017).

- [89] H. Ghosh and S. Sen, J. Phys. Chem. Solids **103**, 170–178 (2017).
- [90] N. Xu, P. Richard, X. Shi, A. van Roekeghem, T. Qian, E. Razzoli, E. Rienks, G.-F. Chen, E. Ieki, K. Nakayama, T. Sato, T. Takahashi, M. Shi and H. Ding, Phys. Rev. B **88**, 220508 (2013).
- [91] L. Wang, F. Hardy, A. E. Böhmer, T. Wolf, P. Schweiss and C. Meingast, Phys. Rev. B **93**, 014514 (2016).
- [92] C. Liu, A. D. Palczewski, R. S. Dhaka, T. Kondo, R. M. Fernandes, E. D. Mun, H. Hodovanets, A. N. Thaler, J. Schmalian, S. L. Bud’ko, P. C. Canfield, and A. Kaminski, Phys. Rev. B **84**, 020509 (2011).
- [93] T. Iye, Y. Nakai, S. Kitagawa, K. Ishida, S. Kasahara, T. Shibauchi, Y. Matsuda and T. Terashima, Phys. Rev. B **85**, 184505 (2012).
- [94] A. Ghosh, H. Ghosh and S. Sen, Intermetallics **107**, 126–136 (2019).
- [95] S. Kawasaki, T. Mabuchi, S. Maeda, T. Adachi, T. Mizukami, K. Kudo, M. Nohara and G.-q. Zheng, Phys. Rev. B **92**, 180508 (2015).
- [96] T. Xie, D. Gong, W. Zhang, Y. Gu, Z. Huesges, D. Chen, Y. Liu, L. Hao, S. Meng, Z. Lu, S. Li and H. Luo, Supercond. Sci. Technol. **30**, 095002 (2017).
- [97] A. A. Kordyuk, Low Temp. Phys. **38**, 9 (2012).
- [98] A. A. Kordyuk, Low Temp. Phys. **44**, 6 (2018).
- [99] D. V. Evtushinsky, D. S. Inosov, V. B. Zabolotnyy, M. S. Viazovska, R. Khasanov, A. Amato, H.-H. Klauss, H. Luetkens, Ch. Niedermayer, G. L. Sun, V. Hinkov, C. T. Lin, A. Varykhalov, A. Koitzsch, M. Knupfer, B. Buchner, A. A. Kordyuk, and S. V. Borisenko, New J. Phys. **11**, 055069 (2009).
- [100] S. V. Borisenko, V. B. Zabolotnyy, A. A. Kordyuk, D. V. Evtushinsky, T. K. Kim, I. V. Morozov, R. Follath, and B. Buchner, Symmetry **4**, 251 (2012).

- [101] D. V. Evtushinsky, V. B. Zabolotnyy, T. K. Kim, A. A. Kordyuk, A. N. Yaresko, J. Maletz, S. Aswartham, S. Wurmehl, A. V. Boris, D. L. Sun, C. T. Lin, B. Shen, H. H. Wen, A. Varykhalov, R. Follath, B. Buchner, and S. V. Borisenko, *Phys. Rev. B* **89**, 064514 (2014).
- [102] D. V. Evtushinsky, A. A. Kordyuk, V. B. Zabolotnyy, D. S. Inosov, T. K. Kim, B. Buchner, H. Luo, Z. Wang, H.-H. Wen, G. Sun, C. Lin, and S. V. Borisenko, *J. Phys. Soc. Jpn.* **80**, 023710 (2011).
- [103] S. Aswartham, M. Abdel-Hafiez, D. Bombor, M. Kumar, A. U. B. Wolter, C. Hess, D. V. Evtushinsky, V. B. Zabolotnyy, A. A. Kordyuk, T. K. Kim, S. V. Borisenko, G. Behr, B. Buchner, and S. Wurmehl, *Phys. Rev. B* **85**, 224520 (2012).
- [104] D. V. Evtushinsky, V. B. Zabolotnyy, L. Harnagea, A. N. Yaresko, S. Thirupathiah, A. A. Kordyuk, J. Maletz, S. Aswartham, S. Wurmehl, E. Rienks, R. Follath, B. Buchner, and S. V. Borisenko, *Phys. Rev. B* **87**, 094501 (2013).
- [105] C. Liu, A. D. Palczewski, R. S. Dhaka, T. Kondo, R. M. Fernandes, E. D. Mun, H. Hodovanets, A. N. Thaler, J. Schmalian, S. L. Bud'ko, P. C. Canfield, and A. Kaminski, *Phys. Rev. B* **84**, 020509 (2011).
- [106] S. V. Borisenko, V. B. Zabolotnyy, A. A. Kordyuk, D. V. Evtushinsky, T. K. Kim, I. V. Morozov, R. Follath, and B. Buchner, *Symmetry* **4**, 251 (2012).
- [107] C. He, Y. Zhang, B. P. Xie, X. F. Wang, L. X. Yang, B. Zhou, F. Chen, M. Arita, K. Shimada, H. Namatame, M. Taniguchi, X. H. Chen, J. P. Hu, and D. L. Feng, *Phys. Rev. Lett.* **105**, 117002 (2010).
- [108] J. Maletz, V. B. Zabolotnyy, D. V. Evtushinsky, A. N. Yaresko, A. A. Kordyuk, Z. Shermadini, H. Luetkens, K. Sedlak, R. Khasanov, A. Amato, A. Krzton-Maziopa, K. Conder, E. Pomjakushina, H.-H. Klauss, E. D. L. Rienks, B. Buchner, and S. V. Borisenko, *Phys. Rev. B* **88**, 134501 (2013).

- [109] S. Thirupathaiah, T. Sturzer, V. B. Zabolotnyy, D. Johrendt, B. Buchner, and S. V. Borisenko, *Phys. Rev. B* **88**, 140505 (2013).
- [110] A. Charnukha, S. Thirupathaiah, V. B. Zabolotnyy, B. Buchner, N. D. Zhigadlo, B. Batlogg, A. N. Yaresko, and S. V. Borisenko, *Sci. Rep.* **5**, 10392 (2015).
- [111] A. Charnukha, D. V. Evtushinsky, C. E. Matt, N. Xu, M. Shi, B. Buchner, N. D. Zhigadlo, B. Batlogg, and S. V. Borisenko, *Sci. Rep.* **5**, 18273 (2015).
- [112] A. Varlamov, V. Egorov, and A. Pantsulaya, *Adv. Phys.* **38**, 469 (1989).
- [113] Y. Blanter, M. I. Kaganov, A. V. Pantsulaya, and A. A. Varlamov, *Phys. Rep.* **245**, 159 (1994).
- [114] Z. R. Ye, Y. Zhang, F. Chen, M. Xu, J. Jiang, X. H. Niu, C. H. P. Wen, L. Y. Xing, X. C. Wang, C. Q. Jin, B. P. Xie and D. L. Feng, *Phys. Rev. X* **4**, 031041 (2014).
- [115] M. Yi, Meng Wang, A. F. Kemper, S.-K. Mo, Z. Hussain, E. Bourret-Courchesne, A. Lanzara, M. Hashimoto, D. H. Lu, Z.-X. Shen and R. J. Birgeneau, *Phys. Rev. Lett.* **115**, 256403 (2015).
- [116] M. Yi, Z.-K Liu, Y. Zhang, R. Yu, J.-X. Zhu, J.J. Lee, R.G. Moore, F.T. Schmitt, W. Li, S.C. Riggs, J.-H. Chu, B. Lv, J. Hu, M. Hashimoto, S.-K. Mo, Z. Hussain, Z.Q. Mao, C.W. Chu, I.R. Fisher, Q. Si, Z.-X. Shen, and D.H. Lu, *Nat. Commun.*, **6**, 7777 (2015).
- [117] A. A. Abrikosov, *Fundamentals of the theory of metals*, Elsevier Science Publishers B. V. (1988), ISBN 0444 870954.
- [118] G. E. Volovik, *Fizika Nizkikh Temperatur* **43**, 57-67 (2017).
- [119] R. G. Parr, W. Yang (1994). *Density-Functional Theory of Atoms and Molecules*. Oxford: Oxford University Press. ISBN 978-0-19-509276-9.
- [120] P. Hohenberg and W. Kohn, *Physical Review* **136**, B864 (1964).

- [121] W. Kohn and J. Sham Physical Review **140**, 4A (1965).
- [122] S. H. Vosko, L. Wilk and M. Nusair, Can. J. Phys. 58 (8): 1200–1211 (1980).
Bibcode:1980CaJPh..58.1200V. doi:10.1139/p80-159.
- [123] D. C. Langreth, M. J. Mehl, Physical Review B. **28** (4): 1809 (1983).
- [124] D. A. Becke, Physical Review A. **38** (6): 3098–3100 (1988).
- [125] J. P. Perdew, K. Burke, and M. Ernzerhof, Phys. Rev. Lett. **77**, 3865 (1996).
- [126] L. Bellaiche, D. Vanderbilt, Phys. Rev. B **61**, 7877-7782 (2000).
- [127] B. Himmetoglu, A. Floris, S. de Gironcoli, and M. Cococcioni, International Journal of Quantum Chemistry **114**, 14-49 (2014).
- [128] S.J. Clark, M. D. Segall, C. J. Pickard, P. J. Hasnip, M. J. Probert, K. Refson, M. C. Payne, Z. fuer Kristallogr. **200**, 567 (2005).
- [129] S. Sen, H. Ghosh, Eur. Phys. J. B. **12**, 277 (2016).
- [130] <http://www.tcm.phy.cam.ac.uk/castep/documentation/WebHelp/content/modules/castep/thcastepdisorder.htm>.
- [131] P. Larson and S. Satpathy, Phys. Rev. B **79**, 054502 (2009).
- [132] S. Sen and H. Ghosh, Eur. Phys. J. B **89**, 277 (2016).
- [133] H. J. Monkhorst and J. D. Pack, Phys. Rev. B **13**, 5188 (1976).
- [134] J. D. Pack and H. J. Monkhorst, Phys. Rev. B **16**, 1748 (1977).
- [135] P. Giannozzi *et al*, J. Phys. Condens. Matter **21** 395502 (2009).
- [136] Z.H. Liu, T. K. Kim, A. Sala, H. Ogino, J. Shimoyama, B. Bchner and S. V. Borisenko, Appl. Phys. Lett. **106**, 052602 (2015).
- [137] A. Ghosh, H. Ghosh, S. Sen, Intermetallics **107**, 126–136 (2019).

- [138] A. Ghosh, H. Ghosh, Computational Materials Science **160**, 62–71 (2019).
- [139] T. Xie, D. Gong, H. Ghosh, A. Ghosh, M. Soda, T. Masuda, S. Itoh, F. Bourdarot, L.-P. Regnault, S. Danilkin, S. Li, H. Luo, Physical Review Letters **120**, 137001 (2018).
- [140] A. Ghosh and H. Ghosh, International Journal of Environmental Analytical Chemistry, 1-12 (2019).
- [141] A. Ghosh, S. Sen and H. Ghosh, Computational Materials Science **186**, 109991 (2021).
- [142] A. Ghosh, S. Ghosh and H. Ghosh, Computational Materials Science **183**, 109802 (2020).
- [143] A. Charnukha, S. Thirupathaiah, V. B. Zabolotnyy, B. Büchner, N. D. Zhigadlo, B. Batlogg, A. N. Yaresko and S. V. Borisenko Sci. Rep. **5** 10392; doi: 10.1038/srep10392 (2015).
- [144] W. Malaeb, T. Shimojima, Y. Ishida, K. Okazaki, Y. Ota, K. Ohgushi, K. Kihou, T. Saito, C. H. Lee, S. Ishida, M. Nakajima, S. Uchida, H. Fukazawa, Y. Kohori, A. Iyo, H. Eisaki, C.-T. Chen, S. Watanabe, H. Ikeda, and S. Shin, Phys. Rev. B **86**, 165117 (2012).
- [145] Yoshihiko Okamoto, Atsushi Nishio, and Zenji Hiroi, Phys. Rev. B **81**, 121102 (R) (2010).
- [146] I. R. Shein and A. L. Ivanovskii, Phys. of the Sol. St. **52**, 1 (2010).
- [147] S. Sen and H. Ghosh, Phys. Lett. A **379**, 843–847 (2015).
- [148] A. Joshua, S. Pecker, J. Ruhman, E. Altman, S. Ilani, Nat. Comm. **3:1129**, DOI: 10.1038/ncomms2116.
- [149] P. Cheng, B. Shen, J. P. Hu and H. H. Wen, Phys. Rev. B **81** , 174529 (2010).

- [150] F. Hammerath, P. Bonfà, S. Sanna, G. Prando, R. De Renzi, Y. Kobayashi, M. Sato, and P. Carretta, *Phys. Rev. B* **89**, 134503 (2014).
- [151] M. N. Gastiasoro, F. Bernardini, and B. M. Andersen, *PRL* **117**, 257002 (2016).
- [152] M. D. Lumsden and A. D. Christianson, *J. Phys. Condens. Matter* **22**, 203203 (2010).
- [153] J. M. Schoen, *Phys. Rev.* **184**, 858 (1969).
- [154] T. Xie, D. Gong, H. Ghosh, A. Ghosh, M. Soda, T. Masuda, S. Itoh, F. Bourdarot, L.-P. Regnault, S. Danilkin, S. Li, and H. Luo, *Phys. Rev. Lett.* **120**, 137001 (2018).
- [155] S. Thirupathaiah, T. Sturzer, V. B. Zabolotnyy, D. Johrendt, B. Buchner, and S. V. Borisenko, *Phys. Rev. B* **88**, 140505(R) (2013).
- [156] S. Sen, H. Ghosh, *J. Alloys Compd.* **618**, 102–109 (2015).
- [157] A. Charnukha, D. V. Evtushinsky, C. E. Matt, N. Xu, M. Shi, B. Büchner, N. D. Zhigadlo, B. Batlogg, and S. V. Borisenko, *Sci. Rep.* **5**, 18273 (2015).
- [158] M. Yi, Y. Zhang, Z.-X. Shen & D. Lu, *npj Q. Mat.* **2**, 57 (2017).
- [159] D. Wu, S. Wang, J. Yuan, B. Yangab, and H. Chen, *Phys. Chem. Chem. Phys.* **19**, 11771 (2017).
- [160] D. Wu, S. Wang, S. Zhang, Y. Liu, Y. Ding, B. Yanga, and H. Chen, *Phys. Chem. Chem. Phys.* 2018, DOI: 10.1039/c8cp05008b.
- [161] H. Li, Z. Zhang, Y. Liu, W. Cen, and X. Luo, *Nanomaterials*, **8**, 589 (2018).
- [162] D. Wu, B. Yang, H. Chen, and E. Ruckenstein, *Energy storage materials*, doi:10.1016/j.ensm.2018.09.001 (2018).
- [163] R. Yu and Q. Si, *Phys. Rev. Lett.* **110**, 146402 (2013).

- [164] Y. Nagai, H. Nakamura, M. Machida and K. Kuroki, J. Phys. Soc. Jap. **84**, 093702 (2015).
- [165] H. Ota, K. Kudo, T. Kimura, Y. Kitahama, T. Mizukami, S. Ioka, M. Nohara, J. Phys. Soc. Jap. **86**, 025002 (2017).
- [166] M. Y. Li, Z. T. Liu, W. Zhou, H. F. Yang, D. W. Shen, W. Li, J. Jiang, X. H. Niu, B. P. Xie, Y. Sun, C. C. Fan, Q. Yao, J. S. Liu, Z. X. Shi and X. M. Xie, Phys. Rev. B **91**, 045112 (2015).
- [167] A. Ghosh, H. Ghosh, and S. Sen, Intermetallics **107**, 126 (2019).
- [168] M. Y. Li, Z. T. Liu, W. Zhou, H. F. Yang, D. W. Shen, W. Li, J. Jiang, X. H. Niu, B. P. Xie, Y. Sun, C. C. Fan, Q. Yao, J. S. Liu, Z. X. Shi, and X. M. Xie, Phys. Rev. B **91**, 045112 (2015).
- [169] A. Ghosh, H. Ghosh, Comput. Mater. Sci. **160**, 62 (2019).
- [170] S. Thirupathaiah, T. Sturzer, V.B. Zabolotnyy, D. Johrendt, B. Buchner, S.V. Borisenko, Phys. Rev. B **88**, 140505 (2013).
- [171] C.-H. Lee, A. Iyo, H. Eisaki, H. Kito, M. T. F.-Diaz, T. Ito, K. Kihou, H. Matsuhata, M. Braden, and K. Yamada, J. Phys. Soc. Jpn. **77**, 083704 (2008).
- [172] G. Kresse and J. Furthmüller, Comp. Mat. Sc. **6**, 15-50 (1996).
- [173] M. Kawamura, Comp. Phys. Commun. **239**, 197 (2019).
- [174] D. Mou, T. Kong, W. R. Meier, F. Lochner, L.-L. Wang, Q. Lin, Y. Wu, S. L. Budko, I. Eremin, D. D. Johnson, P. C. Canfield and A. Kaminski, Phys. Rev. Lett. **117**, 277001 (2016).
- [175] D. V. Suetin, I. R. Shein, J. Supercond. Nov. Magn. **31**, 1683 (2018).

- [176] J. Fink, S. Thirupathaiah, R. Ovsyannikov, H. A. Dürr, R. Follath, Y. Huang, S. de Jong, M. S. Golden, Y.-Z. Zhang, H. O. Jeschke, R. Valentí, C. Felser, S. D. Farahani, M. Rotter and D. Johrendt, *Phys. Rev. B* **79**, 155118 (2009).
- [177] M. Tomic, R. Valenti and H. O. Jeschke, *Phys. Rev. B* **85**, 094105 (2012).
- [178] A. Ghosh, H. Ghosh, *Com. Mat. Sci.* **160**, 62–71 (2019).
- [179] B. Q. Song, M. C. Nguyen, C. Z. Wang and K. M. Ho, *Phys. Rev. B* **97**, 094105 (2018).
- [180] I. M. Lifshitz, *Sov. Phys. JETP* **11**, 1130 (1960).
- [181] K. Iida, Y. Nagai, S. Ishida, M. Ishikado, N. Murai, A. D. Christianson, H. Yoshida, Y. Inamura, H. Nakamura, A. Nakao, K. Munakata, D. Kagerbauer, M. Eisterer, K. Kawashima, Y. Yoshida, H. Eisaki and A. Iyo, *Phys. Rev. B* **100**, 014506 (2019).
- [182] C. Xu, Q. Chen and C. Cao, *Commun. Phys.* **2**, 16 (2019).
- [183] T. Xie, Y. Wei, D. Gong, T. Fennell, U. Stuhr, R. Kajimoto, K. Ikeuchi, S. Li, J. Hu and H. Luo, *Phys. Rev. Lett.* **120**, 267003 (2018).
- [184] S. Graser, T. A. Maier, P. J. Hirschfeld and D. J. Scalapino, *New J. Phys.* **11**, 025016 (2009).
- [185] F. Lochner, F. Ahn, T. Hickel, and I. Eremin, *Phys. Rev. B* **96**, 094521 (2017).
- [186] S. N. Khan and D. D. Johnson, *Phys. Rev. Lett.* **112**, 156401 (2014).
- [187] H. Hodovanets, Y. Liu, A. Jesche, S. Ran, E. D. Mun, T. A. Lograsso, S. L. Bud’ko and P. C. Canfield, *Phys. Rev. B* **89**, 224517 (2014).
- [188] Y. Liu and T. A. Lograsso, *Phys. Rev. B* **90**, 224508 (2014).
- [189] N. Xu, P. Richard, X. Shi, A. van Roekeghem, T. Qian, E. Razzoli, E. Rienks, G.-F. Chen, E. Ieki, K. Nakayama, T. Sato, T. Takahashi, M. Shi and H. Ding, *Phys. Rev. B* **88**, 220508 (2013).

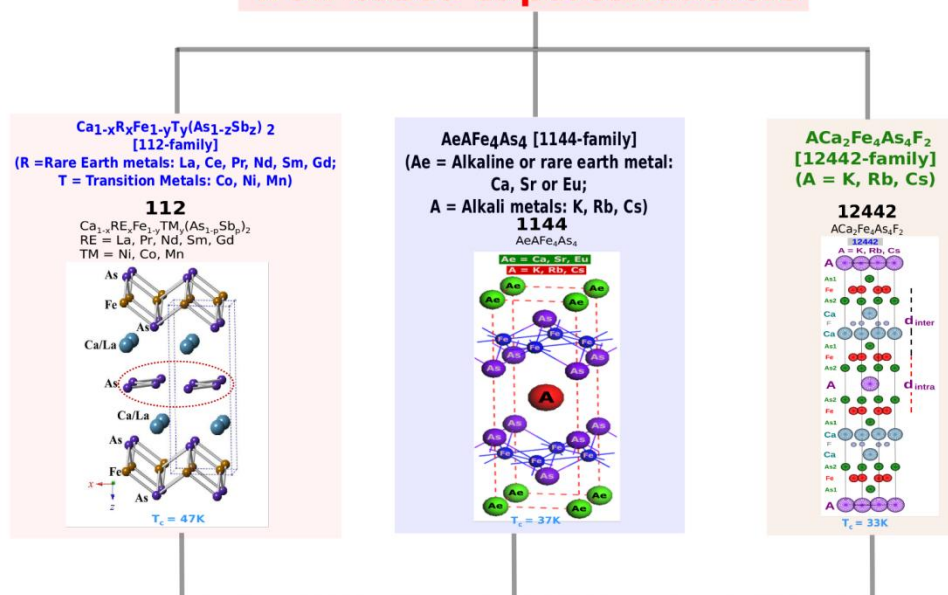
- [190] S. N. Gupta, A. Singh, K. Pal., D. V. S. Muthu, C. Shekhar, M. A. Elghazali, P. G. Naumov, S. A. Medvedev, C. Felser and U. V. Waghmare, *J. Phys. Condens. Matter.* **30** 185401 (2018).
- [191] Ptok, A., Kapcia, K. J., Cichy, A., Oles, A. M. & Piekarz, P. L. *Sci. Rep.* **7**, 41979 (2017).
- [192] M. Yi, Z. -K. Liu, Y. Zhang, R. Yu, J. -X. Zhu, J. J. Lee, R. G. Moore, F. T. Schmitt, W. Li, S. C. Riggs, J. -H. Chu, B. Lv, J. Hu, M. Hashimoto, S. -K. Mo, Z. Hussain, Z. Q. Mao, C. W. Chu, I. R. Fisher, Q. Si, Z. -X. Shen, *Nat. Comm.* **6**, 7777 (2015).
- [193] P. O. Sprau, A. Kostin, A. Kreisel, A. E. Bohmer, V. Taufour, P. C. Canfield, S. Mukherjee, P. J. Hirschfeld, B. M. Andersen, J. C. S. Davis, *Science* **357**, 75 (2017).
- [194] M. Yi, M. Wang, A. F. Kemper, S.-K. Mo, Z. Hussain, E. B.-Courchesne, A. Lanzara, M. Hashimoto, D. H. Lu, Z.-X. Shen and R. J. Birgeneau, *Phys. Rev. Lett.* **115**, 256403 (2015).
- [195] Q. Si, E. Abrahams, J. Dai and J.-X. Zhu, *New J. Phys.* **11**, 045001 (2009).
- [196] C. L. Chen, C. L. Dong, J. L. Chen, J. -H. Guo, W. L. Yang, C. C. Hsu, K. W. Yeh, T. W. Huang, B. H. Mok, T. S. Chan, J. F. Lee, C. L. Chang, S. M. Raoa and M. K. Wu, *Phys. Chem. Chem. Phys.* **13**, 15666-15672 (2011).
- [197] A. Charnukha, K. W. Post, S. Thirupathaiah, D. Präpper, S. Wurmehl, M. Roslova, I. Morozov, B. Büchner, A. N. Yaresko, A. V. Boris, S. V. Borisenko and D. N. Basov, *Sci. Rep.* **6**, 18620 (2016).
- [198] E. M. Nica, R. Yu, & Q. Si, *npj Q. Mat.* **2**, 26 (2017).
- [199] A. Kreisel, B. M. Andersen, P. O. Sprau *et al.*, *Phys. Rev. B* **95**, 174504 (2017).
- [200] F. Kruger, S. Kumar, J. Zaanen, and J. Brink, *Phys. Rev. B* **79**, 054504 (2009).

- [201] A. A. Mostofi, J. R. Yates, G. Pizzi, Y. S. Lee, I. Souza, D. Vanderbilt, N. Marzari, Comput. Phys. Commun. **185**, 2309 (2014).
- [202] J. Wang, Y. Wu, X. Zhou, Y. Li, B. Teng, P. Dong, J. He, Y. Zhang, Y. Ding and J. Li, ADVANCES IN PHYSICS: X, **6**, 1, 1878931 (2021).
- [203] D. Mou, T. Kong, W. R. Meier, F. Lochner, L.-L. Wang, Q. Lin, Y. Wu, S. L. Bud'ko, I. Eremin, D. D. Johnson, P. C. Canfield, and A. Kaminski, Phys. Rev. Lett. **117**, 277001 (2016).
- [204] J. Fink, S. Thirupathaiah, R. Ovsyannikov, H. A. Dürr, R. Follath, Y. Huang, S. de Jong, M. S. Golden, Y.-Z. Zhang, H. O. Jeschke, R. Valentí, C. Felser, S. D. Farahani, M. Rotter, and D. Johrendt, Phys. Rev. B **79**, 155118 (2009).
- [205] Y. Yamakawa, S. Onari, and H. Kontani, Phys. Rev. X **6**, 021032 (2016).
- [206] K. Momma and F. Izumi, J. Appl. Crystallogr. **44**, 1272-1276 (2011).
- [207] T. Terashima , Y. Matsushita , H. Yamase, N. Kikugawa, H. Abe, M. Imai, S. Uji, S. Ishida , H. Eisaki, A. Iyo, K. Kihou, C.-H. Lee, T. Wang, and G. Mu, Phys. Rev. B **102**, 054511 (2020).
- [208] L. d. Medici, Springer Series in Materials Science, **211**, 409-441 (2015).
- [209] D. Mou, T. Kong, W. R. Meier, F. Lochner, L.-L. Wang, Q. Lin, Y. Wu, S. L. Bud'ko, I. Eremin, D. D. Johnson, P. C. Canfield, and A. Kaminski, Phys. Rev. Lett. **117**, 277001 (2016).
- [210] S. Maiti, M. M. Korshunov, T. A. Maier, P. J. Hirschfeld, and A. V. Chubukov, Phys. Rev. Lett. **107**, 147002 (2011).
- [211] D. Wu, W. Hong, C. Dong, X. Wu, Q. Sui, J. Huang, Q. Gao, C. Li, C. Song, H. Luo, C. Yin, Y. Xu, X. Luo, Y. Cai, J. Jia, Q. Wang, Y. Huang, G. Liu, S. Zhang, F. Zhang, F. Yang, Z. Wang, Q. Peng, Z. Xu, X. Qiu, S. Li, H. Luo, J. Hu, L. Zhao, and X. J. Zhou, Phys. Rev. B **101**, 224508 (2020).

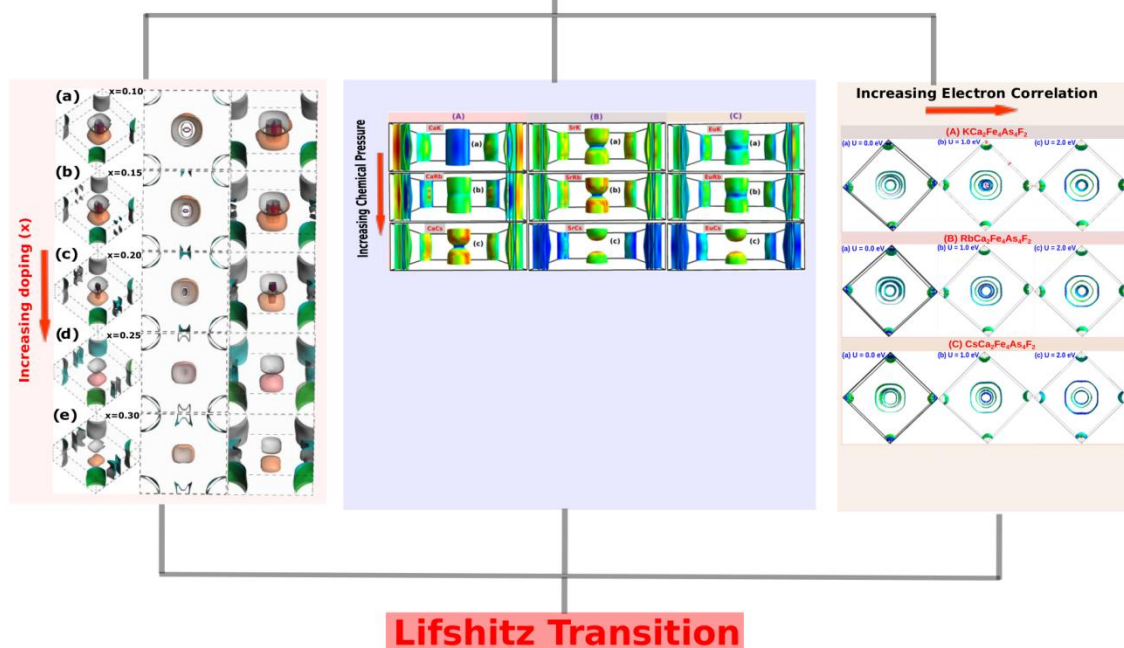
- [212] P. O. Sprau, A. Kostin, A. Kreisel, A. E. Bohmer, V. Taufour, P. C. Canfield, S. Mukherjee, P. J. Hirschfeld, B. M. Andersen, J. C. S. Davis, *Science* **357**, 75 (2017).
- [213] E. M. Nica, R. Yu, and Q. Si, *npj Quantum Materials* **2**, 26 (2017).
- [214] A. Kreisel, B. M. Andersen, P. O. Sprau, A. Kostin, J. C. S. Davis, and P. J. Hirschfeld, *Phys. Rev. B* **95**, 174504 (2017).
- [215] N. Marzari and D. Vanderbilt, *Phys. Rev. B* **56**, 12847 (1997).
- [216] I. Souza, N. Marzari, D. Vanderbilt. *Phys. Rev. B.* **65** 035109 (2002).
- [217] A. A. Mostofi, J. R. Yates, Y. -S. Lee, I. Souza, D. Vanderbilt, N. Marzari, *Comput. Phys. Commun.* **178**, 685 (2008).
- [218] J. Kunes, R. Arita, P. Wissgott, A. Toschi, H. Ikeda, K. Held, *Comput. Phys. Commun.* **181**, 1888 (2010).
- [219] T. Miyake, K. Nakamura, R. Arita, and M. Imada, *Journal of the Physical Society of Japan*, **79**, 044705 (2010).
- [220] D. Wu, W. Hong, C. Dong, X. Wu, Q. Sui, J. Huang, Q. Gao, C. Li, C. Song, H. Luo, C. Yin, Y. Xu, X. Luo, Y. Cai, J. Jia, Q. Wang, Y. Huang, G. Liu, S. Zhang, F. Zhang, F. Yang, Z. Wang, Q. Peng, Z. Xu, X. Qiu, S. Li, H. Luo, J. Hu, L. Zhao, and X. J. Zhou, *Phys. Rev. B* **101**, 224508 (2020).
- [221] A. Ghosh, S. Ghosh, H. Ghosh, *Computational Materials Science* **183** (2020) 109802.

Thesis Highlight

Iron based superconductors



Electronic Structure



Lifshitz Transition

Figure 1: Schematic of the electronic structure study of iron based superconductors revealing Lifshitz transition.